NASA/CR—2012-217628

Measurements and Simulations of Surface Dielectric Barrier Discharges Used as Plasma Actuators

Final Report

Alan R. Hoskinson
University of Wisconsin-Madison, Madison, Wisconsin

September 2012

NASA STI Program . . . in Profile

Since its founding, NASA has been dedicated to the advancement of aeronautics and space science. The NASA Scientific and Technical Information (STI) program plays a key part in helping NASA maintain this important role.

The NASA STI Program operates under the auspices of the Agency Chief Information Officer. It collects, organizes, provides for archiving, and disseminates NASA's STI. The NASA STI program provides access to the NASA Aeronautics and Space Database and its public interface, the NASA Technical Reports Server, thus providing one of the largest collections of aeronautical and space science STI in the world. Results are published in both non-NASA channels and by NASA in the NASA STI Report Series, which includes the following report types:

- TECHNICAL PUBLICATION. Reports of completed research or a major significant phase of research that present the results of NASA programs and include extensive data or theoretical analysis. Includes compilations of significant scientific and technical data and information deemed to be of continuing reference value. NASA counterpart of peer-reviewed formal professional papers but has less stringent limitations on manuscript length and extent of graphic presentations.

- TECHNICAL MEMORANDUM. Scientific and technical findings that are preliminary or of specialized interest, e.g., quick release reports, working papers, and bibliographies that contain minimal annotation. Does not contain extensive analysis.

- CONTRACTOR REPORT. Scientific and technical findings by NASA-sponsored contractors and grantees.

- CONFERENCE PUBLICATION. Collected papers from scientific and technical conferences, symposia, seminars, or other meetings sponsored or cosponsored by NASA.

- SPECIAL PUBLICATION. Scientific, technical, or historical information from NASA programs, projects, and missions, often concerned with subjects having substantial public interest.

- TECHNICAL TRANSLATION. English-language translations of foreign scientific and technical material pertinent to NASA's mission.

Specialized services also include creating custom thesauri, building customized databases, organizing and publishing research results.

For more information about the NASA STI program, see the following:

- Access the NASA STI program home page at *http://www.sti.nasa.gov*

- E-mail your question to *help@sti.nasa.gov*

- Fax your question to the NASA STI Information Desk at 443–757–5803

- Telephone the NASA STI Information Desk at 443–757–5802

- Write to:
  STI Information Desk
  NASA Center for AeroSpace Information (CASI)
  7115 Standard Drive
  Hanover, MD 21076–1320

NASA/CR—2012-217628

Measurements and Simulations of Surface Dielectric Barrier Discharges Used as Plasma Actuators

Final Report

Alan R. Hoskinson
University of Wisconsin-Madison, Madison, Wisconsin

Prepared under Cooperative Agreement NNX07AB84A
Prepared under Grant FA9550–07–1–0025

National Aeronautics and
Space Administration

Glenn Research Center
Cleveland, Ohio 44135

September 2012

Acknowledgments

All of this work was conducted under the guidance of Dr. Noah Hershkowitz, my advisor for 5 years at the University of Wisconsin-Madison. He has always encouraged me to follow my interests, even when they lead to less familiar research territory and a semester as a teaching assistant.

My research has also benefited over the years from numerous conversations with members of my doctoral committee: Dr. Carl Sovinec and Dr. Riccardo Bonazza from the Engineering Physics department, and Dr. Amy Wendt and Dr. John Scharer from the Electrical and Computer Engineering department. Several others have also provided me with technical advice and support. Dr. David Ashpis of the NASA Glenn Research Center provided numerous suggestions regarding pressure measurements in low-speed gas flows. Dr. Lutfi Oksuz, an associate professor at Süleyman Demiral University in Turkey and a visiting scientist at UW, assisted with the acquisition of the nanosecond-scale optical imaging data. Dr. Jon Ahn, a visiting professor from Sejong University in South Korea, provided helpful advice regarding the setup of the differential pressure sensor. Funding for this work was provided by NASA through cooperative agreement NNX07AB84A, monitored by Dr. David Ashpis, and by the Air Force Office of Scientific Research (AFOSR) through Grant no. FA9550–07–1–0025, monitored by Dr. Robert Barker.

My studies have been supported indirectly by numerous others. Over the years I have had many helpful and interesting discussions with the other graduate students in my lab, particularly Ben Longmier, Scott Baalrud, Dongsoo Lee, and Young-Chul Kim. My undergraduate thesis advisor, Dr. Sven Bilén of Penn State, has continued to show interest in my progress and provide career advice in the years since I worked with him.

This work was sponsored by the Fundamental Aeronautics Program at the NASA Glenn Research Center.

Level of Review: This material has been technically reviewed by NASA technical management.

Available from

NASA Center for Aerospace Information
7115 Standard Drive
Hanover, MD 21076–1320

National Technical Information Service
5301 Shawnee Road
Alexandria, VA 22312

Available electronically at http://www.sti.nasa.gov

Abstract

Asymmetric surface dielectric barrier discharges (DBDs) have shown promise for use as aerodynamic actuators which can prevent flow separation from airfoils in low-Reynolds number gas flow. Our DBDs used a symmetric triangular high voltage waveform to generate plasma in atmospheric pressure air. Plasma forms and decays in many nanosecond-scale microdischarges during each millisecond-scale half cycle of the applied voltage, and the device induces a time-averaged force on the nearby air. Time-averaged measurements indicated that the induced force of a single-barrier actuator design (one electrode insulated from the plasma) can be increased exponentially above the results of previous studies by decreasing both the length and thickness of the electrode exposed to the plasma. This increased force may allow these devices to control flow separation in a wider range of flow environments. Experiments using an intensified digital camera to examine the plasma on time scales of a few nanoseconds up to the applied voltage period showed that, in addition to the previously-observed filamentary and jet-like plasma structures, discharges with very thin exposed electrodes exhibited a weak but constant plasma immediately adjacent to those electrodes. In double-barrier actuators (both electrodes insulated), decreasing the diameter of the narrower electrode lead to increasing forces, and recorded images showed the simultaneous existence of both filamentary and jet-like plasma structures. The development and application of a time-dependent, two-dimensional fluid plasma model has aided in undestanding the detailed physics of surface DBDs at all time scales. For simulated single-barrier discharges, the model qualitatively reproduced the filamentary and jet-like microdischarge structures. The model was somewhat successful in reproducing the observed characteristics of double-barrier actuators. For both actuator geometries, the model indicated that the majority of the forces induced on the neutral gas occur in between microdischarges as the plasmas decay.

Table of Contents

Page

Page

List of Figures

Figure Page

Figure Page

Figure Page

Figure Page

Chapter 1

Introduction

The ability to generate non-thermal plasmas at gas pressures on the order of one atmosphere makes novel applications of plasma physics possible. This work describes the study and optimization of one method of high-pressure plasma generation, the surface dielectric barrier discharge, for use as a method of active aerodynamic flow control. The results may also be useful for other applications. We have conducted these investigations experimentally and by developing and applying a computational plasma model. This chapter briefly describes the use of such a discharge for aerodynamics applications, the specific goals of this investigation, and summarizes the major contributions of the work.

1.1 Applications of Surface Dielectric Barrier Discharges

A dielectric barrier discharge (DBD) consists of two electrodes with at least one layer of insulating material in between them. An oscillating voltage is applied to one of the electrodes, while the other electrode is usually grounded. When the electric field in a gas region near the electrodes exceeds the breakdown threshold, plasma is formed via an avalanching ionization process. The presence of the insulating layer prevents the formation of arcs. In contrast to many other plasma systems, in a DBD the plasma forms and is extinguished many times as the applied voltage oscillates. In this work we focus on surface discharges, in which the electrodes either sit on or immediately underneath a dielectric plane. This type of discharge is discussed in more detail in section 2.2.2.

Volumetric DBDs are currently used in industry to generate ozone, treat polymer surfaces, and as components in plasma televisions [1]. Surface DBDs are not as widely used, but have been suggested for a variety of applications including both materials processing and modifying air flow in jet turbines and over wing surfaces. Our work focuses on these latter applications, while also studying the physics of the discharge, which may be of use to the former. The two areas of application are discussed in sections 2.2.2 and 2.3. Surface DBDs with asymmetric configurations, such as that in figure 1.1, affect gas flows by exerting a force on the neutral gas. In quiescent air, this force generates a flow of neutral gas like that in figure 1.1.

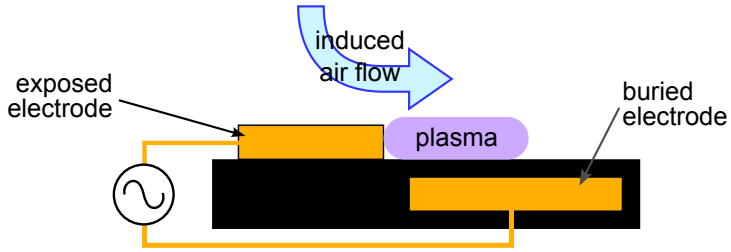

Figure 1.1: Conceptual diagram of a DBD plasma actuator showing electrodes, dielectric (black), and approximate direction of induced air flow

Work in recent years has shown that surface DBDs with one insulated electrode can reduce or eliminate flow separation when placed on the leading edges and surfaces of airfoils . Flow separation increases the drag and reduces the lift of airfoils. When used to limit separation of flows from surfaces, the DBDs are commonly referred to as "plasma actuators" or "DBD actuators." The mechanism by which flow re-attachment occurs is only partially understood [2], but generally increases as the actuator force increases [3]. Wind tunnel experiments have shown that plasma actuators reduce or eliminate flow separation for background flow velocities $\lesssim$ 20 m/s (Reynolds numbers of $\lesssim 1.6 \times 10^5$) [3–5]. The effectiveness depends on many factors including the location and properties of the plasma actuator, the shape of the airfoil, the Reynolds number, the amount of freestream turbulence, and the angle of attack of the airfoil relative to the background flow.

1.2 Motivation of the Current Work

The most-studied potential application of plasma actuators is in jet turbine engines. In the low-pressure stage of commercial jet turbines, flow is fully attached during take-off and landing when the Reynolds number of the flow is large. At cruising altitudes the Reynolds number decreases to the order of 10^5 due in part to reductions in the gas density, and some flow separation occurs from turbine blades [6, 7]. This separation leads to a several percent loss in turbine efficiency at these altitudes [8]. While seemingly small, due to the large number of miles flown and fuel consumed by commercial and military aircraft a few percent increase in fuel efficiency can have large economic and environmental benefits.

Early attempts to use plasma actuators to eliminate flow separation in conditions like those in low-pressure turbines have had only limited success [2, 5]. Increasing the force induced by these actuators is expected to improve their performance in such environments, as well as opening up new uses of plasma actuators. Our research works towards increasing the ability of plasma actuators to cause flow re-attachment by examining the parameters which most strongly affect the magnitude of the forces on the neutral gas.

Past studies of DBD plasma actuators have focused on single-barrier discharge geometries, in which one of the electrodes is insulated and one is exposed to the plasma [e.g. 3]. In contrast, studies examining surface DBDs for materials processing applications [9, 10] have used double-barrier discharges, in which both of the electrodes are insulated. Comparing the two different systems helps us determine the effects of geometry on the plasma and the induced forces.

The research presented in this work examines several questions about the relationships between the discharge design, plasma dynamics, and the induced forces. These include:

- How does the electrode geometry affect the induced forces? What properties can be adjusted to increase these forces?
- How does the plasma structure vary over the course of the applied voltage cycle?
- How does the plasma vary between single- and double-barrier devices?

- Is a 2-dimensional fluid model sufficient to explain plasma behavior in a surface DBD?

1.3 Summary of Contributions by the Current Work

This work makes contributions to the experimental plasma actuator community by examining new device designs, validating force diagnostic techniques and making optical measurements of plasma dynamics. It makes contributions to the computational plasma actuator community by modeling the plasma in double-barrier systems, showing the effects of finite electrode size, and qualitatively validating the simulated plasma dynamics and time-averaged forces against experimental measurements. The major results, innovations, and demonstrations of new techniques of our work are summarized here.

We have demonstrated that the force induced by single-barrier actuators can be dramatically increased by using short, thin exposed electrodes instead of the more commonly-used planar electrodes. Previously only a weak dependence on the thickness of the exposed electrode had been observed. The material of these electrodes does not affect actuator behavior. We have also conducted the first systematic measurements of the double-barrier actuator geometry, using one narrow and one wide electrode. While actuators using this geometry are less powerful and efficient than single-barrier devices, they provide an additional system in which we can compare the experimental and simulated results. Double-barrier discharges are also more commonly employed in processing applications, so our observations of these devices may be of use to that community. Both electronic balances [e.g. 11] and stagnation probe measurements [e.g. 12] have been used by other groups to determine the induced forces. We have made quantitative comparisons between these techniques, showing what assumptions may be safely made when interpreting the stagnation probe data. Detailed results of our force measurements of different actuator designs are included in chapter 4.

Using an intensified digital camera, we have measured features of the plasma microdischarges that occur on the actuator surface when the applied voltage is rising and falling. We have identified a new plasma regime that only occurs in single-barrier actuators with very short and thin exposed electrodes, corresponding to the parameter space of increased device efficiency. We have also

examined the behavior of average microdischarges in actuators with a variety of geometries, and characterized the propagation velocity and lifetime of microdischarges in a single-barrier actuator. These measurements can be used for comparisons to computational model results. The recorded images are displayed and discussed in chapter 5.

We have developed a new 2-dimensional fluid model, partially based on the published work of Bouef et al. [13, 14]. Our implementation has two features not included in existing codes: an adaptive time-stepping algorithm to resolve short-time scale phenomenon without greatly increasing computation time, and the ability to model systems with arbitrary electrode shapes and positions. The code is described in chapter 6. Using this code, we have simulated actuator systems with the same dimensions as our experimental devices. The simulated microdischarges qualitatively resemble those recorded using the digital camera. We have run the first simulations of actuators using the double-barrier geometry. For both geometries, the simulation indicates that the time-averaged force occurs primarily between microdischarges as the plasma decays. These results of our simulation runs are detailed in chapter 7.

Chapter 2

Background and Review of Previous Research

The plasma actuators discussed in this work fall into the class of plasma discharges known as surface dielectric barrier discharges (DBDs). These discharges often, as is the case in this work, operate at or near atmospheric pressure. At these pressures, the behaviors of plasmas are strongly influenced by collisions. The physics of discharges operating in this regime are summarized in sections 2.1 and 2.2

Many studies of DBD actuators have been conducted since the devices were first described in 2000 by Roth et al. [15]. The general field of active flow control, of which DBD actuator research is a subset, is briefly reviewed in section 2.3. Section 2.4 reviews the experimental measurements that have been previously conducted regarding plasma actuator performance. It includes flow measurements near actuators operating in both quiescent air and with background flow velocities, as well as observations of the plasmas themselves. Section 2.5 summarizes existing efforts to model important characteristics of the plasma actuator system.

We note that a significant portion of the research conducted on plasma actuator technology is disseminated via the conference proceedings of several meetings of the American Institute of Aeronautics and Astronautics (AIAA). Unfortunately, much of this work is not subsequently published in peer-reviewed journals. We cite such AIAA papers in this chapter only when no peer-reviewed versions are available.

2.1 Collisional Plasma Theory

A variety of gas discharges operate at or near atmospheric pressure including the surface DBDs discussed in this work, parallel-plate DBDs such as the one pictured in figure 2.1, some microwave discharges, and some of the DC discharges discussed in section 2.2.1. The frequency of collisions in plasmas determine the transport properties, which are central to any theoretical or computational attempts to describe a plasma system. In the analysis presented in this section, we consider plasma with singly-charged ion populations.

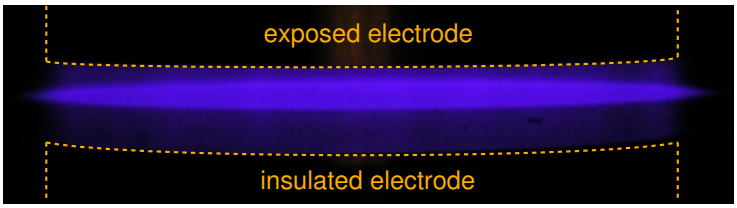

Figure 2.1: Volumetric DBD plasma in air at 10 Torr between two disc-shaped electrodes

2.1.1 The Highly-Collisional Regime

While in general high-pressure plasmas may be expected to be highly collisional, verifying this for a particular system requires some analysis. Whether collisional or collisionless approximations are valid for a given species depends on whether the energy relaxation length for that species is shorter or longer, respectively, than the appropriate scale length for the phenomenon of interest [16]. Different species or different phenomenon in the same plasma may have different collisionalities.

For the phenomena of interest here, the relevant scale length is the Debye length,

$$\lambda_D = \left(\frac{\epsilon_0 T_e}{e^2 n_e} \right)^{1/2}, \tag{2.1}$$

the characteristic length for changes in the electrostatic potential in the plasma. Here T_e is the electron temperature in electron Volts, e is the fundamental charge, and n_e is the electron density. Low-temperature plasmas such as those in DBDs, glow discharges, and other devices have only a

small fraction of the available particles ionized. Consequently, collisions between charged particles are relatively rare and charged particle-neutral collisions dominate the dynamics.

For elastic ion-neutral collisions, both particles are of comparable mass so significant energy transfer is possible between particles. The ion energy relaxation length is therefore approximately equal to the mean free path for ion-neutral collisions. Due to the large mass difference between electrons and neutral particles, little energy is transferred in elastic collisions between them, so many collisions are necessary for electron energy equilibration. The energy relaxation length for electrons experiencing only elastic collisions with neutrals is approximately

$$\lambda_{\epsilon,e} \approx \lambda_{\text{el},e}(m_g/2m_e)^{1/2}, \tag{2.2}$$

where $\lambda_{\text{el},e}$ is the mean free path for elastic electron-neutral collisions, while m_g and m_e are the masses of neutral gas molecules and electrons, respectively [16].

When inelastic collisions are significant, the electron energy relaxation length will decrease. At larger average electron energies the contributions of inelastic collisions may dominate. For atomic gases the inelastic processes include ionization, electron attachment, and electronic excitation. In molecular gases the list also includes rotational excitation, vibrational excitation, and numerous dissociation processes [17]. In this case, the electron energy relaxation length is approximately equal to the effective mean free path for all inelastic processes:

$$\lambda_{\epsilon,e} \approx \lambda_{\text{in},e}. \tag{2.3}$$

The mean free path for each inelastic process depends on the details of the cross section for the process as well as on the electron energy distribution function.

2.1.2 The Drift-Diffusion Approximation

In a non-magnetized, partially-ionized, collisional plasma, the bulk forces on each particle species are caused by the electric field, pressure gradients, and a drag force which we assume to be proportional to the average particle velocity. For a charged-particle species α, the momentum

balance equation is:

$$m_\alpha n_\alpha \left(\frac{\partial \vec{v}_\alpha}{\partial t} + \vec{v}_\alpha \cdot \nabla \vec{v}_\alpha \right) = \pm e n_\alpha \vec{E} - \nabla p_\alpha - m_\alpha n_\alpha \nu_{m\alpha} \vec{v}_\alpha, \tag{2.4}$$

where $\vec{v}$ is the fluid velocity, $\vec{E}$ is the local electric field, p is the pressure of the species under consideration, and ν_m is the effective particle-neutral momentum transfer frequency. In using this momentum transfer frequency, we are implicitly assuming that the effects of charged particle-charged particle collisions are negligible relative to charged particle-neutral collisions. At high pressures, like those being considered in this work, the inertial term $\vec{v} \cdot \nabla \vec{v}$ is small relative to the collisional term and can be neglected [17].

At high pressures particles will experience many collisions and reach steady-state flow velocities quickly. The time taken for this process is roughly equal to the inverse of the effective momentum transfer frequency. This frequency depends on the particle and neutral gas species, and increases for larger neutral densities and electric fields. Based on published mobility data [18, 19], we estimate that for large electric fields at atmospheric pressure, reasonable times to reach steady-state are 10^{-11} s for ions and 10^{-13} s for electrons. Since we are not concerned with plasma motion or oscillation at or below these time scales, it is reasonable to neglect the time derivative in equation 2.4.

Using $p = nT$ with the particle temperature T is assumed to be constant, the particle flux Γ can be written as

$$\vec{\Gamma}_\alpha \equiv n_\alpha \vec{v}_\alpha = \pm n_\alpha \mu_\alpha \vec{E} - D_\alpha \nabla n_\alpha, \tag{2.5}$$

where the sign taken is the same as that on the particle charge [17]. Here we have also defined a charged-particle mobility,

$$\mu_\alpha = \frac{e}{m_\alpha \nu_{m\alpha}}, \tag{2.6}$$

and a diffusion coefficient,

$$D_\alpha = \frac{T_\alpha}{m_\alpha \nu_{m\alpha}} = \frac{\mu_\alpha T_\alpha}{e}. \tag{2.7}$$

The two terms on the right-hand side of equation (2.5) are the electric field-induced particle drift and the diffusive flux, leading to the description of this equation as the drift-diffusion approximation. It allows a concise description of charged-particle fluxes in highly-collisional systems.

2.1.3 Electrohydrodynamic Forces

As described in section 2.1.2, charged particles moving in an electric field will experience collisions predominantly with neutral gas particles. These collisions transfer directed momentum to the neutral gas, generating a force on the neutral gas. In the field of DBD plasma actuators this force is often called the electrohydrodynamic (EHD) force, while in corona discharge the same effect is known as the electric wind [13, 20]. Researchers examining plasma actuators generally ascribe their behavior to this force. Here we derive a mathematical description of the force for a highly-collisional plasma containing electrons and singly-charged positive and negative ions. It generally follows the development given by Boeuf and Pitchford [13].

In a system where the background flow velocity is subsonic (or zero, as in the experiments and simulations of this work), the neutral gas molecules are relatively cold and have negligible directed velocity compared to the velocities of the charged particles. Consequently we neglect any momentum transfer from the neutrals to plasma particles. The EHD force density acting on the neutral gas is then equal to the frictional drag on the plasma particles, summed over all particles species:

$$\vec{f}_{\text{EHD}} = \sum_{\alpha} n_\alpha m_\alpha \vec{v}_\alpha \nu_{m\alpha},$$

This expression is obtained by noting that each plasma particle, on average, transfers a momentum $m_\alpha \vec{u}_\alpha$ to the neutral gas once per effective collision period $1/\nu_{m\alpha}$. Using the definition of charged particle mobility in equation (2.6) and assuming the plasma contains one species each of positive ions (p), electrons (e), and negative ions (n), this becomes

$$\vec{f}_{\text{EHD}} = \frac{e n_p \vec{v}_p}{\mu_p} - \frac{e n_e \vec{v}_e}{\mu_e} - \frac{e n_n \vec{v}_n}{\mu_n} = \frac{e\vec{\Gamma}_p}{\mu_p} - \frac{e\vec{\Gamma}_e}{\mu_e} - \frac{e\vec{\Gamma}_n}{\mu_n}.$$

By applying the drift-diffusion approximation for the fluxes given by equation (2.5), we can expand this as

$$\vec{f}_{\text{EHD}} = e(n_p - n_e - n_n)\vec{E} - T_p \nabla n_p - T_e \nabla n_e - T_n \nabla n_n. \tag{2.8}$$

We note that the force on the neutral gas does not depend at all on particle mobilities. The physical explanation of this is that while massive particles with lower mobilities transfer more momentum

per collision, this is exactly balanced by the larger number of collisions experienced by lighter, higher-mobility particles.

In systems like DBDs where the applied voltages are in the kilovolt range, the electric field terms will dominate over the density gradient terms [13]. This allows us to neglect the latter terms and simplify equation (2.8) into simply the net charge density times the electric field:

$$\vec{f}_{\text{EHD}} \approx e(n_p - n_e - n_n)\vec{E}. \tag{2.9}$$

We apply equation (2.9) to calculate the induced force in our simulations, as described in section 6.3.

2.1.4 Ionization and Attachment

Electron-positive ion pairs may be generated by electron-impact ionization. In high-pressure plasmas, electron impact ionization is most commonly modeled by using an ionization coefficient α. In an electropositive gas, the rate at which new electron-ion pairs are created by ionization is given [17] by

$$S_{iz} = \alpha \Gamma_e. \tag{2.10}$$

By making an analogy to reaction rate equations, the dependence of the ionization coefficient on the local electric field can be reasonably approximated as

$$\alpha \approx \frac{\text{const}}{\lambda_{\epsilon,e}} \exp\left(\frac{-\mathcal{E}_{iz}}{eE\lambda_{\epsilon,e}}\right)$$

where $\mathcal{E}_{iz}$ is the ionization energy of the gas. This equation is valid for large electric fields in which the energy electrons acquire between collisions, approximately $eE\lambda_{\epsilon,e}$, exceeds the electron temperature T_e. In situations where the energy relaxation length is inversely proportional to the gas density, the ionization coefficient can be simply modeled using this equation. That relation breaks down when the collision cross-sections vary with the electric field. For oxygen that occurs when the reduced electric field E/p exceeds about 10^4 V m^{-1} Torr^{-1}, where p is the gas pressure.

We note that often (and perhaps more appropriately from a perspective of determining particle energy between collisions) the reduced electric field is specified as E/n_g, where n_g is the number

density of the neutral gas, instead of E/p. Since much published data regarding physical parameters are given as functions of E/p for gases at room temperature, however, we use that definition of the reduced electric field in this work.

In an electronegative gas, an electron attachment coefficient η is defined similarly to the ionization coefficient. The rate at which negative ions are created by electron attachment is given by

$$S_{att} = \eta \Gamma_e. \tag{2.11}$$

For each electron removed from the plasma, a negative ion is created.

2.2 High Pressure Discharges

The plasmas discussed in this work exist at atmospheric pressure and have a low ionization fraction. Because of these features, the plasma dynamics are dominated by collisions. The basic equations describing such a system were reviewed in section 2.1. Additional physics specific to DBDs are summarized in section 2.2.2. Since descriptions of DBD physics includes analogies and references to high pressure DC discharges, relevant aspects of those DC systems are described in section 2.2.1.

2.2.1 DC Discharge Regimes

Due to the maturity of research on high-collisionality DC discharge systems, groups studying DBD plasmas often make analogies to DC discharge phenomena even though DBDs are powered by oscillating voltages. For example, the DBD literature at times refers to the diffuse mode of a DBD as an "atmospheric pressure glow discharge" (APGD), even though glow discharges do not form and extinguish repeatedly as the plasmas do in DBDs. Only the DC discharge types and mechanisms most relevant to DBD research are briefly discussed here. Figure 2.2 describes many of the equilibrium states of a DC discharge between a cathode and anode. It also roughly describes the breakdown regimes through which a discharge progresses as it moves from turn-on (no current) to its equilibrium state.

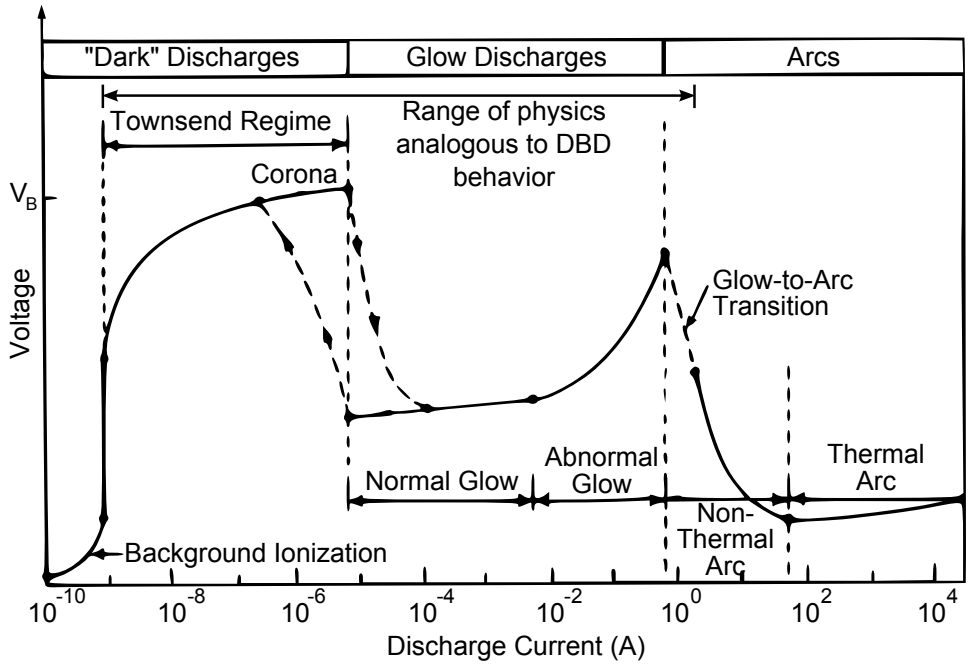

Figure 2.2: Operating regimes of a DC electric discharge tube, adapted from Roth [21]. V_B is the breakdown voltage of the discharge system.

In the Townsend regime, plasma formation relies on an external source of electrons. Depending on the system under consideration, these electrons may come from thermionic or field emission from the cathode, from the minimal background ionization of the gas, or from other sources. Because these "seed" electrons must come from outside the plasma, the discharge is considered non-self sustained. The strength of a discharge in the Townsend regime is controlled in part by the rate at which these electrons are produced. A discharge relying on background ionization, for instance, draws a barely measurable current [22].

If a strong electric field exists in the region where electrons are produced, some of the electrons will gain enough energy to ionize neutral particles. Ionization produces new free electrons, which may then be accelerated and cause additional ionization. This process is known as an electron avalanche. A single avalanche ends when the electrons are either blocked by a material surface or enter a region where the electric field is too weak to provide enough energy for ionization. In the Townsend regime, the space charge density is generally too low to significantly alter the electric field from its vacuum distribution.

Due to the high mobility of electrons relative to ions, avalanches leave behind a cloud of positive charge. In situations where that space charge is large enough to modify the electric field, the positive space charge shifts the region of strong electric field away from the cathode. If the shift uncovers new free electrons, new avalanches occur and the process repeats. The result is a growing narrow column of space charge, often appearing jagged like a spark or lightning. Such a plasma column is commonly called a streamer. The streamer continues propagating until the region of strong electric field is too weak to support significant ionization, too few free electrons exist in the new region of strong electric field, or the streamer reaches the anode. In many situations the new free electrons are provided by photoionization caused by photons emitted during the avalanche phases [23]. The streamer breakdown regime occurs most frequently when the region of concentrated electric field is near the anode. It may not exist in some discharge configurations, such as the electric discharge tube on which figure 2.2 is based.

In addition to background ionization and photoionization, free electrons may be supplied by secondary emission caused by ion bombardment of the cathode surface. The flux of secondary electrons from a surface is given by

$$\Gamma_e^{SE} = -\gamma \Gamma_p. \tag{2.12}$$

Here γ is the secondary electron emission coefficient of the surface, which in general is a function of the surface material and condition, the bombarding ion species, and the energy and angular distributions of the bombarding ions [17]. The negative sign indicates that the flux of secondary electrons is away from the surface when the flux of positive ions is towards it. Secondary electrons may be emitted from dielectric surfaces as well as electrodes, although the surface potential will change due to this emission. The secondary emisison coefficients may be comparable to or larger than those for electrodes. Surface bombardment by neutral metastable particles and high-energy electrons may also cause secondary electron emission, but we do not consider these processes in this work.

If, on average, at least one secondary electron is emitted due to the bombardment of all the ions created in one avalanche, the discharge is self-sustained as it no longer requires an external source of electrons. In this case, the plasma density quickly increases and the resulting system is termed

a glow discharge. The threshold for transition from the Townsend to the glow regime is given by the requirement for electron replacement [24]:

$$\gamma \left[\exp \int_0^{x_{\max}} (\alpha - \eta)\, dx - 1 \right] \geq 1. \tag{2.13}$$

Here α and η are the ionization and electron attachment coefficients of the gas described in section 2.1.4. The α, η, and γ coefficients are often referred to as the first, second, and third Townsend coefficients, respectively. Both α and η vary with the local reduced electric field. The integral in equation (2.13) is evaluated over a region $0 < x < x_{\max}$ in which the net electron production is positive, i.e. $\alpha(x) - \eta(x) > 0$.

The term "corona discharge" is used in the literature to refer to several different mechanisms of plasma formation near an electrode with a small radius of curvature. The biased electrode, most commonly a needle-like point or a thin wire, produces a strongly inhomogeneous electric field distribution around it. The physics governing the discharge depend on the polarity of the applied bias, the distribution of the electric field, and the properties of the gas medium. In this work we will distinguish between the types by their discharge mechanisms, and refer to Townsend, streamer, or glow coronas. The corona regime noted in figure 2.2 includes only Townsend coronas.

When the sharper electrode is used as the cathode, the plasma is commonly called a negative corona. Depending in part on the electric field strength, the discharge may operate as either a Townsend or a glow corona, with at least some of the electrons supplied by secondary emission from the cathode. The plasma is largely confined to a narrow region around the cathode where the electric field is strong enough to cause ionization. Outside of this space, electrons and negative ions drifting to the anode provide current continuity while positive ions are essentially absent.

When the sharper electrode is used as the anode, the plasma is commonly called a positive corona. Due to the weaker electric field near cathode compared to the negative corona, field emission and secondary emission from the cathode are generally not important. Unless an additional source of electrons is available, the positive Townsend corona is quite weak. Increasing the applied voltage causes a transition into a streamer corona regime. If the field at the cathode becomes large enough to support secondary emission, the plasma will transition into a glow corona [22].

2.2.2 Dielectric Barrier Discharges

We use analogies to the DC discharges described above to describe the operation of dielectric barrier discharges, which are the focus of this work. A dielectric barrier discharge (DBD) is conventionally described as a system in which a plasma forms between two electrodes, at least one of which is insulated from the plasma, with an alternating high voltage applied between the electrodes. In the absence of a dielectric layer, the plasma would quickly transition to a thermal arc discharge. In a DBD the plasma deposits charge on the dielectric layer, shielding out the electric field in the gas region and preventing this transition. DBDs differ strongly from DC discharges due to their time-varying nature. The plasma in a DBD forms and extinguishes at least once, and often many times, during each half cycle of the oscillating applied voltage.

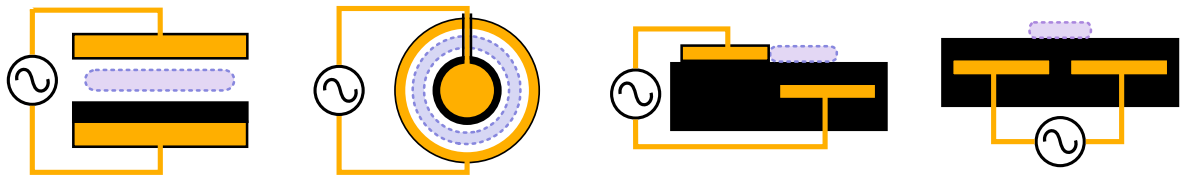

(a) (b) (c) (d)

Figure 2.3: Common DBD configurations, showing electrodes, dielectric materials (in black), and the approximate plasma regions (inside dashed outlines). The drawings show (a) a single-barrier parallel-plate discharge, (b) a single-barrier concentric discharge, (c) a single-barrier surface discharge and (d) a double-barrier surface discharge, also called a coplanar discharge.

DBDs are operated at neutral gas pressures from tens of Torr to atmospheric pressure or higher, with applied voltages amplitudes typically in the kilovolt range. Applied voltage frequencies typically range from 50 Hz [e.g. 25–27] to tens of kilohertz [e.g. 28, 29], but some experiments have been carried out at even higher frequencies [30]. The most common discharge configurations are shown in figure 2.3. Parallel-plate designs, like figure 2.3(a) are often employed in materials processing applications. The concentric cylinder design of figure 2.3(b) was designed by Werner von Siemens in 1857 to generate ozone, and is still widely used for that purpose today [1]. This work focuses on single- and double-barrier surface discharges, shown in figures 2.3(c) and 2.3(d) respectively.

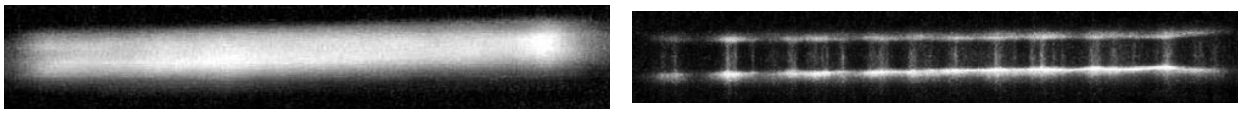

(a) (b)

Figure 2.4: Images of (a) a diffuse discharge in neon and (b) a filamentary discharge in argon between parallel-plate electrodes at the top and bottom of each image. From Trunec et al. [34].

Volume DBDs have been shown to operate in at least two distinct modes: diffuse and filamentary. In a diffuse discharge the plasma forms and is extinguished exactly once per half-cycle of the applied voltage, accompanied by a single current pulse in each half cycle [31]. At each point in time in this regime the plasma appears uniform in directions parallel to the discharge electrodes, as in figure 2.4(a). In contrast, filamentary discharges consist of many short-lived, narrow channels of plasma, as in figure 2.4(b) that form and quench on time scales of a few nanoseconds to hundreds of nanoseconds. These streamer-like microdischarges are spread out in time, corresponding to many short current pulses in a "spiky" discharge current waveform similar to the one in figure 2.5. The microdischarges are often spread out in space as well, although in some circumstances they may self-organize [32, 33].

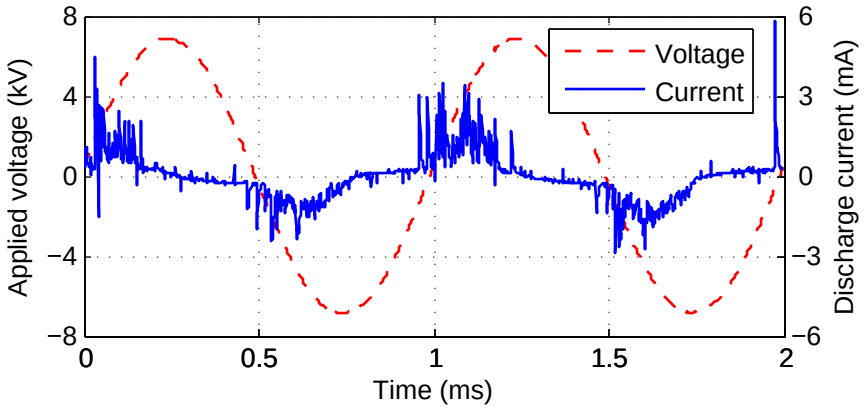

Figure 2.5: Discharge current for a surface DBD operating in the filamentary mode, showing the many current spikes corresponding to individual microdischarges. The DBD is driven by a 1 kHz sinusoidal voltage.

Numerous factors influence which mode is present. These include the species, purity, pressure, and flow rate of the gas, the discharge geometry and construction materials, and the shape, amplitude, and frequency of the applied voltage waveform. The primary way experimentalists achieve diffuse modes is to add helium to the gas mixture [35], while the addition of oxygen tends to lead to filamentary discharge modes [36]. Relatively large electrode gaps and voltages far above the breakdown voltage tend to generate filamentary discharges.

The plasma dynamics specific to surface DBDs have not been studied in the same depth as those in volume DBDs. The characteristics unique to these surface DBDs so far discovered are discussed here. Korzec et al. [37] operated a single-barrier surface discharge in pure helium at various pressures and found some characteristics shared with both filamentary and homogeneous modes. The plasma had significant spatial visible inhomogeneity, suggesting the existence of filaments, but also had electrical signals and light emission similar to a homogeneous discharge. In our work, all of the discharges were operated in atmospheric pressure air at voltages well above breakdown, and all of the discharges were filamentary in nature.

Gibalov and Pietsch [38] examined a single-barrier surface discharge and showed that the plasma, as measured by deposited surface charge, extended much further away from the exposed electrode after a single positive voltage pulse was applied to the exposed electrode than after a single negative one. Enloe et al. [39] observed the light emission from a similar discharge driven by a sinusoidal waveform, and observed that the plasma extended a similar distance both when the applied voltage was increasing and decreasing. The rates of plasma expansion were noted to be similar in the two half cycles. Due to the differences in applied voltages and methods of observation, these two studies are not directly comparable, but they are among the only experiments to examine plasma expansion in surface DBDs. Gibalov and Pietsch [40, 41] developed a 2-D simulation of the filamentary regime for double-barrier surface DBDs. Based on their numerical experiments they concluded that photoemission of electrons from the dielectric surface is essential for the appearance of a streamer-like structure. Without photoemission, they observed only a weaker, non-propagating plasma and significantly longer duration current pulse.

DBDs have seen a surge of new ideas for and research into possible applications in the last 10 to 15 years. In addition to their historical (and current large-scale) use in the production of ozone [1], volume DBDs have been used in plasma display panels [42] and studied for use in the destruction of hazardous gases [43], surface cleaning [44], and etching of polymers [45]. Surface DBDs have also been proposed for several materials processing applications, including the conversion of cellophane surfaces into perfluorinated surfaces [9] and increasing the wettability of polypropylene fabric [10]. The surface DBD configuration offers some advantages for materials processing, as the surface being modified is not part of the discharge circuit. In contrast, in parallel-plate systems the processed material generally serves as the dielectric layer.

2.3 Active Flow Control

Active flow control is generally defined as intentionally modifying a fluid flow field in a way that is controllable during system operation. For external flow fields, characteristics that may be desirable to modify include the laminar-to-turbulent transition, flow separation (or the location of separation) from an airfoil surface, and the level of free-stream turbulence [46]. Before discussing some of the specific applications of active flow control in section 2.3.2 and the various technologies used to effect flow control section 2.3.3, a brief summary of relevant background material in fluid dynamics is given in section 2.3.1.

2.3.1 Basic Fluid Dynamics Concepts

Systems including fluid motion can be analyzed by applying a control volume formulation, in which physical laws are applied to a specified region of space. For a two-dimensional, non-accelerating control "volume" of gas like the one in figure 2.6, Newton's second law of motion can be written as

$$\frac{\vec{F}_{\text{surf}}}{L} + \frac{\vec{F}_{\text{body}}}{L} = \frac{\partial}{\partial t} \iint_{\text{area}} \vec{u}\, \rho_g \, dA + \oint_{\text{edge}} \vec{u}\, \rho_g \, \vec{u} \cdot d\vec{\ell}. \tag{2.14}$$

$\vec{F}_{\text{surf}}$ includes all forces acting on the edges of the control volume, while $\vec{F}_{\text{body}}$ includes all forces acting inside the control volume. Surface forces commonly include pressure forces, shear forces,

and the reaction forces of structures in contact with the fluid. The most commonly considered body force is the weight of the fluid, but we will consider the electrohydrodynamic force described in section 2.1.3. In equation (2.14), $\vec{u}$ is the fluid velocity of the gas, ρ_g is its mass density, and L is a unit length perpendicular to the plane of figure 2.6.

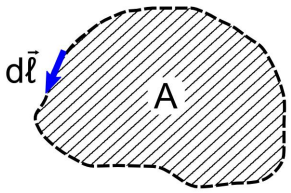

Figure 2.6: Two-dimensional control "volume"

The pressures that contribute to the surface forces in equation (2.14) are thermodynamic pressures. In fluid dynamics these pressures are more commonly called static pressures, here denoted as p. A pressure sensor whose opening faces into a flowing gas would measure a larger pressure, known as the stagnation pressure. The stagnation pressure p_0 is given by

$$p_0 = p + \frac{1}{2}\rho_g u^2, \tag{2.15}$$

with the increase in pressure caused by the stopping of the flow as it enters the pressure sensor. The static pressure in a flowing fluid can be measured by ensuring that the opening to the sensor faces in a direction perpendicular to the flow velocity $\vec{u}$.

A key parameter in determining the flow regime is the Reynolds number, which is a dimensionless ratio approximating the ratio of inertial forces to viscous forces. Flows with larger Reynolds numbers tend to be more turbulent, while flows with smaller Reynolds numbers are more likely to be laminar [47]. Determining the Reynolds number requires identifying a characteristic length. For gas flow over airfoils, this length is commonly chosen to be the chord length of the airfoil, ℓ_c [3]. The chord length is the length of a straight line connecting the leading and trailing edges of an airfoil. These edges are identified in figure 2.7. For all of the discussions in this work, the Reynolds number used is the chord Reynolds number,

$$\mathrm{Re}_c = \frac{\rho_g u\, \ell_c}{\mu_g}, \tag{2.16}$$

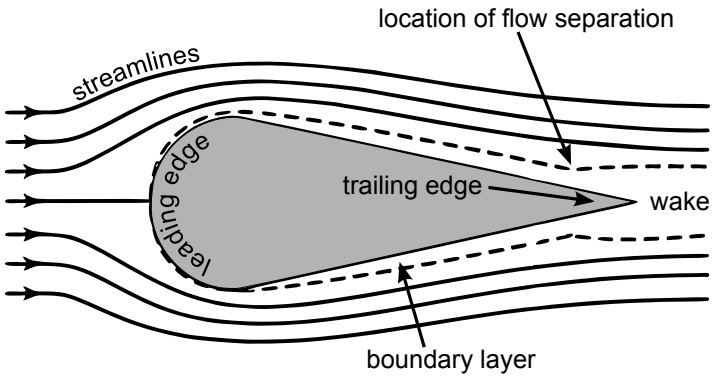

Figure 2.7: Diagrammatic representation of the boundary layer, flow separation, and wake of an airfoil. Adapted from Fox and McDonald [47].

where μ_g is the dynamic viscosity of the neutral gas.

When fluid flows along a solid surface, the system is usually analyzed by splitting it into two separate components: the free-stream flow far from the surface and a boundary layer near the surface. Typically, when a flowing fluid encounters a surface the initial boundary layer will be laminar, with smooth streamlines. At some point along the surface, the flow will transition from laminar to turbulent. The location of this point depends on many factors including the shape of the surface, the surface roughness, the level of turbulence in the free-stream flow, the free-stream velocity, the fluid viscosity, and the pressure gradient along the surface.

Depending on the shape of the solid surface, the pressure in the boundary layer may decrease or increase as the flow moves along the surface. The former case is referred to as a favorable pressure gradient, as the pressure tends to reinforce the existing flow pattern. The latter case, in which $\partial p/\partial x > 0$, is known as an adverse pressure gradient. The presence of an adverse pressure gradient makes flow separation from the surface possible. Flow separation, pictured in figure 2.7, occurs when the velocity in the boundary layer is reduced to (or below) zero. It significantly increases the drag on a surface. While flow separation may occur for both laminar and turbulent boundary layers, for given free-stream conditions a smaller adverse pressure gradient is required to cause flow separation in laminar boundary layers. Turbulent boundary layers carry more momentum, making it more difficult to slow the boundary flow down to zero velocity and cause separation.

2.3.2 Applications of Active Flow Control

Plasma actuator technologies like DBD plasma actuators and those discussed in section 2.3.3 have been shown to be most effective in flows with relatively low Reynolds numbers (on the order of 10^5 or smaller) [48]. Consequently the applications described in this section involve gas flows with either small flow velocities or low gas densities. While many of the papers cited in this section concern the use of DBD plasma actuators for specific applications, the other technologies discussed in section 2.3.3 could also potentially be used. More in-depth reviews of the applications of plasma actuators may be found in works by Corke and Post [48] and Moreau [46].

In the low-pressure stage of jet turbines, the flow over the turbine blades, like those shown in figure 2.8, is fully attached during the conditions usually present during take-off and landing. At cruise altitudes, however, the reduction in air density causes the Reynolds number to drop to about 80,000 [8]. Due to the this drop, the flow becomes more laminar and may separate early on the blades before reattaching further on. This feature is known as a "separation bubble," [6] and it causes noticeable turbine efficiency losses [8]. The reattachment of the flow occurs due to a laminar-to-turbulent transition. If this transition occurs prior to the point of separation, the separation bubble can be largely suppressed [7].

While passive flow control methods could increase the free-stream turbulence of the flow, these would have detrimental effects during take-off and landing. Active flow control can also increase the turbulence while still allowing the turbine to operate at peak efficiency [2, 5] for both high and low Reynolds number flows by only operating the control device at cruise altitudes. Computational fluid dynamics (CFD) simulations have demonstrated the viability of flow control techniques that inject momentum into the flow both continuously and at reduced duty cycles [49]

Reducing flow detachment in the low-pressure stage of jet turbines may be particularly useful in the context of high-altitude unmanned aerial vehicles (UAV). At high altitudes the reduction in air density pushes the Reynolds number lower, and engineers desire to increase the blade spacing to save on turbine weight [50], which worsens the adverse pressure gradient. Both of these increase the likelihood of flow separation [51]. Mission profiles for such aircraft call for long-duration missions, making fuel efficiency a high priority.

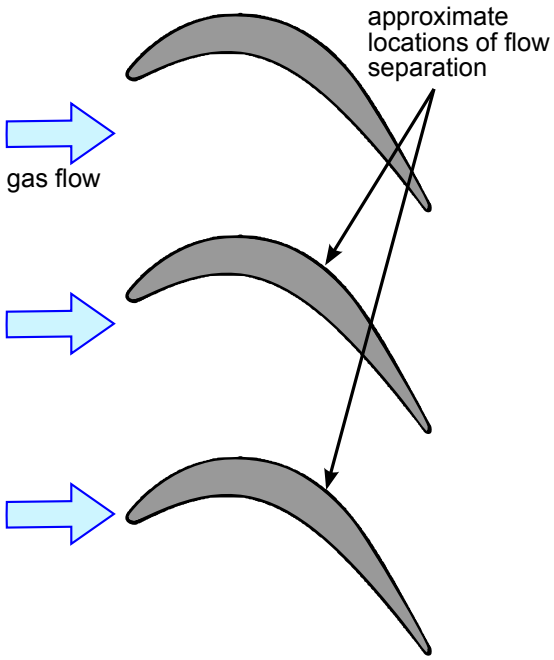

Figure 2.8: Typical blade structure in the low-pressure stage of a jet turbine, also noting typical points of flow detachment for low Reynolds number flows

In some situations, separation can cause the generation of flow instabilities in an object's wake. These instabilities are a significant source of aircraft noise. Thomas et al. [52] demonstrated that active flow control can be used to significantly limit flow separation noise production caused by flow over a cylinder mimicking a landing-gear strut. Active flow control has also been suggested for use in limiting the noise caused by jet engine exhaust [53]. Other proposed uses include eliminating flow separation on the wings of slow-flying UAV's [54] and improving lift on helicopter blades [48].

2.3.3 Active Flow Control Technologies

The DBD plasma actuators discussed in this work represent only one method currently being researched to effect flow control. While many techniques exist to modify flow fields, only the ones which have effects similar to those of DBD actuators (and thus have been proposed for similar uses) are reviewed here. These technologies include direct gas injection into the flow, synthetic jets using piezoelectric actuators, and plasma synthetic jets. In order to be useful in a particular application,

DBD actuator technology must advance to the point where there are significant advantages over these other techniques.

Active flow control using gas injection functions simply by forcing gas out through small holes in an airfoil surface. The injected gas jets can alter the flow field in several ways, such as by adding momentum to the boundary layer or promoting the laminar-to-turbulent transition. McAuliffe and Sjolander [55] used steady gas injection at about a 40° angle to the surface of turbine-like blades, and found the technique to be useful only when free-stream turbulence levels were low. In some designs suction is used in addition to injection [56], while in others the gas injection may be pulsed for improved efficiency [50]. Gas injection techniques have the advantage of being relatively straightforward to model, but require gas lines and valves to be placed inside the airfoil structure.

Synthetic jets seek to eliminate the disadvantages of direct gas injection. These devices consist of a small cavity embedded in the airfoil surface, as shown in figure 2.9, with a piezoelectric surface on one side of the cavity. The piezoelectric actuator is driven at a frequency resonant with the cavity, with the result that gas is drawn in from near the airfoil surface and then pushed away. The cavities are often cylindrical, with numerous cavities spaced along the span of the airfoil, but may also be designed using other shapes [57]. Synthetic jets have been show to reduce flow detachment both experimentally [e.g. 58] and computationally [e.g. 59]. Synthetic jets require significantly less hardware than direct gas injection, and can achieve large jet velocities. Due to the dependence on a resonance mechanism, such actuators do require tight tolerances in the fabrication of the resonant cavities.

Plasma synthetic jets are a fusion between synthetic jets and DBD actuators. These devices are DBDs, and may be either annular or linear [60]. These two geometries are pictured in figure 2.10, with the annular device having rotational symmetry and the linear device having uniformity in the direction perpendicular to the plane of figure 2.10. Both geometries accelerate flow from several directions toward the center of the device. The flows meet and turn upwards, yielding a flow structure similar to a piezoelectric synthetic jet [61]. Plasma synthetic jets were developed relatively recently, so their effectiveness for flow control has not been evaluated as extensively as the other techniques described here.

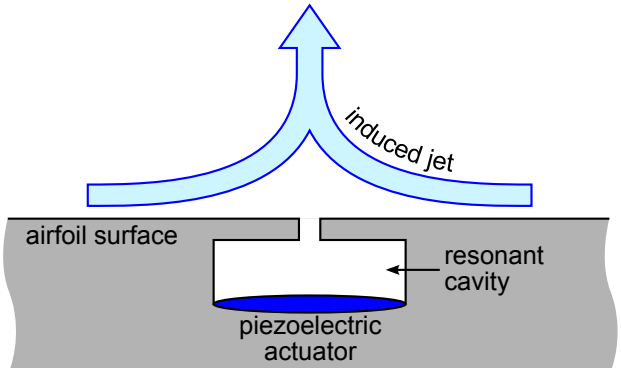

Figure 2.9: A synthetic jet actuator

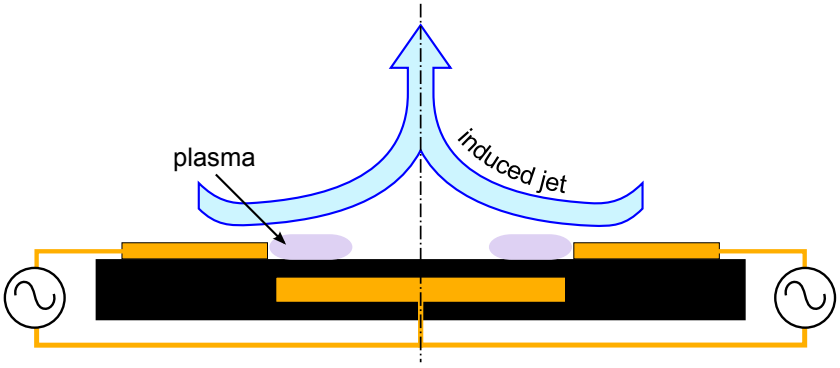

Figure 2.10: A plasma synthetic jet actuator. The annular geometry has a rotational axis of symmetry in the center of the figure, while the linear geometry is uniform in the dimension perpendicular to the plane of the figure.

2.4 Experimental Observations of DBD Plasma Actuators

Since the DBD plasma actuator was first described by Roth et al. [15] in 2000, the field has seen an increasing number of investigations into both the physics and applications of this device. This section reviews some of the experiments conducted in this area, including descriptions of the general device characteristics and the demonstration of their efficacy when used for reducing flow detachment. It also describes specific experiments dealing with the effects of discharge geometry and optical measurements of plasma behavior that have direct bearing on the current work. A more comprehensive review of experimental plasma actuator research, including DC corona actuators in addition to DBDs, was recently conducted by Moreau [46].

The majority of DBD actuator research has examined single-barrier geometries similar to that shown in figure 1.1, with both electrodes having rectangular cross sections. Most actuators are driven by sinusoidal voltages applied to the exposed electrode, and are operated in atmospheric pressure air. Unless stated otherwise, all of the experiments and actuators below had these characteristics. The general characteristics of this type of actuator are described in section 2.4.2. Effects of altering the discharge geometry are dealt with specifically in section 2.4.3. The experiments described in section 2.4.1 were conducted in wind tunnels with non-zero background flow velocities, while the remainder of section 2.4 deals with DBD operation in quiescent gas.

2.4.1 Flow Control Using DBD Actuators

Numerous experimental studies have examined the ability of the plasma actuator to reduce drag and delay the onset of flow separation on airfoils. These studies have been conducted in wind tunnels with various airfoil shapes, actuator positions, and flow conditions. Several of these studies are summarized here to demonstrate the effectiveness of DBD actuators for active flow control.

Several groups have used DBD actuators to eliminate flow separation from airfoils, as shown in figure 2.11. On the top surface of an airfoil, Roth [4] placed a series of actuators which induced forces parallel to the background flow, and succeeded in causing flow re-attachment for some angles of attack in flow speeds greater than 7 m/s. By placing an actuator on the leading edge of the airfoil (which induced forces perpendicular to the top airfoil surface), Post and Corke [3] achieved flow re-attachment for background velocities up to 30 m/s. Roupassov et al. [62] found similar results using actuators arranged to generate forces perpendicular to the background flow but parallel to the surface. These actuators were driven by positive voltage pulses rather than a sinusoidal waveform. Taken together, these results suggest that the direction of the induced force is not critical to the results. The flows likely re-attach due to a forced transition to a turbulent boundary layer rather than to direct momentum injection into the boundary layer.

Huang et al. [5] used a DBD actuator inducing force parallel to the air flow to eliminate detachment on a cascade of turbine-like blades similar to that shown in figure 2.8. They examined flow conditions with Reynolds numbers ranging from 10^4 to 10^5, and found the technique to be as

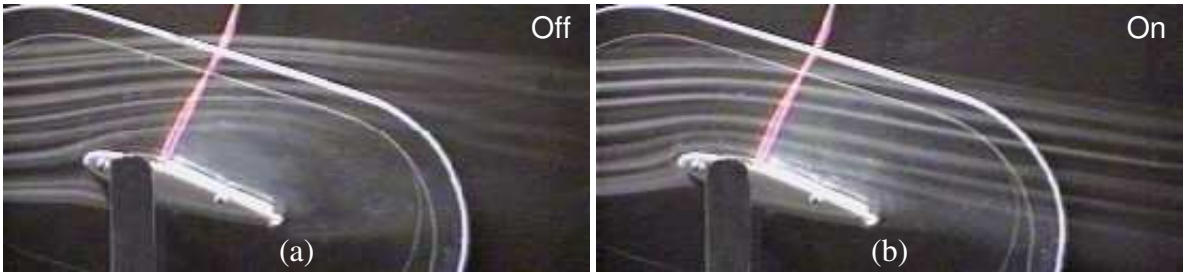

Figure 2.11: Demonstration of (a) flow separation on an airfoil and (b) flow re-attachment when a plasma actuator on the leading edge is turned on. From Corke and Post [48].

effective as a passive control technique, with the additional advantage of being able to turn off the actuators at higher Reynolds numbers where flow separation is not problematic.

2.4.2 DBD Actuator Operation in Quiescent Gas

Much research, including that presented in chapters 4 and 5 of this document, has examined the behavior of DBD actuators in quiescent air. Operating in air simplifies many experimental details, allowing groups to examine a variety discharge parameters in order to optimize actuator design. Designs are generally optimized for maximum induced force or maximum flow velocity (which are roughly proportional to one another) in the direction parallel to the dielectric surface. Maximizing the force should increase the effectiveness of the actuator for flow control purposes regardless of whether the mechanism for this control is momentum injection into the boundary layer or inducing a laminar-to-turbulent transition.

Pons et al. [63] were among the first groups to directly measure the flow induced by an actuator operating in quiescent air. Using a stagnation probe technique they showed that the induced flow was confined within about a centimeter of the surface. They also noted that the efficiency of the actuator in transferring electrical energy into flow energy was on the order of 0.05%. Jukes et al. [64] used a hot-wire anemometer with a pulsed actuator to verify that an induced velocity was indeed due to some plasma-air interaction and not due to thermal effects alone, as had been previously suggested.

Not surprisingly, numerous researchers have demonstrated that the flows induced by DBD actuators increase as the amplitude of the applied voltage signal increases. Enloe et al. [39] found that both the maximum induced flow velocity and the discharge power increased proportionally to the voltage amplitude raised to the $7/2$ power, so the increased flow velocities are largely due to increased power dissipation; the efficiencies of the actuators remain essentially unchanged. Increasing the frequency of the applied voltage also increases the discharge power over at least the range 200 Hz to 10 kHz [65–67]. Depending on the discharge geometry and the voltage amplitude, however, the induced forces or flow velocities may increase linearly [67], saturate above about 1 kHz [66], or, for larger voltage amplitudes, decrease with increasing frequencies [65].

The composition of the neutral gas also plays a significant role. DBD actuator efficiency increases linearly with the fraction of oxygen in the gas [68]. Oxygen forms both positive and negative ions more easily than nitrogen, and one or both of these properties likely contribute to the increase. Flow measurements by Kim et al. [69] qualitatively point to the importance of negative ion motion as a key driver of the induced force. We note that the net actuator force remains in the same direction even as oxygen concentration is reduced to zero [68]. If negative ions play a large role in generating the observed force, their action must be in same direction as that generated by positive ion motion.

Measurements of induced forces and velocities provide relatively little information about the plasma itself. To study plasma behavior, several groups have examined the light emitted from it. We summarize their measurements here and compare them to our own in chapter 5. Enloe et al. [39, 70] focused a photomultiplier tube on narrow spatial regions to obtain temporally- and spatially-resolved data describing the plasma light emission. Using this technique they observed that the plasma increased in length as the applied voltage was rising, extinguished when dV/dt changed sign, and formed anew and expanded again as the applied voltage decreased. The expansion rates for both half cycles were identical, but increased as the applied voltage amplitude increased [70].

High-speed digital cameras have also been used to observe the plasma structure. Two groups [71, 72] examined images with exposure times much longer than the duration of a microdischarge, and noted that plasma structures differ significantly between the two half cycles of the applied

voltage. When the applied voltage (to the exposed electrode) is increasing, the plasma appears in narrow filaments like those in figure 2.12(a). When the applied voltage is decreasing, the plasma appears in more diffuse jet-like structures like those seen in figure 2.12(b). Sasoh et al. [73] recorded images with exposure times down to ten nanoseconds. They noted that the microdischarges appeared at random locations along the electrode width, and were randomly distributed in time during periods when the applied voltage was large enough to cause ionization. They estimated the microdischarge lifetime when the applied voltage was positive-going to be on the order of 10 ns.

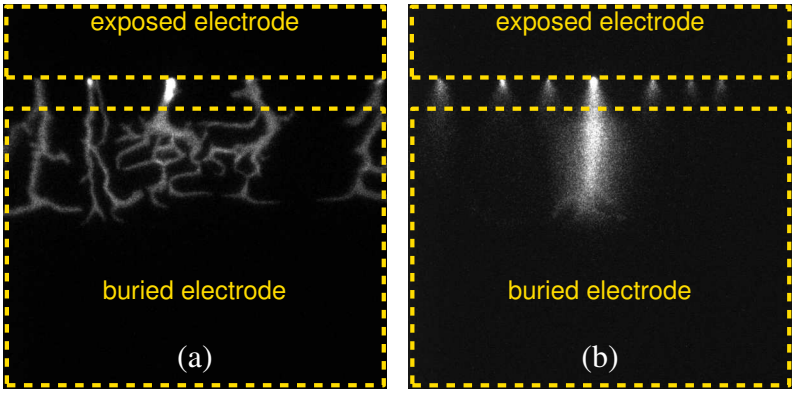

Figure 2.12: Example images of (a) filamentary and (b) jet-like microdischarges in a single-barrier actuator

Several attempts have been made to measure the induced force or velocity as a function of time to determine which portion of the voltage cycle. Forte et al. [74] measured the air velocity near the downstream edge of an actuator using laser Doppler velocimetry (LDV) and found that it oscillated at the applied voltage frequency. This indicates that the two halves of the applied voltage cycle function differently from one another, but due to an unknown transit time of the air between the plasma and the measurement location the relative actions of each half cycle could not be determined.

Enloe et al. [68] used a laser-deflection technique to observe fluctuations in gas density. Their measurements indicated that when the applied voltage was decreasing, a region of higher density air formed near the plasma and moved downstream as the plasma quenched, leaving behind a

region of lower density. This lower density slowly disappeared over the course of the positive-going half cycle. The same group used a pendulum system to determine that the contribution of the negative-going half cycle to the induced force dominates that of the positive-going half cycle by a ratio as large as 97 to 3 [71]. Phase-locked particle image velocimetry measurements by Kim et al. [69] qualitatively corroborated the importance of the negative-going half cycle. The dominance of the negative-going half cycle, combined with the influence of oxygen concentration on the force discussed above, suggest that negative ion acceleration when the applied voltage is decreasing plays a central role in actuator performance. During the negative-going half cycle, the electric field is directed towards the exposed electrode, so the EHD force described by equation (2.9) will be in the measured direction only when acting on electrons and negative ions.

More recently, Enloe et al. [75] found that the induced force of a DBD actuator oscillates over the course of a single half cycle of the applied voltage. When the voltage was positive-going the force was initially positive, then became negative; the same oscillation was observed when the voltage is negative-going. While the gross positive forces were comparable for both half cycles, the negative force was much larger when the applied voltage was positive-going. Both half cycles induced positive *net* forces, but the net force was much larger during the negative-going half cycle, which is consistent with the results described above. The authors attributed the negative forces to drag between the induced air flow and the dielectric surface [75].

All of these studies of single-barrier actuators with rectangular cross-section electrodes and sinusoidal applied voltages point to several important, repeatable results. The efficiencies of the actuators in transferring electrical energy into flow energy are quite small. While the total power transferred can generally be increased by raising the amplitude or frequency of the applied voltage, the efficiency is only strongly affected by changes in the electrode geometry (discussed below) and the gas environment. That the removal of oxygen from the gas greatly decreases the actuator efficiency strongly suggests that the formation of negative ions plays a large role in momentum transfer. This idea is reinforced by experiments showing that the great majority of this momentum transfer from plasma to gas occurs when the applied voltage is decreasing.

2.4.3 Effects of Actuator Geometry

When used for active flow control, the gas environment of a DBD actuator is set by external conditions. Improvements to actuator performance can be achieved by adjusting either the driving voltage or the discharge geometry. Previous work in optimizing the device geometry is summarized here. The dimensions that have been adjusted in previous research are shown schematically in figure 2.13

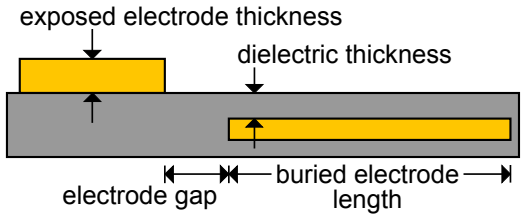

Figure 2.13: Single-barrier DBD actuator dimensions examined in previous research

Several variations to the exposed electrode diameter shape and location have been examined. Enloe et al. [39] tested actuators with a range of exposed electrode thicknesses, using electrodes with both rectangular and cylindrical cross sections. They found a linear increase in the actuator efficiency (force / power) and no change in discharge power as the electrode thickness was reduced, although we re-examine these findings in section 4.2.3. An exposed electrode constructed from a thin mesh was used by Abe et al. [67], and yielded somewhat increased forces compared to rectangular cross-section exposed electrodes for the same applied voltages. Gibson et al. [76] used a rectangular exposed electrode of constant thickness, but varied how deeply embedded it was in the dielectric. They observed no plasma when the top of exposed electrode extended 0.5 mm or more above the dielectric surface, and the largest induced force when the top of the exposed electrode was 0.5 mm below the dielectric surface. All of their measured forces, however, were significantly smaller than a "standard" actuator with the entire exposed electrode above the dielectric surface.

Increasing the length of the buried electrode increases the maximum observed flow velocity, but this effect saturates above a certain value [66]. That value depends on the amplitude of the applied voltage signal [39]. It is likely that the length of the buried electrode only affects actuator

performance when it is short enough to restrict the expansion of the plasma along the dielectric surface above it.

Forte et al. [66] examined actuators with different electrode gaps, finding a maximum in the induced flow velocity in between 3 and 7 mm, although the 2 mm dielectric thickness used in those tests was large compared to most other groups. The same group tested several different dielectric thicknesses. For a constant applied voltage, actuators with thinner dielectric layers induced faster air flows, but this dependence was removed when normalizing to the amount of power consumed by each actuator [66].

2.5 Computational Modeling of DBD Plasma Actuators

The modeling of plasma actuators discussed in the literature varies between focusing entirely on the aerodynamic effects of the actuator while ignoring the details of the plasma [e.g. 77] to detailed simulations of the plasma generation yielding only qualitative information about the induced flow [e.g. 13]. Our computational model falls on the latter end of this continuum, so while a variety of approaches to actuator modeling are summarized in section 2.5.1, sections 2.5.2 and 2.5.3 deal exclusively with fluid models of only the plasma. As with the description of previous experimental work, the actuators examined here are exclusively single-barrier actuators with rectangular cross-section exposed and buried electrodes. The described voltages are applied to the exposed electrodes, while the buried electrodes are grounded. All of the described models include only two spatial dimensions.

2.5.1 Approaches to Plasma Modeling

Computational studies of DBD actuators span a wide range of complexities, from highly simplified models used to couple forces into computational fluid dynamics (CFD) codes to first-principles models of the plasma dynamics. This range is briefly summarized here, roughly from least to most focus on the plasma itself. More detail is given on the codes focused on modeling the plasma dynamics, as that is the focus of the model used in this work.

Among the most simplified plasma models are those like the one employed by Hall et al. [77], in which a doublet, or a collocated flow source and sink, replaces the actuator in a CFD model. An earlier model by Shyy et al. [78] approximated the plasma as a constant body force within a triangular region defined by the region of strongest electric field, and used coupled this force into CFD simulations. A lumped circuit model of the plasma by Orlov and Corke [79] captured some of the temporal characteristics of the plasma, and has recently been applied as part of CFD calculation [80]. The CFD calculations in all of these studies yielded flow patterns in qualitative agreement with experimental velocity measurements.

Limited attempts have been made to use particle-in-cell (PIC) codes to model surface DBD plasma dynamics. Font [81] modeled an actuator operating in pure nitrogen with constant biases applied to the exposed electrode. He obtained microdischarge structures in some ways similar to those described in section 2.5.2, with quick discharges forming and extinguishing when the voltage on the exposed electrode was negative and longer discharges appearing when it was positive. The plasma size appeared to be limited by the short buried electrode length chosen. More recently Huerta and Ludeking [82] used a commercial PIC code to simulate a similar system, but were limited to the initial stages of the ionization avalanche due to restrictions on the number of particles allowed.

Several groups have used the collisional approximations described in section 2.1 to model the DBD actuator plasma. These models solve the following system of equations. First Poisson's equation,

$$\nabla \cdot (\epsilon \nabla \phi) = -e\left(n_+ - n_-\right), \tag{2.17}$$

is solved for the electrostatic potential ϕ. Here ϵ is the permittivity of the medium, while n_+ and n_- are the total number densities of positively- and negatively-charged particles, respectively. Continuity equations are then solved for each of the considered particle species:

$$\frac{\partial n_\alpha}{\partial t} = -\nabla \cdot \Gamma_\alpha + \sum S_\alpha - \sum R_\alpha, \tag{2.18}$$

where S and R are source and sink rates, respectively, for each of the modeled processes that introduce or remove particles from the system. Drift-diffusion approximations, described by equation (2.5), are used to describe the particle fluxes. The models differ in which particle species are considered, what source and sink processes for each species are included in the models, and the numerical methods used to solve these equations.

Singh and Roy [83] used a finite element scheme to solve the system of equations for a single-barrier DBD operating in helium, considering field-dependent ionization but no other sources of electrons. By coupling the calculated EHD forces to a CFD code they modeled an induced flow confined within a few millimeters of the actuator surface [84], similar to experimental data. In the CFD computation, this force was sufficient to eliminate separation in background flows of 10 m/s [85]. The plasma model, however, indicated significant space charge density above the exposed electrode and past the downstream end of the buried electrode [83, 84]. In contrast, experiments have observed plasma only on the downstream edge of the exposed electrode, and the plasma never extends significantly beyond the edge of the buried electrode [39]. Extending the model to include the major positive and negative ion species present in air plasmas did not qualitatively change their results [86].

Two groups have solved the above same system of equations using finite difference techniques, although the exact methods have evolved in order to adapt the models to specific problems of interest. The groups, based out of the Université Paul Sabatier in France and Princeton University in the United States, have both studied single-barrier actuators with thin (one grid cell thick) exposed and buried electrodes. The sources and sinks included by the two groups are electron-impact ionization, recombination, secondary-electron emission, and dielectric charging [13, 87]. Recently the Princeton group has incorporated photoionization as well [88]. Both groups use only limited plasma chemistry. Initial studies by the French group included only electrons and a single species of positive ions [13, 14, 89], while more recent work [90] and all of the Princeton results [87, 91] add a single negative-ion species. The published work of the French group was used as the basis for the model used in our research. The differences between their work and our own are noted along with a detailed description of our model in chapter 6.

Both groups observed the formation of short duration (5–100 ns) microdischarge events. If the applied voltages increase or decrease with time, numerous microdischarges may occur, such as the repeated nanosecond-width peaks in the electron density in figure 2.14. The properties of individual microdischarge events simulated by these two groups are described in section 2.5.2, while the new phenomena that arise when repeated microdischarges occur are described in section 2.5.3.

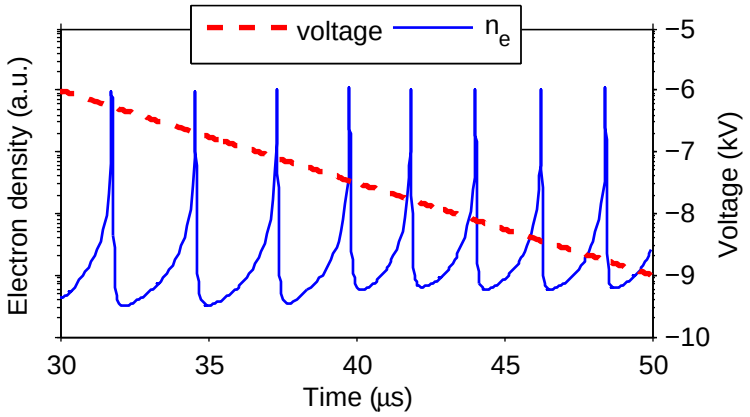

Figure 2.14: Simulated microdischarges for a single-barrier DBD actuator with a linearly decreasing applied voltage

2.5.2 Characteristics of Single Microdischarges

The physics of microdischarges depend strongly on the direction of the electric field in the gas region. This field direction depends on the potential difference between the exposed electrode and the dielectric surface. We consider the cases when the exposed electrode is at a higher and lower potential than the dielectric surface separately below.

When the potential of the exposed electrode is higher than that of the dielectric surface, electrons and negative ions are accelerated into exposed electrode, while positive ions are pushed towards the dielectric. With this polarity, two regimes are possible: a corona-like regime at lower voltages and a streamer-like regime at higher voltages. These "positive" microdischarges are described here. Initially, electron avalanches occurs in a region of strong electric field, generally next to the edge of the exposed electrode. The field strength, which is partially determined by the electrode geometry, and the level of background ionization affect the density of the resulting

plasma [88]. Positive ion flux from this plasma to the dielectric surface will supply secondary electrons to the plasma, with the rate of secondary electron flux controlled by the incident ion flux, and therefore the initial plasma density.

If the plasma generated through the initial avalanches is insufficiently dense, the secondary electron flux to the plasma will be too small to lead to further increases in the plasma density. In this case, the microdischarge behaves like a positive Townsend corona [14, 87, 89], and is sometimes referred to as "corona-like". Electrons drawn in from the background gain enough energy to cause avalanches only very near the exposed electrode. The newly-born positive ions are slowly pushed away from the exposed electrode. The net charge densities are not large enough to significantly modify the potential contours, and the ion flux charges up the dielectric surface slowly compared to the streamer-like microdischarges.

If the plasma is sufficiently dense, the secondary electrons from the dielectric surface will more than replace electrons lost to the exposed electrode. These electrons cause new avalanches, further increasing the plasma density. The charging of the dielectric surface by positive ion bombardment and electron emission shifts the region of strongest electric field away from the exposed electrode. The cycle of secondary electron emission, ionization, and dielectric charging repeats for a section of dielectric farther from the exposed electrode. The result is a dense region of plasma, depicted in figure 2.15, that propagates along the dielectric surface away from the exposed electrode [13]. It continues propagating until the electric field within it is no longer sufficient to support significant ionization. The charging of the dielectric surface by the microdischarge results in the potential on that surface being raised to approximately the potential on the exposed electrode. The dense, moving plasma shares many characteristics with the streamer discharge mechanism discussed in section 2.2.1, with the "uncovered" electrons provided in this case by secondary emission. Because of this similarity, these microdischarges are often simply referred to as streamers.

In 2-dimensional fluid models, the natural background electron density in air of approximately 10^7 m^{-3} is insufficient lead to streamer formation at voltages comparable to those in experiments unless photoionization is included in the model [88]. Since modeling photon transport is computationally expensive, most existing models avoid it by using elevated initial densities [e.g. 13] or

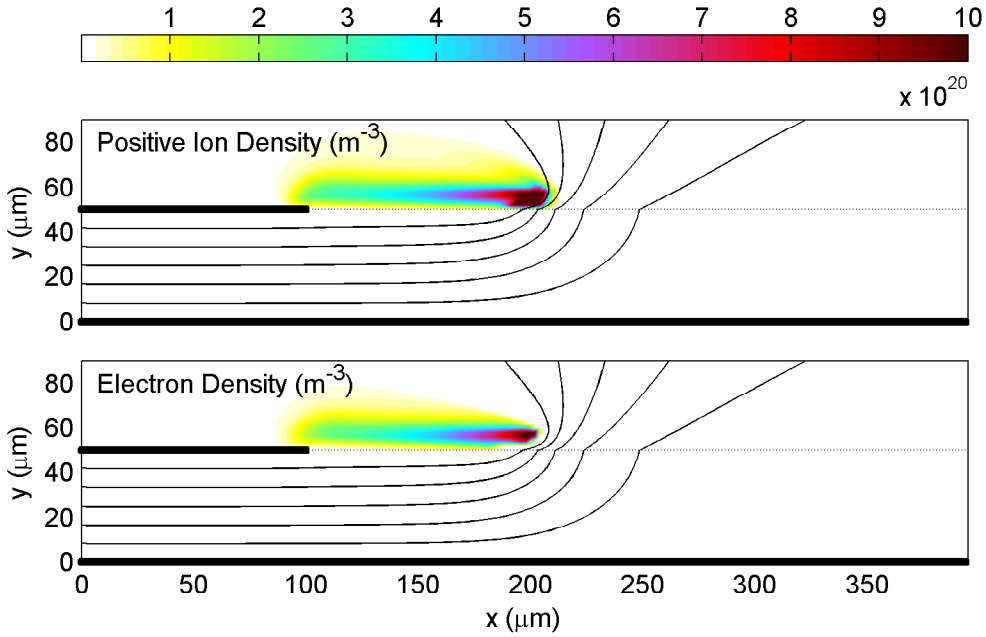

Figure 2.15: Simulated streamer-like plasma formed with +1200 V applied to the exposed electrode. The electrodes are shown in black, with the exposed electrode at $y = 50$ μm and the buried electrode at $y = 0$. The dashed line shows the dielectric surface and the contours represent equipotential surfaces.

by providing additional electrons by specifying a minimum background plasma density [e.g. 87]. Recently Likhanskii et al. [88] included an approximate model for photoionization. They found that it both removed the necessity for an elevated background plasma density and increased the propagation velocity of the streamer front by a factor of two to three.

When the potential of the exposed electrode is lower than that of the dielectric surface, positive ions are pulled into the exposed electrode while electrons and negative ions are accelerated to the dielectric surface. Due to the differences in particle motion, the behaviors of these microdischarges are quite different from those described above. The "negative" microdischarge proceeds as described here.

Initially, as with the positive microdischarge, electron avalanches occur in a region of strong electric field. Again, this is usually near the edge of the exposed electrode. Positive ion bombardment of the exposed electrode provides secondary electrons which cause new avalanches, increasing the plasma density. Unlike in the streamer-like microdischarge, the ion density remains

highest in a region near the exposed electrode throughout the discharge [13]. This region bears some resemblance to the negative Townsend and glow corona regimes described in section 2.2.1. No photoionization is required for the negative microdischarge to occur, even with small levels of initial plasma density [88]. This is likely due to the ready supply of secondary electrons from positive-ion bombardment of the exposed electrode.

Electrons are pushed out of the dense plasma region by the electric field. This leaves behind a cathode sheath-like structure, which supports a significant voltage drop across it. The electrons stream towards the dielectric, either reaching it and charging its surface or attaching to an electronegative particle and forming a negative ion on the way [87]. Some electrons may start new avalanches, although these will be relatively weak due to the lowered electric field strength away from the exposed electrode. The charging of the dielectric adjusts the electric field so that it pushes electrons (and negative ions) towards a location further away from the exposed electrode, as shown in figure 2.16. Charge deposition on the dielectric surface reduces the electric field only to just below the level needed to support electron avalanches, rather than completely shielding it as is the case for the positive microdischarge. Due to the high mobility of electrons, the lifetime of the negative microdischarge is much shorter than that of the positive microdischarge.

In both positive and negative microdischarges, the plasma dynamics are largely controlled by secondary electron emission caused by incident positive ion flux. With a positive voltage applied to the exposed electrode, the positive ion flux is directed at the dielectric surface. Due to surface charging, the point where this flux strikes the surface and causes electron emission changes with time, and we observe a propagating plasma region. With a negative voltage, positive ions are pullled into the exposed electrode. Since the electrode's voltage is held constant, the source of secondary electrons does not move and the region of dense plasma remains stationary.

2.5.3 Repeated Microdischarges

DBDs operated in a filamentary mode have many microdischarges during each half-cycle of the applied voltage, as described in section 2.2.2. To accurately model the plasma, then, simulations must examine the interactions of these events with each other. Since after each microdischarge

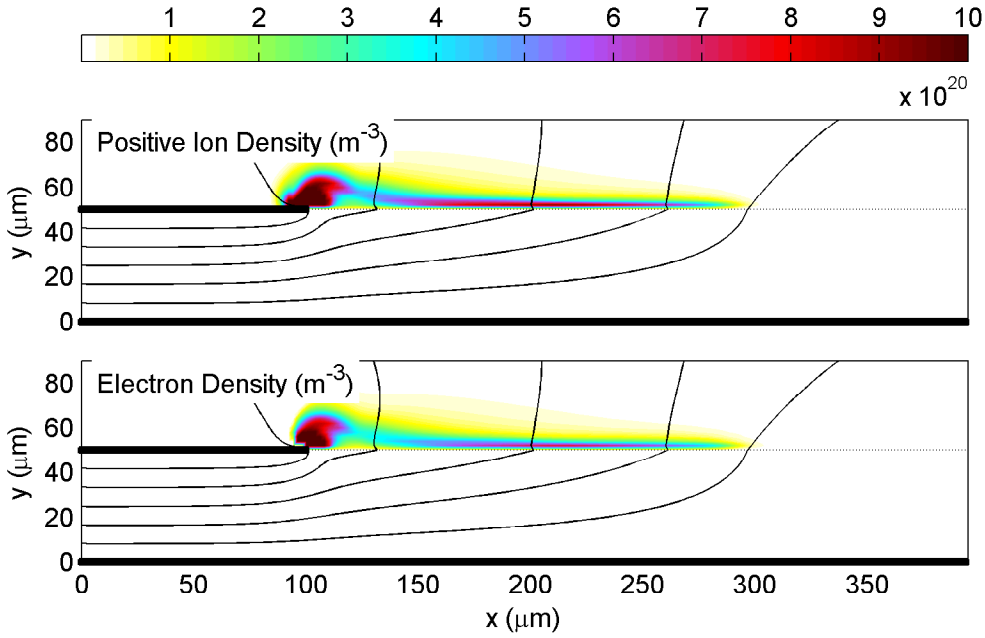

Figure 2.16: Simulated plasma formed with -1200 V applied to the exposed electrode. The electrodes are shown in black, with the exposed electrode at $y = 50$ μm and the buried electrode at $y = 0$. The dashed line shows the dielectric surface and the contours represent equipotential surfaces.

the applied voltage is partially or entirely shielded by charge deposition on the dielectric surface, generating repeated discharges requires a time-varying applied voltage. In this work, we use the term "positive-going" to refer to a situation in which the voltage drop from the exposed electrode to the buried electrode is increasing and positive microdischarges occur. We use the term "negative-going" to refer to a situation in which the voltage drop from the exposed electrode to the buried electrode is decreasing and negative microdischarges occur. Similar to section 2.5.2, we describe the plasma with positive- and negative-going voltages separately.

With a positive-going voltage, actuators move through both corona-like and streamer-like phases. Initially the voltage is relatively small and cannot support a streamer-like microdischarge discharge. As it increases, eventually a threshold is reached and a streamer-like microdischarge occurs [14, 89]. The rate at which the streamers occur is set by the ramp rate of the applied voltage. Generally the duration of a streamer-like event is on the order of 100 ns, while the corona-like phase persists for most of the time in between streamer-like microdischarges. Because of

the long duration of the corona-like phase relative to the streamer-like phase, the majority of the time-averaged EHD force induced by an actuator with a positive-going voltage occurs during the corona-like phase, even though the absolute force is larger during the streamer-like phase [14].

Microdischarges with a positive-going voltage are relatively independent of one another. Each streamer raises the potential on the dielectric surface to nearly the potential on the exposed electrode; the entire voltage drop needed to drive subsequent microdischarges must be supplied by the increase in applied voltage since the last streamer. Electrons for the corona-like phase are, however, supplied by free electrons remaining from the previous microdischarge, so increasing the voltage ramp rate increases the initial electron density since the plasma from the previous microdischarge has had less time to decay. Consequently, the rate at which streamers occur increases somewhat faster than linearly with the voltage ramp rate [14].

Since secondary electron emission plays a large role in streamer formation and propagation, one might expect that adjusting the secondary emission coefficient of the dielectric surface would have large effects on the discharge. Unfer et al. [92], however, noted that a reduction in this coefficient in the model by a factor of 5000 had only modest effects, reducing the number of streamer microdischarges in one half cycle of a sinusoidal applied voltage from 5 to 3 and the total induced EHD force by about 10%. This finding is favorable for actuator modeling, since secondary emission coefficients for dielectric surfaces are not well characterized and may depend on the details of surface condition and other factors.

Qualitatively, microdischarges with a positive-going voltage are also independent of the gas chemistry, although some quantitative effects exist. The addition of a negative ion species to the model reduces the electron density during the decay phase immediately following a streamer [90]. In addition, the motion of negative ions towards the exposed electrode during the corona-like phase cause a small EHD force in the opposite direction as the prevailing force [87]. The inclusion of electron detachment from negative ions results in an extended corona-like phase and an accompanying increase in the time-averaged induced force [92].

The behavior of the plasma with a negative-going applied voltage depends strongly on whether the model allows for the formation of negative ions via electron attachment (and the presence of an

electronegative gas). We first summarize the plasma behavior in pure nitrogen (an electropositive gas) before describing the changes that occur when negative ions are included.

The negative microdischarge described above depends partially on the background positive ion concentration to start the discharge process, via secondary emission of electrons from the exposed electrode. Ion motion to the exposed electrode is slow, due to the low mobility of ions, so the positive ion density decays much more slowly after a microdischarge than does the electron density for a positive microdischarge. In addition, in a negative microdischarge the charge deposition on the dielectric surface only partially shields out the applied voltage. As a result, for the same rate-of-change of applied voltage and a pure nitrogen background, negative microdischarges occur on the order of 30 times more frequently than do positive streamers [14]. Beyond the use of the positive ion density from the previous microdischarge to start a new one, each microdischarge in nitrogen is relatively unaffected by the others.

When an electronegative gas (in these simulations, oxygen) is present, the large electron fluxes through the regions of smaller electric fields away from the exposed electrode promote the formation of negative ions. For more information about attachment coefficients, see section 6.1. Because of this process, ion densities during and after negative microdischarges are considerably larger than in positive microdischarges.

Unlike in an electropositive gas, negative microdischarges in an electronegative gas interact strongly with one another. Since the mobility of negative ions is much lower than that of electrons, some of the negative ions created in one microdischarge will not reach the dielectric, and thus are still present, by the start of the next microdischarge. Over the course of several microdischarges a negative ion "cloud" builds up [87, 90]. The cloud is not solely composed of negative ions; positive ions are also present, but in smaller concentrations. The action of the electric field on the negative ion cloud in between breakdown events is the dominant cause of the EHD force with a negative-going voltage. This force is in the same direction as the force observed for a positive-going voltage. The contributions of the positive-going and negative-going forces to the time-averaged force are comparable to one another for the discharge conditions that have been modeled [93].

A few direct comparisons have been made between the plasma-focused simulations and experimental measurements. Orlov et al. [72] found qualitative agreement between the structure of simulated microdischarges in nitrogen and optical imaging of plasma structures in air using exposure times much longer than an individual microdischarge. We have performed similar comparisons, which are described in chapter 5. Boeuf et al. [93] simulated actuators with a variety of different effective frequencies and voltage amplitudes, and found approximately the same trends in the induced force as seen experimentally by Roth and Dai [65].

Chapter 3

Experimental Methods

We have conducted several experimental measurements to characterize the behavior of DBD plasma actuators with a variety of discharge geometries. These actuators are described in more detail in section 3.1. In order to better determine the ideal actuator design to maximize the induced force, we have measured the force. To ensure the accuracy of these results, we employed two techniques: direct measurement using an electronic balance and a stagnation probe method. High-speed imaging experiments were performed in order to observe the plasma dynamics on short time scales not accessible by the force measurements.

All the experimental measurements in this work were conducted in atmospheric pressure air. The air was simply room air in our laboratory. No attempts were made to control for daily or seasonal fluctuations in air temperature, humidity, etc. In addition, as described in section 3.1.2 all actuators were hand-made and undoubtedly varied slightly in quality. Based on our experimental results, the effects of these variations were small relative to the effects of changing the actuator geometry or the applied voltage. Since the exact level of these fluctuations are unknown, however, they are not included in the uncertainty levels presented with the results of chapters 4 and 5.

3.1 DBD Actuator Description

We have studied a range of DBD plasma actuators, which are described in this section. The geometric variations we have examined experimentally are described in section 3.1.1 along with the reason each variation was selected. These actuators were all constructed by hand. The materials

and methods used to build them are described in section 3.1.2. Finally, the circuitry and the applied voltages we used to drive the actuators are described in section 3.1.3.

3.1.1 Actuator Geometries

In the experimental portion of this work, we have primarily examined single-barrier DBD actuators, while also performing some measurements on double-barrier actuators. We consider several variations to the geometry of the single-barrier actuators in order to determine which parameters are most important. Both single- and double-barrier geometries have been shown to induce air flow in the nearby neutral gas [70]. All of the figures in this section are drawn such that the induced air flow moves from left to right.

As described in section 2.2.2, single-barrier surface discharges include two electrodes, one of which is insulated. We refer to the insulated electrode as the buried electrode, since it is placed beneath a layer of dielectric, and the non-insulated electrode as the exposed electrode. In all the single-barrier actuators used in this work, the dielectric thickness was 0.25 mm and the buried electrode length was 15 mm. The actuators spanned 60 mm in the direction perpendicular to the schematics of figure 3.1.

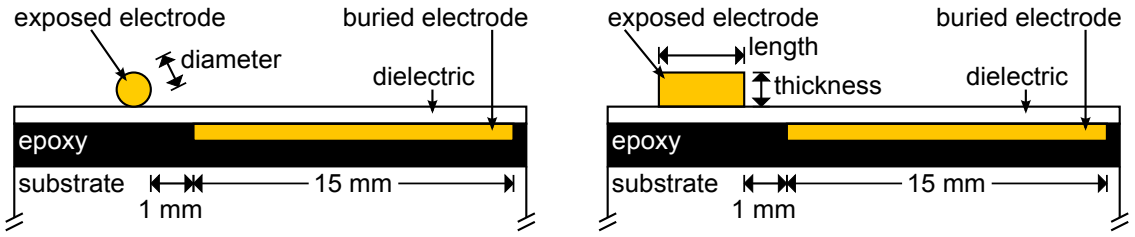

(a) (b)

Figure 3.1: Schematics of single-barrier actuators with (a) a cylindrical exposed electrode and (b) a rectangular cross-section exposed electrode

The experimental measurements in this work primarily examine the differences in actuator behavior between devices with exposed electrodes of various sizes, shapes, and materials. Some tests use cylindrical exposed electrodes, as shown in figure 3.1(a). The results of force measurements using this actuator design are described in sections 4.1, 4.2.1, 4.2.3, and 4.4. We have also

studied single-barrier actuators with exposed electrodes of rectangular cross-section, shown in figure 3.1(b). The results of force measurements using these actuators are included in sections 4.2.2, 4.2.3, and 4.2.4. For both of these designs, the horizontal gap between the rightmost edge of the exposed electrode and the leftmost edge of the buried electrode was 1 mm, as shown in figure 3.1. Optical measurements of both designs are described in chapter 5.

To aid in examining the differences between actuators with rectangular and cylindrical exposed electrodes, we have used actuators with several cylindrical electrodes placed side-by-side, as pictured in figure 3.2. This design allowed us to maintain a curved electrode edge while expanding the effective length. Adjusting the number of cylinders controls this length. Cylinders were always added or removed from the left-hand edge so that no gaps existed between the cylinders, and the electrode gap was held constant at 1 mm. Force measurements of actuators with this design are discussed in section 4.2.4.

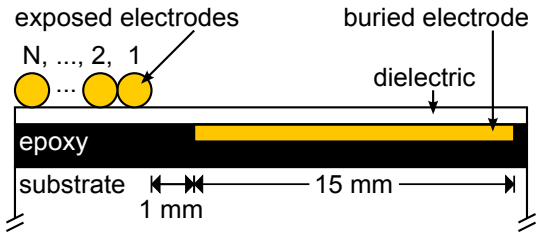

Figure 3.2: Single-barrier actuator with side-by-side cylindrical exposed electrodes

We have also examined double-barrier DBD actuators, in which both electrodes are insulated. To provide the geometric asymmetry required to induce a net force, all of the double-barrier actuators used one narrow electrode and one wide electrode. Both are placed immediately below the dielectric layer. The double-barrier geometry is shown schematically in figure 3.3. Similar to the single-barrier geometry, the dielectric thickness was 0.25 mm, the wide electrode length was 15 mm, and the devices spanned 60 mm in the direction perpendicular to the figure. The horizontal gap betweeen the rightmost edge of narrow electrode and the leftmost edge of the wide electrode was set to be 2 mm, as shown in figure 3.3. The gap was larger than the electrode gap in the single-barrier geometry due to the high likelihood of arc formation through the epoxy observed in double-barrier actuators with 1 mm electrode gaps.

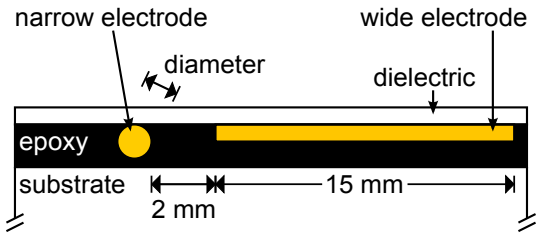

Figure 3.3: Schematic of a double-barrier actuator

In general, double-barrier actuators require larger applied voltages to generate plasma and induce smaller forces than single-barrier actuators [94]. We include them in this study for a variety of reasons. The double-barrier geometry has fewer possible sources of irregularities compared to single-barrier discharges. Double-barrier actuators have no features above the surface to impede the induced air flow, and the electrodes are not in physical contact with the plasma so their material characteristics cannot affect the discharge. Such actuators may also find practical applications, as the lack of an exposed electrode means they will be less prone to arcing to nearby materials and not susceptible to degradation via dielectric deposition on an electrode. Most importantly for our work, double-barrier actuators provide an additional system in which we can compare our experimental data to the results of the computational model.

3.1.2 Actuator Construction

For all actuators used in this work, the dielectric was made from a 0.25 mm thick polyester film. The relative dielectric constant of the film, ϵ_d, was given by the manufacturer as 3.3. In order to avoid plasma formation underneath the dielectric layer, we filled this space with Stycast 2651-40 epoxy, which had a similar relative dielectric constant of 3.8. A 10 mm thick acrylic layer placed below the epoxy was used to mount the actuators, and is not believed to have played any role in the discharge. The buried and wide electrodes were made from copper foil tape 0.04 mm thick with a 0.05 mm acrylic adhesive. The tape was mounted to the dielectric film, so the adhesive was between the film and the buried or wide electrodes in figures 3.1–3.3.

Cylindrical exposed and narrow electrodes in single- and double-barrier actuators were constructed of copper (Cu), tungsten (W), or stainless steel (SS). They consisted either of straightened

wires (for smaller diameters) or straight rods (for larger diameters). Rectangular cross-section exposed electrodes in single-barrier actuators were made from either copper or stainless steel. The 0.04 mm thick copper electrodes used the same foil tape as the buried electrodes. Images of single-barrier actuators with cylindrical and rectangular exposed electrodes are shown in figure 3.4.

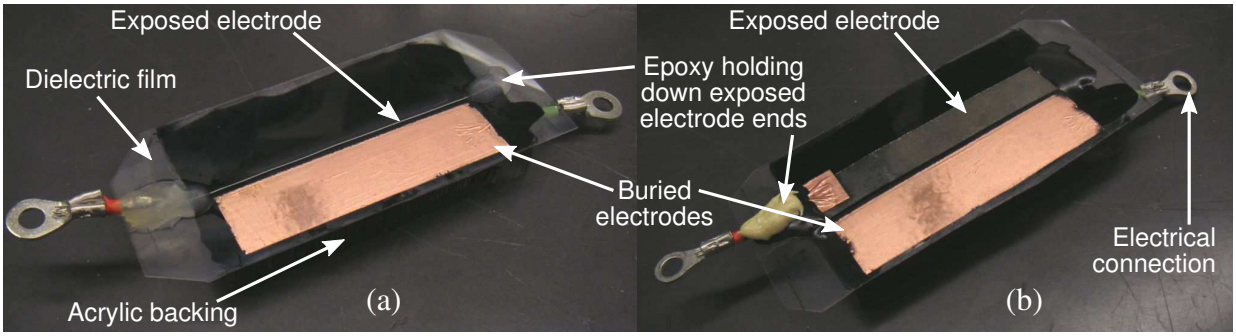

Figure 3.4: Photographs of single-barrier actuators with (a) a cylindrical exposed electrode and (b) with a rectangular cross-section exposed electrode

We constructed actuators from the dielectric layer down. For a single-barrier actuator, the buried electrode was affixed to the bottom of the dielectric. Several layers of the insulating epoxy were then applied to build up thickness before attaching the acrylic backing. After flipping the actuator over, an exposed electrode was placed on top of the dielectric film. The exposed electrode was held in place with tape while applying epoxy to both ends. That epoxy is noted in figure 3.4. The tape was removed prior to use. Construction of double-barrier actuators proceeeded similarly, except that the narrow electrode was epoxied in place immediately after the wide electrode was affixed. A step-by-step procedure describing actuator construction is included in appendix A.

3.1.3 Applied Voltage

We created the applied voltage waveforms using an arbitrary signal generator and routed the output to a Trek 20/20B high voltage amplifier. The output of the amplifier was passed through a two-stage low-pass filter to remove megahertz-frequency noise on the signal before being connected to the exposed electrode (for single barrier actuators) or the narrow electrode (for double barrier actuators). The buried or wide electrodes were always grounded. A circuit diagram describing the connections is shown in figure 3.5. We used the resistor or capacitor in the ground

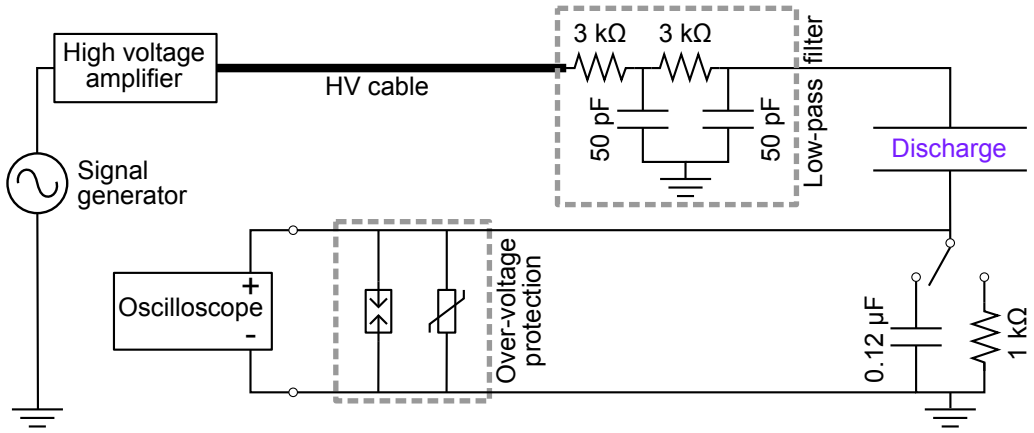

Figure 3.5: Discharge circuit diagram

path of the discharge to measure the current or accumulated charge, respectively, as described in section 3.2.3.

In this study all force, flow, power, and optical emission measurements were made on actuators driven by symmetric triangle waveforms oscillating at 1 kHz, except for the stability and uniformity experiments of section 4.1 which used 500 Hz sine waves. The triangular voltage shape was chosen to simplify comparisons between the experimental measurements and the simulations. 1 kHz was the highest frequency that could be achieved by the HV amplifier for the range of voltage amplitudes used. With symmetric triangle voltages, plasma ignition occurred for single-barrier discharges when the amplitude was between about 3 and 4 kV. For double-barrier actuators, ignition generally occurred between 10 and 11 kV amplitude signals. At voltage amplitudes above 13 kV, the dielectric film would degrade and allow arc formation, destroying the actuator.

3.2 Force and Power Measurements

Prior research has used several methods to measure the action of DBD actuators on the neutral gas. One such method consists of simply mounting the actuator being tested on an electronic balance and directly measuring the force [e.g. 39]. A separate technique involves the measurement of the stagnation pressure of the induced flow velocity [e.g. 95]. We have applied both of the balance and the stagnation pressure techniques, with the details described in sections 3.2.1 and 3.2.2

respectively. Often in the literature actuator forces are reported in terms of the force per unit input power. To make comparisons to these data, we also determined the input power by the method described in section 3.2.3. All of the measurements described in this section are time-averaged, and consider only forces parallel to the dielectric surface.

3.2.1 Electronic Balance

We have measured the forces induced by our plasma actuators using an Ohaus model PA313 electronic balance with 1 mg (equivalent to 10^{-5} N) resolution. While the sensitivity of the scale is less than that allowed by the stagnation probe technique described in section 3.2.2, it provides a direct measurement of the induced forces. The force measurement was made by mounting an actuator on a stand with the air flow directed upwards. The balance then measures the downward reaction force on the actuator as a positive force.

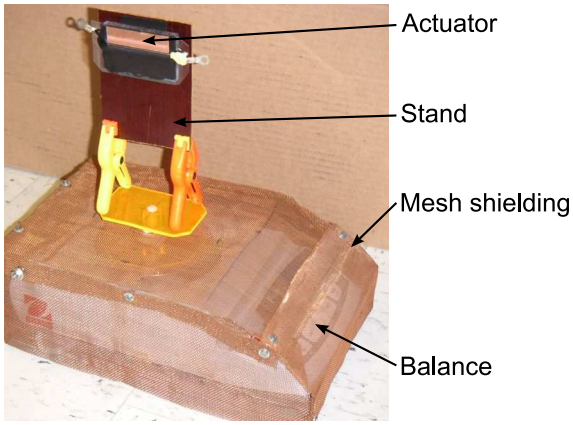

Figure 3.6: The shielded balance and actuator stand used for direct force measurements

To eliminate RF interference between the applied high voltage and the internal balance electronics, we covered the balance using a grounded copper mesh with a hole above the balance pan. An insulating platform, on which the actuator stand stood, fit through this hole. The balance, stand, and an actuator are shown in figure 3.6. Electrical connections were made using light 32 AWG wire to eliminate additional forces due to sagging wires. The high voltage wire was held several inches above the copper mesh to eliminate electrostatic attraction between the two conductors. An

acrylic box 25 cm $\times$ 61 cm $\times$ 36 cm housed the balance, shielding, and actuator. The box blocked ambient air currents from influencing the measurement and prevented the ozone generated during DBD operation from escaping into the lab air.

Time variations in the induced forces could not be directly observed due to the tendency of the balance reading to slowly drift during actuator operation. To eliminate the effects of this drift, after conditioning (see section 4.1) and immediately prior to recording data the high voltage was turned off, the balance zeroed, and the high voltage quickly turned back on.

In order to directly compare our results from the balance measurements with the stagnation probe data, we converted the former into forces per unit length by dividing by the width of buried or wide electrode (60 mm). This is a good, but not exact, estimate of the plasma width, which varies slightly from actuator to actuator. Based on visual observation we estimate the plasma width variation to be on the order of $\pm 5\%$, leading to uncertainties comparable to the uncertainty in the force measurement itself.

3.2.2 Stagnation Probe

We have measured induced gas velocities using a small movable stagnation probe, shown in figure 3.7. To aid in positioning, eliminate ambient air currents, and prevent ozone from entering the lab air, stagnation probe measurements were conducted inside a sealed cylindrical metal chamber. The chamber was 17 cm tall and 30 cm in diameter, with the actuator located near the center of the chamber. The probe itself consisted of a glass capillary tube with a 0.4 mm inner diameter and 0.2 mm wall thickness. Tube pressure was determined using a Dwyer model 607-01 differential pressure transmitter, with the low pressure side connected to a port on the bottom of the chamber. This measurement technique is similar to that used successfully by Pons et al. [63].

In order to compare the stagnation probe and balance measurements, we converted the measured pressures into induced forces using the method derived below. The derivation is similar to that performed by Baughn et al. [12], although our system has no background flow velocity. To analyze the system, we consider a rectangular control volume on the actuator surface which includes the entire plasma volume, such as that shown in figure 3.7. The momentum balance, described by

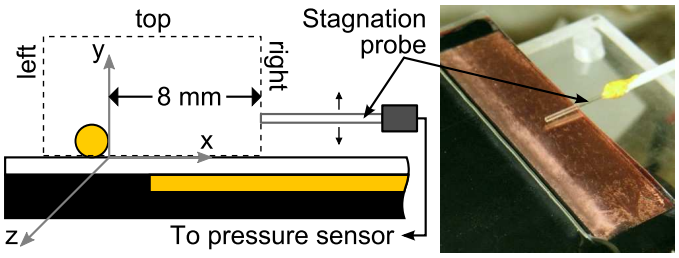

Figure 3.7: Coordinate system, with the control volume used in the velocity-to-force conversion indicated by a dashed rectangle (left), and an image of the stagnation probe near a single barrier actuator (right)

equation (2.14), can be written for the x direction of this system as

$$\frac{F_{\text{plasma}}}{L_z} + \frac{F_{\text{shear}}}{L_z} = \underbrace{\rho \int_{\text{right}} u_x^2 \, dy}_{\text{I}} + \underbrace{\rho \int_{\text{top}} u_x u_y \, dx}_{\text{II}} - \underbrace{\rho \int_{\text{left}} u_x^2 \, dy}_{\text{III}} + \underbrace{\int_{\text{right}} p \, dy}_{\text{IV}} - \underbrace{\int_{\text{left}} p \, dy}_{\text{V}} . \tag{3.1}$$

The integral subscripts indicate over which side of the control volume the integral is performed, and L_z is a unit length in the z direction. The only body force considered here is the electrohydrodynamic force of the plasma on the air, F_{plasma}. The included surface forces are static pressure forces on left and right surfaces and shear force, F_{shear}, acting between the dielectric layer and the air flow. We note that since the shear force acts to slow the $+x$-directed flow, it will always be negative.

For our initial analysis, we simplify equation (3.1) with several assumptions that limit the data required to infer each actuator's force. The effects of these assumptions are investigated in section 4.4. First, we assume the static pressure of the gas is constant everywhere and equal to the reference pressure at the chamber bottom:

$$p = p_{\text{ref}}.$$

As the chamber was open to room air prior to being sealed off to reduce measurement noise, p_{ref} is approximately equal to atmospheric pressure for all measurements. The assumption of constant static pressure allows us to neglect terms IV and V in equation (3.1), as they will cancel. It also permits a simple conversion from the measured stagnation pressure to a velocity by rearranging equation (2.15):

$$u_x \approx \sqrt{2(p_0 - p_{\text{ref}})/\rho_g}. \tag{3.2}$$

Here p_0 is the measured stagnation pressure and ρ_g is equal to 1.17 kg/m^3, the mass density of air. Previous measurements by Enloe et al. [68] indicated that density fluctuations near plasma actuators are generally smaller than 2% of the background, so the density may be reasonably assumed to be constant. The assumption of a constant static pressure was implicitly made by Pons et al. [63] in their measurements near a single-barrier DBD actuator, as they used equation (3.2) to determine the velocity.

In addition to the assumption of constant static pressure, in our initial analysis we neglect the momentum flux into the control volume through the left and top edges. With this assumption, terms II and III in equation (3.1) can be neglected:

$$\int_{\text{top}} u_x u_y \, dx \approx 0 \quad \text{and} \quad \int_{\text{left}} u_x^2 \, dy \approx 0.$$

In section 4.4 we show that term III makes a significant, although not dominant, contribution to the total force.

Once these assumptions are made, equation (3.1) simplifies to

$$\frac{F_{\text{plasma}}}{L_z} + \frac{F_{\text{shear}}}{L_z} \approx \rho \int_{\text{right}} u_x^2 \, dy. \tag{3.3}$$

In practice, we fit an analytic function to the observed velocities and use that in equation (3.3). We used a skewed Gaussian,

$$u_{\text{fit}} = u_0 \sqrt{y} \exp\left[-\left(\frac{y - y_0}{L_0} \right)^2 \right],$$

where u_0, y_0, and L_0 are free parameters. This function was chosen both due to its excellent empirical fits to the observed data and because it always satisfies the no-slip condition of zero flow velocity at a material surface. An example fit is shown in figure 3.8.

Equation (3.3) is equivalent to the calculations by Baughn et al. [12] with the background velocity reduced to zero. That study measured the absolute plasma force and so also subtracted a shear force. In this work we compare the calculated forces to those measured directly with an electronic balance; since the balance measurements inherently include the shear force, we leave it on the left-hand side of (3.3). The stagnation pressures used for force estimates in chapter 4 were measured at $x = 8$ mm. Our calculations therefore only include the shear force up to 8 mm, while

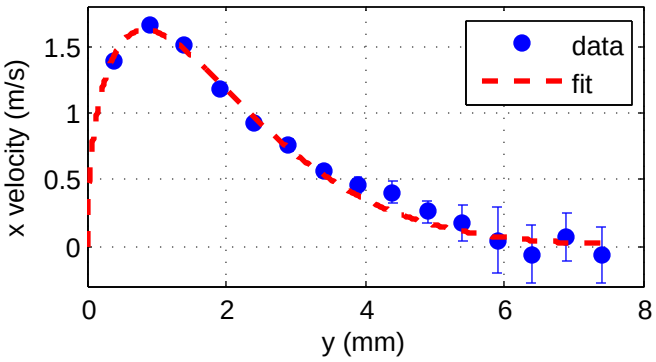

Figure 3.8: Typical velocity data and skewed Gaussian fit

the balance measurements include the shear force out to the edge of the dielectric at approximately 16 mm. We estimate the effect of this discrepancy in section 4.4.

3.2.3 Discharge Power

To determine the electrical power dissipated by the plasma actuators, we placed a 0.12 µF capacitor in the ground path of the actuator, as shown in figure 3.5. Provided its capacitance is much larger than the capacitance of the actuators (which were generally smaller than 10 pF), the circuit characteristics are unaffected by its presence. The charge deposited in the actuator is equal to that on the measurement capacitor, and can be determined by measuring the voltage across the capacitor. Typical data are shown in figure 3.9(a). Plotting the charge against the applied voltage yields a parallelogram-like shape, sometimes called a Lissajous figure, such as the one in figure 3.9(b).

The average actuator current can be found by taking the time derivative of the charge on the capacitor. The time-averaged power is then determined by integrating the product of the applied voltage and the actuator current over an integer number of voltage cycles [63]. This is equivalent to finding the area inside the parallelogram of figure 3.9(b). The total dissipated power includes losses to dielectric heating, power required to generate the plasma, energy transfer to the neutral flow, and a small amount of reflected power [65].

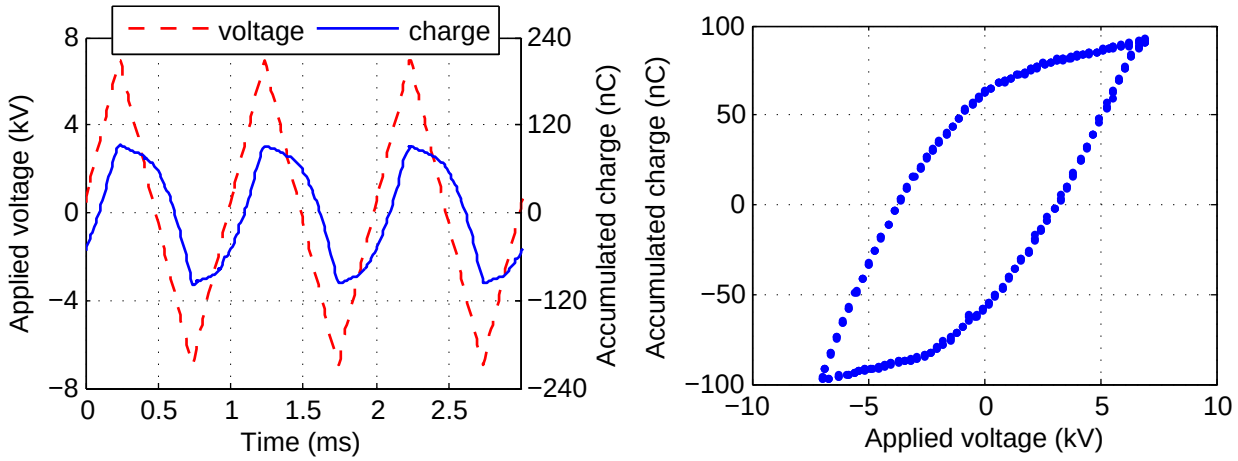

(a) (b)

Figure 3.9: Typical charge and voltage data for a single-barrier actuator. The same data are plotted (a) versus time and (b) as a Lissajous figure.

The discharge current can be determined by placing a resistor in ground path of the DBD. Discharge currents are typically "spiky," like the current shown in figure 2.5. The individual current spikes are so short that they are sometimes missed by a digital oscilloscope examining an entire applied voltage cycle. Consequently, integrating the product of the applied voltage and the observed current is not as accurate as the charge-voltage method described above.

3.3 Optical Imaging

We conducted measurements of the visible light emission from the plasma using intensified charge-coupled device (ICCD) cameras. This type of camera is capable of observing light emission at time scales as short as 2 ns, allowing us to observe the structure of microdischarges as well as the average plasma behavior on the time scales of the applied voltage. In all measurements of single-barrier actuators, the actuators were powered by a 7 kV amplitude symmetric triangle waveform at 1 kHz. For measurements of double-barrier actuators, the amplitude of the applied voltage was increased to 12 kV.

3.3.1 Imaging System

The observations of microdischarge formation and propagation in section 5.2.3 were performed using an Andor iStar ICCD camera. All other measurements used a Princeton PI-MAX ICCD camera. Both cameras have similar capabilities. The observed image in an ICCD camera is formed by the following processes. Photons entering the camera strike a photocathode, releasing electrons. These electrons are drawn into a microchannel plate (MCP). Electrons exiting the MCP strike a phosphor, which emits photons that are collected by the CCD array. When biased, the MCP serves as an electron multiplier, intensifying the signal. When unbiased, the MCP effectively blocks any signal from reaching the CCD. The bias signal to the MCP then controls both the gain of the camera and the time period during which collected light will reach the CCD array. The length of this time period is known as the gate width of the intensifier, and is functionally equivalent to the exposure time of a traditional film camera.

Due to the extremely short duration of individual microdischarges, described in section 5.2.3, camera gating could not be triggered by the microdischarges themselves. Instead, gating was controlled by a trigger signal from the waveform generator. Since the delay between the trigger signal and the gating pulse could be set via software commands, we were able to observe the plasma at any specified time during the applied voltage cycle.

All imaging experiments were conducting with the camera pointed at the dielectric surface; this view is equivalent to looking downwards from above in figures 3.1 and 3.3. Prior to the examination of the plasma in each actuator, we recorded a reference image of the actuator in ambient light. Since images of the plasma were recorded in the dark, these reference images were essential to determining the physical location of the plasma relative to the electrodes. Example reference images are shown in figure 3.10 for a single-barrier actuator and figure 3.11 for a double-barrier actuator.

Most camera images captured square areas approximately 11 mm by 11 mm, as shown in figures 3.10 and 3.11. The short-gate width images of section 5.2.3 captured a slightly smaller area of approximately 9 mm by 9 mm. In general, the field of view varies slightly from actuator to actuator due to small variations in the distance between the camera and the actuator surface. In

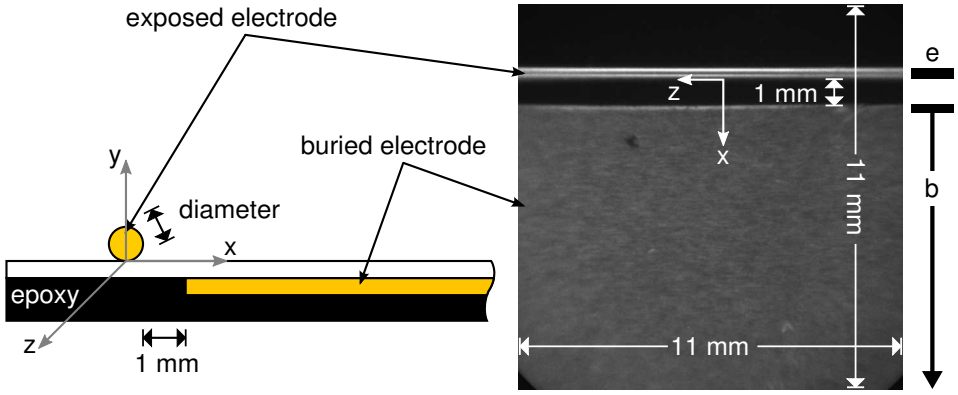

Figure 3.10: Image field of view for a single-barrier actuator

addition, the positions of the electrodes in the field of view vary slightly from actuator to actuator. Each image shown in chapter 5 is accompanied by guide marks showing the positions of the electrodes. For each image of a single-barrier actuator the exposed electrode position and length is indicated by a line marked with an ‘e’, while the position of the buried electrode is indicated by a ‘b’, as shown in figure 3.10. Similarly, for each image of a double-barrier actuator the position and approximate diameter of the narrow electrode is indicated with an ‘n’, while the position of the wide electrode is denoted with a ‘w’, as in figure 3.11.

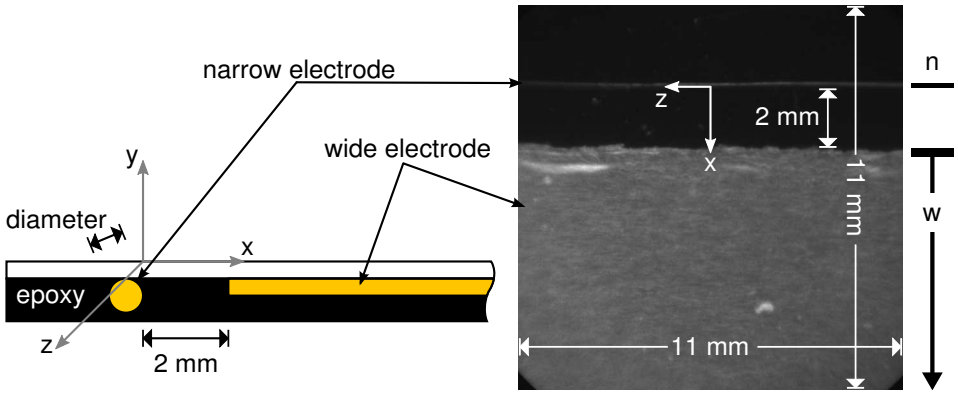

Figure 3.11: Image field of view for a double-barrier actuator

3.3.2 Plasma Imaging

Radiation emission from plasmas occurs when excited states of neutral molecules and ions return to a lower energy state via photon emission. In millitorr-pressure plasmas photon emission occurs via electric dipole radiation [17], while at atmospheric pressure this de-excitation is more likely collision-induced. The excitation of ground-state particles may occur via either electron or ion impact. Which particle dominates the excitation process is a complicated function of charged-particle energy distributions and excitation cross-sections. Since the particle energy distribution functions are dependent on the local electric fields, which may change rapidly, the light emission described in chapter 5 should not be taken as corresponding to the density of a particular species. Instead, we only take the observed images as loosely corresponding to the plasma structure. We use these images to make qualitative comparisons to simulation results in section 7.4, and to observe variations in actuator behavior on time scales not accessible to our force measurements.

As discussed in section 2.4.2 and shown experimentally in section 5.1, the plasma structure in surface DBDs depends largely on the rate-of-change of the applied voltage, rather than its absolute value. It is then logical to divide our applied symmetric triangle voltage into two halves: one in which the voltage applied to the exposed or narrow electrode is rising, and one in which this voltage is falling. We refer to these periods as the positive-going and negative-going half cycles, respectively.

Microdischarges occur during only a portion of each of the half cycles. As discussed in section 2.5, microdischarges deposit charge on the dielectric surface to shield out the applied voltage. When the voltage rate-of-change switches direction, the electric field in the gas region is too weak to cause ionization until the applied voltage rises (or falls) to a level sufficient to supply the required field. Once the applied voltage reaches this critical level, microdischarges occur throughout the remainder of the half cycle. These periods of inactivity and activity are visible in the discharge current shown in figure 3.12.

Based on our observations using the cameras, microdischarges occur roughly randomly distributed in time throughout the active periods of each half cycle. Since camera gating was triggered based on the applied voltage cycle, individual image acquisitions only sometimes contained

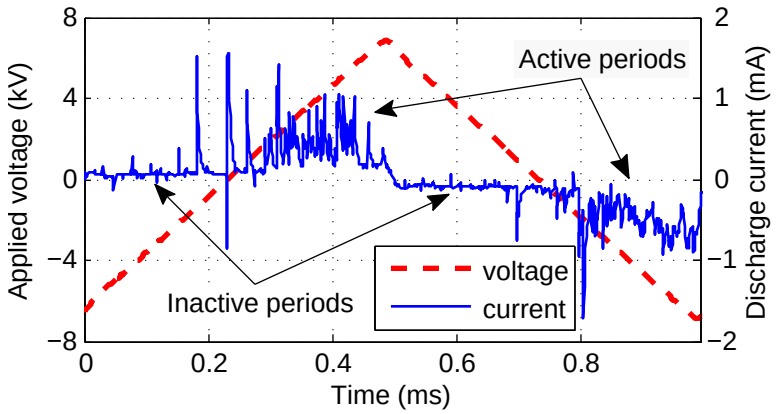

Figure 3.12: Discharge current during the positive- and negative-going half cycles of a single-barrier actuator, showing periods of activity and inactivity

light-emitting plasma. The fraction of acquired images containing plasma varied depending on camera gate width, which half-cycle was under investigation, and the actuator geometry. As rough averages, plasma was visible in approximately 50% of images at a gate width of 10 µs, while finding a single microdischarge image at a gate width of 10 ns required acquiring and discarding hundreds or thousands of empty images. The images presented in chapter 5 are representative of images in which plasma was visible. Unless noted otherwise, the brightness of all those images have been scaled to emphasize the observed plasma structures rather than to allow comparisons between images.

In sections 5.2.1 and 5.3 we examine the average behavior of microdischarges during each half cycle. We used the following method to perform this averaging. The applied voltage cycle was divided into 100 segments, each 10 µs long. For each of those segments, we applied 100 identical gating pulses to the camera, effectively integrating the light from 100 exposures (each of the same segment of the cycle, but at a different time) onto a single image. This gave us 100 images with tens to hundreds of microdischarges in each image. For each image, we then added together the collected signal of each column of pixels. This is equivalent to compressing the image in the direction of actuator uniformity, which is the z direction of figures 3.10 and 3.11. These steps yield, for each segment of the applied voltage cycle, the average light emission as a function of

x, the distance from the edge of the high voltage electrode. Examples of the results are shown in figures 5.7, 5.8, and 5.18.

Chapter 4

Experimental Force Measurements

We have performed force measurements on a variety of single- and double-barrier DBD plasma actuators, as described in chapter 3. All of the measured forces and velocities described in this chapter are in the the x direction in figure 3.7, that is the direction parallel to the dielectric surface and perpendicular to the electrode edges. Section 4.1 examines the spatial uniformity and temporal stability of the induced air flow. Sections 4.2 and 4.3 describe our measurements of single- and double-barrier discharges, respectively. Finally, section 4.4 quantitatively compares the results from the electronic balance and stagnation probe measurements. Many of these results were published in Hoskinson et al. [94].

4.1 Discharge Uniformity and Stability

The usefulness of our force measurements depends on the validity and repeatability of those measurements. Since the stagnation probe technique yields a force per unit length, while the balance technique measures an absolute force, a valid comparison requires that the force is approximately uniform along the actuator width. Validity is further addressed in section 4.4 by comparing the stagnation probe and electronic balance measurements. We address both the uniformity and repeatability of the actuator force in this section.

The plasmas formed in plasma actuators, like most DBD air plasmas at atmospheric pressure, are visibly non-uniform. The plasma forms numerous narrow filaments bridging between the two electrodes. The induced velocities, however, are relatively uniform. We have scanned the stagnation probe along the z direction (see figure 3.7) of two actuators, with the results shown in

figure 4.1. At each point, we estimated the flow velocity by applying equation (3.2). The actuators were a single-barrier actuator with a 0.25 mm diameter cylindrical exposed electrode and a double-barrier actuator with a 1.0 mm diameter narrow electrode. For all measurements, the stagnation probe was 8 mm away from the exposed or narrow electrode edge and 0.5 mm above the dielectric surface.

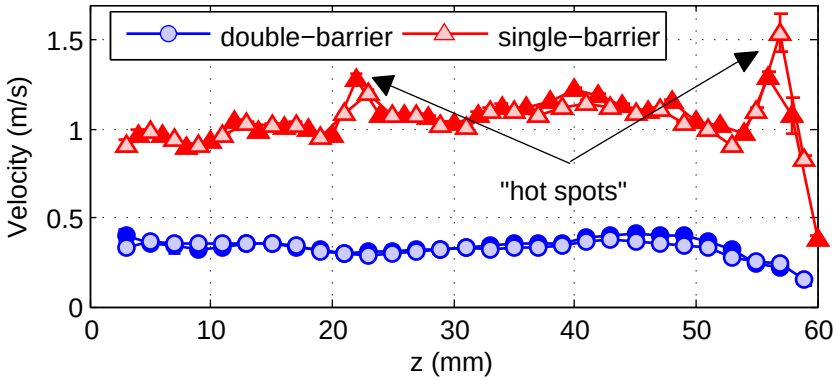

Figure 4.1: Variation of the induced flow velocity in the z (uniform) direction. The point $z = 30$ mm corresponds to the center of the 60 mm wide electrodes. The stagnation probe was scanned in both directions, with the data points from each direction having different shading.

At two locations along the single-barrier actuator, velocities were noticeably larger than the average. These two locations corresponded to "hot spots" on the actuator; the plasma was visibly brighter in these areas than along the rest of the device. We have previously created similar bright filaments by intentionally introducing a small protrusion on the exposed electrode of a single barrier actuator. It is likely the hot spots are caused by small non-uniformities in the actuator materials behaving in a similar fashion.

Neglecting the variation at such hot spots and at the actuator edges, the velocities near the single-barrier actuator were always within $\pm 20\%$ of their values at the center. Double-barrier velocities showed similar uniformity: always within $\pm 30\%$ of their values at the center. This relative homogeneity is reasonable, since the visible plasma non-uniformity is on the scale of 1 mm or less, while the velocities were measured several millimeters away from the plasma. The stagnation probe measurements discussed in the remainder of the work avoided examining velocities near

"hot spots." The additional force provided by these regions will be implicitly included in the balance measurements, but as long as they are not numerous this will have only a small effect on the measured forces.

Early stagnation probe measurements showed large run-to-run variations, with stronger variations for double-barrier actuators. We observed that this variability diminished as the actuator run time immediately prior to the measurement increased. Velocity profiles for both single- and double-barrier actuators reached steady state after 15–45 minutes of run time, but the variability returned if the actuators were left off overnight. This variability in velocity profiles is illustrated in figures 4.2 for actuators driven by 500 Hz sinusoidal waveforms. In both sets of measurements, run 2 was conducted 24 hours after run 1. While the four profiles of the single barrier actuator show only relatively small differences, the peak velocity for the double barrier actuator increased by almost 50% after conditioning for 90 minutes.

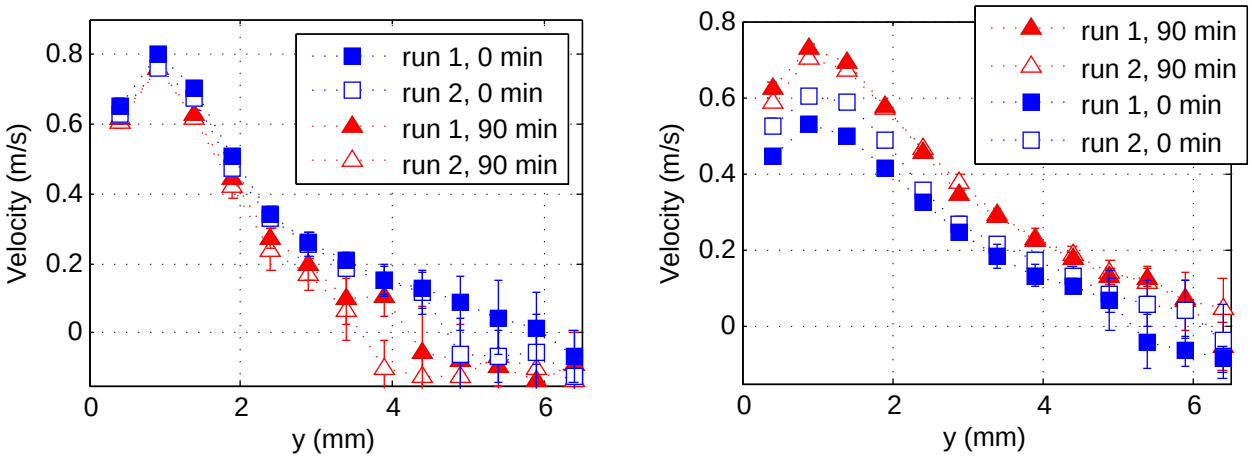

Figure 4.2: Run-to-run variation and conditioning in (a) a single-barrier actuator with a 0.40 mm cylindrical exposed electrode and (b) a double-barrier actuator with a 0.25 mm narrow electrode. The times indicated how much run-time elapsed immediately prior to the measurement.

The power dissipated in double-barrier actuators changed by less than 12% over the conditioning period, with the direction of the change appearing to be random. Single-barrier actuators exhibited a slightly larger change in the power (less than 15%), but all actuators dissipated less

power after conditioning. In order to eliminate this source of uncertainty, immediately prior to all force and power measurements we ran each single-barrier actuator for at least 15 minutes, and each double-barrier actuator for at least 30 minutes.

Shin and Raja [96] observed similar run-to-run variation and stabilization of the discharge current after conditioning on the same time scales for a parallel-plate DBD. They eliminated thermal effects and the build-up of gas impurities as possible causes of the variation, which they ascribed to plasma modification of the dielectric surface's secondary electron emission coefficient. This coefficient is likely to change upon exposure to room air, leading to the run-to-run variation.

4.2 Single-Barrier Actuators

Our force measurement efforts have focused on single-barrier actuators. The results of those experiments are included in this section. As described in section 2.4, this geometry has been much more widely studied by other groups, providing opportunities to compare to previous research, which we do in section 4.2.3. We have discovered, as described in section 4.2.1, that when the exposed electrode is cylindrical, the induced time-averaged force increased exponentially as the diameter is decreased. The increase in force appears to be largely due to the reduction in the electrode size in the dimension parallel to the dielectric surface, rather than the reduction in electrode thickness. Only a relatively small force increase is seen in actuators with rectangular cross-section exposed electrodes if only the thickness, and not the length, is reduced.

4.2.1 Effects of Cylindrical Exposed Electrode Diameter

We have conducted force and power measurements on single-barrier actuators with cylindrical exposed electrodes ranging from 0.03 mm to 1.0 mm in diameter, as described in section 3.1. Force measurements were made using both the electronic balance, described in section 3.2.1, and the stagnation probe technique, described in section 3.2.2. Discharge powers were determined as described in section 3.2.3.

The measured discharge powers for these actuators were independent of the material used to make the exposed electrode. For exposed electrode diameters above approximately 0.2 mm, the

power was also independent of the diameter, as shown in figure 4.3. Below this size, however, the dissipated power decreased with decreasing electrode diameter. In section 5.2.2 we show that this is due to the reduced number of filamentary microdischarge events in actuators with these small diameter electrodes. Fewer microdischarges corresponds to a reduced current draw, and therefore less dissipated power. In the range examined, the dissipated power was approximately proportional to the applied voltage amplitude for all actuators.

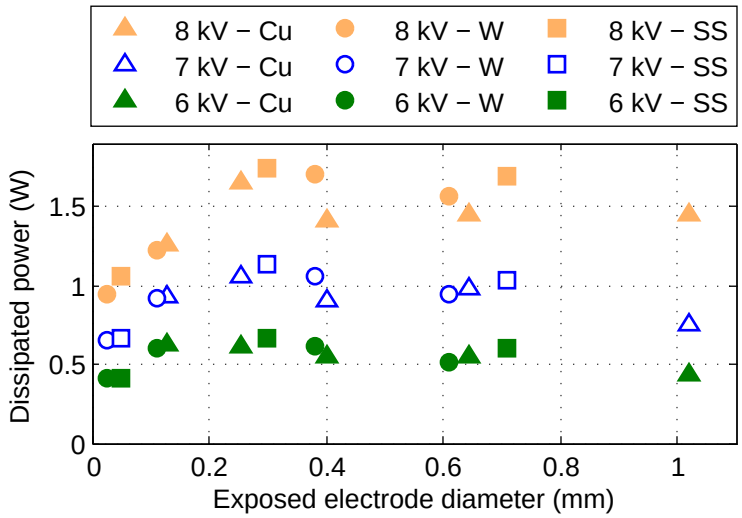

Figure 4.3: Power dissipated by single-barrier actuators with cylindrical exposed electrodes of various diameters and materials. The indicated voltages are the amplitudes of the applied symmetric triangle waveform.

In contrast to the power, the induced forces increased sharply as the exposed electrode diameter decreased. This phenomenon is shown in figure 4.4 in both the electronic balance and the stagnation probe data. The indicated voltages in that figure are the amplitudes of the applied symmetric triangle waveform, and the fit lines are described below. We also note that the material composition of the exposed electrode had no noticeable effect on the data; actuators with similarly-sized electrodes induced approximately the same force.

It is likely that the major difference between electrode materials relevant to plasma formation is their differing secondary electron emission coefficients, although the literature regarding these for appropriate ions and energies is sparse. Based on simulation results, Boeuf et al. [93] predicted that the value of the emission coefficient of the electrode (which, in their model, was set equal to

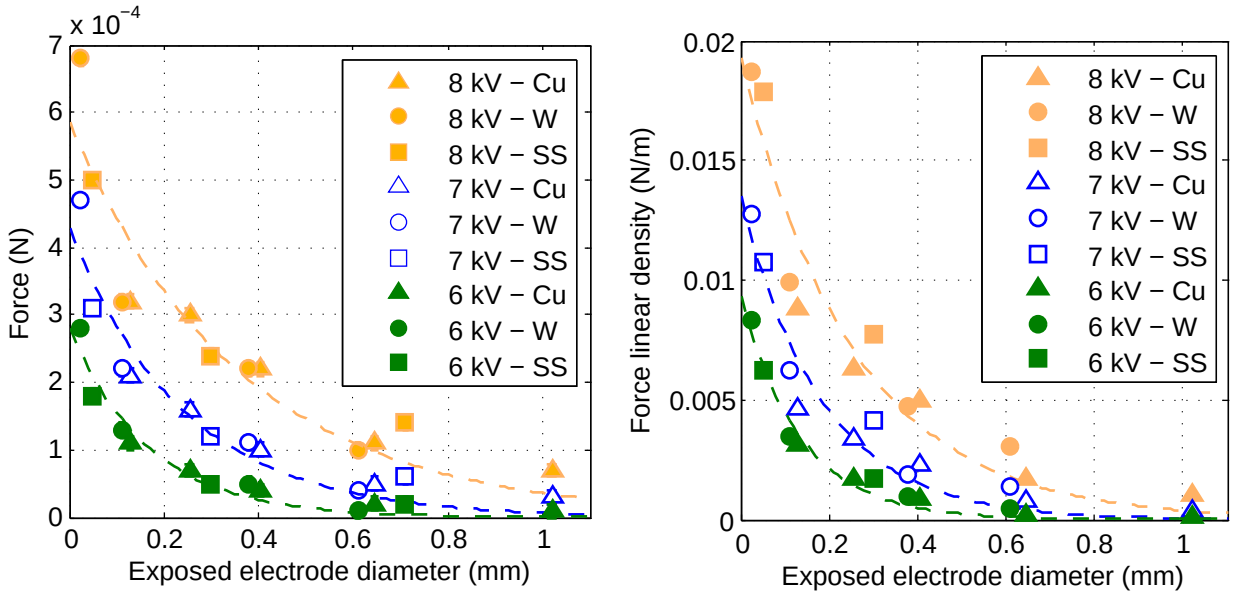

(a) (b)

Figure 4.4: Measured (a) forces, determined with the electronic balance, and (b) linear force densities, determined with the stagnation probe technique. All data are for single-barrier actuators with cylindrical exposed electrodes.

the coefficient for the dielectric) has little effect on the force induced by the actuator, while being a strong predictor of dissipated power. Our data suggest that changing the emission coefficient of just the exposed electrode has little effect on the induced force or on the dissipated power.

The variation of the actuator force and linear force density with the diameter of the exposed electrode can be reasonably approximated by an exponential function:

$$F_{\text{fit}} = F_0 \exp(-d/d_0), \tag{4.1}$$

where F_0 and d_0 are free parameters and d is the electrode diameter. We have fit equation (4.1) to the data from both the balance and stagnation probe techniques, with the units of F_0 chosen to match the data. These fits are shown in figures 4.4(a) and (b). Fitted values of d_0 for the electronic balance measurements were 0.17 ± 0.02, 0.24 ± 0.04, and 0.36 ± 0.06 mm for the 6, 7, and 8 kV tests, respectively. The values of d_0 for the stagnation probe data were similar but slightly smaller, at 0.14 ± 0.01, 0.18 ± 0.03, and 0.25 ± 0.04 mm. Further quantitative comparisons between the two measurement techniques are described in section 4.4. The increase in the value of d_0 as the voltage

increases indicate that equation 4.1 is a simple empirical fit, and does not completely separate the dependencies of the force on electrode geometry and voltage.

4.2.2 Effects of Rectangular Exposed Electrode Thickness

We have also measured the forces induced by single-barrier actuators with rectangular cross-section exposed electrodes of varying thickness. This design was depicted in figure 3.1(b). All of the actuators discussed here had exposed electrode lengths of 10 mm or greater; shorter exposed electrodes are considered in section 4.2.4. These long rectangular exposed electrodes are similar to the designs studied extensively by other groups, as discussed in section 2.4. For these actuators, we have measured the forces only using the electronic balance.

The electrical power consumed by actuators with exposed electrode thicknesses ranging from 0.01 mm to 1.1 mm is plotted in figure 4.5. Since we have shown that the material of the exposed electrode does not affect either force or power, we do not distinguish here between electrodes of different composition. Outside of small variations at small thicknesses, the electrical power use was essentially independent of electrode thickness. The power dissipation at each voltage level was comparable to that of single-barrier actuators with thick cylindrical electrodes.

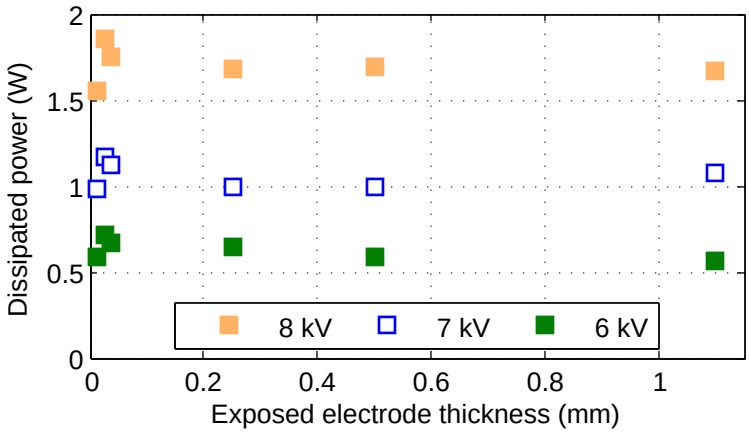

Figure 4.5: Power dissipated by single-barrier actuators with rectangular cross-section exposed electrodes of various diameters. The indicated voltages are the amplitudes of the applied symmetric triangle waveform.

At thicknesses greater than approximately 0.4 mm, the forces induced by actuators with rectangular exposed electrodes were similar to those induced by actuators with cylindrical electrodes of the same thickness. While the forces of actuators with rectangular electrodes increased at thicknesses smaller than this, they did so relatively slowly, as shown in figure 4.6. For example, at the same applied voltages an actuator with a 0.03 mm diameter cylindrical exposed electrode induced forces 2 to 5 times larger than an actuator with a 0.03 mm thick rectangular exposed electrode. The differences between the electrode shapes is examined in section 4.2.4.

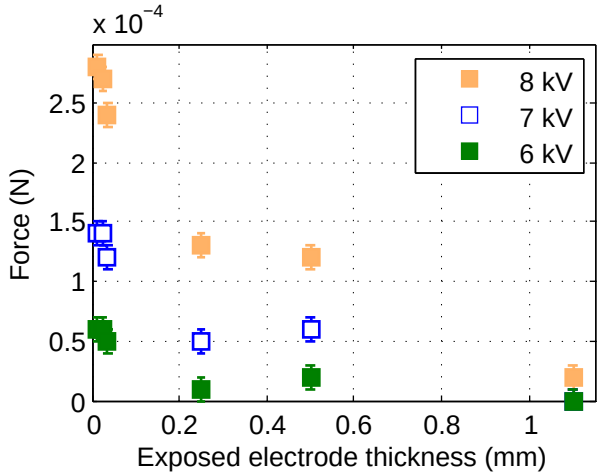

Figure 4.6: Measured forces, determined with the electronic balance, of single-barrier actuators with rectangular cross-section exposed electrodes. The indicated voltages are the amplitudes of the applied symmetric triangle waveform.

In addition to the data included in figure 4.6, we measured the forces induced by an actuator using an exposed electrode made from copper foil tape with a conductive adhesive (for a total thickness of 0.09 mm). This device induced slightly larger forces than would be expected from considering the data in figure 4.6 for reasons that are still unclear. We found that this design, however, was abnormally sensitive to sub-millimeter variations in the electrode gap, making it difficult to replace the actuator if it was damaged during operation. We have omitted the data from this actuator.

4.2.3 Comparison to Previous Experiments

Previous experiments examining the effects of electrode size on actuator performance examined force efficiency (force / power) rather than absolute force. The trends of force efficiency for our measurements were similar to those for absolute force described above, since the powers were similar for all actuators except those with very narrow cylindrical exposed electrodes. The force efficiencies for single-barrier actuators with both cylindrical and rectangular exposed electrodes are plotted in figure 4.7. The division by the discharge power largely, but not completely, removes the dependence on the applied voltage amplitude in the range we have examined.

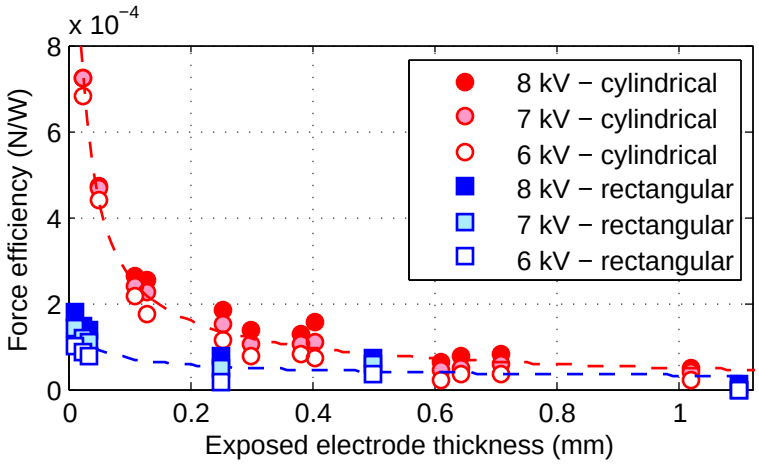

Figure 4.7: Force efficiencies of single-barrier actuators with cylindrical and long rectangular exposed electrodes. The indicated voltages are the amplitudes of the applied symmetric triangle waveform.

In section 2.4.3 we referenced the results of Enloe et al. [39], who found that the force efficiency of single-barrier actuators increased linearly with decreasing exposed electrode thickness regardless of the shape of the electrode. They tested cylindrical electrodes with diameters between about 0.35 and 1.0 mm and rectangular electrodes with thicknesses between about 0.08 and 0.7 mm. Our results are consistent with these findings. Above 0.35 mm thickness, figure 4.7 shows that the force efficiencies of actuators with both cylindrical and rectangular electrodes were similar. The force efficiencies depart from a linear dependence on electrode thickness only below approximately 0.3 mm thickness for cylindrical electrodes and 0.05 mm for rectangular electrodes.

Quantitative comparisons between the current work and previous studies by other groups have to be made with care due to the differences in actuator geometry, applied voltages, and measurement techniques between groups. Enloe et al. [39] measured a maximum force efficiency of 8×10^{-5} N/W. That measurement was made using an actuator with a 0.08 mm thick rectangular exposed electrode, and fits with our results in figure 4.7. We achieved a maximum force efficiency using an actuator with a 25 μm diameter exposed electrode, and measured a value of 7.2×10^{-4} N/W, or nearly an order of magnitude larger than previous tests. Several other groups have published data showing the force induced by their actuator designs, but have not provided enough information for us to make direct comparisons.

Other groups have focused on measurements of the induced flow velocities in air instead of the time-averaged forces. Pons et al. [63] measured a maximum induced flow velocity in air of approximately 3.3 m/s using a discharge power per unit length of 47 W/m, but did not report any total forces. Forte et al. [66] were able to induce larger flow velocities on the order of 6 m/s by increasing the discharge power to approximately 170 W/m. Even larger powers on the order of 500 W/m were used by Roth and Dai [65] to achieve maximum flow velocities of approximately 5 m/s. Our most efficient actuator induced a maximum flow velocity of 3.2 m/s, but required only 16 W/m of electrical power to do so.

4.2.4 Variation with Exposed Electrode Length

As described in the preceding sections, single-barrier actuators with cylindrical and rectangular exposed electrodes exhibited significant differences, even when the electrode thicknesses were similar. To determine the source of those differences we have investigated a variety of actuator designs, each examining one aspect of the electrode geometry. These tests looked at the height of the exposed electrode above the dielectric surface, the sharpness of the electrode edge, and the length of the electrode. Despite being dismissed by other researchers as having a negligible influence on the actuator [39], only the electrode length was observed to have a large enough effect to explain the difference between cylindrical and rectangular electrodes, as described below. To simplify testing procedures, all force measurements described in this section were made using

just the electronic balance, and all actuators were driven by 7 kV amplitude symmetric triangle voltages.

We used the side-by-side cylindrical actuator design of figure 3.2 to approximate the length of a (short) rectangular electrode while retaining the electrode edge profile of a cylindrical electrode. We stacked eight 0.13 mm diameter stainless steel cylinders side-by-side for a maximum effective length of just over 1 mm. After measuring the force using the electronic balance, we removed the cylinder furthest from the buried electrode and repeated the measurement, continuing until only one cylinder remained. As each cylinder was removed, the induced force increased, as shown in figure 4.8.

We have also examined actuators with rectangular cross-section exposed electrodes of varying lengths. As we reduced the length of the rectangular electrode, the force increased. Due to difficulties in accurately cutting narrow strips of metal, we have examined only a few actuators with electrode lengths smaller than 1 mm. In order to compare the forces of actuators with different electrode thicknesses, we divided each of the measured forces by the force that was induced by an actuator with a long (>10 mm) rectangular electrode of the same thickness. In the case of the 0.13 mm cylinders, the appropriate reference force was extrapolated from existing data of actuators with rectangular electrodes of similar thicknesses.

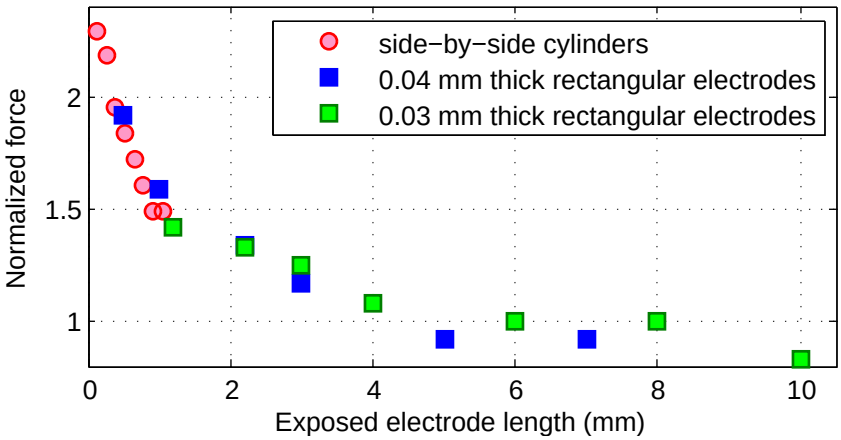

Figure 4.8: Normalized forces for actuators with varying electrode lengths. The measured forces were divided by the force for an actuator with a long rectangular exposed electrode of the same thickness. The applied voltage amplitude was 7 kV.

The results of these measurements are plotted in figure 4.8. They showed a smooth increase in the normalized force as the electrode length was reduced. The rapid increase at electrode lengths below 2 mm suggests that the differences between actuators with rectangular and cylindrical exposed electrodes are primarily due to differences in electrode length, rather than the exact shapes of the electrode edges. For the actuators examined here, reducing the electrode length below approximately 3 mm had a much stronger effect than did reducing the electrode thickness.

The power dissipated by a single-barrier actuator was independent of the length of its exposed electrode except for very short lengths. This is shown in figure 4.9, where the power use is effectively constant except for the single-cylinder actuator. For that device, the power dropped by 15%, similar to the reduction in power seen for small diameter cylindrical electrodes in figure 4.3.

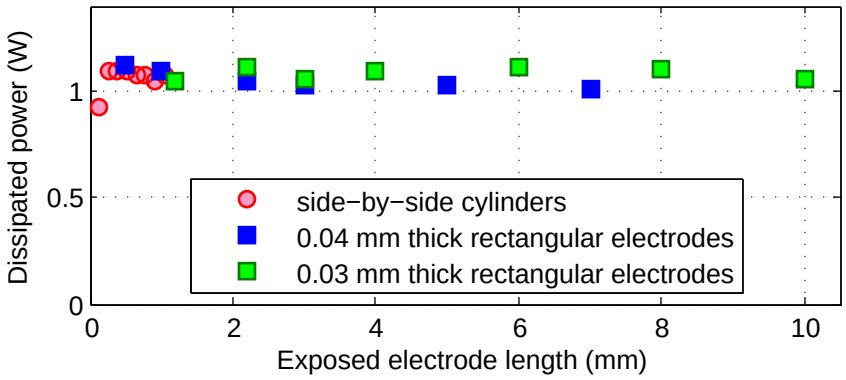

Figure 4.9: Power dissipated by single-barrier actuators with exposed electrodes of varying lengths. The applied voltage amplitude was 7 kV.

4.3 Double-Barrier Actuators

We have also conducted measurements of the forces induced by double barrier actuators. This geometry was depicted in figure 3.3 and described in section 3.1.1. The force data were obtained using the procedures described in sections 3.2.1 and 3.2.2. Because neither electrode is in contact with the plasma for this geometry, we have not presented data for different materials separately. No dependence of force or power on the narrow electrode material was observed.

Data from the electronic balance and stagnation probe measurements are shown in figure 4.10. The indicated voltages are the amplitudes of the applied symmetric triangle waveform, and the fit lines are described below. Similar to the single barrier actuators, the induced force increased with decreasing electrode diameter, although here it was the narrow electrode rather than an exposed electrode that was varied.

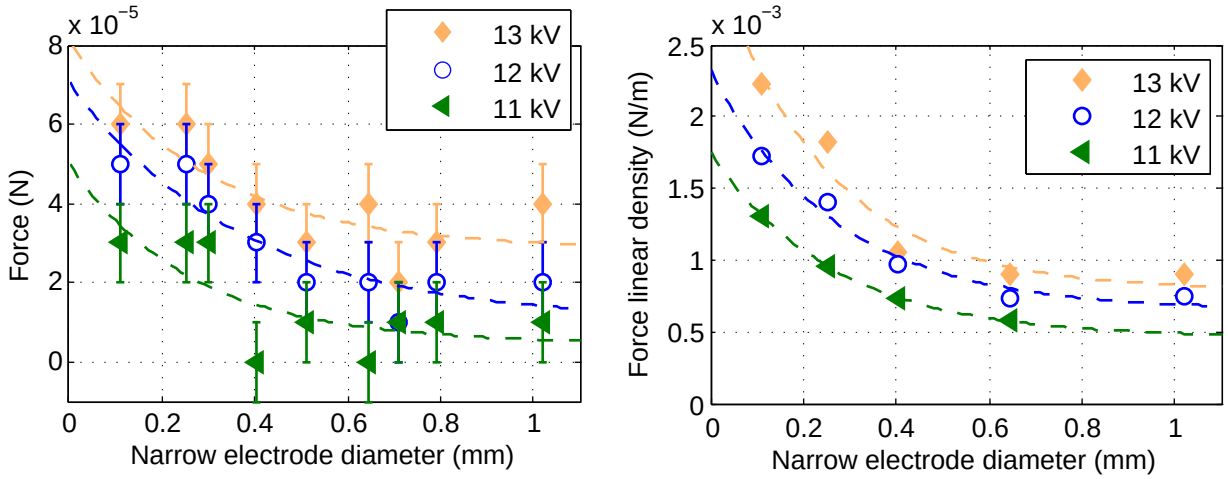

(a) (b)

Figure 4.10: Measured (a) forces, determined with the electronic balance, and (b) linear force densities, determined with the stagnation probe technique. All data are for double-barrier actuators with various diameter narrow electrodes.

The measured forces were small enough to approach the sensitivity limit of the balance, leading to large relative uncertainties in the balance data. The absolute levels of the force were a factor of 5 to 10 smaller than those seen for single barrier actuators for the configurations studied here. For actuators with narrow electrodes smaller than 0.1 mm in diameter, the dielectric layers tended to quickly erode and allow arcing, so no data were recorded for these devices.

In contrast to the data from single barrier actuators, at large diameters the induced forces did not decrease towards zero but rather asymptoted to a small but finite value. At larger values of narrow electrode diameter, the electrode geometry does not become symmetric, which may explain the non-zero force at large diameters. Rather, there is still an asymmetry in the shape of the electrode cross sections (circular for the narrow electrode and rectangular for the wide electrode).

To make reasonable approximations of the force behavior, instead of using equation (4.1) we have fit

$$F_{\text{fit}} = F_0 \exp(-d/d_0) + F_1 \tag{4.2}$$

to the data in figure 4.10. Here F_0, F_1, and d_0 are free parameters. For the balance data, the fitted values of d_0 were 0.26 ± 0.25, 0.37 ± 0.22, and 0.29 ± 0.23 for the 11, 12, and 13 kV tests, respectively. The values for the balance data have large confidence intervals due to the large relative scatter of the measurements. The stagnation probe data were somewhat more accurate, and had fitted d_0 values of 0.26 ± 0.01, 0.27 ± 0.10, and 0.24 ± 0.11. Further quantitative comparisons between the two measurement techniques are described in section 4.4.

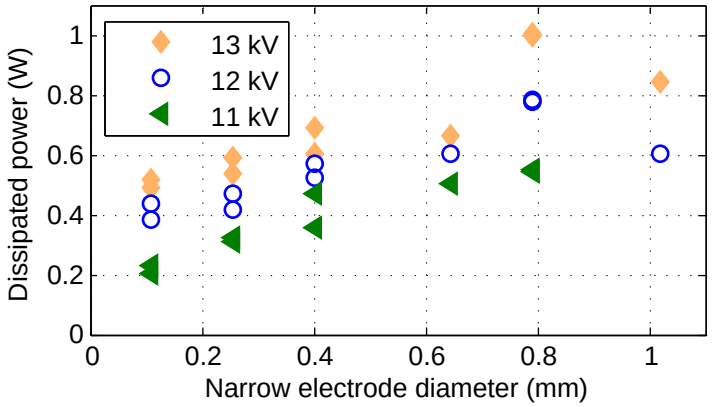

Figure 4.11: Power dissipated by double-barrier actuators with various narrow electrode diameters. Most actuators were tested several times, with the results of each test plotted separately.

In order to produce a plasma, double barrier actuators required much higher applied voltages than do the single barrier actuators. The rates of discharge events, as determined by both current measurements and ICCD imaging, however, were much lower. The resulting reduced discharge current lead to somewhat lower levels of power dissipation, shown in figure 4.11, for the range of applied voltages considered here. The dissipated power decreased approximately linearly with decreasing narrow electrode diameter. As with single-barrier actuators, actuators with small diameter electrodes were notably more efficient. The force efficiencies of double-barrier actuators were, on average, a factor of about 2 smaller than those of single-barrier actuators.

4.4 Comparison of Balance and Stagnation Probe Techniques

As described in sections 4.2.1 and 4.3, the same general trends in the induced forces with electrode diameter have been observed using both the electronic balance and stagnation probe measurement techniques. When the balance data were converted to forces per unit length, as described in section 3.2.1, they were consistently smaller than those calculated from stagnation probe measurements using the assumptions of section 3.2.2. The two approaches are clearly proportional to one another, however, as shown in figure 4.12. The stagnation probe data were approximately a factor of two larger for all measurements.

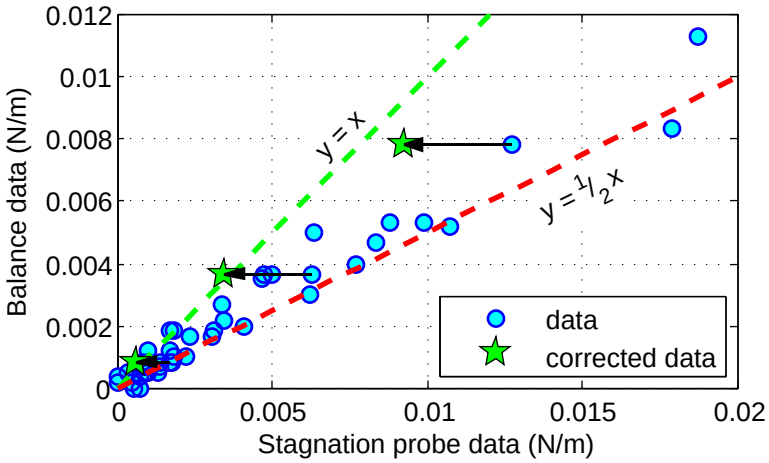

Figure 4.12: Comparison of forces measured using the electronic balance and stagnation probe. The circles were calculated using the using the assumptions of section 3.2.2, while the corrected data is described in this section.

We have found that this difference is largely due to the assumptions made in converting the measured stagnation pressures into induced forces. While each assumption made in section 3.2.2 has a relatively small effect on the calculated force, these effects add and lead to a significant overestimation of the force when using the stagnation probe technique. To show this, we have made additional detailed measurements around three actuators: single-barrier actuators driven at 7 kV with cylindrical exposed electrodes 0.03 and 0.11 mm in diameter, and a double-barrier actuator driven at 12 kV with a narrow electrode 0.11 mm in diameter. The corrections provided

by these data were sufficient to explain this observed difference between stagnation probe and balance data.

We measured static pressures using a 2.5 mm diameter alumina tube sealed at one end, with a 1 mm diameter hole drilled 7 mm from the sealed end. The tube was oriented in the $-x$ direction, with the hole facing the z direction. Stagnation and static pressure measurements at three locations near the single-barrier, $d = 0.11$ mm actuator are shown in figure 4.13. The data confirm that the static pressure is constant downstream ($+x$ direction) of the high voltage electrode, but show a small non-zero static pressure upstream. The exposed electrode is considered to be at $x = 0$.

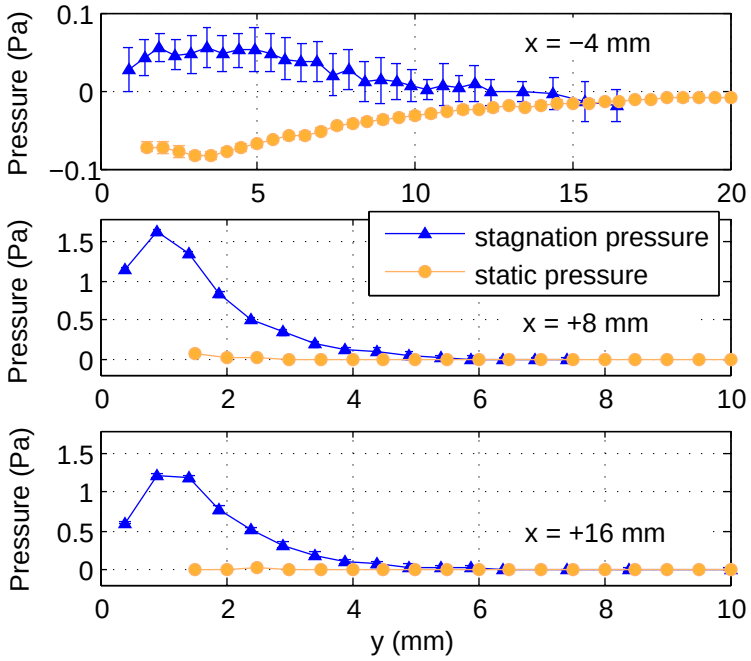

Figure 4.13: Stagnation and static pressures measured at $x = -4$ (top), $+8$ (middle), and $+16$ mm (bottom) for a single barrier actuator with $d = 0.11$ mm driven at 7 kV

Using these data for the single-barrier actuator, we can evaluate the right-hand side of equation (3.1), except for term II. We use the measured static pressure in place of the reference pressure in equation (3.2). Evaluating terms I and IV along the surface at $x = 8$ mm and terms III and V at $x = -4$ mm, we find a linear force density of 4.2×10^{-3} N/m, or 68% of the original force estimate for these conditions. If we repeat the calculation and instead evaluate terms I and IV at

$x = 16$ mm, thereby including the shear force all the way to the actuator edge, we calculate a linear force density of 3.5×10^{-3} N/m. This is 56% of the original estimate, and compares well to the balance-measured value of 3.7×10^{-3} N/m. The largest correction to equation (3.3) for the 0.11 mm single-barrier actuator was the inclusion of term III, the flux of momentum into the left side of the control volume. This term was equal to 35% of the uncorrected force estimate.

Corrections for the other two actuators yielded similar improvements in the quantitative agreement between the stagnation probe and balance measurements. Using stagnation and static pressures measured at $x = -4$ and $x = +16$ mm, the calculated linear force density for the 0.03 mm single-barrier actuator was 9.2×10^{-3} N/m (72% of the original estimate), compared to the balance-measured value of 7.8×10^{-3} N/m. The corrected force density for the 0.11 mm double-barrier actuator was 6.4×10^{-4} N/m (37% of the original estimate), compared to the balance-measured value of 8.3×10^{-4} N/m.

It is clear from the improved agreement between the two measurement techniques that care must be taken to quantitatively determine forces from pressure measurements. Our estimate of term III in equation (3.1) itself may be slightly in error: the static probe was large enough to possibly disturb the gas flow in the region of measurement. Still, we believe including the term as measured is likely to be more accurate than continuing to neglect it completely.

We have not estimated the effect of the flux of x momentum through the top surface (term II in equation (3.1)), as we cannot accurately measure u_y in that region. PIV measurements [60] and calculations [97] suggest that on the top surface u_x is much smaller than its values on the left- and right-hand edges of the control volume and comparable to u_y, because most of the acceleration occurs inside the control volume closer to the surface. This behavior would make our neglect of term II reasonable. The relatively close agreement between the corrected stagnation probe and balance measurements also supports this conclusion.

Chapter 5

Optical Imaging

Imaging with the ICCD camera allowed us to observe plasma behavior on the different time scales of interest for DBD plasma actuators. Individual microdischarges exist for times on the order of 5 to 100 ns. Images of microdischarges on these time scales are shown in section 5.2.3. Since all of the applied voltages oscillated at 1 kHz, plasma variations with the applied voltage level occurred at time scales on the order of 10 μs. We show our observations of these variations in sections 5.2.1 and 5.3. In examining all of the acquired images, we noted that the plasma structures could be grouped in three distinct categories, which we describe in section 5.1. Many features of plasma structures have been qualitatively reproduced in our simulation results, which are described in sections 7.1, 7.4.1, and 7.4.2. Additional observations of one of those structures, the newly-discovered filament-free plasma regime, are included in section 5.2.2.

5.1 Observed Microdischarge Structures

In our imaging experiments, we have observed three distinct plasma structures. These structures arise in a variety of different actuator types as described in this section. We refer to these structures as filamentary, jet-like, and filament-free structures. The filamentary and jet-like structures have been previously observed, as described in section 2.4.2. The filamentary structure is occasionally referred to in the literature as a streamer. The jet-like structure is sometimes referred to as a "diffuse" microdischarge; we avoid that terminology as it only appears diffuse relative to

the filamentary structure. The filament-free structure has not been previously identified. This latter structure has some similarities to the corona-like plasma that has been observed in actuator simulations, a corrspondence that is discussed in more detail in section 7.4.

In single-barrier actuators, filamentary microdischarges appeared during the positive-going half cycle. Typical discharge structures of this type are shown in figure 5.1. They are on the order of 0.1 mm thick, with numerous branches forming in directions parallel to the dielectric surface. The total microdischarge length varied with the applied voltage, as described in section 5.2.1. The gate widths used to record the images in figure 5.1 were long relative to the lifetime of a filamentary microdischarge, so the pictured structures are fully developed.

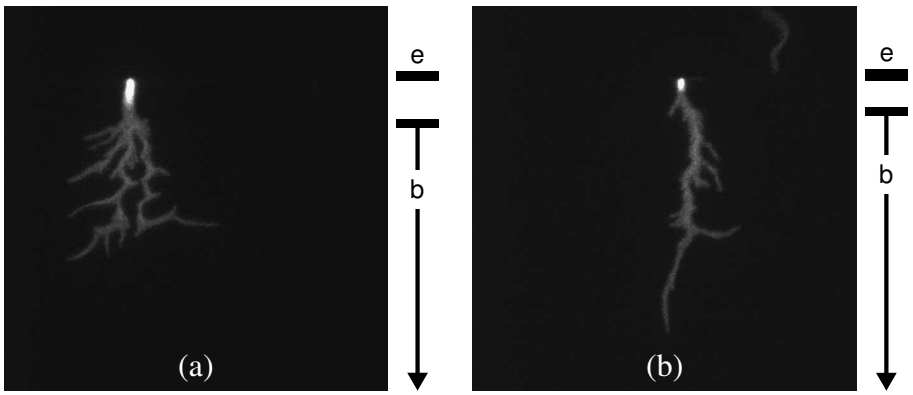

Figure 5.1: Images of typical filamentary plasma structures. These images were recorded in single-barrier actuators and used gate widths of 10 µs.

During the negative-going half cycle in single-barrier actuators, jet-like plasma structures formed and dissipated. Like the filamentary structures, they touched a single point on the exposed electrode. Jet-like structures are so named because they resemble a diffusing gas jet: dense at the point of origin, growing gradually weaker at greater distances. The jet-like plasma structures pictured in figures 5.2(a) and 5.2(b) show the range of variation in this type of plasma structure. Some microdischarges, like the one in figure 5.2(a), are nearly symmetric and decrease in brightness uniformly with distance away from brightest spot. Others, such as the plasma shown in figure 5.2(b), have a less symmetric structure, with a brighter region near the center of the plasma. This latter variation tended to occur more frequently in single-barrier actuators with thicker exposed electrodes.

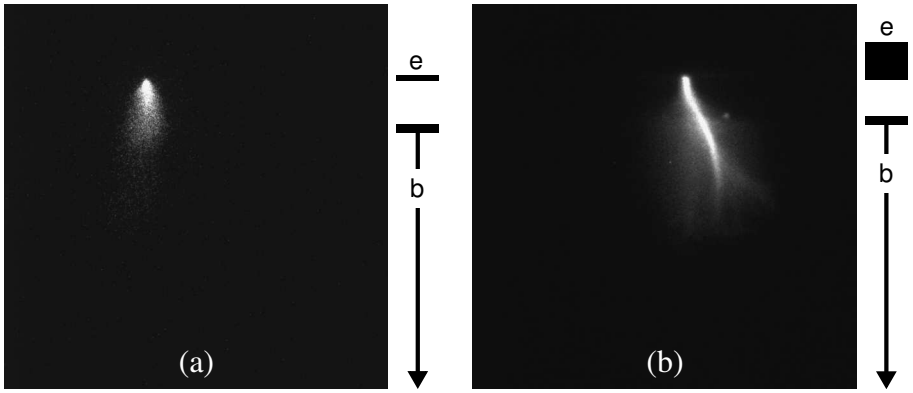

Figure 5.2: Images of typical jet-like plasma structures. These images were recorded in single-barrier actuators and used gate widths of 10 μs.

In single-barrier actuators with thin cylindrical exposed electrodes (smaller than about 0.15 mm in diameter), we observed a third discharge structure, which we call the filament-free plasma. This structure appeared only during the positive-going half cycle, generally after an initial phase of filamentary microdischarges. It appeared as a weakly glowing band of plasma on the edge of the exposed electrode nearest the buried electrode, as shown in figure 5.3. Unlike the filamentary and jet-like microdischarges described above, the filament-free plasma did not form and extinguish multiple times during the course of a single half-cycle. Instead, during the portions of the voltage cycle in which we observed it, the filament-free plasma was visible in every recorded image, at gate widths as short as a few nanoseconds. We describe this plasma structure in more detail in section 5.2.2.

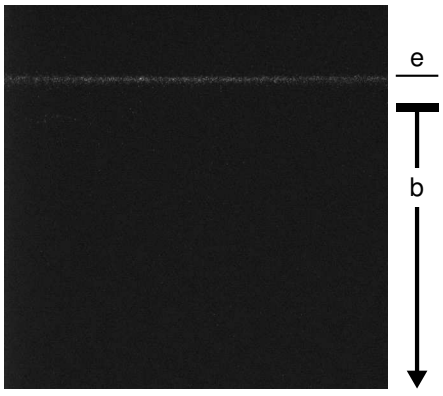

Figure 5.3: Image of a typical filament-free plasma structure. This image is of a single-barrier actuator, and used a gate width of 10 μs.

Microdischarges in double-barrier systems were observed to consist simultaneously of both filamentary and jet-like plasma structures. During the positive-going half cycle, a short jet-like structure formed between the center of the electrode gap and the region above the narrow electrode, while a much longer filamentary structure extended from a point in the electrode gap downwards over the wide electrode. This type of microdischarge is shown in figure 5.4(a). The opposite type of structure appeared during the negative-going half cycle, as shown in figure 5.4(b). In this case, the filamentary structure existed between the center of the electrode gap and the surface above the narrow electrode, while a longer jet-like plasma extended from the electrode gap over the wide electrode.

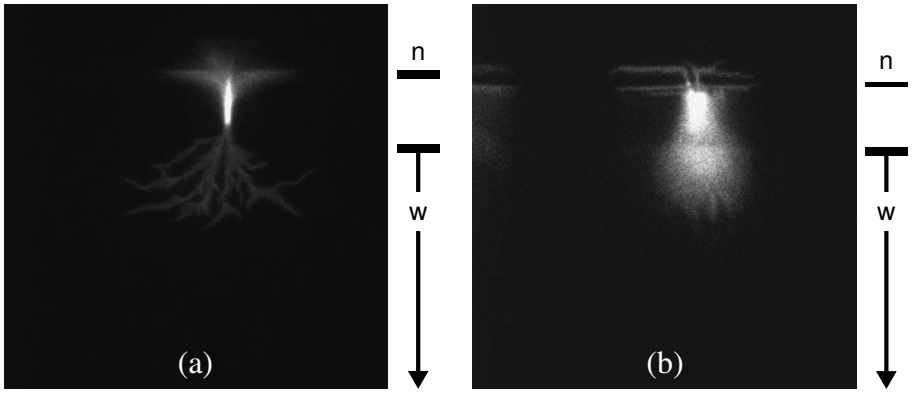

Figure 5.4: Images of typical microdischarges in a double-barrier actuator. The microdischarge during (a) the positive-going half cycle consists of a short jet-like structure and a long filamentary structure, while that during (b) the negative-going half cycle is made up of a short filamentary structure and a long jet-like structure.

The existence of similar plasma structures in both single- and double-barrier actuators suggests that plasma behavior does not depend exclusively on the electrode structure. Since both filamentary and jet-like structures form in double-barrier systems, we conclude that the plasma structure is at least in part determined by the direction of the local electric field relative to the dielectric surface.

5.2 Single-Barrier Actuators

In section 5.1 we described the different types of microdischarges present in a single-barrier surface DBD. Here we examine several characteristics of microdischarge behavior. We note that,

for single-barrier actuators with cylindrical exposed electrodes, microdischarges also occurred on the "back" side of the electrodes, away from the buried electrode. Filamentary and jet-like microdischarges on this side of the exposed electrode are shown in figure 5.5. In the remainder of this section we neglect these microdischarges, only considering the longer microdischarges which extend from the exposed electrode edge towards the buried electrode.

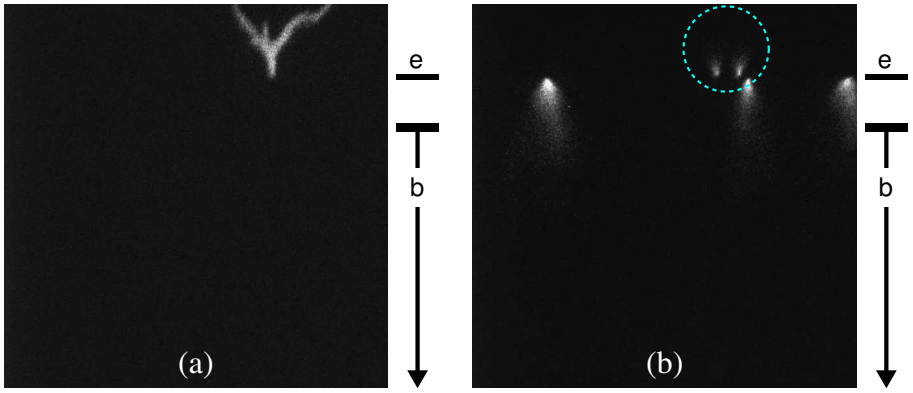

Figure 5.5: "Backwards" (a) filamentary microdischarge during the positive-going half cycle and (b) jet-like microdischarges during the negative-going half cycle in a single-barrier actuator. Several microdischarges appear in (b), with the backwards discharges circled. Both images used gate widths of 10 μs.

5.2.1 Average Microdischarge Lengths

As each half-cycle of the applied voltage progressed, the observed filamentary and jet-like microdischarges extended farther from the exposed electrode. This increase in microdischarge length is evident from the early- and late-half cycle images shown in figure 5.6. We have observed similar increases in all actuators we have tested.

To allow us to determine average microdischarge lengths, we have applied the accumulation and averaging procedures described in section 3.3.2 to a variety of single-barrier actuators with both cylindrical and rectangular exposed electrodes. The results for a single-barrier actuator with a 0.11 mm diameter exposed electrode are shown in figure 5.7. The phases of the voltage cycle during which filamentary, filament-free, and jet-like plasmas exist for this actuator are noted on the figure. Figure 5.7 shares many characteristics with the results of Enloe et al. [39], who used

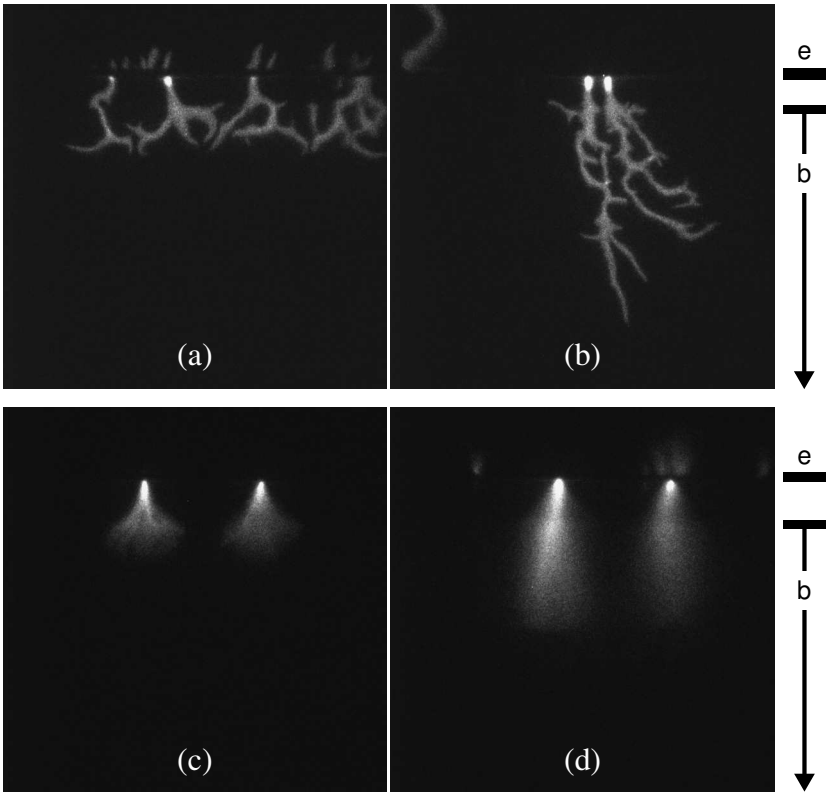

Figure 5.6: Increasing single-barrier microdischarge length from (a) 50% (0 V) to (b) 95% (6.3 kV) of the way through the positive-going half cycle and from (c) 50% (0 V) to (d) 95% (−6.3 kV) of the way through the negative-going half cycle.

a movable photomultiplier tube to measure the light emission as a function of time at a variety of x locations. They examined a single-barrier actuator with a rectangular exposed electrode, and noted that the regions of emitted light grew at approximately the same rate during the positive- and negative-going half cycles, and that this rate varied with the applied voltage amplitude [70].

In order to determine the growth or expansion rates for our own discharges, estimates of the average microdischarge lengths are required at each point in the voltage cycle. To find these lengths, we applied two fitting algorithms to the average light emission data. The first fitting routine, which we refer to as the edge-based algorithm, initially checked the first derivative of the data, identifying the peak with the largest value of x. It then fit a decaying exponential function only to the light emission data at larger x values than the peak. Two example fits using this algorithm are shown in figures 5.8(a) and 5.8(b). The second fitting routine, which we refer to

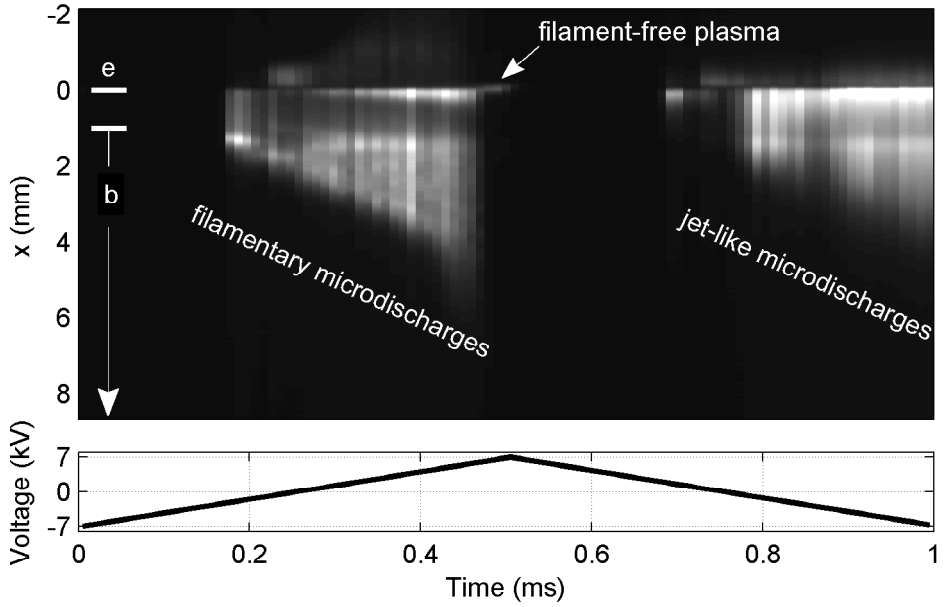

Figure 5.7: Average light emission during the applied voltage cycle for a single-barrier actuator with a 0.11 mm diameter exposed electrode. Each column of pixels corresponds to the average light emission from a 10 µs period.

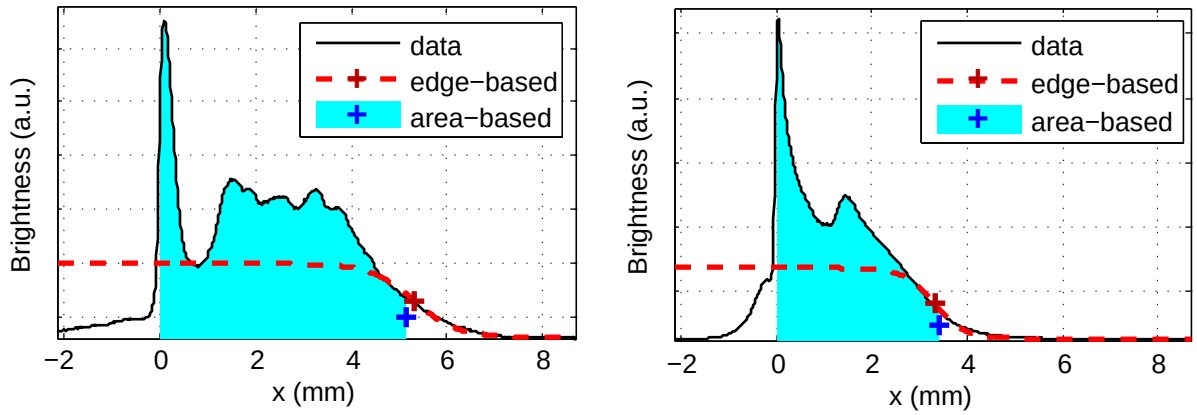

Figure 5.8: Average light emission and edge fitting during times in the (a) positive-going and (b) negative-going half cycles. The + symbols indicate the x locations defined as the average microdischarge edges by the fitting algorithms.

as the area-based algorithm, integrated the light emission plotted from the edge of the exposed electrode in the positive x direction. It defined the edge of the average microdischarge as the point at which the integration has reached 95% of its final value. Example fits using this algorithm are also shown in figures 5.8(a) and 5.8(b). The linear fits made by Enloe et al. [39, 70] to their emission data were similar to our edge-based fits, with the edge threshold defined by the sensitivity of their instruments.

The two edge-finding algorithms yielded similar, but not identical, results. The algorithms depend on the precise shape of the emitted light curve, including how much noise is present, and each returns questionable results for curves of certain shapes. We chose to present results from both algorithms because these two methods use different features of fitted curves. The results from these two techniques provide a reasonable estimate of which observed features are independent of the chosen fitting technique.

From the fitting algorithms we obtained the average microdischarge length as a function of time for each examined actuator. For most actuators, these lengths increased approximately linearly for the majority of each half cycle of the applied voltage. The only exception to this was the single-barrier actuator with the smallest diameter exposed electrode, which quickly transitioned to a non-changing filament-free plasma. Lengths for two single-barrier actuators, determined using the edge-based method, are shown in figure 5.9. The periods of linearly increasing microdischarge lengths are evident in this figure. In each of the these periods we have made a linear fit to the data, the slope of which is the rate at which the average microdischarge length increases.

These expansion rates for all tested single-barrier actuators are shown in figure 5.10 for both fitting algorithms. While there were quantitative differences between the results from each fitting algorithm, we did find some consistent qualitative features. For actuators with cylindrical exposed electrodes, the expansion rates, shown in figures 5.10(a) and 5.10(c), were effectively independent of diameter when that diameter was larger than about 0.15 mm. Below this diameter, the expansion rates for filamentary microdischarges increased, while those for jet-like microdischarges decreased. This 0.15 mm threshold is similar to the diameter at which the measured force efficiencies of figure 4.7 began to increase sharply. The relatively large uncertainty for the actuator with

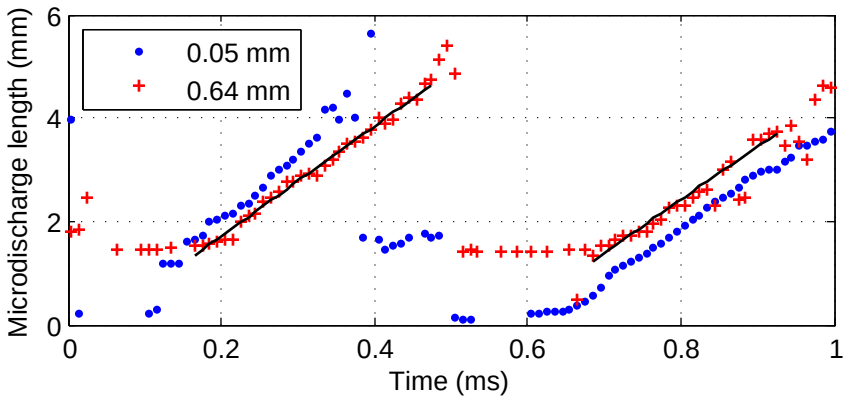

Figure 5.9: Average microdischarge lengths for single-barrier actuators determined using the edge-based algorithm. Example fits to the linear regions, used to determine the expansion rates of figure 5.10, are shown for the actuator with the 0.64 mm diameter exposed electrode.

the 0.03 mm diameter cylindrical electrode in figure 5.10(a) was due to the very short filamentary period of this actuator (see section 5.2.2).

Previously we reported an expansion rate of about 5 m/s for jet-like microdischarges in an actuator with a 0.3 mm diameter exposed electrode [98]. This low value was due to averaging fewer exposures together and using only an edge-based fitting method. The difference between those measurements and the more recent ones shown in figure 5.10 demonstrate that the observed rates are dependent on the methods of observation and the fitting algorithms. Due to these dependences, here we have focused only on consistent changes in the rates with electrode geometry.

Expansion rates for actuators with rectangular exposed electrodes, shown in figures 5.10(b) and 5.10(d), behaved differently. The expansion rates increased slightly at very small thicknesses, and this increase was similar between the filamentary and jet-like microdischarges. The rates did not diverge like those for actuators with cylindrical exposed electrodes at small diameters. These differences in behavior between actuators with cylindrical and rectangular exposed electrodes correlate with the variations in forces between the two geometries. This qualitative correlation suggests that further studies of the visible plasma structure will likely be useful in understanding the induced EHD forces.

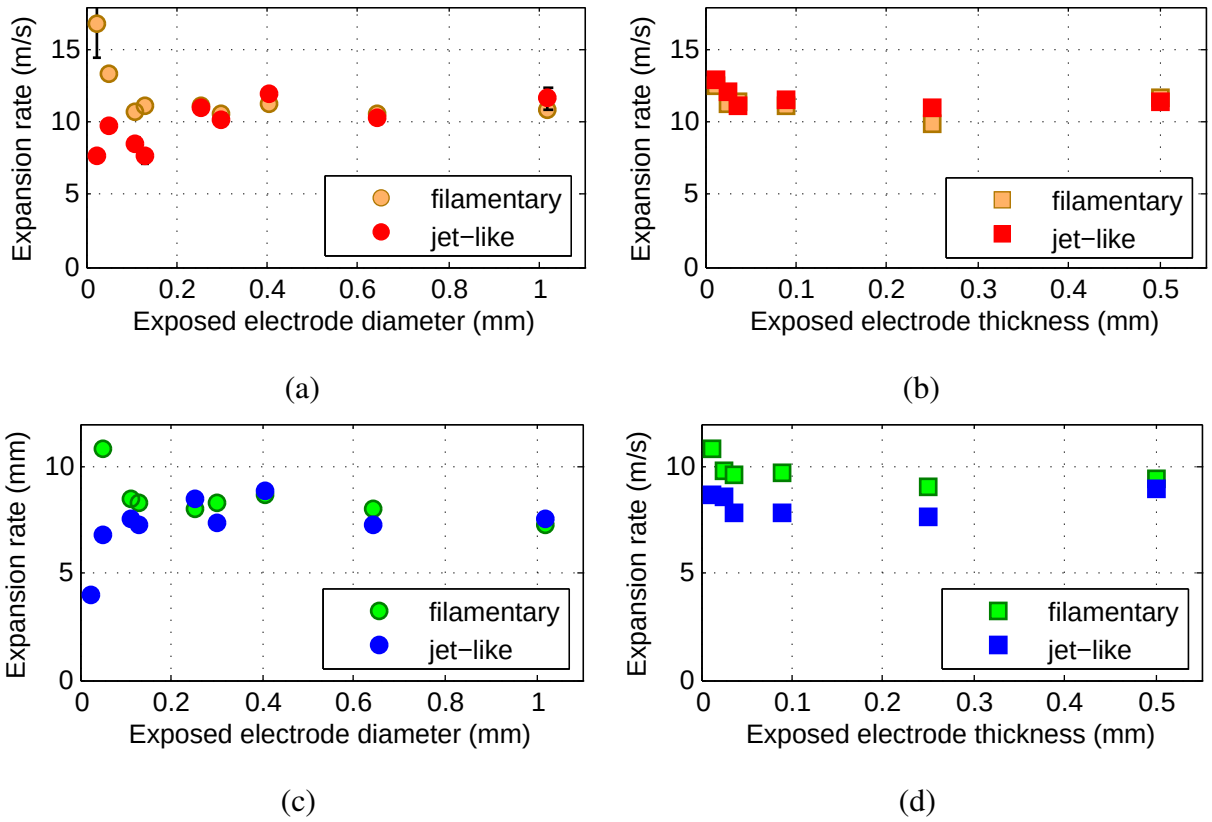

Figure 5.10: Rates at which the average microdischarges length increases for single-barrier actuators. Lengths in the upper graphs were determined using the edge-based algorithm for actuators with (a) cylindrical and (b) rectangular cross-section exposed electrodes. Lengths in the lower graphs were determined using the area-based algorithm for (c) cylindrical and (d) rectangular cross-section exposed electrodes.

5.2.2 Filamentary to Filament-Free Transition

The filament-free plasma identified in section 5.1 appeared only in single-barrier actuators with narrow cylindrical electrodes. We observed the filament-free mode in actuators with exposed electrode diameters of 0.03, 0.05, 0.11, and 0.13 mm. The next largest electrode tested was 0.25 mm in diameter, so the disappearance of the mode occurred as the electrode diameter increased above approximately 0.2 mm.

The filament-free mode appeared gradually as the applied voltage rose during the positive-going half cycle. In the initial stage of the positive-going cycle, the electric field is not strong

enough to sustain a plasma, so no light is emitted. When the voltage rose sufficiently, filamentary microdischarges began to occur. At some later point, the filament-free plasma appeared near the exposed electrode, coexisting with the filamentary microdischarges, as in figure 5.11(a). As the applied voltage continued to rise, filamentary microdischarges occurred less frequently, as illustrated in figures 5.11(b) and 5.11(c). Eventually the filamentary microdischarges ceased occurring, and the "full" filament-free mode of figure 5.3 continued until the end of the positive-going half cycle.

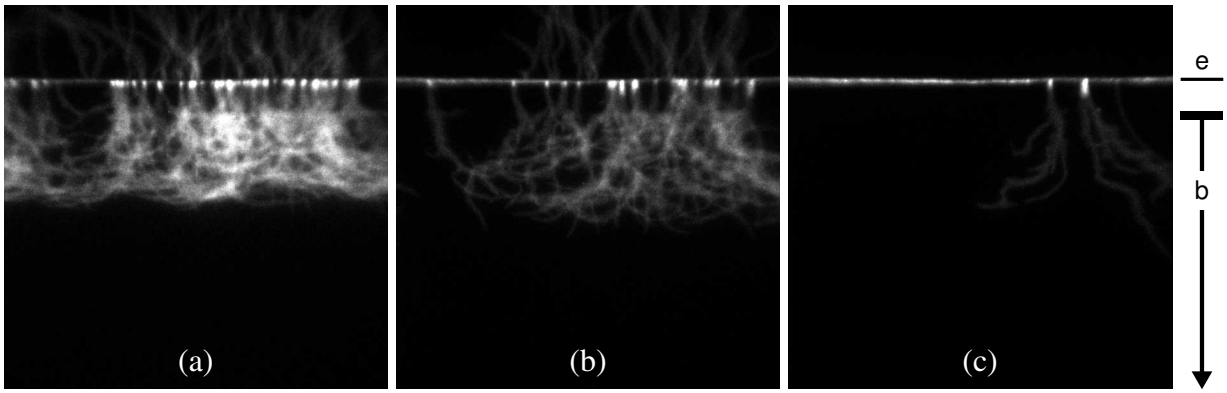

Figure 5.11: Simultaneous appearance of filament-free plasma and filamentary microdischarges in a single-barrier actuator. Each image used a gate width of 10 µs, but is the sum of 100 accumulated exposures. The images were recorded at (a) 0.31 ms, (b) 0.34 ms, and (c) 0.37 ms into the 0.50 ms long positive-going half cycle of a single-barrier actuator with a 0.05 mm diameter exposed electrode.

The time at which the plasma transitioned to a completely filament-free mode was strongly dependent on the diameter of the exposed electrode. As shown in figure 5.12, the filament-free mode occurred earlier in the half cycle for actuators with smaller exposed electrodes. The times at which the filament-free mode initially appeared were more difficult to determine, as the dim filament-free plasmas were sometimes obscured by the many filamentary microdischarges. Approximately, however, the onset occurred 70 µs ($\sim$2 kV) prior to the transition to a fully filament-free mode. This gap between the initial appearance of the filament-free mode and the total disappearance of filamentary microdischarges was independent of the exposed electrode diameter.

The transition to a filament-free mode is responsible for the reduction in dissipated power for single-barrier actuators with small diameter cylindrical exposed electrodes. The actuators used less

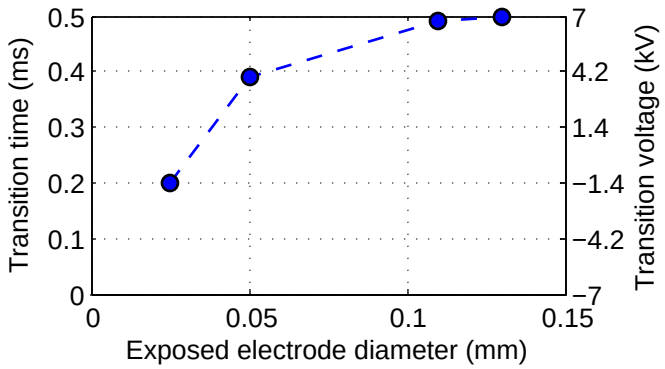

Figure 5.12: Times and voltages at which transition to fully filament-free modes occur for single-barrier actuators with cylindrical exposed electrodes. 0.5 ms is the end of the positive-going half cycle.

power, as shown in figure 4.3, when they spent a longer portion of the positive-going half cycle in the filament-free mode. The current spikes seen during the filamentary period, as in figures 3.12 and 5.13, were largely suppressed during the filament-free mode, as shown in figure 5.13. This lack of current spikes reduced the average discharge current and thus the dissipated power.

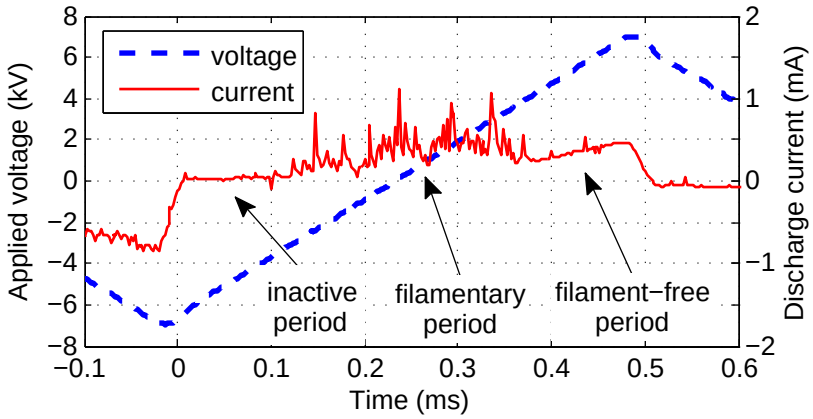

Figure 5.13: Discharge current for a single-barrier actuator with a 0.05 mm diameter cylindrical exposed electrode. The filament-free phase of the discharge had notably fewer current spikes.

5.2.3 Microdischarge Formation and Propagation

In addition to the examination of the plasma on time scales comparable to the applied voltage, as described above, we have also studied plasma behavior on the time scales of individual microdischarges. Rather than examining different times during the applied voltage cycle, here we fixed the examined time and varied the gate width of the image. While the collected images are of different microdischarges, they can yield information about the time evolution of an average microdischarge. The images in this section are all of a single-barrier actuator with a 0.3 mm diameter cylindrical exposed electrode, and a 7 kV amplitude symmetric triangle voltage at 1 kHz. We have examined only times near the end of each half cycle. During the positive-going half cycle this was just prior to the voltage reaching 7 kV; during the negative-going half cycle this was just prior to the voltage reaching -7 kV. We have published the results of this section in Hoskinson et al. [98].

Since the actuator had a 0.3 mm diameter exposed electrode, only filamentary microdischarges occurred during the positive-going half cycle. At the shortest gate width examined, 2 ns in figure 5.14(a), we observed a plasma region little more than a millimeter in length. As we increased the gate width the plasma length increased, as shown in figures 5.14(a) through 5.14(e). This behavior suggests that filamentary microdischarges actually consist of a dense, bright plasma region propagating along the dielectric surface. Since the camera integrates the light emitted from the plasma, at longer gate widths the plasma has moved farther and thus appears longer.

By measuring the length of the bright plasma region as a function of camera gate width, as in figure 5.15, we estimated the propagation velocity of a microdischarge during the positive-going half cycle. The slope of the fitted line indicates a velocity of 3×10^4 m/s. If the microdischarge began or ended during the image acquisition time the measured length will be too short, so we believe the calculated velocity represents a lower bound on the actual propagation velocity. Based on the saturation of the lengths above 100 ns gate widths, shown in figure 5.15, we estimate 100 ns to be an upper bound on the lifetime of a filamentary microdischarge in this actuator. The propagation shown in figures 5.14 and 5.15 describes the motion of the plasma *during* a microdischarge, in contrast to the much slower variations in the average plasma behavior *over the course of the applied voltage cycle* which we described in section 5.2.1.

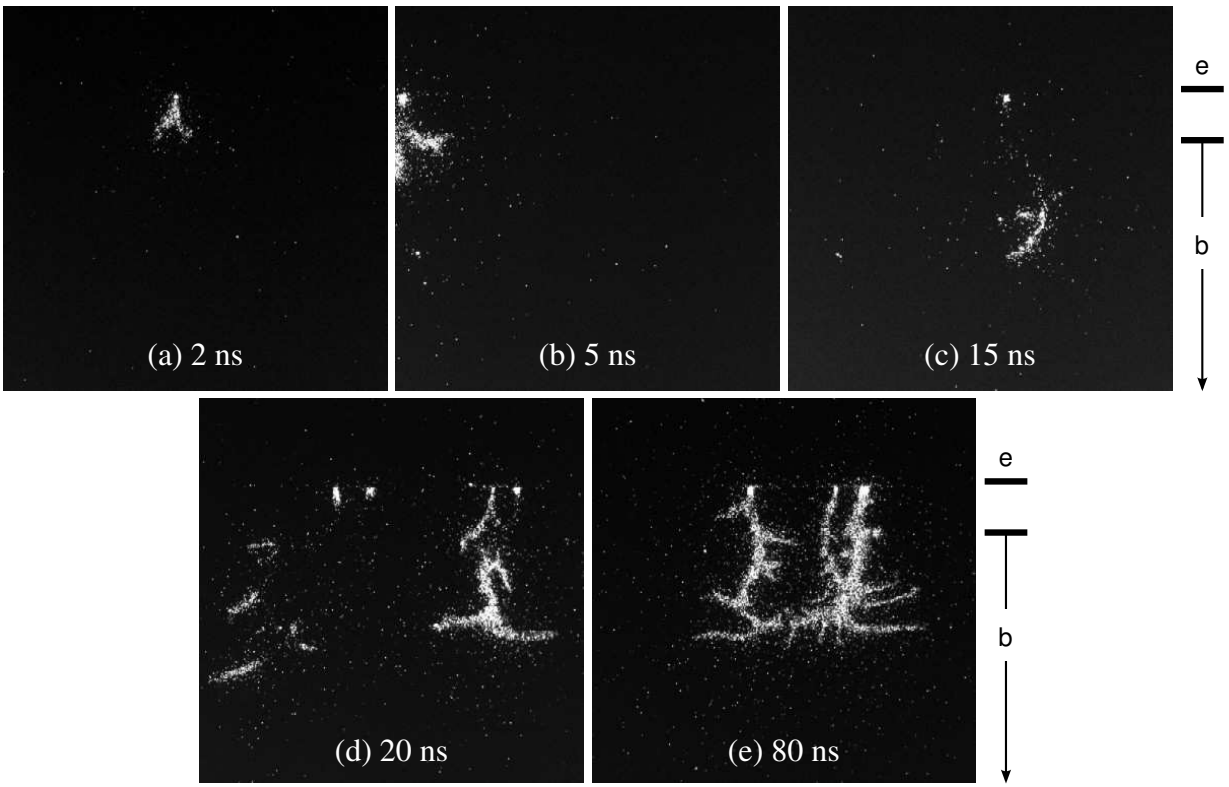

Figure 5.14: Nanosecond gate width images of filamentary microdischarges. The plasma length increases at larger gate widths. Gate widths are stated below each image.

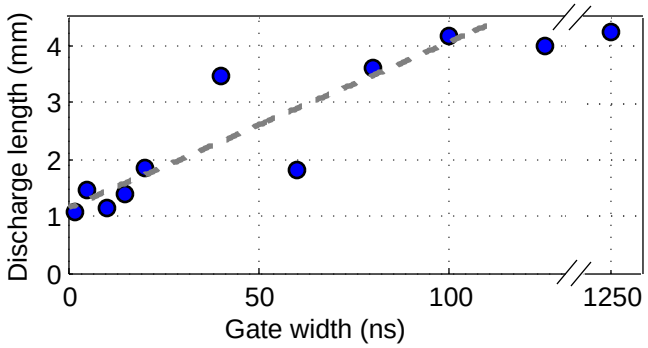

Figure 5.15: Plasma length increases with camera gate width during the positive-going half cycle, suggesting plasma propagation. The dashed line shows the linear fit used to determine the propagation velocity.

In contrast to the filamentary microdischarges, the jet-like microdischarges during the negative-going half cycle appeared to form quickly and remain in place. Figures 5.16(a) through 5.16(d) show plasmas of essentially the same length, suggesting that the plasma did not grow or propagate in the 5 to 1000 ns time frame. The images in figures 5.16(a) and 5.16(b), the shorter gate width images, were much dimmer than those in figures 5.16(c) and 5.16(d). In contrast, we noted little difference in the light intensity between images with gate widths of 20 ns and 1 μs. This suggests that while the microdischarges form in a time on the order of a few nanoseconds, their lifetime may be as long as 20 ns. If the microdischarge continued emitting light for a longer time we would expect the longer gate-width images, which show total integrated light, to be brighter.

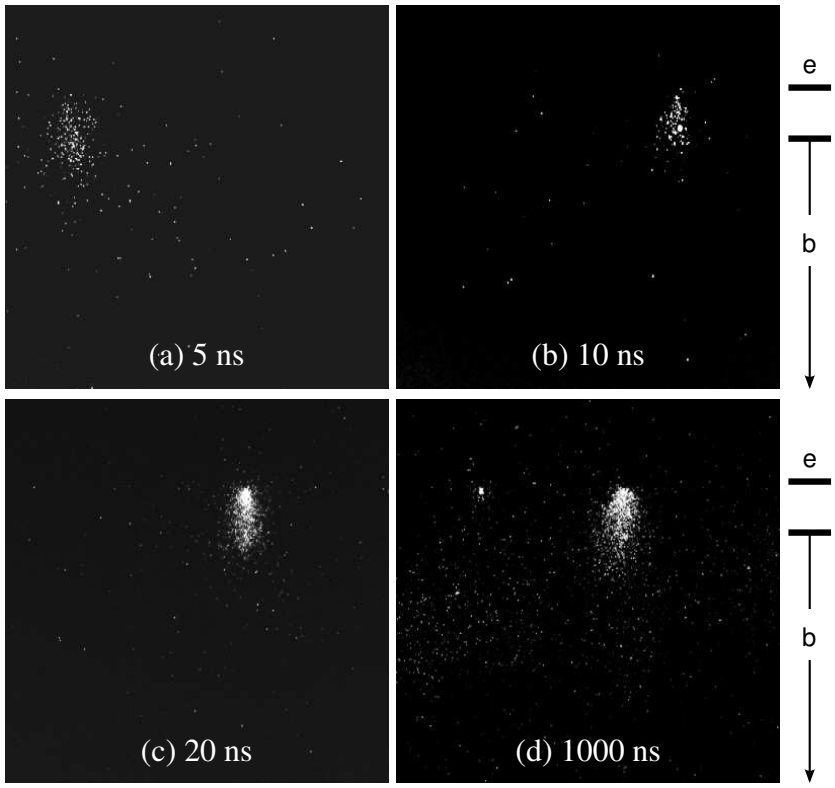

Figure 5.16: Nanosecond gate width images of jet-like microdischarges. The plasma length remains approximately constant with camera gate width during the negative-going half cycle. Gate widths are stated below each image.

5.3 Double-Barrier Actuators

We have also examined the average behavior of microdischarges in double-barrier actuators. These experiments were conducted on several double-barrier devices driven by 12 kV amplitude symmetric triangle voltages oscillating at 1 kHz. As described in section 4.3, microdischarges occurred less frequently in double-barrier actuators than in the single-barrier geometry at the voltage levels examined here. Nanosecond-scale gate width measurements were not attempted for these actuators due to the rarity of microdischarges occurring during the exposure.

Due to the lower frequency of microdischarge occurrence, plasma appeared in a smaller fraction of captured images than when we examined single-barrier actuators. Despite this, in nearly all of the 10 μs gate-width images in which at least one microdischarge appeared, a few to tens of microdischarges were captured. This suggests that the distribution of microdischarges in time is not strictly random. We hypothesize that the electrons from one microdischarge may provide the necessary "seed" electrons in the gas for a microdischarge to occur in an adjacent space, leading to multiple microdischarges occurring simultaneously or in rapid succession. The microdischarges we observed in double-barrier actuators also exhibited more variation in the plasma structure from image to image.

Similar to single-barrier devices, in double-barrier actuators we observed changes in the microdischarge structures as each half-cycle of the applied voltage progressed. Because the microdischarges in double-barrier actuators consisted simultaneously of both filamentary and jet-like plasma structures, these changes are more complicated than simple increases in microdischarge length. As the positive-going half cycle progressed, the filamentary structure extended further away from the narrow electrode. Concurrently, the jet-like portion of the microdischarge increased in length, not by extending past the narrow electrode, but by spanning a greater portion of the electrode gap. Figures 5.17(a) and 5.17(b) show microdischarge structures early and late in the positive-going half cycle, demonstrating both of these changes.

During the course of the negative-going half cycle, the average lengths of the jet-like portions of the microdischarges increased. This can be clearly seen in figures 5.17(c) and 5.17(d), with the

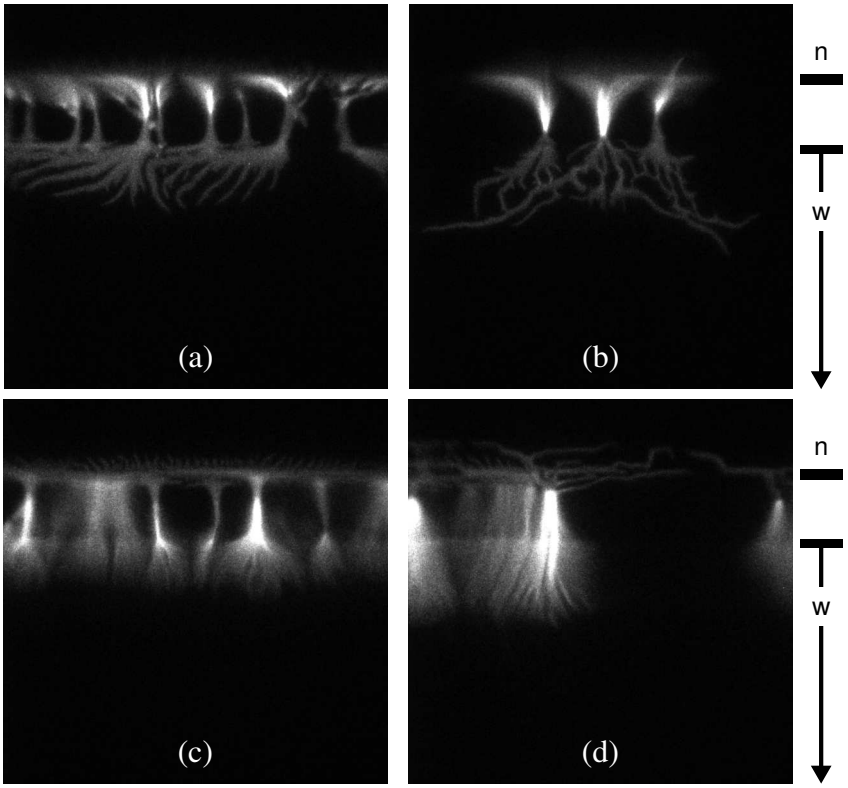

Figure 5.17: Changing double-barrier microdischarge structure from (a) 50% (0 V) to (b) 95% (10.8 kV) of the way through the positive-going half cycle and from (c) 50% (0 V) to (d) 95% (−10.8 kV) of the way through the negative-going half cycle.

jet-like structures extending further over the wide electrode later in the half cycle. The filamentary portions of the microdischarges appeared to extend slightly further past the narrow electrode later in the half cycle, but this was difficult to measure objectively. Unlike the positive-going half cycle, we observed no variation in the position of the filamentary/jet-like transition during the negative-going half cycle.

To obtain more quantitative measures of changes in the average microdischarge structure, we performed the same averaging and length-finding procedures as in section 5.2.1. The average light emission from a double-barrier actuator with a 0.13 mm diameter narrow electrode is shown in figure 5.18. The increase in average microdischarge lengths is evident in this figure, although the expansion was neither as rapid nor as uniform as in single-barrier actuators.

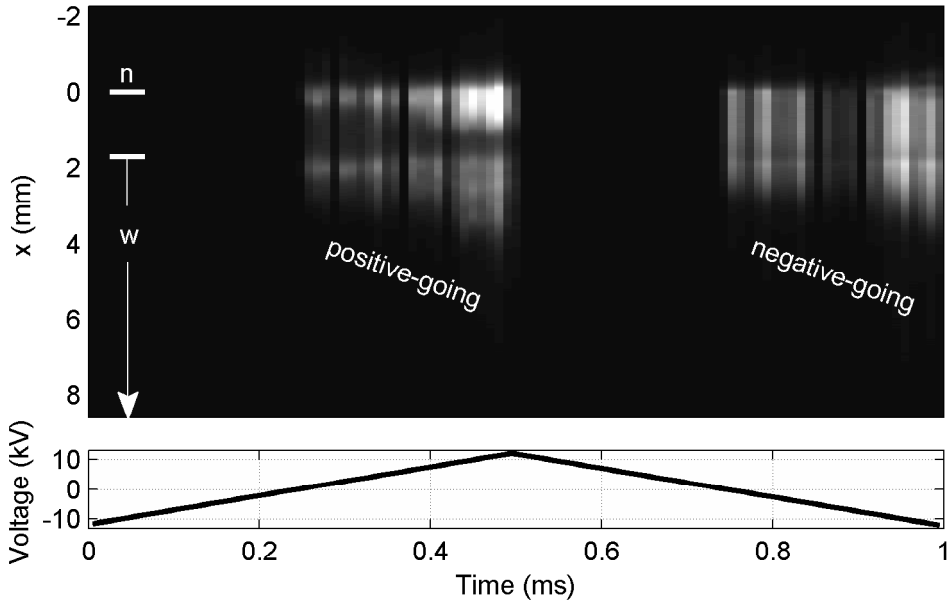

Figure 5.18: Average light emission during the applied voltage cycle for a single-barrier actuator with a 0.13 mm diameter narrow electrode. Each column of pixels corresponds to the average light emission from a 10 μs period.

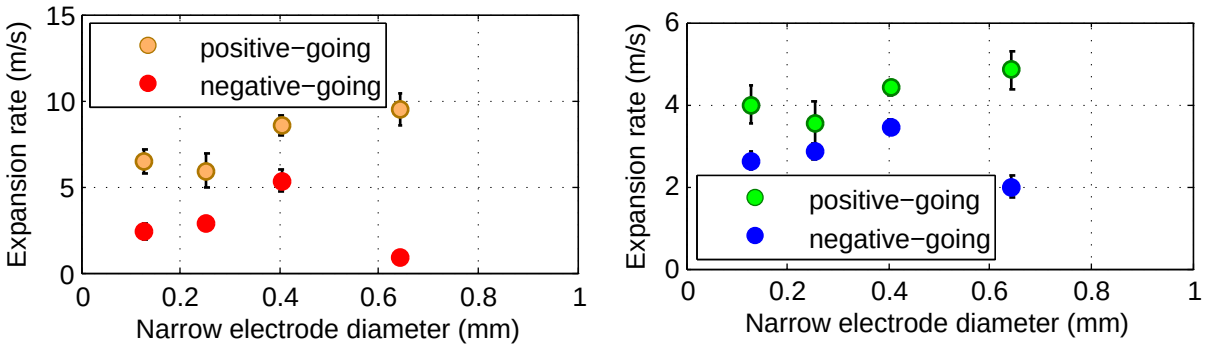

(a) (b)

Figure 5.19: Rates at which the average microdischarge length increases for double-barrier actuators, determined using (a) the edge-based algorithm and (b) the area-based algorithm

The edge- and area-based fitting algorithms also functioned effectively on the average light emission curves for double-barrier actuators. Because both methods find only the positive-x plasma edge, the measured plasma length was the length from the edge of the narrow electrode to the plasma edge above the wide electrode. This length did not include any portion of the plasma extending from the narrow electrode away from the wide electrode. Performing these fits and then finding the slopes of the regions where the average microdischarge length is linearly increasing yielded the expansion rates of figure 5.19. Unlike the single-barrier devices, we did not observe any strong trends in the microdischarge expansion rates as the electrode diameter was varied. We do note that the expansion rates for microdischarges during the negative-going half cycle were always smaller than those during the positive-going cycle.

Chapter 6

Computational Model Description

In order to gain additional insight into the plasma dynamics that occur on time and space scales too short to measure experimentally, we have developed a computational model of the surface DBD system. This model is based on the published work of Boeuf et al. [13, 14], but is an independent implementation. In addition to the features of that model, we have added the ability to model systems with electrodes of arbitrary shape and size. We have also, as described in section 6.2.5, included a dynamically-adjustable time step.

Due to limitations in computational power, the model is two-dimensional. It assumes uniformity in the z direction of figures 3.7 and 3.10. The images of chapter 5 indicate that the plasma is in fact non-uniform in this direction, which is rightly taken as a limitation of this model. Despite this, two-dimensional plasma models by ourselves and other groups have succeeded in reproducing numerous features of the plasma actuator system.

6.1 Physical Model

The simulation code written as part of this work is a two-dimensional fluid model. The model is designed to simulate relatively slow processes, using Poisson's equation to find the electrostatic potential. Each particle species is each governed by a continuity equation. Electron-impact ionization, electron attachment, positive ion-electron recombination, and positive ion-negative ion recombination processes are considered as the only sources and sinks. Particle transport is governed by the drift-diffusion approximation, which is valid for highly-collisional systems.

6.1.1 Modeled System

The simulated system always includes a high voltage electrode, a grounded electrode, and a rectangular dielectric layer, as in figure 6.1. The dielectric layer extends the full width of the system, and always extends from the bottom of the domain ($y = 0$) to a specified height. The code uses a single value for the dielectric constant inside of this dielectric layer, and assumes $\epsilon = \epsilon_0$ everywhere outside of this material. The relative dielectric constant ϵ_d for this layer was set equal to 3.0 for all simulations described in this work. The electrodes may have any shape, size, and position.

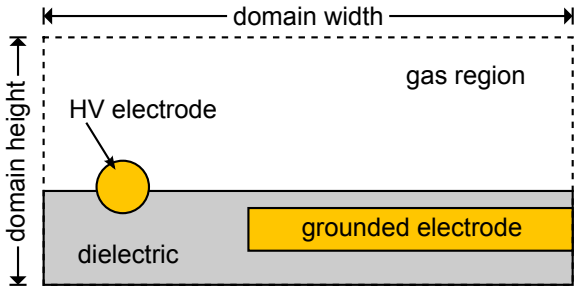

Figure 6.1: A generic simulation geometry including a high voltage electrode, a grounded electrode, and a dielectric layer

The model includes only three particle species: positive ions, electrons, and negative ions. All particles are assumed to be singly charged. A real plasma in air will contain many particle species; the number of species here is limited to avoid sacrificing computational efficiency. Unfer et al. [92] modeled a more detailed system including two positive ion species, one negative ion species, electrons, and a metastable species, and found qualitatively similar behavior to the simplified chemistry. The major effect of the additional particle species was to allow the plasma to expand further away from the exposed electrode in a single-barrier system. Our ion species are intended to represent averages of the actual variety of ions present. The positive and negative ions are treated as having properties equal to the respective weighted averages of the properties of the major positive- and negative-ion species in a real plasma. This averaging process is described in section 6.1.3. All of the simulations presented in this work used an air-like mixture of 600 Torr (partial pressure) of nitrogen and 160 Torr of oxygen.

6.1.2 Governing Equations

Poisson's equation, given by equation (2.17), can be written for the system described above as

$$\nabla \cdot (\epsilon \nabla \phi) = -e(n_p - n_e - n_n) - \delta_s \sigma. \tag{6.1}$$

The subscripts p, e, and n indicate positive ions, electrons, and negative ions, respectively. The surface charge density σ is evaluated only at the dielectric surface, as indicated by the delta function δ_s. It is self-consistently calculated by time-integrating the charged particle flux to the surface.

Poisson's equation is coupled to three continuity equations: one for each particle species, each including the appropriate source and sink terms. The continuity equation was stated for a general species α in equation (2.18), repeated here for reference:

$$\frac{\partial n_\alpha}{\partial t} = -\nabla \cdot \Gamma_\alpha + \sum S_\alpha - \sum R_\alpha, \tag{2.18}$$

Here Γ is the particle flux, while S and R are source and sink terms for the particle species. The sums are taken over all relevant processes for each species. In our simulation, positive ions are created via electron-impact ionization, and removed by recombination with either electrons or negative ions. New electrons are introduced via electron-impact ionization and secondary electron emission from surfaces, and removed by recombination with positive ions and attachment to neutral particles. Negative ions are formed via electron attachment, and removed through positive ion-negative ion recombination. Each of these processes is described further below. All particles may also be lost to exposed material surfaces. No photoionization processes are included. Some recent work suggests they may be required for streamer propagation during positive bias [91]. This requirement was avoided in these simulation runs by introducing an initial "seed" density of 10^{13} m^{-3} electrons and the same density of positive ions, which is larger than the charged-particle density in sea level air.

In all cases the particle transport is assumed to obey the drift-diffusion approximation given by equation (2.5). That equation describes a vector flux; in the simulation's algorithms, the continuity equations are split into x and y equations. For example, the positive ion flux in the x-direction, Γ_{px}, is given by

$$\Gamma_{px} = +\mu_p E_x n_p - D_p \frac{\partial n_p}{\partial x}, \tag{6.2}$$

with similar expressions applied to the other directions and species. Here μ is the particle mobility, $E_x = -\partial\phi/\partial x$ is the electric field strength in the x direction, and D is the particle diffusion coefficient.

As described in section 2.2.1, electrons may be emitted from material surfaces via secondary electron emission. In our simulation code, the total electron flux near a surface is given by

$$\vec{\Gamma}_e = \vec{\Gamma}_e^{\text{bulk}} - \gamma\vec{\Gamma}_p, \tag{6.3}$$

where γ is the secondary electron emission coefficient of surface. The bulk electron flux in equation (6.3) is simply that calculated using the appropriate drift-diffusion equation. The minus sign indicates that secondary electron flux *away* from a surface is proportional to the ion flux *into* that surface. Equation (6.3) is evaluated only for ions accelerated into a surface by the local electric field. For positive ions this is when the electric field is directed into the surface. Ions diffusing to the surface against the electric field are assumed to not have enough energy to "knock out" electrons.

The simulation code accepts two constant values for secondary electron emission coefficient: one for electrode surfaces, and one for the dielectric surface. For all results described in this work, we used values of 0.05 secondary electrons per incident ion for both surfaces. This allowed us to to compare our results more directly to those in the literature [e.g. 13], where the same values were used. Actual coefficients are dependent on many factors including the energy of the bombarding particle, the species of the bombarding particle, the surface temperature, and other surface conditions. We were unable to find empirical data useful for parameter ranges relevant for our system.

The rates of electron-impact ionization and electron attachment are calculated using equations (2.10) and (2.11), respectively, with the coefficients treated as functions of the local reduced electric field:

$$S_{iz} = \alpha\left(E/p\right)\left|\vec{\Gamma}_e\right| \qquad \text{and} \qquad S_{att} = \eta\left(E/p\right)\left|\vec{\Gamma}_e\right|.$$

The functional forms of both the ionization and attachment coefficients are described in section 6.1.3. Similar to secondary electron emission, both ionization and attachment are evaluated

only where the electron flux is accelerated by the local electric field. Electrons diffusing against the field are assumed to not have enough energy to attach to or ionize neutral particles.

Recombination rates, both between positive ions and electrons (pe) and between positive ions and negative ions (pn), are treated as proportional to the local densities of the recombining species, similar to the models of Tuszewski and White [99] and Boeuf and Pitchford [13]. For positive ions and electrons,

$$R_{pe} = r_{pe} n_p n_e,$$

where r_{pe} is the relevant recombination coefficient. Positive ion-negative ion recombination is handled similarly.

6.1.3 Physical Parameters

Many of the physical parameters used in the simulation code are in reality functions of particle velocity or energy distribution functions. In order to limit the amount of computational effort devoted to calculating these parameters, we have treated them as functions of the local reduced electric field, E/p. This method is sometimes known as the local field approximation (LFA). In the simulation, all parameters are calculated from analytic fits to published data. Where possible the analytic functions have been chosen to follow known scaling laws; in most cases, however, the functions are chosen purely for their good fit to the available data.

Particle mobilities are based on fits to empirical data from several sources [18, 19]. For positive ions, the scaled mobilities, in $\mathrm{m^2\ Torr\ V^{-1}\ s^{-1}}$, are approximated by

$$\mu_p\, p = 0.05492 \exp\left(\frac{-E/p}{6858}\right) + 0.07509 \exp\left(\frac{-E/p}{38175}\right) + 0.0308 \quad \text{for } \mathrm{N_2} \tag{6.4}$$

and

$$\mu_p\, p = 0.06841 \exp\left(\frac{-E/p}{59678}\right) + 0.09194 \exp\left(\frac{-E/p}{12763}\right) + 0.0320 \quad \text{for } \mathrm{O_2}, \tag{6.5}$$

where p is the total gas pressure in Torr and E/p is the reduced total electric field in $\mathrm{V\ m^{-1}\ Torr^{-1}}$. Mobilities are calculated separately for the x and y directions, using slightly different values for

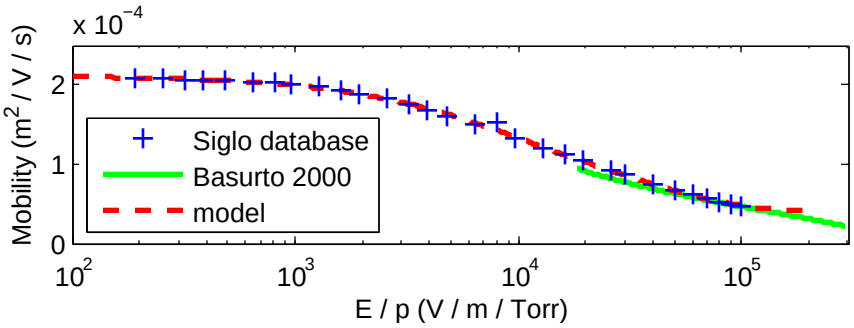

Figure 6.2: Mobility of N_2^+ in N_2 from two sources [18, 19] and equation (6.4), all for atmospheric pressure nitrogen gas at room temperature

the total electric field as described in section 6.2.1. Positive ion mobilities in nitrogen are shown in figure 6.2, while those in oxygen are in figure 6.3.

For electrons, we approximated the scaled mobilities by fitting to empirical data from the Siglo database [19], using

$$\mu_e\, p = 24.32 \exp\left(\frac{-E/p}{1057}\right) + 19.38 \exp\left(\frac{-E/p}{23430}\right) + 14.45 \tag{6.6}$$

in N_2 and

$$\mu_e\, p = 173.1 \exp\left(\frac{-E/p}{195.1}\right) + 36.19 \exp\left(\frac{-E/p}{3134.4}\right) + 31.73 \exp\left(\frac{-E/p}{18205}\right) + 12.49 \tag{6.7}$$

in O_2. Electron mobilities in both nitrogen and oxygen are shown in figure 6.4. Few data are available for the mobility of negative oxygen ions in any gas, so we use a scaled average mobility

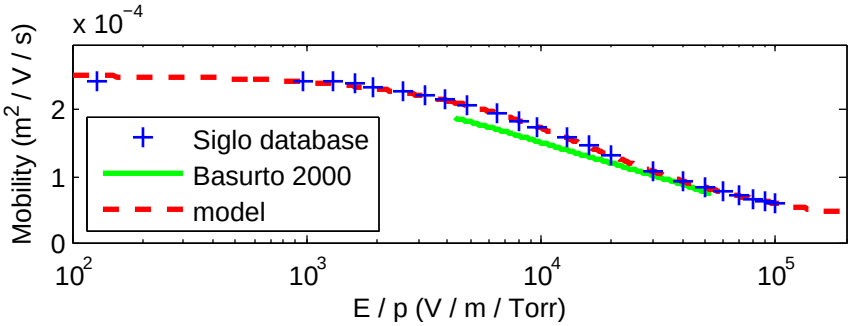

Figure 6.3: Mobility of O_2^+ in O_2 from two sources [18, 19] and equation (6.5), all for atmospheric pressure oxygen gas at room temperature

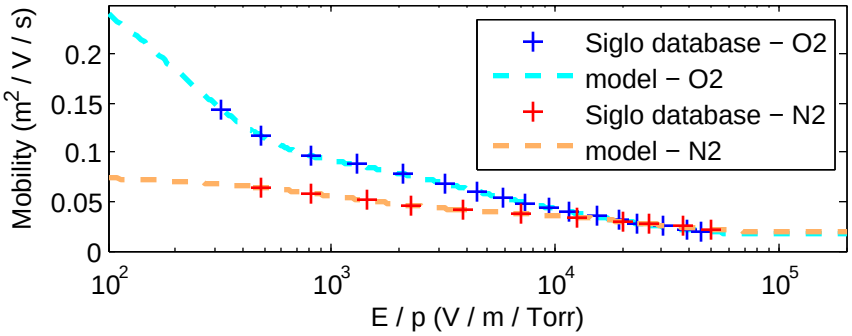

Figure 6.4: Mobilities of electrons in N_2 and O_2 [19], plotted with equations (6.6) and (6.7). Both gases are assumed to be at atmospheric pressure and room temperature.

which is constant with respect to the electric field [19]:

$$\mu_n p = 0.181125 \text{ m}^2 \text{ V}^{-1} \text{ s}^{-1}. \tag{6.8}$$

For simulations with multiple gases present we determine effective mobilities by averaging the calculated mobilities for each gas, weighting each value by the partial pressure of the parent gas:

$$\mu_{\text{eff}} = \frac{1}{p^2}\left[p_{\text{N2}}\left(\mu_{\text{N2}} p\right) + p_{\text{O2}}\left(\mu_{\text{O2}} p\right)\right], \tag{6.9}$$

where p_{N2} and p_{O2} are the partial pressures of nitrogen and oxygen respectively. This is not a true effective mobility for ions, as the mobilities of the ions in their non-parent gas is not taken into account. Perhaps more importantly, the proportion of positive ion belonging to each species is unknown. For air-like mixtures, we would expect oxygen ions to be much more prevalent, as the ionization coefficient for oxygen is larger than that for nitrogen. Despite these uncertainties, the use of equation (6.9) likely introduces less error than the other simplifications we have employed.

The drift-diffusion equations also require knowledge of the diffusion coefficients for all particles. The simulation code applies the Einstein relation, equation 2.7, to determine these coefficients, using constant particle temperatures. In this work, we have chosen values appropriate for a low-temperature non-equilibrium plasma, setting T_e equal to 1.0 eV, and both ion temperatures to room temperature: $T_p = 0.025$ eV and $T_n = 0.025$ eV.

The ionization coefficient for N_2 is approximated by

$$\frac{\alpha}{p}(\mathrm{N_2}) = \begin{cases} 4.71 \times 10^{-11} \left|E/p\right|^3, & |E/p| < 1.4 \times 10^4 \text{ V m}^{-1}\text{Torr}^{-1} \\ 3.32 \left(|E/p| - 12500\right)^{1/2}, & |E/p| > 1.4 \times 10^4 \text{ V m}^{-1}\text{Torr}^{-1} \end{cases}, \tag{6.10}$$

where α/p is in m^{-1} Torr^{-1}, and E/p is in V m^{-1} Torr^{-1}. This was obtained from a fit to the experimental data compiled in several sources [19, 100]. The ionization coefficient for O_2 has been obtained similarly from a fit to the experimental data compiled in in the Siglo database [19], using the same functional form as the N_2 coefficient at large E/p:

$$\frac{\alpha}{p}(\mathrm{O_2}) = \begin{cases} 1.17 \times 10^{-10} \left|E/p\right|^3, & |E/p| < 1.1 \times 10^4 \text{ V m}^{-1}\text{Torr}^{-1} \\ 0.0319|E/p| - 211, & 1.1 \times 10^4 < |E/p| < 2.1 \times 10^4 \\ 6.32 \left(|E/p| - 16300\right)^{1/2}, & |E/p| > 2.1 \times 10^4 \text{ V m}^{-1}\text{Torr}^{-1} \end{cases}. \tag{6.11}$$

The analytic approximations and experimental data for both gases are shown in figure 6.5.

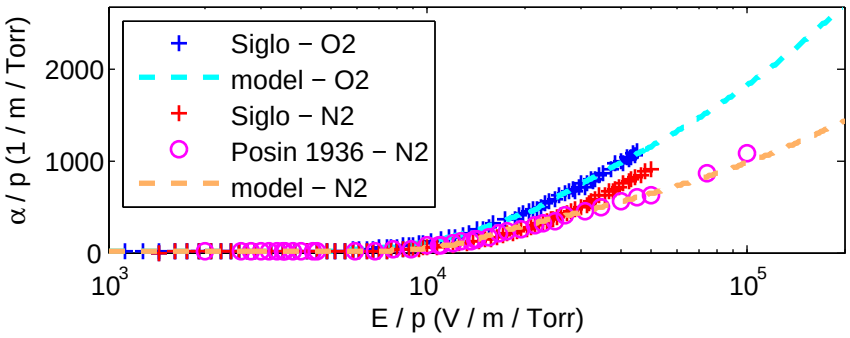

Figure 6.5: Reduced ionization coefficients in both nitrogen and oxygen

When both gases are present, the ionization coefficients are averaged according to

$$\alpha_{\text{eff}} = \left[\frac{\alpha}{p}(\mathrm{N_2})\right] p(\mathrm{N_2}) + \left[\frac{\alpha}{p}(\mathrm{O_2})\right] p(\mathrm{O_2}). \tag{6.12}$$

Based on a fit to the simulated data compiled in the Siglo database [19], we use

$$\eta \approx \left[1.307 + \frac{33200}{|E/p|} \exp\left(\frac{-\left(\ln|E/p| - 9.04\right)^2}{2.53}\right)\right] p_{\mathrm{O2}},$$

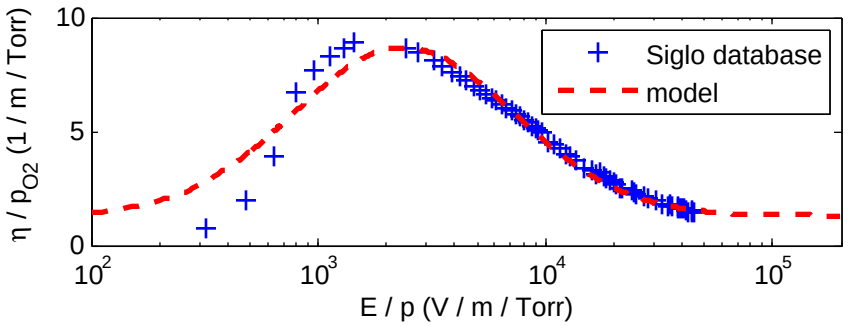

Figure 6.6: Reduced attachment coefficient for oxygen

to approximate the attachment coefficient in oxygen. Here η is in m^{-1} and p_{O2} is in Torr. This fit to the available attachment data is shown in figure 6.6. Nitrogen is an electropositive gas, so its attachment coefficient is always zero.

For our model, a value of 10^{-13} m^3/s is used for the recombination coefficients r_{pe} and r_{pn} [14, 99]. Both coefficients are assumed to be constant.

6.1.4 Range of Validity

Many of the simplifications used in this model stem from assumptions of high collisionality and a neglect of self-induced magnetic fields. We discussed this highly-collisional regime in section 2.1.1, and the simplifications that regime allows throughout section 2.1. The neglect of magnetic field terms is discussed below.

The drift-diffusion equations and the local field approximation (LFA) require that charged particles are in equilibrium with the local electric fields. To satisfy this requirement, the plasma must be highly collisional as described in section 2.1.1. In particular, particle energy relaxation must occur on a scale shorter than the Debye length:

$$\lambda_\epsilon < \lambda_D \tag{6.13}$$

The Debye length was given by equation 2.1. Boeuf [101] has suggested that when this criterion is not satisfied, the effect of applying the LFA is to overstate the ionization rate in regions of strong electric field and to understate it in the bulk plasma.

To estimate the validity of our simulation runs, we have examined two simulated situations in each of two simulation runs in detail. The simulations were of a positive-going voltage and a negative-going voltage applied to a reduced-scale single-barrier actuator with a 25 μm diameter exposed electrode, and we examined times both during and in between microdischarge events. Details regarding the simulated system are included in section 6.4, while other results from these runs are described in sections 7.1 and 7.2. Due to their low mobilities and short energy relaxation lengths, the ions were always highly collisional, so we focus on the collisionalities of the electrons.

During microdischarge events for both applied voltages, electron densities peaked around 10^{21} m^{-3}. The electric field strengths peaked around 8×10^{7} V/m at approximately the same locations as the maximum densities. Using the assigned electron temperature of 1 eV, the minimum Debye lengths were on the order of 2×10^{-7} m. In such dense, high-field regions, ionization processes are the dominant mechanism of energy transfer. From equation (2.3), energy relaxation lengths for electrons in such regions are equal to the ionization length, which can be calculated using equations (6.10), (6.11), and (6.12). We found an ionization length on the order of 10^{-6} m, making it notably longer than the Debye length. The ratios of energy relaxation lengths to Debye lengths were approximately constant throughout the length of the plasma channel. Consequently, our description of the plasma behavior during microdischarges is not strictly accurate. The overestimation of ionization in this region suggested by Boeuf [101] may not be as problematic as might initially be expected, as it will help compensate for the lack of photo-ionization in the model, which would primarily occur in regions of dense plasma.

During the build-up phases prior to microdischarge events for both applied voltages, the plasma densities and electric field strengths were lower than their values during microdischarges. The maximum electron densities were on the order of 5×10^{17} m^{-3}, corresponding to Debye lengths on the order of 10^{-5} m. The electric field strengths were on the order of 10^{7} V/m. At this field strength, both ionization and elastic collision processes are important. We determined the ionization length as described above, and calculated the energy relaxation length due to elastic collisions from the mobility using equations (2.6) and (2.2). The effective total energy relaxation length was on the order of 6×10^{-6} m, or somewhat shorter than the Debye length. If excitation processes were

included, the energy relaxation length would be even smaller. Consequently, we conclude that electrons are highly collisional in between microdischarge events, and criterion (6.13) is satisfied in these conditions.

Even when the above criterion is satisfied, the local field approximation (LFA) may still not be strictly valid, particularly in the determination of the ionization coefficient. The distribution function for electrons will, even in steady-state, be non-smooth. Certain energy ranges will be depleted by inelastic excitation collisions and collisions with material boundaries. These effects can only be completely accounted for with a kinetic treatment [102]. The LFA is employed in this work due to its large advantages in computational efficiency.

The use of Poisson's equation as the sole description of the electromagnetic physics imposes an additional restriction on the simulation. In using it, we have explicitly ignored any magnetic field effects. These effects become significant when the Lorentz force can change the direction of a particle's trajectory before it experiences a collision. Electrons will be more strongly affected by a magnetic field than heavy ions, so we write the restriction for them:

$$\omega_{ce} \ll \nu_{eg}, \tag{6.14}$$

where $\omega_{ce} = e|\vec{B}|/m_e$ is the electron-cyclotron frequency in a magnetic field $\vec{B}$, and ν_{eg} is the electron-neutral collision frequency. Stated more concisely, magnetic field effects on transport can be ignored when many collisions prevent a particle from gyrating in the magnetic field [17].

Since we assume no background magnetic field, and applied voltage varies relatively slowly for all simulations described here, induction by plasma current is the dominant source of magnetic fields. The various simulations described in chapter 7 had peak plasma currents between about 20 and 200 A/m, calculated as described in section 6.3. These currents flowed in thin channels of plasma, so it is reasonable to describe them as sheet currents. Doing so allows us to calculate the induced magnetic fields, which would range up to about 10^{-4} T. Corresponding electron-cyclotron frequencies are of the order 10^7 s^{-1}. Using equation (2.6) and the data of section 6.1.3, we estimate the minimum electron-neutral collision frequencies to be of the order 10^{12} s^{-1}. Consequently, condition (6.14) is well satisfied at all times during the simulations in this work. In real systems, as shown in chapter 5, the plasma current sometimes constricts into narrow filaments, which may

increase the local magnetic field. This behavior cannot, however, be captured in a 2-dimensional simulation.

6.2 Numerical Methods

The simulation code first solves Poisson's equation and then solves the continuity equations using semi-implicit methods. The simulation domain is discretized in both space and time, with the equations solved iteratively at each time step. The numerical methods used in the code are first order accurate in both space and time. The solution methods generally follow those of Boeuf et al. [14], with adaptations to allow arbitrary electrode geometries and a dynamic time-step size. We have implemented the code primarily in MATLAB®, with several of the most computationally-intensive functions written in C.

This section uses the following notation. Subscripts i and j indicate that a quantity is evaluated at the i^{th} grid index in the x direction and the j^{th} grid index in the y direction. A superscript m indicates that a quantity is evaluated at the m^{th} time step of the simulation. The length of a time step is Δt, which is set by the dynamic time-stepping adjustment described in section 6.2.5.

6.2.1 Numerical Grid

The model imposes a Cartesian grid onto the simulation region described in section 6.1.1. The intersection points of the grid are conventionally specified by integer indices i and j in the x and y directions, respectively. For all of the simulations here, the grid spacing sizes Δx and Δy were equal. They are, however, carried through separately in some of the derivations below and in appendix B.

Different quantities are defined at different locations on the numerical grid, as shown in figure 6.7. All particle densities n are located at integer grid indices (i, j), as are the values of the potential ϕ. The x-directed components of the particle fluxes and electric field are located at half-integer indices in x and integer indices in y, i.e. at $(i + \frac{1}{2}, j)$. Conversely, y-directed components are located at $(i, j + \frac{1}{2})$: integer indices in x and half-integer indices in y.

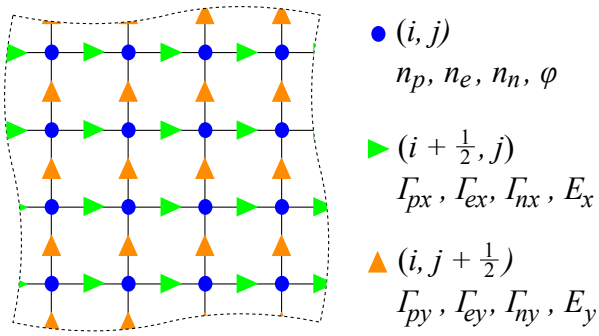

Figure 6.7: Portion of the numerical grid, noting the quantities defined at different locations

Many of the physical parameters discussed in section 6.1.3 are functions of the electric field magnitude. The magnitudes, which are required at each integer and half-integer grid point, are calculated as

$$\begin{aligned}
\left|\vec{E}\right|_{i,j} &= \sqrt{\frac{1}{4}\left(E_{x_{i+\frac{1}{2},j}} + E_{x_{i-\frac{1}{2},j}}\right)^2 + \frac{1}{4}\left(E_{y_{i,j+\frac{1}{2}}} + E_{y_{i,j-\frac{1}{2}}}\right)^2} \\
\left|\vec{E}\right|_{i+\frac{1}{2},j} &= \sqrt{\left(E_{x_{i+\frac{1}{2},j}}\right)^2 + \frac{1}{16}\left(E_{y_{i+1,j+\frac{1}{2}}} + E_{y_{i+1,j-\frac{1}{2}}} + E_{y_{i,j+\frac{1}{2}}} + E_{y_{i,j-\frac{1}{2}}}\right)^2} \\
\left|\vec{E}\right|_{i,j+\frac{1}{2}} &= \sqrt{\frac{1}{16}\left(E_{x_{i+\frac{1}{2},j+1}} + E_{x_{i+\frac{1}{2},j}} + E_{x_{i-\frac{1}{2},j+1}} + E_{x_{i-\frac{1}{2},j}}\right)^2 + \left(E_{y_{i,j+\frac{1}{2}}}\right)^2}.
\end{aligned} \tag{6.15}$$

Electrode and dielectric geometries are defined via their positions on the grid. Grid points included in electrode definitions are treated as fully inside the electrode; the electrode surface lies somewhere between the included point and the adjacent grid point. The dielectric layer is defined by a single value: the y index of its horizontal surface. All grid points below that y index are inside the dielectric, while all points above are in a gaseous region. Points at that index lie precisely on the dielectric surface.

6.2.2 Scharfetter-Gummel Discretization

The numerical stability of both the Poisson's equation solver and continuity equation solver depend on the use of the Scharfetter-Gummel discretization of the particle fluxes [103]. This discretization is a type of upwinding scheme that is commonly employed in semiconductor physics

simulations. While the scheme succeeds in removing the grid-based instabilities that would otherwise appear, it does so at the cost of reducing the algorithm spatial accuracy to first order and allowing numerical diffusion at larger spatial step sizes. One derivation is described below.

The particle fluxes are described by the drift-diffusion approximation, given by equation (2.5). Since the flux is defined at half-integer indices, we enforce the equation there. For transport in the x direction,

$$\Gamma_x\Big|_{i+\frac{1}{2},j} = \pm\mu E_x\Big|_{i+\frac{1}{2},j} n - D\frac{\partial n}{\partial x}\Big|_{i+\frac{1}{2},j},$$

with the plus sign taken for positive ions and the minus sign for electrons and negative ions. Since the particle densities are defined at integer grid indices, the density at $(i+\frac{1}{2}, j)$ is unknown. In other situations this density would be obtained by averaging the values at i and $i+1$, but here this procedure leads to a numerically unstable algorithm except for small electric fields on fine grids [103].

Instead, the above equation is solved as a first-order ordinary differential equation in n. In doing so we treat the flux, electric field, mobility, and diffusion coefficient as approximately constant, relative to the density changes, in the region between i and $i+1$. The solution, applying boundary conditions of the "known" values of n at i and $i+1$, is

$$n_{i+1,j} = \frac{(\Gamma_x)_{i+\frac{1}{2},j}}{(\mu E_x)_{i+\frac{1}{2},j}} + \left[n_{p_{i,j}} - \frac{(\Gamma_x)_{i+\frac{1}{2},j}}{(\mu E_x)_{i+\frac{1}{2},j}}\right] \exp\left[\pm\frac{(\mu E_x)_{i+\frac{1}{2},j}}{D_{i+\frac{1}{2},j}}\Delta x\right].$$

Solving for the flux in a symmetric form yields the Scharfetter-Gummel discretization:

$$\Gamma_x\Big|_{i+\frac{1}{2},j} = \frac{D_{i+\frac{1}{2},j}}{\Delta x}\left(\frac{z_{i+\frac{1}{2},j}}{1-e^{z_{i+\frac{1}{2},j}}}\right) n_{i+1,j} + \frac{D_{i+\frac{1}{2},j}}{\Delta x}\left(\frac{z_{i+\frac{1}{2},j}}{1-e^{-z_{i+\frac{1}{2},j}}}\right) n_{i,j} \tag{6.16}$$

where

$$z_{i+\frac{1}{2},j} = \frac{\pm(\mu E_x)_{i+\frac{1}{2},j}}{D_{i+\frac{1}{2},j}}\Delta x = \frac{\pm E_{x_{i+\frac{1}{2},j}}}{T}\Delta x. \tag{6.17}$$

Similar expressions exist for y-directed fluxes. We use expressions like equation (6.16) for the particle fluxes in solutions to both Poisson's equation and the continuity equations. No averaging is required to find any of the values in the above equations with the grid defined as described in section 6.2.1. As before, the plus sign is taken for positive ions and the minus sign for electrons and

negative ions. In each case, the appropriate parameter values must be used for each species. We note that equation (6.16) reduces to the correct limits, namely the diffusive flux for small electric fields, using

$$\lim_{z\to 0}\left(\frac{z}{1-\mathrm{e}^{z}}\right) = -1,$$

and the drift flux for large electric fields.

6.2.3 Poisson's Equation Solver

Poisson's equation, given in equation (6.1) for this system, requires knowledge of the charge distribution. Finding the potential at a new time step $m+1$ then requires knowledge of the charge distribution at time $m+1$. Since Poisson's equation is solved prior to the continuity equations, the charge at $m+1$ is not known. A fully explicit solution would use the charge densities of the previous time step. This technique, however, restricts the amount the charge is allowed to change during a given time step, limiting the maximum time step to the dielectric relaxation time [104]:

$$\Delta t < \epsilon_0/\sigma_p,$$

where σ_p is the total plasma conductivity (which depends on the particle densities and mobilities). Since the time scales of interest in plasma actuators are generally many orders of magnitude larger than the dielectric relaxation time, this restriction makes explicit simulations impractical for our desired uses of the simulation. An alternate technique, used here, is to make a prediction of the charge density at time $m+1$. Using a first-order Taylor expansion of the densities at $m+1$ allows us to rewrite Poisson's equation in the plasma bulk as

$$\epsilon_0\nabla^2\phi^{m+1} = -e\left[n_p^m - n_e^m - n_n^m + \Delta t\left(\frac{\partial n_p}{\partial t} - \frac{\partial n_e}{\partial t} - \frac{\partial n_n}{\partial t}\right)\right]. \tag{6.18}$$

The density time derivatives are obtained from the set of continuity equations, given by equation (2.18). Since that set conserves net charge, all of the source and sink terms exactly cancel, leaving only the divergences of the fluxes:

$$\frac{\partial n_p}{\partial t} - \frac{\partial n_e}{\partial t} - \frac{\partial n_n}{\partial t} = -\nabla\cdot\Gamma_p + \nabla\cdot\Gamma_e + \nabla\cdot\Gamma_n. \tag{6.19}$$

Each of these fluxes is evaluated using the drift-diffusion equation, given by equation (6.2). The solver routine uses the semi-implicit method suggested by Ventzek et al. [105], in which potential is taken at time $m+1$ while all densities use the known values at time m. For the positive-ion flux, this is written as

$$\vec{\Gamma}_{px} \approx +{n_p}^m \mu_p \vec{E_x}^{m+1} - D_p \frac{\partial}{\partial x}\left({n_p}^m\right),$$

with similar expressions for the other fluxes. Each of the flux equations is then discretized using the Scharfetter-Gummel method, given by equation (6.16), and inserted into equation (6.19). The result is then substituted back into equation (6.18), yielding an equation depending only on potentials at time step $m+1$ and densities at time step m. That equation can then be discretized using standard second-order finite difference approximations for the spatial derivatives. We rearrange it into the form

$$\phi_{i,j}^{m+1} = C1(i,j)\phi_{i+1,j}^{m+1} + C2(i,j)\phi_{i-1,j}^{m+1} + C3(i,j)\phi_{i,j+1}^{m+1} + C4(i,j)\phi_{i,j-1}^{m+1} + C5(i,j), \quad (6.20)$$

where each C term depends only on quantities evaluated at time m. The derivation of equation (6.20) is described in greater detail in Appendix B.1, including corrections necessary at the dielectric surface and to take secondary electron emission into account. We solve equation 6.20 using a successive over-relaxation method [106] with a relaxation parameter of 1.9. The iteration is continued until the maximum change in the potential is less than a specified error value. The chosen error values for each simulation run are given in table 6.1.

6.2.4 Continuity Solver

The particle continuity equations, given by equation (2.18), are solved after the solution of Poisson's equation. They can be solved at time $m+1$ in a more straightforward manner than Poisson's equation, because the potential at time $m+1$ is already known. The flux terms are directly evaluated at time $m+1$ using the Scharfetter-Gummel discretization of the drift-diffusion equation. The source and sink terms described in section 6.1.2 depend non-linearly on the particle densities, and so cannot be directly included in an implicit solution scheme. Instead, they are evaluated using quantities from time step m, which is discussed further below. The general continuity

equation evaluated at time $m+1$, as implemented in the continuity solver, is

$$\left.\frac{\partial n}{\partial t}\right|_{i,j}^{m+1} = -\nabla \cdot \Gamma^{m+1} + \sum S^m - \sum R^m. \tag{6.21}$$

The time derivative in equation (6.21) is evaluated using the first-order backwards difference formula, so this method is first-order accurate in time. Once the flux expressions and source term values are substituted into equation (6.21), and finite difference formulas have been applied to the derivatives, it can be solved for the the particle density at $m+1$. This solution is described in detail in Appendix B.2. For each particle species, we find an equation of the general form

$$n_{\alpha i,j}^{m+1} = C1(i,j)n\phi_{i+1,j}^{m+1} + C2(i,j)n_{i-1,j}^{m+1} + C3(i,j)n_{i,j+1}^{m+1} + C4(i,j)n_{i,j-1}^{m+1} + C5(i,j). \tag{6.22}$$

We solve equation (6.22) for each particle species using the Gauss-Seidel method [106], with the process continuing until no relative change in a density value $\Delta n/n$ exceeds a specified error in a single iteration. For all of the simulations described here, that error was 10^{-3}.

Models for source and sink processes were described in section 6.1.2. While the evaluations of secondary electron emission, positive ion-electron recombination, and positive ion-negative ion recombination are straightforward, the calculations of ionization and attachment rates bear additional comment. Both of these rates depend on the electron flux. Fluxes, as described in section 6.2.1, are defined at half-integer spatial indices. Equation (6.21), however, requires the ionization and attachment rates at integer spatial indices in order to update the particles densities. To determine the appropriate fluxes for these rates, we simply average the nearby fluxes, using

$$\left|\vec{\Gamma}_e\right|_{i,j} \approx \sqrt{\frac{1}{4}\left(\Gamma_{ex}\Big|_{i+\frac{1}{2},j} + \Gamma_{ex}\Big|_{i-\frac{1}{2},j}\right)^2 + \frac{1}{4}\left(\Gamma_{ey}\Big|_{i,j+\frac{1}{2}} + \Gamma_{ey}\Big|_{i,j-\frac{1}{2}}\right)^2}.$$

Since any averaging scheme can increase the effective numerical diffusion, this is not necessarily the ideal solution. At present not enough work has been done analyzing the effects of this averaging on simulation behavior to determine whether a different method would be more desirable.

6.2.5 Adaptive Time-Stepping

The Poisson's equation solver, as described in section B.1.1, uses first-order Taylor expansions to linearize the expressions for particle fluxes. This expansion requires

$$\begin{aligned} \left|\frac{\Delta E \Delta x}{T_e}\right| \ll 1 \qquad \text{where} \qquad \left|\frac{E\Delta x}{T_e}\right| < 1 \qquad \text{and} \\ \frac{\Delta E}{E} > -1 \qquad \text{where} \qquad \left|\frac{E\Delta x}{T_e}\right| > 1. \end{aligned} \tag{6.23}$$

Here we have used the electron temperature for T. While the accuracy of the Taylor expansions strictly require that condition (6.23) be satisfied for each particle species, the mobility of electrons is so high that electron motion affects the calculated potentials for much smaller electric fields than do ion motions. In its computations, the solver routine uses an arbitrary value of 0.5 as the threshold for acceptably small values of $|\Delta E \Delta x / T_e|$. This value represents a compromise between mathematical accuracy and computation speed.

In order to ensure that condition (6.23) is satisfied during each time step, while still maintaining reasonable computation times, we have implemented an adaptive time-stepping scheme. Our simulation runs exhibit short periods of rapid change during microdischarges interspersed with longer periods of plasma decay, as shown in figure 2.14. With an adjustable time-step size, the simulation can take small steps when the plasma evolves quickly and large steps when the system is relatively stable, as shown in figure 6.8.

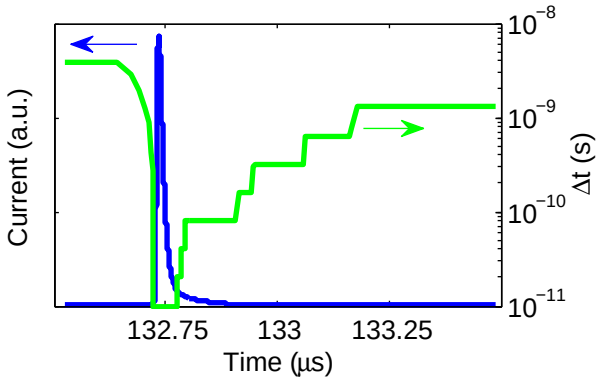

Figure 6.8: Dynamic time step adjustment during a single microdischarge event

In the code, the appropriate time-step size to ensure that condition (6.23) is satisfied is estimated at the beginning of each simulation loop and later verified. The estimation is based on how well condition (6.23) was satisfied during the previous time step. If the minimum values of either $\Delta E/E$ or $-a_f|\Delta E \Delta x/T_e|$ (where a_f is a user-set adjustment factor) are more negative than a set threshold, Δt is reduced. If the value is smaller than the threshold / 20, Δt is increased. Immediately following the solution of the Poisson equation, compliance with condition (6.23) is checked for the current time step. If it has been violated, Δt is reduced and the solution is repeated. This repetition reduces the computational efficiency, and is strongly affected by the chosen value of the adjustment factor a_f. Based on several test runs, we chose adjustment factors of 1 for runs with positive-going applied voltages and 2 for runs with negative-going voltages.

The threshold described above is chosen based on the current size of the time step. We have chosen a functional form for this threshold of

$$\text{threshold} = -\left(\frac{\Delta t}{\Delta t_{\text{min}}}\right)^{[1/(\log_{10}\Delta t_{\text{min}} - \log_{10}\Delta t_{\text{max}})]},$$

which is plotted in figure 6.9. The parameters Δt_{min} and Δt_{max} are described below. The form was chosen to make Δt "easier" to decrease when large time steps are being taken and "harder" to decrease when Δt is already relatively small.

The code restricts the range in which Δt is allowed to vary to between specified values of Δt_{min} and Δt_{max}. If Δt is allowed to increase too far, details of the plasma evolution can be lost before the simulation has a chance to "slow down" by decreasing the time-step size. In the extreme

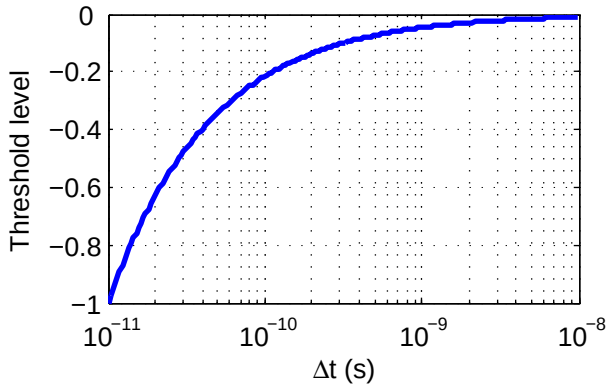

Figure 6.9: The sliding threshold used to estimate new time-step sizes

case of an unbounded Δt and a time period of stable plasma behavior, Δt has been observed to increase until the majority of the simulation occurs during a single time step. While maintaining strict accuracy would require no minimum bound on Δt, in practice this can result in long (and unpredictable) computation times. A minimum bound yields shorter computation times by sacrificing some amount of accuracy. The maximum and minimum bounds used for each simulation run are described in section 6.4.

6.2.6 Boundary Conditions

At the four edges of the simulation region, symmetry boundary conditions are applied to the potential as well as to all particle densities. This condition on ϕ is equivalent to setting the component of the electric field perpendicular to the boundary to zero. The conditions on the densities are equivalent to setting the diffusive flux of each species out of the system to zero. With no electric field, the drift flux is also zero, so the combination of boundary conditions effectively prevents all particles from leaving the system.

At grid cells inside the electrodes and dielectric all particle densities are set to zero. At grid cells on the dielectric surface the particle densities are also set to zero, but a non-zero surface charge density is permitted. At each time step, the surface charge density σ is calculated using

$$\sigma_i^{m+1} = \sigma_i^m + \Delta t \left(-\Gamma_{py}\Big|_{i,js+\frac{1}{2}}^{m+1} + \Gamma_{ey}\Big|_{i,js+\frac{1}{2}}^{m+1} + \Gamma_{ny}\Big|_{i,js+\frac{1}{2}}^{m+1} \right), \tag{6.24}$$

where the $js + \frac{1}{2}$ index indicates that these are the fluxes just above the surface of the dielectric, which is located at the y index js.

As described in section 6.1.2, secondary electron emission is considered from all surfaces. The electrodes are allowed to have arbitrary geometries, with the flux of emitted electrons always assumed to be normal to the local surface. This calculation is described in more detail in section B.1.3.

At grid cells inside the electrodes, the potential is set to a given value (either the applied voltage or ground). At grid cells inside the dielectric, the potential is calculated normally, save with the dielectric constant adjusted to $\epsilon_0\epsilon_d$, where ϵ_d is the relative coefficient of the dielectric material.

The potential at the dielectric surface is calculated by treating the dielectric constant on the surface is equal to $\epsilon_0(1 + \epsilon_d)/2$ and applying Poisson's equation. This calculation includes the surface charge, and is described in more detail in section B.1.6.

6.2.7 Limitations

In addition to the restrictions discussed in section 6.1.4, the discretization of the spatial domain adds additional restrictions and innacuracies to the model. In order to ensure that the drift-diffusion approximation and the local field approximation are satisfied at every grid point, the simulations should satisfy the restriction that

$$\lambda_\epsilon < \Delta x.$$

This restriction ensures that each particle is in equilibrium with the applied field by the time it passes the next grid point. A particle in a system which violated the restriction should in reality increase in velocity and energy as it passed by each successive grid point until it finally reaches the mobility-limited flow velocity of $\mu\vec{E}$. In such a system, the drift-diffusion approximation would yield larger fluxes at some grid points than would be predicted by a more accurate physical model. In spite of this, decreasing the grid spacing does not reduce the global accuracy of the system. Rather, the stated condition places a limit on the effective spatial resolution of the system: there is no benefit to reducing Δx below the energy relaxation length. Any real plasma structures at smaller spatial scales would be removed by the application of the drift-diffusion approximation. Using the energy relaxation lengths calculated in section 6.1.4, we see that this condition is marginally satisfied in our full-scale simulations. The finer grid spacing of the reduced-scale simulations provides slightly more resolution than is needed to resolve simulated plasma structures.

Where the electric field varies rapidly, strict accuracy requires

$$\Delta x < \lambda_D. \tag{6.25}$$

While the solution to the Poisson equation on a spatial grid is approximately correct even when this condition is not satisfied, it will spatially average peak electric fields. This will have relatively little effect on the drift-diffusion approximation, which depends linearly on the electric field. Some

of the source and and sink terms, however, depend non-linearly on the electric field. The additional spatial averaging of the electric field will in general decrease the ionization constant and increase particle particle mobilities, but how these changes will affect the source and sink rates will depend on the details of the situation. As with restriction (6.13), we see that due to the large densities during microdischarge events condition (6.25) is only satisfied between microdischarge events. Considering criterion (6.25) as well as the validity criteria discussed in section 6.1.4, we see that the model is generally accurate during the plasma build-up and decay phases in between microdischarge events, but loses some accuracy when simulating the strong electric fields and high plasma densities present during the microdischarges.

The choice of numerical methods also affects the accuracy of the results. The use of the Scharfetter-Gummel scheme for determining the particle fluxes adds non-physical diffusion to the simulated system [92]. The additional diffusion likely reduces the density in the front of a streamer-like microdischarge, among other effects. The use of solution algorithms that are first order in both space and time also reduces the accuracy of the results. The use of dynamic time-stepping helps to reduce the errors caused by large time steps. Boeuf et al. [14] examined the effects of increasing the spatial step size, finding that error levels were acceptable at step sizes of 7 μm and smaller.

6.3 Measured Quantities

Typical simulation runs involve densities and potentials defined at about 5×10^5 grid points, evaluated at each of about 10^6 time steps. Recording all data at each time step would have required prohibitive amounts of storage capacity. Instead, we primarily recorded and examined a small number of spatially- or temporally-averaged quantities as described in this section.

As described in section 2.1.3, the plasma in a dielectric barrier discharge plasma actuator exerts a force on the background gas. This force is calculated at each point using equation (2.9):

$$\vec{f}_{\text{EHD}} \approx e(n_p - n_e - n_n)\vec{E}. \tag{2.9}$$

Since the electric fields are defined at half-integer grid indices while the densities are defined at integer grid indices, we shift the electric fields by averaging adjacent values. The EHD forces in each direction are spatially-integrated into linear force densities and recorded as functions of time. The results presented in chapter 7 deal with force densities in the x direction unless noted otherwise.

The simulation code calculates the linear current density, in Amperes per meter, supplied by an external circuit to each electrode in the simulation. Current to an electrode is calculated as the sum of the direct particle current incident on the electrode and the change in the electrode surface charge necessary to maintain the specified voltage. The former can be calculated directly from the particle fluxes. The latter is determined by applying the 2-dimensional form of Gauss's law:

$$\oint \epsilon \vec{E} \cdot d\vec{\ell} = Q/L_z,$$

where Q/L_z is the linear charge density on the electrode, and the integral is taken around the surface of the electrode. The change in Q/L_z over one time step is the capacitive portion of the circuit current. If an electrode extends beyond the simulation boundaries, only the current to the portions inside the simulated region is calculated. While in an ideal system the current to each of the two electrodes would be identical, in the finite domain the two currents may differ slightly due to the conditions imposed at domain boundaries. In our simulations, the current to the high voltage electrode was always less noisy than that to the grounded electrode. All current data in chapter 7 are the currents to the high voltage electrode. We have benchmarked the current calculation to the analytic current in a purely capacitive system.

In order to provide a rough picture of the plasma behavior over time, the code also periodically determines the average particle density for each species and estimates the locations of the maximum particle densities. The average particle densities are smaller for larger simulation domains and for systems with large exposed electrodes. Consequently, we will consider only trends in the average density behaviors, and neglect differences in the absolute values. The positions of maximum particle densities are also recorded, and allow a rough estimate of the location of the front of streamer-like microdischarges.

6.4 Description of Simulated Discharges

For both single- and double-barrier geometries, we have conducted two series of simulations: full scale and reduced scale. The dimensions used in the full-scale simulations were chosen to be similar to those of the actuators we have studied experimentally. Reduced-scale systems used spatial dimensions a factor of 10 smaller than the full-scale dimensions. The reduced-scale systems were initially studied for their relatively short computation times, and have also provided insight into the effects of changing the geometric scale as described in section 7.2.

The simulated single- and double-barrier geometries are shown in figure 6.10. For both geometries, we chose to specify a separation between the left-hand edge of the domain and the center of the high voltage electrode rather than the length of the grounded electrode. This choice was made to ensure sufficient separation between the high voltage electrode and the domain boundary to avoid edge effects for all chosen electrode sizes. The dimensions and simulation parameters for these series of simulations are given in table 6.1. The only significant difference between the experimental actuator dimensions and those of the simulated systems was the thickness of the buried and wide electrodes. In the experiments, these electrodes were always 36 μm thick. In the simulations, these electrodes were originally specified to extend to the bottom of the simulation domain for simplicity, and this geometry was maintained through new systems to allow easier comparisons with the older data. This lead to the use of the grounded electrode thicknesses specified in table 6.1, which for the full-scale systems are significantly larger than in the experiments.

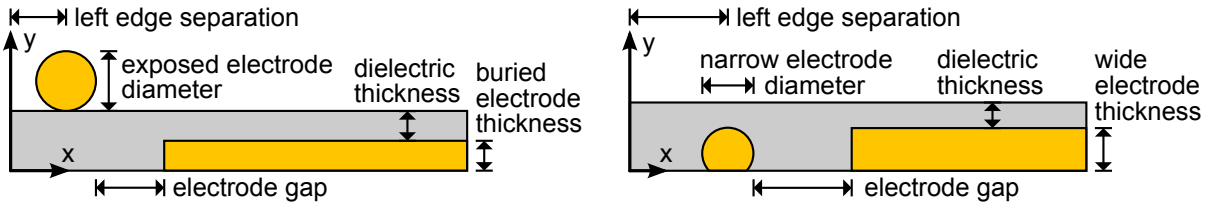

(a) (b)

Figure 6.10: Schematics of the simulated (a) single-barrier and (b) double-barrier actuators, illustrating the dimensions specified in table 6.1

	Single barrier		Double barrier	
	reduced-scale	full-scale	reduced-scale	full-scale
Domain width	2.0 mm	18 mm	2.0 mm	12 mm
Domain height	0.3 mm	1.5 mm	0.3 mm	2.0 mm
$\Delta x = \Delta y$	4 µm	7 µm	4 µm	7 µm
Δt_{max}	10^{-8} s	10^{-8} s	10^{-8} s	2×10^{-8} s
Δt_{min}	10^{-11} s	10^{-11} s	10^{-11} s	10^{-11} s
Absolute allowed error in ϕ	0.1 V	1.0 V	0.1 V	1.0 V
Relative allowed error in n	10^{-3}	10^{-3}	10^{-3}	10^{-3}
Voltage ramp rate	$\pm$50 V/µs	$\pm$150 V/µs	$\pm$100 V/µs	$\pm$200 V/µs
Diameter range	10–100 µm	0.1–1 mm	10–100 µm	0.1–1 mm
Grounded electrode thickness	10 µm	0.25 mm	50 µm	0.50 mm
Dielectric thickness	25 µm	0.25 mm	25 µm	0.25 mm
Electrode gap	0.1 mm	1.0 mm	0.2 mm	2.0 mm
Left edge separation	50 µm	1.0 mm	0.5 mm	1.5 mm

Table 6.1: Simulation parameters for reduced- and full-scale simulations

All simulation runs were conducted with linearly increasing or decreasing voltages applied to the exposed electrodes (for single-barrier systems) or the narrow electrodes (for double-barrier systems). The other electrode in each system was grounded. Linear voltage ramps were chosen to mimic the two half-cycles of the symmetric-triangle waveform used in the experimental measurements of chapters 4 and 5, and to allow comparisons to the simulations of other groups [e.g. 14]. The voltage ramp rates listed in table 6.1 were chosen to ensure that numerous discharge events occurred within a reasonable amount of computation time rather than to match experimental voltages. This resulted in absolute voltage levels larger those used in experimental measurements.

In addition to the single-barrier actuators with cylindrical exposed electrodes described above, we have also simulated a full-scale single-barrier device with a thin rectangular cross-section electrode. A schematic showing this actuator is presented in figure 6.11. With the exception of the

exposed electrode, all system parameters were identical to those in table 6.1 for the full-scale single-barrier actuators. The exposed electrode here was one grid cell thick and 1.5 mm long. The thickness was chosen to mimic the thin exposed electrodes used by Boeuf et al. [14] and Likhanskii et al. [87].

All simulations were run via the Condor batch queuing system [107] on idle Linux workstations in the University of Wisconsin's College of Engineering. Computation times for reduced-scale simulation runs examining 200 μs of simulated time required computation times on the order of one week. Full-scale runs encompassing 200–300 μs required from two to three months.

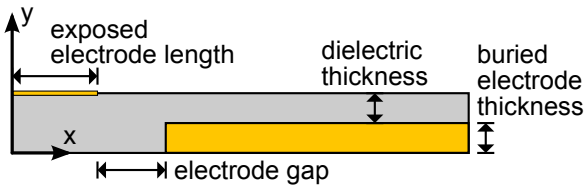

Figure 6.11: Schematic of the simulated single-barrier actuator with a thin rectangular cross-section exposed electrode

Chapter 7

Simulation Results

The two sets of simulation runs provided information about plasma density variations, induced forces, and discharge currents during the simulated time periods. In all simulated systems, the changing voltage lead to the appearance of short, intense microdischarge events when the plasma density increased sharply, separated by periods of lower plasma density and minimal discharge current. The character of these microdischarges is described in section 7.1. While the microdischarges themselves are similar in the reduced- and full-scale systems, the periods between these events change significantly between system scales, as discussed in section 7.2. Detailed data from the set of full-scale simulation runs are presented in section 7.3, while these data are compared to the experimental measurements of chapters 4 and 5 in section 7.4.

Prior to beginning the simulation runs described in this chapter, we performed benchmark tests using the same geometry and applied voltage as that used by Boeuf et al. [14]. The general behavior and induced force levels were quite similar between our runs and those in the literature for both positive- and negative-going voltages. Our simulation, however, produced slightly more microdischarge events with a positive-going voltage, and slightly more than half as many microdischarge events with a negative-going voltage, relative to the results of Boeuf et al. A likely cause of these discrepancies is the difference in the choice of the model for the ionization coefficient, which was specified in the reference [14]. Test runs performed while implementing the variable time-stepping algorithm in our code indicated that the time-step size, not specified in the reference, also had moderate effects on the repetition rate of microdischarges. In a system similar to the single-barrier reduced-scale geometries, lowering the average time-step size roughly an order of magnitude below 1 ns reduced the microdischarge repetition rate by approximately 10%

for positive-going voltages, but left the negative-going microdischarge rate roughly unchanged. Increasing the average time-step size by a factor of roughly 5 increased the repetition rate by approximately 25% for positive-going voltages and decreased it for negative-going voltage by approximately 25% for negative-going voltages.

7.1 Simulated Microdischarge Behavior

As the amplitude of the voltage applied to the exposed electrode increases, microdischarges form and eventually dissipate. An example of the resulting oscillation in the electron density was shown in figure 2.14. Microdischarge frequency and intensity, as well as the plasma evolution between microdischarges, change with geometric parameters as described in sections 7.2, 7.3.1, and 7.3.3. This section describes the qualitative features that are independent of the exact device geometry for both single- and double-barrier actuators. The reduced- and full-scale simulation runs exhibited qualitatively similar microdischarge behaviors. All data shown in this section come from the reduced-scale systems due to the relatively short computation times required to re-run those simulations and capture density data during microdischarge events.

7.1.1 Single-Barrier Actuators

The general characteristics of microdischarges in single-barrier systems with non-thin electrodes were similar to those described in section 2.5.2 for systems with thin electrodes. When the voltage of the exposed electrode was increasing relative to that of the buried electrode, we observed alternating corona-like phases and streamer-like microdischarges. In the corona-like phase, electrons attracted to the exposed electrode cause ionization, but the resulting plasma is not sufficiently dense to alter the background electric field. The action of the electric field on the positive ions in the plasma, however, can produce a significant induced force, as shown in figure 7.1.

When the applied voltage became large enough to support increased ionization, the plasma density increased enough to alter the background field, resulting in a streamer-like microdischarge like that pictured in figure 2.15. A more detailed picture of plasma evolution is given in figure 7.2. During this type of microdischarge, a tenuous plasma formed near the edge of the exposed

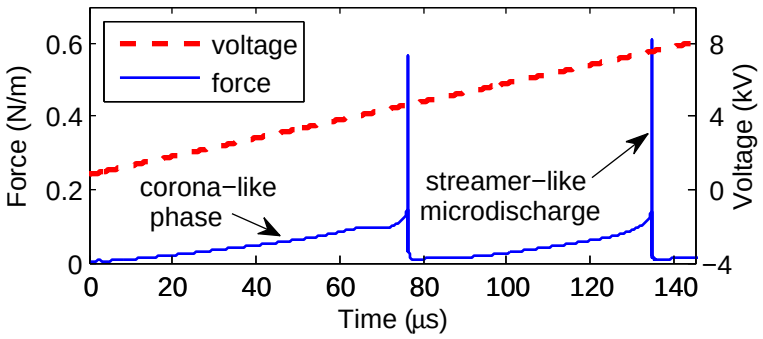

Figure 7.1: Force induced by a simulated reduced-scale single-barrier actuator with a 50 µm diameter exposed electrode. The voltage applied to the exposed electrode was positive-going, and is also shown.

electrode. This is the corona-like phase. The plasma increased in density and arched over the previously-charged region of the dielectric surface, reached the uncharged region of the surface, and began propagating away from the exposed electrode. The propagation ceased either when the electric field was no longer sufficient to sustain the dense plasma region, or when it ran into the edge of the simulation domain. Since the majority of the induced force occurred during the corona-like phase, we do not expect that prematurely-stopped streamers will have a significant effect on the time-averaged forces discussed in section 7.3.

When the voltage of the exposed electrode was decreasing relative to that of the buried electrode, we observed negative microdischarges similar to the one pictured in figure 2.16. The plasma evolution during this type of microdischarge is shown in figure 7.3. Initially a region of dense plasma formed near the exposed electrode edge. The electric field pushed electrons out of this region and towards the dielectric surface, ionizing neutrals on their way and charging the surface negatively. The next electrons moving through are then not be attracted to the negatively-charged part of the dielectric, and moved to a point farther away. The ionization and charging lead to a narrow sliver of plasma that expanded along the surface of the dielectric. It expanded at a rate much faster than the propagation of the streamer-like microdischarges (note the differing time scales in figures 7.2(a) and 7.3(a)). This thin plasma column appearred as positively-charged because the electrons were quickly lost to the surface. Throughout the process, the densest region of plasma remained next to the exposed electrode.

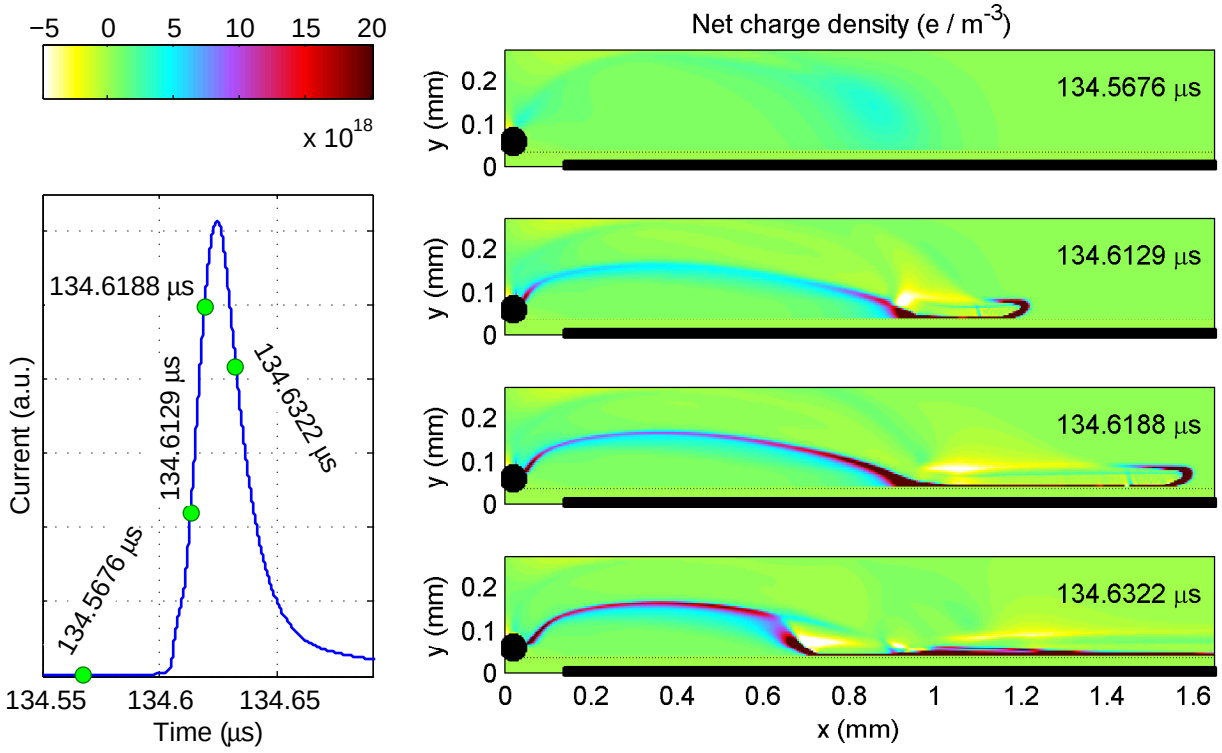

(a) (b)

Figure 7.2: Simulated (a) discharge current and (b) plasma evolution during a streamer-like microdischarge for a reduced-scale single-barrier actuator with a positive-going voltage applied to the 50 µm diameter exposed electrode. The dielectric surface is noted by a dotted line, and the two electrodes are shown in black.

7.1.2 Double-Barrier Actuators

As with the single-barrier actuator simulations, in the double-barrier geometry some general features of the microdischarges were similar in both reduced- and full-scale systems. The microdischarges in double-barrier systems share features with both the streamer-like and negative microdischarges seen in simulated single-barrier systems, described in section 7.1.1. We did not observe any equivalent to the corona-like plasma in double-barrier actuators.

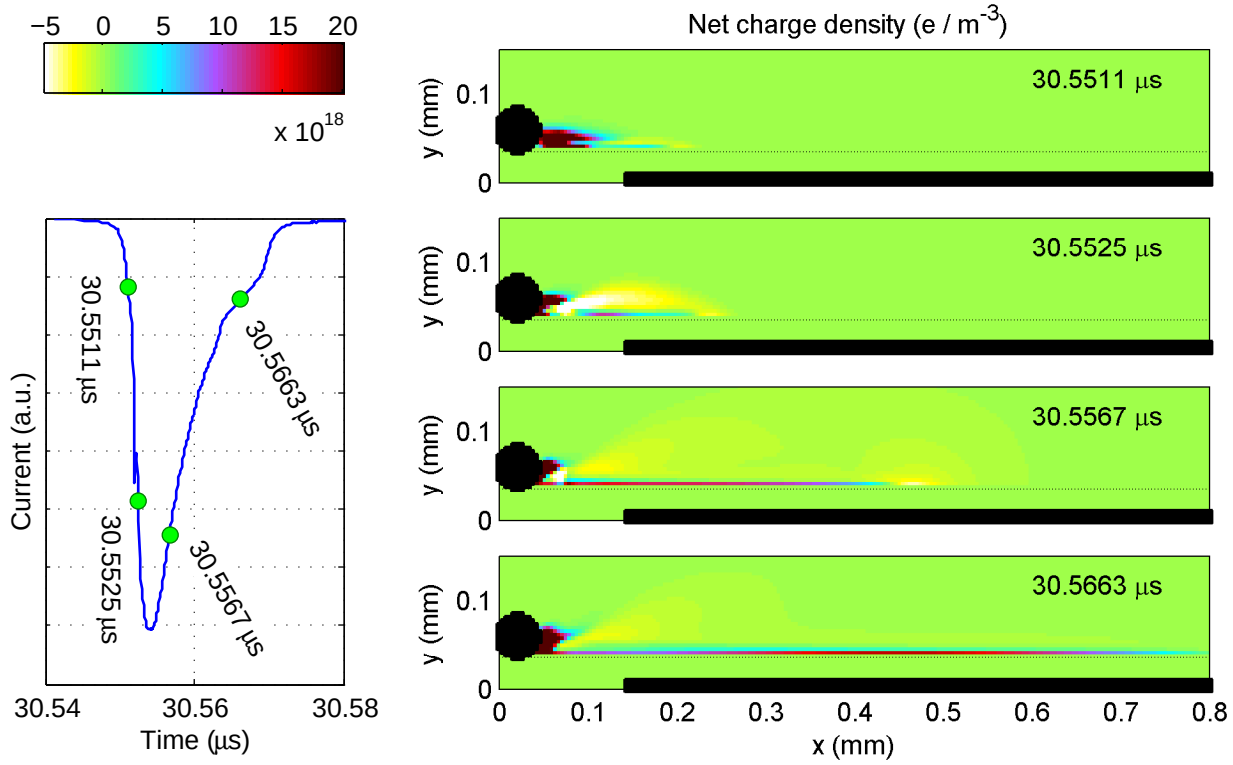

(a) (b)

Figure 7.3: Simulated (a) discharge current and (b) plasma evolution during a negative microdischarge for a reduced-scale single-barrier actuator with a negative-going voltage applied to the 50 µm diameter exposed electrode. The dielectric surface is noted by a dotted line, and the two electrodes are shown in black.

Figure 7.4 shows the plasma evolution in a microdischarge with a positive-going voltage applied to the narrow electrode. Plasma initially formed above the narrow electrode due to electron-impact ionization in the strong electric field there. The charging of the dielectric surface by electrons moved the region of strongest electric field towards the wide electrode. The dense plasma moved in this direction, arching over the electrode gap and propagating along the dielectric surface. This propagating region was essentially identical to the streamer-like microdischarges seen in single-barrier actuators. For the voltages tested here, the length of this microdischarge was always shorter in double-barrier systems. While the streamer-like structure formed and propagates, a weak, thin channel of plasma expanded near the dielectric surface in the opposite direction (left

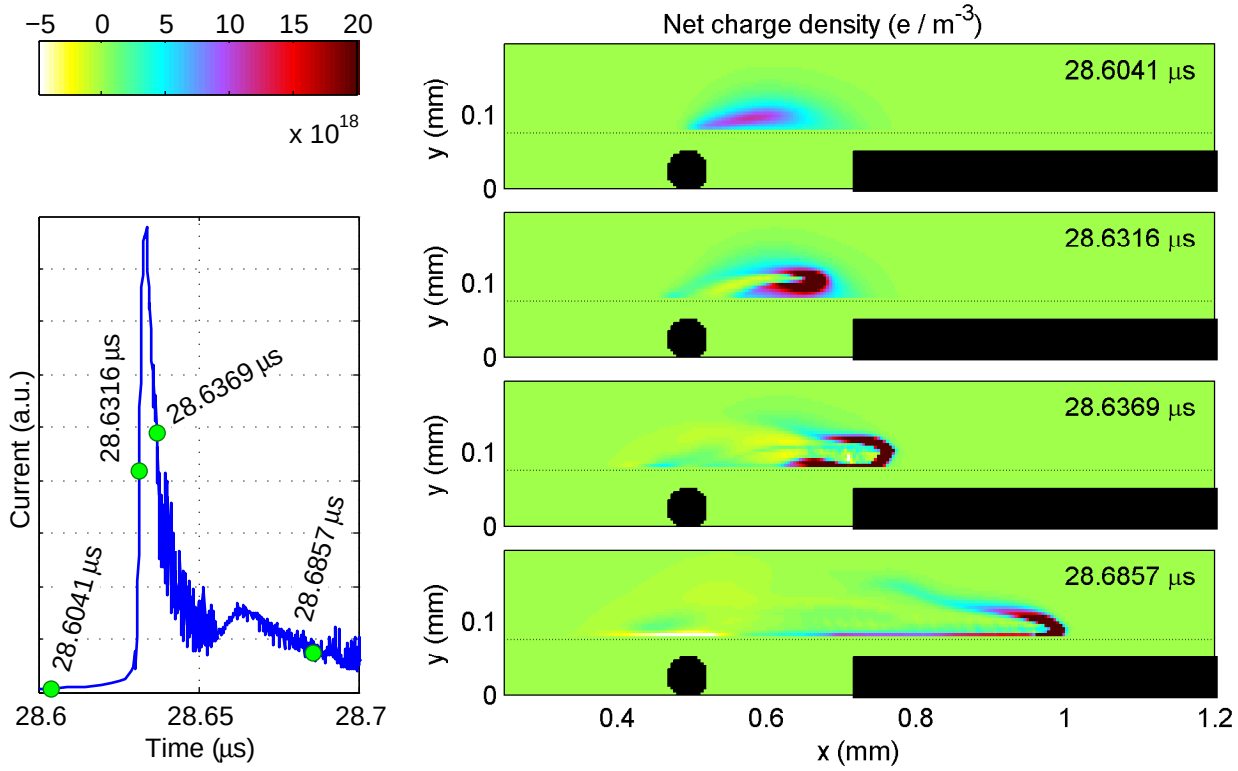

(a) (b)

Figure 7.4: Simulated (a) discharge current and (b) plasma evolution during a microdischarge event in a reduced-scale double-barrier actuator with a positive-going voltage applied to the 50 µm narrow electrode. The dielectric surface is noted by a dotted line, and the two electrodes are shown in black.

in figure 7.4). Its characteristics were similar to those of the negative microdischarge of figure 7.3, although its progress was halted once it reached the far edge of the narrow electrode.

With a negative-going voltage applied to the narrow electrode, the microdischarges were similar to those a positive-going voltage except that they were "flipped" left to right. This type of microdischarge is shown in figure 7.5. The plasma initially formed above the edge of the wide electrode closest to the narrow electrode. A streamer-like plasma arched over the electrode gap, reached the dielectric surface, and propagated until it reached the far edge of narrow electrode. At this point, it began to weaken rapidly as the electric field strength drops off quickly. As this was happening, a thin plasma channel formed over the wide electrode, similar to the negative microdischarge pictured in figure 7.3(b) although significantly less dense.

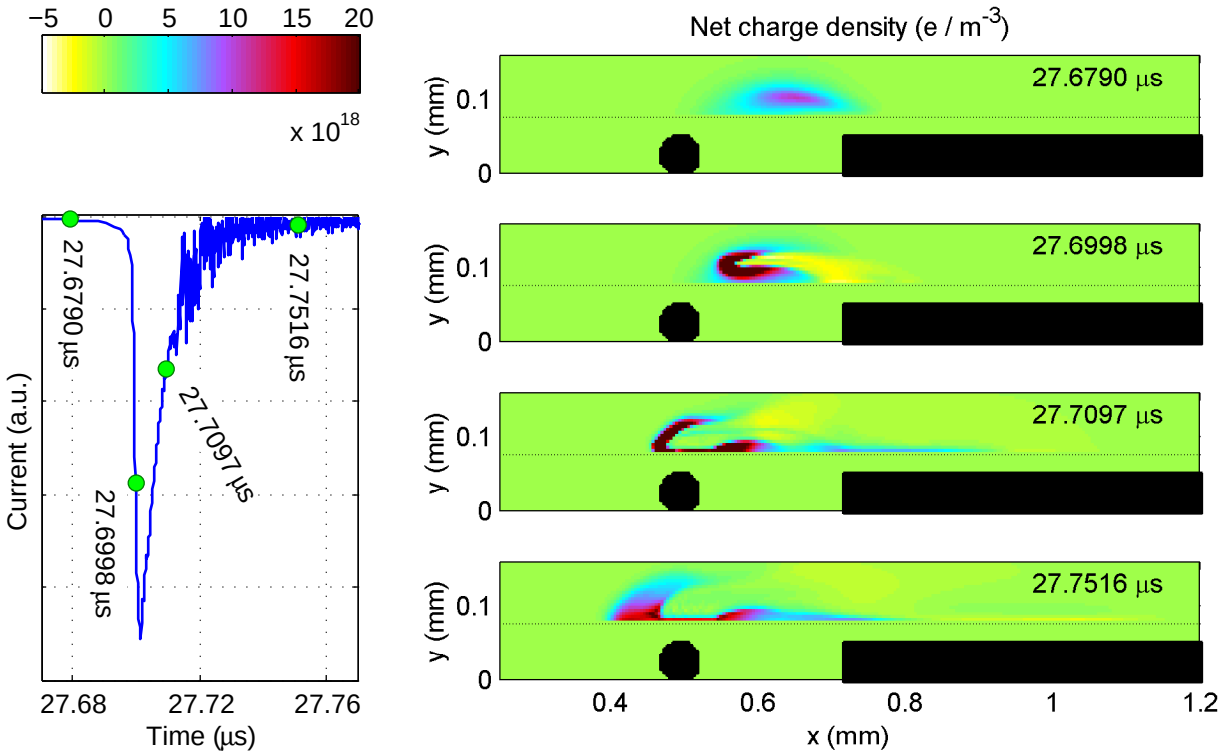

Figure 7.5: Simulated (a) discharge current and (b) plasma evolution during a microdischarge event in a reduced-scale double-barrier actuator with a negative-going voltage applied to the 50 µm narrow electrode. The dielectric surface is noted by a dotted line, and the two electrodes are shown in black.

7.2 Effects of System Scale

Simulations of full-scale single-barrier actuators indicated that the behavior when a positive-going ramp voltage was applied to the exposed electrode was largely the same as has been previously observed for smaller scale discharges [14, 87]. Several sharp spikes in the force parallel to the dielectric surface appeared, corresponding to streamer-like microdischarge events, but the majority of the time-averaged force occurred between these events during the corona-like phases [14], previously noted in figure 7.1. These phases, identified by the regions of steadily increasing force between microdischarge events, were observed in both reduced- and full-scale systems, as shown in figure 7.6(a). The most notable qualitative difference between the two systems was that in the

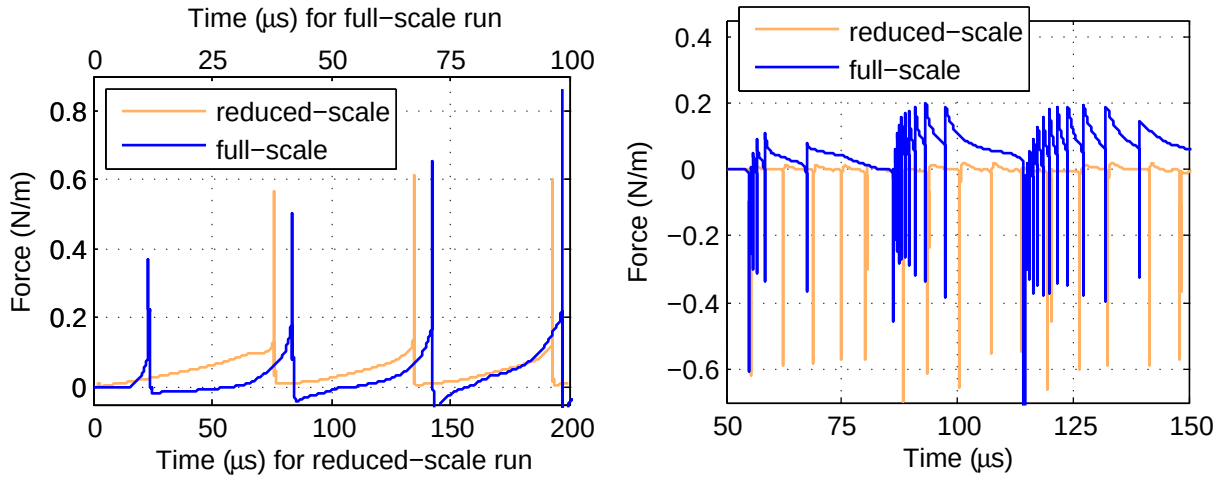

(a) (b)

Figure 7.6: Forces induced by simulated reduced- and full-scale single-barrier actuators with (a) positive-going and (b) negative-going voltages. The reduced- and full-scale systems had exposed electrode diameters of 50 μm and 0.5 mm, respectively.

full-scale systems, following a streamer-like microdischarge, the force briefly became negative ($-x$ direction in figure 6.10) before returning to the corona-like phase.

When negative-going ramp voltages were applied to the exposed electrodes of single-barrier discharges, the behaviors of the reduced- and full-scale systems differed strongly. Both systems exhibited relatively frequent pulses of negative force corresponding to microdischarges, but these pulses in the full-scale system tended to be grouped in time as shown in figure 7.6(b). While in both systems the induced force became positive immediately following each pulse, in the full-scale systems this effect was much more pronounced. Other groups have pointed to the buildup of negative-ion density as the cause of this positive force [87, 90]. This buildup is verified by the data in figure 7.7, which show the increase in the average negative-ion density over the entire simulated period for the full-scale system, but a stable average value (after several microdischarges) for the reduced-scale system. We also note that the decay rate for the negative-ion density was much smaller in the full-scale system.

In double-barrier systems with positive-going voltages applied to the narrow electrodes, the full-scale actuator systems behaved similarly to the reduced-scale ones, as shown in figure 7.8(a).

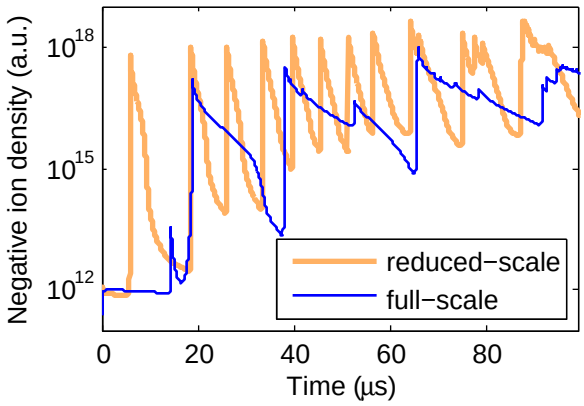

Figure 7.7: Spatially-averaged negative ion densities for negative-going voltages applied to simulated single-barrier actuators. The reduced- and full-scale systems used exposed electrode diameters of 25 μm and 0.25 mm, respectively.

The x-directed force in both cases rose quickly during microdischarges then decayed at a slightly slower rate. The majority of the time-integrated force occurred during this decay period. In full-scale systems after the force decayed they sometimes became briefly negative due to the production of a significant negative ion population during the discharge event. In between microdischarges the forces were negligible.

In contrast, with negative-going applied voltages in the double-barrier geometry, the behavior of the induced forces changed significantly when the dimensions of the simulated system increase, as shown in figure 7.8(b). In both systems the force exhibited a negative spike during a microdischarge event, but in the full-scale system the force became positive for a significant fraction of the time in between microdischarges. This period of positive force indicates that, like in single-barrier systems, a cloud of ions are generated that persist long after an intense microdischarge event. This explanation is verified by examining the negative ion densities in the two systems, shown in figure 7.9. In the full-scale system the negative-ion density decayed much more slowly than in the reduced-scale system. The ratio of peak to minimum negative ion density (after several microdischarges) was also smaller in the full-scale system. The electric field "pushing" the larger negative-ion densities present in the full-scale system between discharge events explains the positive forces seen for the negative-going voltage in figure 7.8(b).

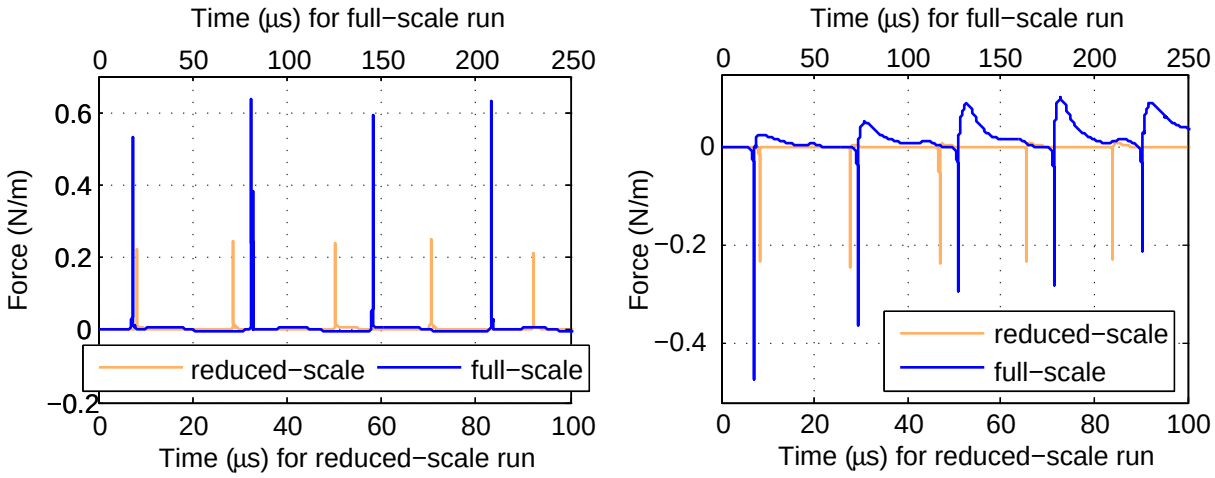

Figure 7.8: Forces induced by simulated reduced- and full-scale double-barrier actuators with (a) positive-going and (b) negative-going voltages. The reduced- and full-scale systems had narrow electrode diameters of 50 μm and 0.5 mm, respectively.

In both single- and double-barrier actuator simulations we observed much more rapid decay in the negative ion populations in reduced-scale systems relative to full-scale systems, shown in figures 7.7 and 7.9. The rates of both positive- and negative-ion decay were more rapid in reduced-scale systems regardless of the applied voltage. The lower plasma decay rates in full-scale systems likely explains the significant forces seen immediately following microdischarges.

For runs with negative-going applied voltages, the positions of maximum negative-ion density were, on average, significantly farther above the dielectric in full-scale systems. This suggests that the ion cloud that forms with a linearly-decreasing voltage is significantly thinner (in the vertical dimension) in reduced-scale systems. Whether this is due to the different electrode geometry itself or simply that the cloud is constrained by the smaller simulation domain size is not yet clear. A thinner cloud, however, means that on average the negative ions are closer to the dielectric surface. In the case of a negative-going applied voltage they would be attracted to the surface and quickly lost from the system, with this process occurring more quickly the closer the negative ions are to the surface. We hypothesize that this collection by the dielectric surface is the dominant loss

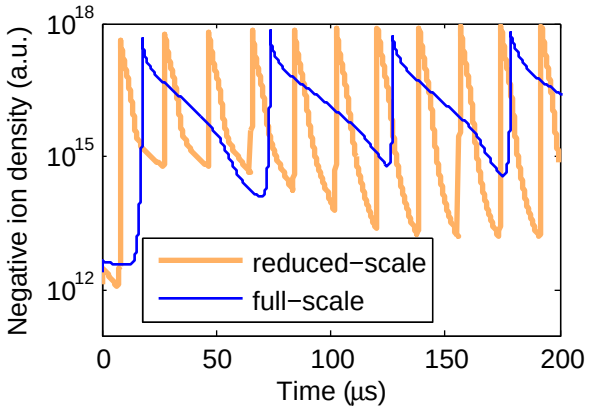

Figure 7.9: Spatially-averaged negative ion densities for negative-going voltages applied to simulated double-barrier actuators. The reduced- and full-scale systems used narrow electrode diameters of 50 μm and 0.50 mm, respectively.

mechanism in reduced-scale systems. The only other negative-ion loss mechanism in the model is positive ion-negative ion recombination, which should be similar in the two systems.

With positive-going applied voltages, the plasma column formed at approximately the same thicknesses in both reduced- and full-scale systems. Positive ions may be lost to the dielectric surface, but negative ions are often born far from the exposed electrode or above the narrow electrode. Consequently, positive ion-negative ion recombination will likely be the dominant loss mechanism for negative ions in these runs. While the decay rates for negative-ion densities were still faster for the reduced-scale systems, possibly due to locally higher densities, the difference was not nearly as strong as when comparing negative-going runs.

7.3 Full-Scale Simulations

As described in section 6.4, the full-scale simulations examined plasma actuator systems with dimensions nearly identical to those of the devices studied experimentally. As in chapter 4, we separate the results based on the shape and location of the high voltage electrode. We consider single-barrier systems with cylindrical exposed electrodes, single-barrier systems with thin rectangular electrodes, and double-barrier systems in their own sections below.

7.3.1 Single-Barrier Actuators with Circular Exposed Electrodes

Our experimental measurements showed that single-barrier actuators with short, thin exposed electrodes induced greater forces. This type of electrode was simplest to obtain by using thin cylindrical wires. Consequently we have focused our two-dimensional simulations on examining single-barrier discharges which used circular exposed electrodes of various diameters.

For the case of a linearly-increasing applied voltage, the primary differences between the forces induced by the different actuators occurred during the corona-like phase. The force induced during this phase was significantly larger for devices with smaller diameter exposed electrodes, as shown in figure 7.10(a). In addition, the periods of negative force immediately following each microdischarge were shorter for actuators with smaller electrodes. We did not observe any strong trend in the positive microdischarge repetition rate as the electrode diameter changed.

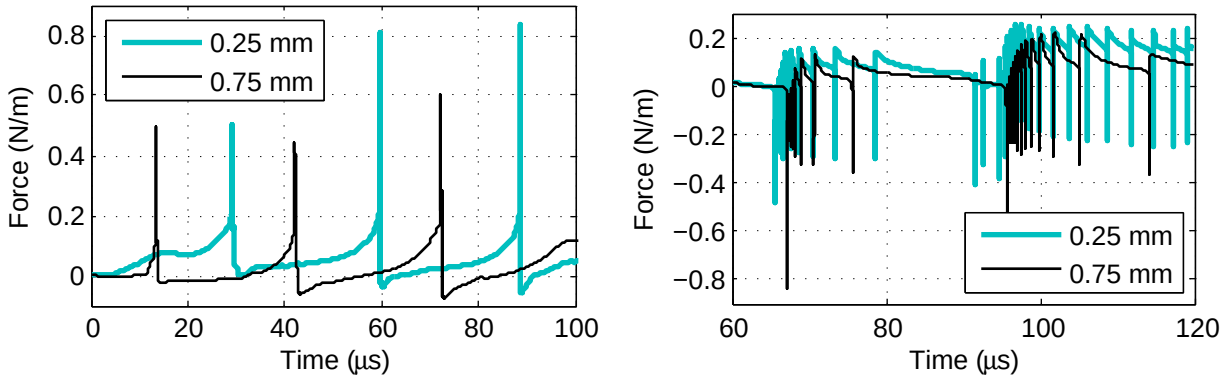

(a) (b)

Figure 7.10: Forces for simulated single-barrier actuators with the indicated exposed electrode diameters for (a) positive-going applied voltages and (b) negative-going applied voltages

Simulations with negative-going applied voltages also showed quantitative and qualitative dependencies on the exposed electrode diameter. Both the average rate at which microdischarges occurred and the level of induced force in between these events dropped markedly as the exposed electrode diameter increased. The discharge events, corresponding to oscillations in the electron density, are shown for two actuators in figure 7.11. While both devices exhibited rapid discharges

at certain times, the actuators with larger exposed electrodes also experienced long periods of inactivity. These inactive periods allowed the plasma to decay to relatively low densities, as shown in figure 7.11, reducing the induced force. While the first microdischarge immediately following an inactive period was stronger (in the sense of higher plasma density) than other microdischarges, over time this did not compensate for the loss of induced force during the inactive periods. The fraction of time spent in inactive periods increased as the exposed electrode diameter increased, although the exact mechanism for this effect is still unknown.

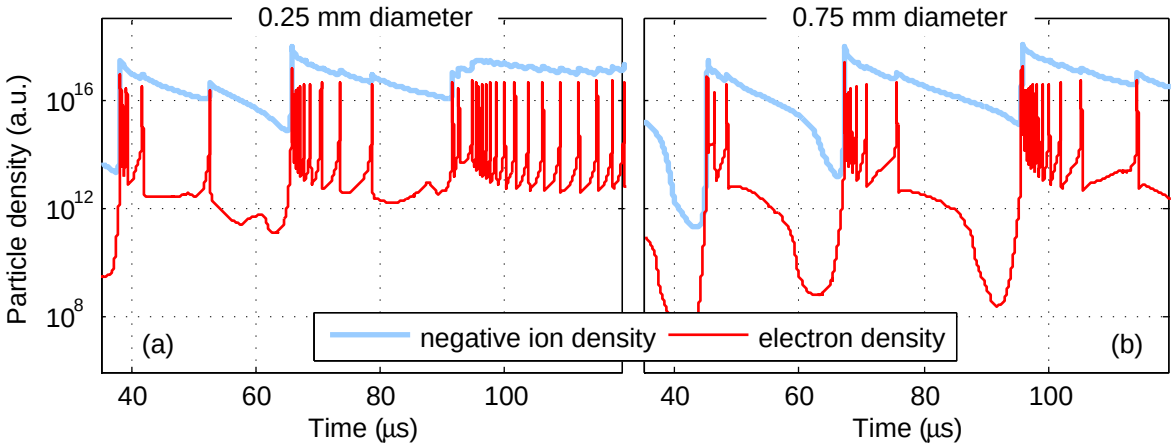

Figure 7.11: Charged-particle densities near simulated single-barrier actuators with negative-going voltages applied to exposed electrodes (a) 0.25 mm in diameter and (b) 0.75 mm in diameter. Positive ion densities were nearly identical to the negative ion densities in all cases.

As described in section 6.4, we ran single-barrier simulations with the applied voltage changing at rates of ± 150 V/μs. When a positive-going voltage was applied to the exposed electrode, we began the simulation runs at $+3.0$ kV, well below the level needed to induce a microdischarge. With negative-going voltages, however, -3.0 kV was large enough to immediately generate a strong, non-physical microdischarge. To remove this effect, the simulations with negative-going voltages were started at -1.5 kV.

The time-averaged forces that resulted from these runs are shown in figure 7.12. The time-averaged forces for all simulated devices increased throughout the simulated time, with the rates

of growth being particularly strong for negative-going applied voltages. Boeuf et al. [93] previously noted that domain widths shorter than the plasma length caused the time-averaged forces for negative-going voltages to reach a steady value. Since we observed increasing forces, as in figure 7.12(b), we conclude that the domain was wide enough to not influence plasma evolution.

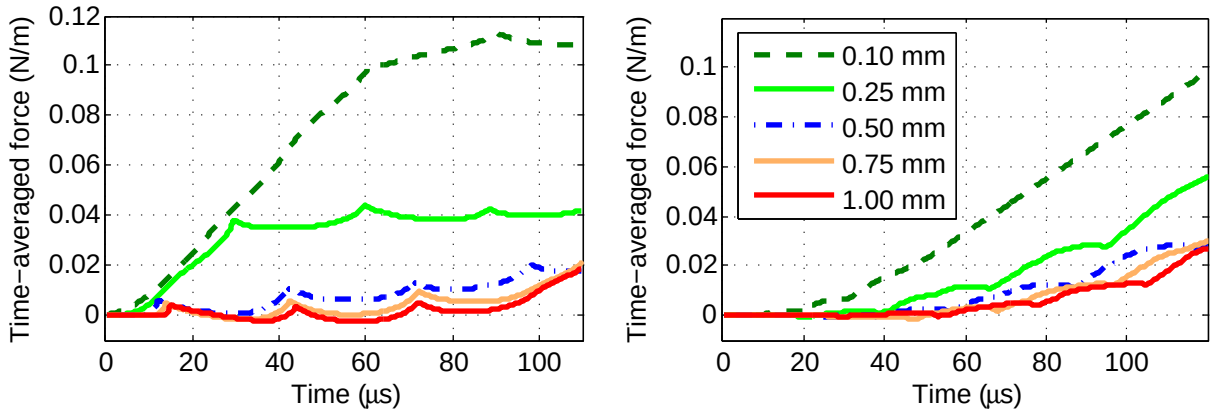

(a) (b)

Figure 7.12: Time-averaged forces (averaged from time 0 to time t) for full-scale single-barrier simulations using (a) positive-going voltages and (b) negative-going voltages. Both plots use the legend in plot (b).

By making two reasonable assumptions, we can consider a positive-going run and a negative-going run taken together as one full cycle of an applied symmetric triangle waveform. First, since the runs were conducted separately, we must assume that the plasma from one half cycle has almost completely decayed by the beginning of the next half cycle. If this is the case, there will be essentially no interaction between the half cycles except via charge deposition on the dielectric surface. Second, we assume that the most important parameter in determining the electric field in the gas region is the voltage drop between the exposed electrode and the dielectric surface, rather than the voltage drop between the two electrodes. If the second assumption is valid, a system with -5 kV applied to the exposed electrode and charge deposited on the dielectric such that the surface potential is -5 kV is essentially identical to a system with 0 V applied to the exposed electrode and no charge on the dielectric surface. This assumption allows us to treat the runs as half cycles even though all run voltages start near 0 V and either increase or decrease.

Applying these assumptions, we take a 110 μs-long positive-going run and a 120 μs-long negative-going run together as a full cycle. The equivalent applied voltage signal would be a 9.8 kV amplitude symmetric triangle wave oscillating at 3.8 kHz. Both the amplitude and the frequency are somewhat larger than the values we tested experimentally, due to our desire to shorten computation times. Simulating systems with voltages similar to those in the experiments would have required significantly increased computation times.

Using combined positive- and negative-going simulation runs as an effective voltage cycle, we estimated time-averaged forces for each actuator design. We did this by integrating the EHD force during each simulation run and dividing by the effective simulated time. We assumed that prior to each simulated time period there was a ramp from 0 V to the starting voltage during which no significant momentum transfer occurred. The resulting cycle-averaged forces are shown in figure 7.13. The time-averaged forces for both positive- and negative-going voltages increased sharply at diameters below 0.5 mm for the reasons described above. The forces for both positive- and negative-going applied voltages were similar for all tested actuators.

In the full-scale simulations, we note that the dominant sources of the induced forces were during the build-up period prior to a microdischarge for a positive-going voltage, or during the decay phases following microdischarges for negative-going voltages. Due to their extremely short

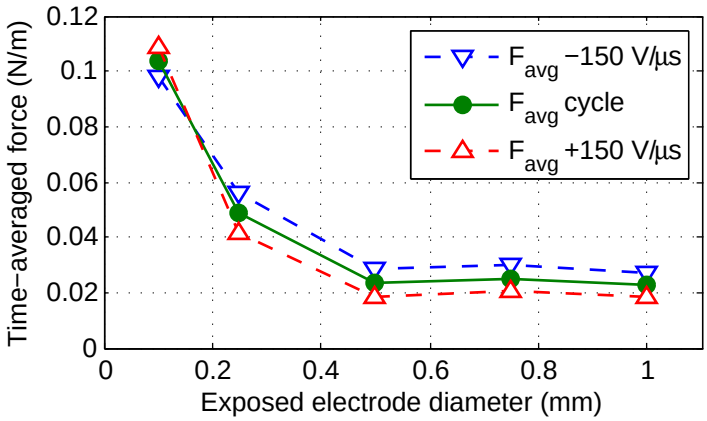

Figure 7.13: Cycle-averaged forces induced by simulated single-barrier actuator with cylindrical exposed electrodes. Results are shown for the positive-going half cycle, the negative-going half cycle, and the entire cycle for the effective voltage described in the text.

duration, the microdischarges themselves directly contributed little to the time-averaged forces. Their importance to the system is to either provide a seed plasma for the next corona-like phase (with a positive-going voltage) or to increase the plasma density prior to a decay phase (for a negative-going voltage).

Since the choice of effective voltage amplitude and frequency was essentially arbitrary, we consider the results of other choices by examining figure 7.12. We can estimate averaged forces for effective voltages of higher frequencies and smaller amplitudes by examining the values of the time-averaged forces at times prior to the ends of the simulation. We conclude that while the exact values of the time-averaged force vary slightly with the chosen time, the general conclusion of increasing force with decreasing exposed electrode holds at all observed times for the chosen voltage ramp rate.

7.3.2 Single-Barrier Actuators with Thin Rectangular Exposed Electrodes

As described in section 2.5, many other groups have modeled single-barrier actuators using rectangular-cross section exposed electrodes with thicknesses of a single spatial step size. Here we compare our full-scale single-barrier simulation runs using a circular cross-section exposed electrode with a 0.10 mm to runs using a rectangular exposed electrode. The rectangular electrode geometry was depicted in figure 6.11.

The actuator with the thin rectangular exposed electrode behaved quite similarly to the actuator with the smallest examined circular electrode diameter. The forces for positive- and negative-going voltages are shown in figures 7.14(a) and 7.14(b). With a positive-going voltage, the actuator with a rectangular electrode induced comparable forces during the corona-like phase to the actuator with a 0.10 mm diameter circular electrode. The rate at which streamer-like microdischarges occur, however, is approximately the same in the two systems.

With a negative-going voltage, the actuator with a rectangular electrode excited more frequent microdischarges than did the actuator with a circular electrode, as seen in figure 7.14(b). The device with the rectangular electrode also had no long inactive periods, unlike our simulations of actuators with relatively thick exposed electrodes. These behaviors follow the same trend as

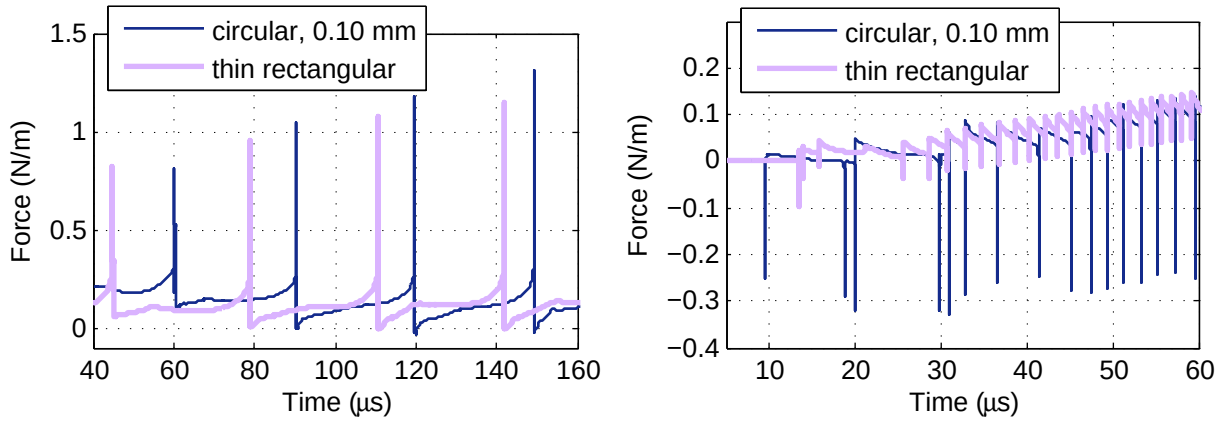

(a) (b)

Figure 7.14: Comparison of the forces for simulated single-barrier actuators with rectangular- and circular-cross section exposed electrodes. Results are shown for (a) positive-going and (b) negative-going applied voltages.

observed for various diameter circular electrodes in section 7.3.1, where actuators with thinner exposed electrodes excited more frequent microdischarges and had shorter periods of inactivity. The rectangular electrode is effectively 7 μm thick. The rapid microdischarges lead to relatively large time-averaged plasma densities, which in turn contributed to the increasing force in figure 7.14(b). This force behavior is qualitatively the same as that observed by Boeuf et al. [93] for a similar geometry.

7.3.3 Double-Barrier Actuators

Double-barrier DBDs with the geometry shown in figure 6.1(b) also induced forces in the positive-x direction when both positive- and negative-going voltages were applied to the narrow electrodes. Compared to the single-barrier geometry, however, runs simulating double-barrier systems changed relatively little as the high voltage electrode diameter varied. The forces induced during runs with positive- and negative-going applied voltages are shown in figure 7.15 for two narrow electrode diameters. For all simulation runs, the peak levels of induced force are comparable to those seen for single-barrier systems, but the average levels were an order of magnitude smaller due to lower microdischarge repetition rates.

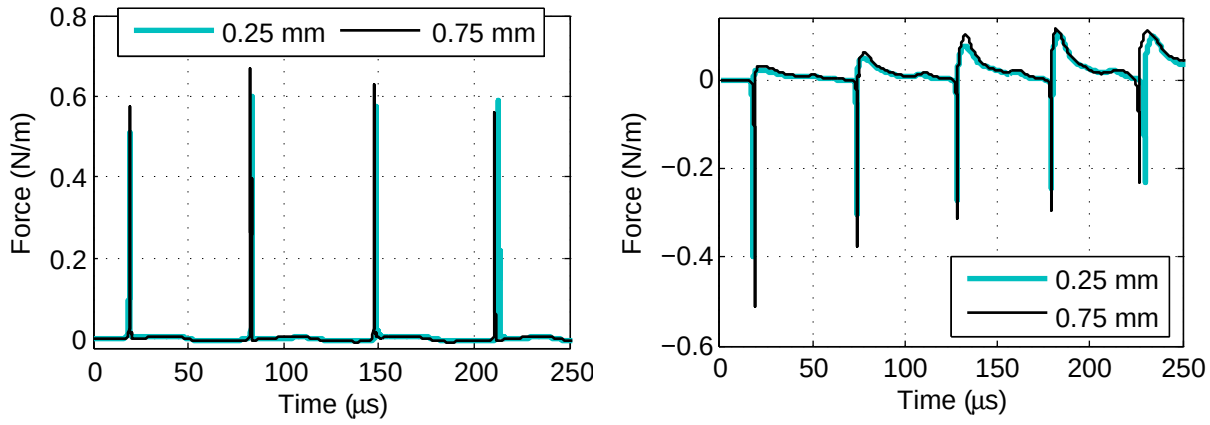

(a) (b)

Figure 7.15: Forces for simulated double-barrier actuators with the indicated narrow electrode diameters for (a) positive-going applied voltages and (b) negative-going applied voltages

With a positive-going applied voltage, neither the microdischarge frequency or intensity change significantly as the narrow electrode size was increased. Indeed, as shown in figure 7.15(a), not even the timing of microdischarge occurrence varied with narrow electrode diameter. The only systematic change in the behavior of the induced force was in a short, weak negative force immediately following microdischarge events. This force became more negative as the narrow electrode diameter increased.

In runs applying negative-going voltages, we also saw relatively little change in plasma behavior with the size of the narrow electrodes. As shown in figure 7.15(b), the peak positive force immediately following a microdischarge increased slowly with increasing narrow electrode diameter. These larger peaks appear to be associated with the generation of higher average plasma densities during negative microdischarges in systems with larger narrow electrodes.

When integrated over several microdischarges, these small variations did have some effects on the time-averaged forces. These time-averaged forces are shown in figure 7.16 as functions of the simulated time. Due to the significant positive forces exerted during the decay periods immediately following microdischarges during negative-going runs, the time-averaged forces for negative-going voltages were nearly an order of magnitude larger than those for positive-going

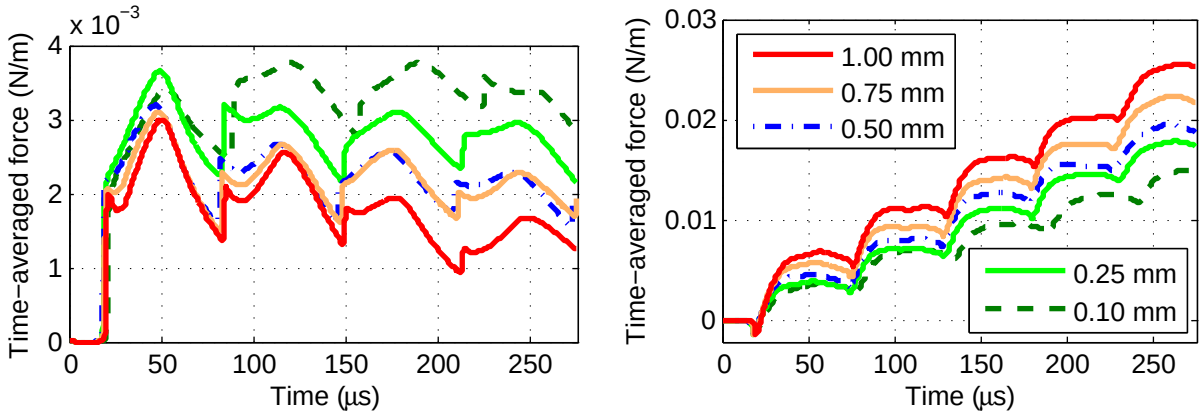

(a) (b)

Figure 7.16: Time-averaged forces (averaged from time 0 to time t) for full-scale double-barrier simulations using (a) positive-going voltages and (b) negative-going voltages. Both plots use the legend in plot (b).

runs. As in the single-barrier simulations, with a negative-going voltage the time-averaged force increased throughout the simulated time period, as shown in figure 7.16(b).

By making assumptions similar to those described in section 7.3.1, we can treat the combination of a positive-going run and a negative-going run as a full cycle of a symmetric triangle voltage waveform. We used 275 µs-long runs for both positive- and negative-going voltages. The runs used starting voltages of ± 6 kV. As in the analysis of single-barrier simulation results, we assume a time period prior to each run in which the voltage moves from 0 V to the starting voltage and no significant force exists. Positive- and negative-going runs may then be considered together as simulating one cycle of a 1.6 kHz symmetric triangle waveform with an amplitude of 30.5 kV. The resulting time-averaged forces are shown in figure 7.17. Considering the results of figure 7.16, the exact choice of simulated time did not effect the resulting trends, as the differences between the forces induced by different geometries remained consistent throughout the simulated time period. As with the single-barrier data, we have only considered a single magnitude for the voltage rate of change.

In general, the cycle-averaged forces increased slowly as the narrow electrode diameter increased. This trend is, in one sense, the opposite of that observed in the single-barrier simulation

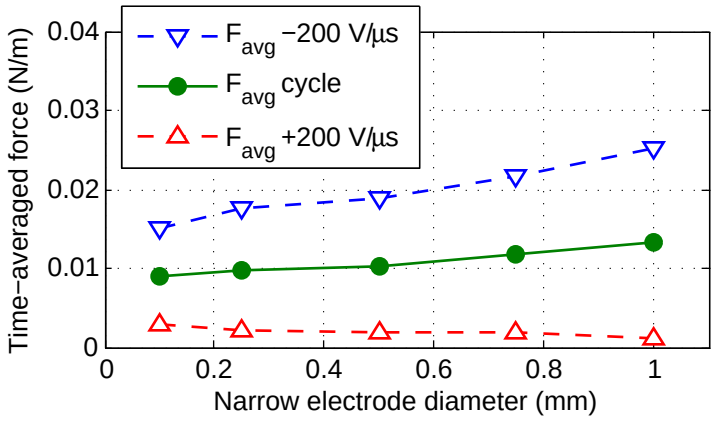

Figure 7.17: Cycle-averaged forces induced by simulated double-barrier actuator with cylindrical narrow electrodes. Results are shown for the positive-going half cycle, the negative-going half cycle, and the entire cycle for the effective voltage described in the text.

runs. As we reduce the diameter of the high voltage electrodes in both cases, in the absence of plasma the electric fields near these electrodes increase. The insulation of this electrode in the double-barrier system, however, clearly leads to significantly different consequences of this increased field strength.

The cycle-averaged forces for our double-barrier simulations showed significantly less variation with electrode diameter than did the single-barrier simulations. The cycle-averaged forces for the double-barrier runs decreased by about 50% as the narrow electrode diameter was decreased from 0.1 to 1.0 mm. In comparison, the cycle-averaged forces for single-barrier simulations increased by 350% as the exposed electrode diameter was decreased through the same size range.

7.4 Comparisons to Experimental Results

Except in ideal circumstances, making comparisons between computational models and experimental results requires caution. In our situation, we do not expect the results of the simulations to quantitatively match the experiments due to the simplifications required to improve computational efficiency, but of limited physical validity. In particular, the code models two-dimensional systems, despite the obviously three-dimensional nature of the microdischarges shown in chapter 5, and employs a highly simplified plasma chemistry. In addition, empirical data for secondary

electron emission coefficients were not available for the relevant ion species, energies, and materials, forcing us to choose relatively arbitrary values. While inaccuracies in these coefficients may not strongly affect the total induced forces, they may change the intensities of the microdischarges [92], and therefore the microdischarge structure. To reduce computation times, we have also used larger voltage rates-of-change than were present in the experimental measurements.

Despite these caveats, we believe it is important to make connections between the computational model and the experiments in order to suggest possible directions for future development in both areas. To date, only very few of these comparisons have been made by other groups [72, 93]. Due to the noted differences between the simulations and the experimental system, we restrict ourselves to making mostly qualitative comparisons. We focus on the observed microdischarge structures in sections 7.4.1 and 7.4.2, and the trends of time-averaged force with changing electrode dimensions in section 7.4.3.

In all of the simulation runs, some general features of the experiments were reproduced. As the voltage in each run increased or decreased, we observed repeated microdischarge events. Each of these microdischarges corresponded to a spike in the simulated discharge current, as observed in the experiments. In addition, all of the simulations predicted a time-averaged force in the $+x$ direction, the same direction as measured experimentally using the electron balance and stagnation probe techniques. We focus on more detailed similarities and differences below.

7.4.1 Single-Barrier Microdischarge Structures

The simulation runs provided information about the distributions of charged-particle densities. The ICCD imaging, in contrast, recorded light emission from both neutral and charged particles that became excited due to collisions with charged particles. In making comparisons, then, we must assume that the emitted light is roughly proportional to the number of collisions, which in turn is roughly proportional to the plasma density. We discussed this assumption in more detail in section 3.3.2. The camera experiments viewed the actuator from above; they imaged the x-z plane as shown in figures 3.10 and 3.11. The simulations modeled the x-y plane, and assumed the system to be uniform in the z direction. Consequently, in both this section and in section 7.4.2 we

focus on plasma variations in the x direction, which is along the dielectric surface moving away from the edge of the exposed or narrow electrode. Similar comparisons between instantaneous plasma structure and ICCD images have been made by Orlov et al. [72]. Here we also discuss the observed microdischarge lengths, plasma regimes, and microdischarge durations. As in section 7.1, the figures in this section and section 7.4.2 use data from the reduced-scale simulation runs due to the relative difficulty in recording plasma density distributions at specific times during a microdischarge in the full-scale runs.

The single-barrier simulations reproduced many features of the microdischarges seen experimentally with ICCD imaging. With a positive-going applied voltage, a short, dense region of plasma formed near the exposed electrode and propagated down the dielectric surface. This process has been called a streamer-like microdischarge, and was described in more detail in section 7.1.1. The plasma during such a microdischarge is shown for a reduced-scale system in figure 7.18(a). The 'e' and 'b' notations in both figures 7.18(a) and 7.18(b) correspond to the exposed and buried electrode locations. We also observed the same general behavior experimentally in filamentary microdischarges, as shown in a 15 ns gate width image in figure 7.18(b) and described in section 5.2.3. The reduced-scale simulations also captured the existence of a significant region of dense plasma immediately adjacent to the exposed electrode, as seen in both figures 7.18(a) and 7.18(b).

In full-scale simulation runs, using the position of maximum plasma density diagnostic described in section 6.3, we determined that the streamer-like microdischarges extended essentially to the edge of the simulation domain. This is approximately equivalent to 17 mm from the exposed electrode edge. Typical experimentally-observed filaments such as those in figures 5.1 and 5.6(b) extended from 5 to 7 mm. We believe the differences in microdischarge lengths are due to two factors. First, the simulations used larger applied voltages than did the experiments. The imaging experiments of section 5.2.1 demonstrated increases in length as the applied voltage rose, so we expect that at voltages as large as those in the simulation runs we would observe longer filaments. Second, the imaged filaments are not straight, but rather jagged. The total path length

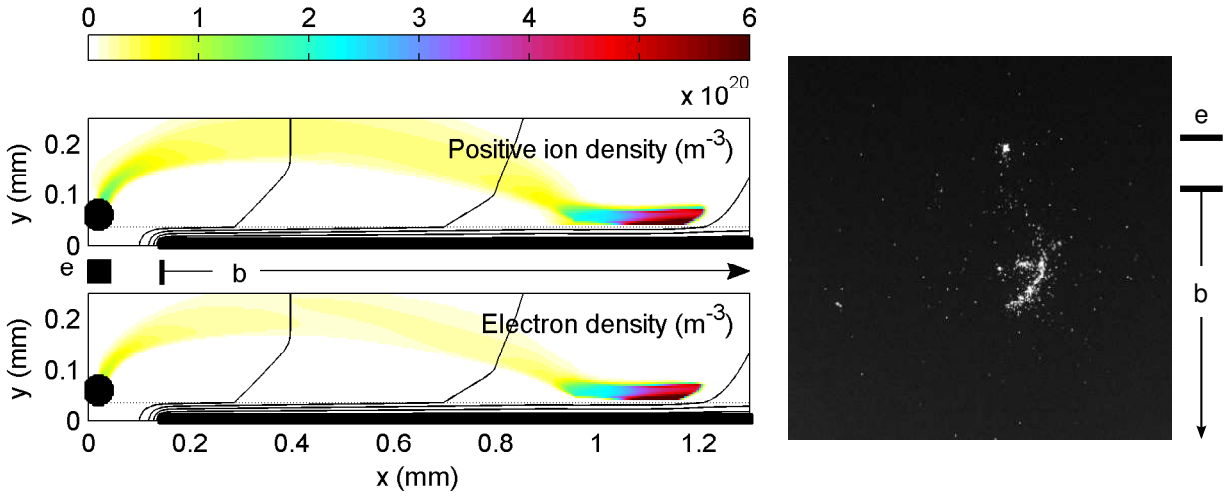

(a) (b)

Figure 7.18: Comparison of (a) simulated densities and (b) an ICCD image recorded for a single-barrier actuator with a positive-going voltage. The simulation was of a reduced-scale system, and includes the same data as figure 7.2. The 15 ns gate-width image is the same as shown in figure 5.14(c).

of a microdischarge will in general be larger than the distance of its end from the exposed electrode. In contrast, the two-dimensional nature of the computational model forces the simulated microdischarge to propagate directly away from the exposed electrode.

While we observed comparable filamentary/streamer-like plasma structures in the imaging experiments and the simulations, the simulations did not reproduce a filament-free regime. We observed this regime experimentally only at the very end of the positive-going half cycle for exposed electrode diameters on the order of 0.1 mm. While the simulations used larger applied voltages, the smallest simulated exposed electrode was 0.10 mm in diameter, close to the threshold for the appearance of the filament-free regime. Additional simulations with smaller exposed electrode sizes would help determine whether the model includes the necessary physics to reproduce this regime.

The single-barrier simulations also reproduced many features of the microdischarges seen experimentally in actuators with negative-going applied voltages. A comparison of a reduced-scale microdischarge and an experimentally-observed image are shown in figures 7.19(a) and 7.19(b),

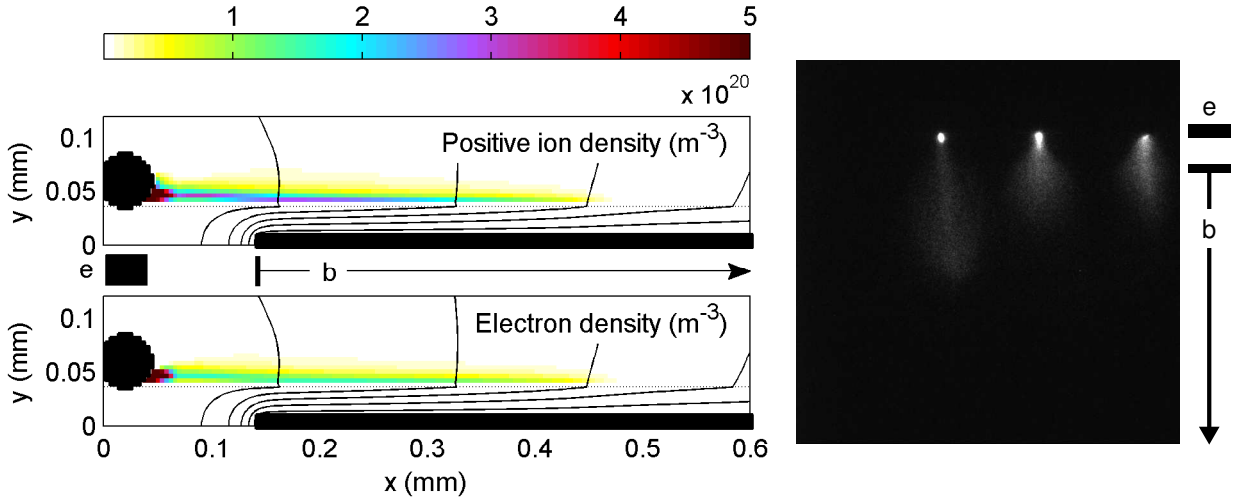

(a) (b)

Figure 7.19: Comparison of (a) simulated densities and (b) an ICCD image recorded for a single-barrier actuator with a negative-going voltage. The simulation was of a reduced-scale system, and includes the same data as figure 7.3. The image used a 10 μs gate width, and is of a single-barrier actuator with a 0.40 mm diameter exposed electrode.

respectively. The computational model predicted a dense region of plasma immediately adjacent to the exposed electrode edge, with a sparser plasma extending along the dielectric surface. This jet-like plasma structure was observed experimentally as well. The horizontal spread of the plasma in figure 7.19(b) could not be reproduced by the model due to its confinement to two spatial dimensions.

We have estimated the duration of microdischarges in the full-scale simulation runs by examining the widths of the current pulses. For positive-going voltages, typical streamer-like microdischarge durations were approximately 50 ns, with no significant variation observed for different exposed electrode diameters. For negative-going voltages, the current pulse widths varied with the exposed electrode diameter. For the run with a 0.10 mm electrode, typical microdischarge durations were approximately 5 ns. For the run with a 1.00 mm electrode the durations varied strongly, with larger current pulses lasting approximately 35 ns and smaller pulses lasting only a few nanoseconds.

A similar analysis of current pulse duration could not be used experimentally due to significant parasitic capacitance in the measurement circuit. We estimated microdischarge lifetime for a single-barrier actuator with a 0.30 mm diameter electrode using the ICCD camera in section 5.2.3. There we estimated an upper bound of 100 ns for the lifetime of a filamentary microdischarge, and an upper bound of 20 ns for a jet-like microdischarge. These values are comparable to those seen in the simulation, although we note that these are only single points of comparison, requiring confirmation before they can be stated as firm evidence of model accuracy.

7.4.2 Double-Barrier Microdischarge Structures

The simulation runs of double-barrier actuators reproduced some of the plasma structures seen experimentally with the ICCD camera. During the positive-going half cycle, the experimental images showed both jet-like and filamentary plasma structures, as pictured in figure 7.20(b). The reduced-scale simulations, from which the example data in figure 7.20(a) were taken, do show a dense propagating plasma similar to the streamer-like microdischarge seen in single-barrier runs. Since we described strong similarities between the simulated streamer-like microdischarges and the experimentally-observed filamentary microdischarges in section 7.4.1, it is reasonable to make the same comparison here. While the experimental image also contains a bright jet-like structure, the simulations predicted only a relatively weak plasma near the narrow electrode. This plasma did tend to be thin, similar to the simulated negative microdischarge described in section 7.1.1, but was much weaker than seen in single-barrier systems.

As noted in section 7.1.2, a negative-going applied voltage applied to simulated double-barrier actuators resulted in plasma behavior flipped from that when a positive-going voltage is used. The simulation, shown in figure 7.21(a), showed a dense propagating region the stopped just past the $-x$ side of the narrow electrode, and thin, weak plasma channel above the buried electrode. This latter feature is more easily visible in figure 7.5. The camera image, shown in figure 7.21(b), was also reversed from the positive-going case. It includes short filamentary structures above the narrow electrode and jet-like structures above the wide electrode. While the simulation has reproduced

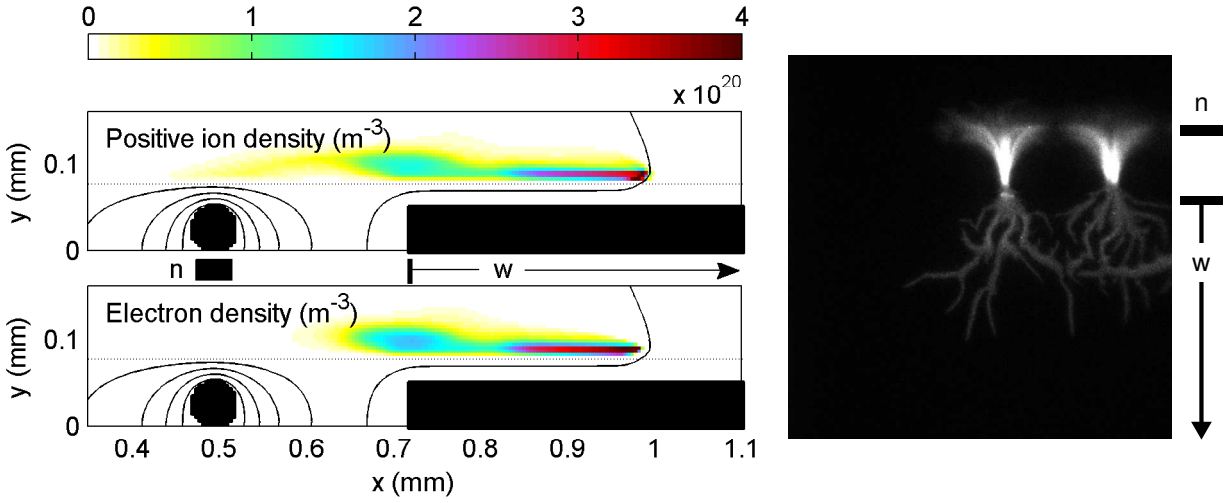

(a) (b)

Figure 7.20: Comparison of (a) simulated densities and (b) an ICCD image recorded for a double-barrier actuator with a positive-going voltage. The simulation was of a reduced-scale system, and includes the same data as figure 7.4. The image used a 10 µs gate width, and is of a double-barrier actuator with a 0.40 mm diameter narrow electrode.

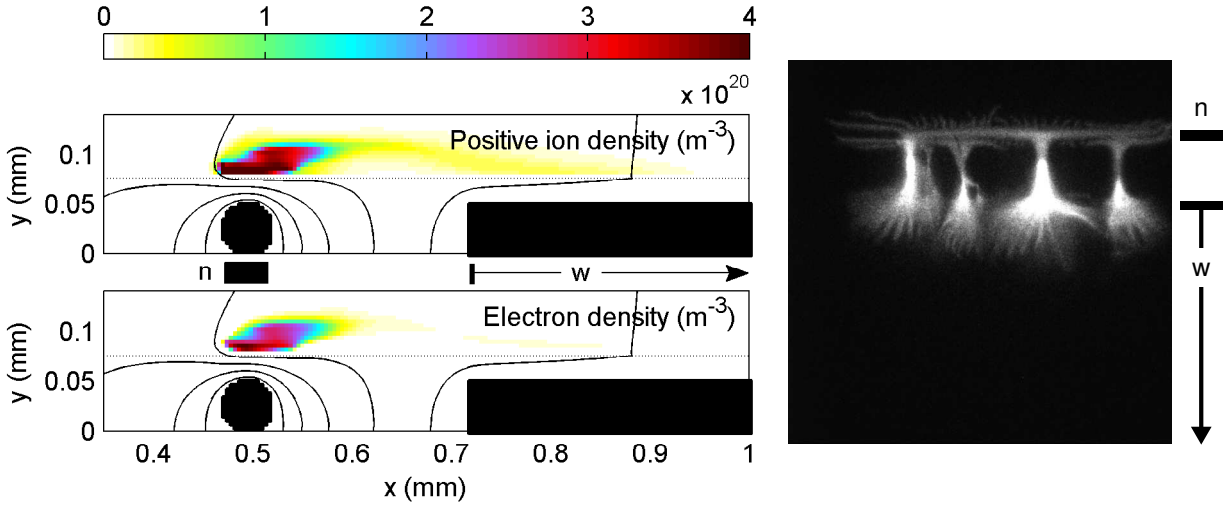

(a) (b)

Figure 7.21: Comparison of (a) simulated densities and (b) an ICCD image recorded for a double-barrier actuator with a negative-going voltage. The simulation was of a reduced-scale system, and includes the same data as figure 7.5. The image used a 10 µs gate width, and is of a double-barrier actuator with a 0.40 mm diameter narrow electrode.

both observed structures, as with a positive-going voltage the simulated plasma corresponding to the jet-like structure was quite weak compared to the brightness of the camera image.

For both positive- and negative-going applied voltages, the simulation appears to under-predict the plasma in the regions where we experimentally observed jet-like plasma structures. The major simplifications made in the model—two-dimensionality, limited plasma chemistry, and lack of photoionization and photoemission—are also present in single-barrier simulations, in which we do see a negative microdischarge with many similarities to the jet-like structure. The exact reason for the discrepancy in double-barrier microdischarge behavior between the experiments and the simulations remains unclear.

7.4.3 Time-Averaged Forces

As with our examinations of microdischarge structure, comparisons of simulated and measured time-averaged forces require careful considerations of the differences between the physical and modeled systems. In particular we note that the effective voltages and amplitudes used in the simulations are larger than for the experimentally-applied voltage waveforms. While in general we expect that the larger voltage amplitudes and frequencies will increase the simulated force, this has only been proven for single-barrier actuators [93]. We also note that our discussions of the effective voltage waveforms in the simulations include the same assumptions stated in section 7.3.1, primarily that the two half-cycles would not interact with each other if modeled sequentially.

As discussed in section 7.3.1, the set of full-scale simulation runs allowed us to calculate a cycle-averaged forces for single-barrier actuators. The cycle was an effective voltage waveform oscillating at 3.8 kHz with an amplitude of 9.8 kV. We can directly compare these simulated forces to the experimentally-measured forces described in section 4.2. Figure 7.22 shows the simulated and measured forces together as functions of the exposed electrode diameter. Qualitatively the two sets of data show the same general trend of increasing at smaller diameters.

The two force scales in figure 7.22 indicate that the simulated forces were an order of magnitude larger than those measured experimentally. This discrepancy likely has two major sources. First, as noted above, both the effective amplitude and frequency are significantly larger for the

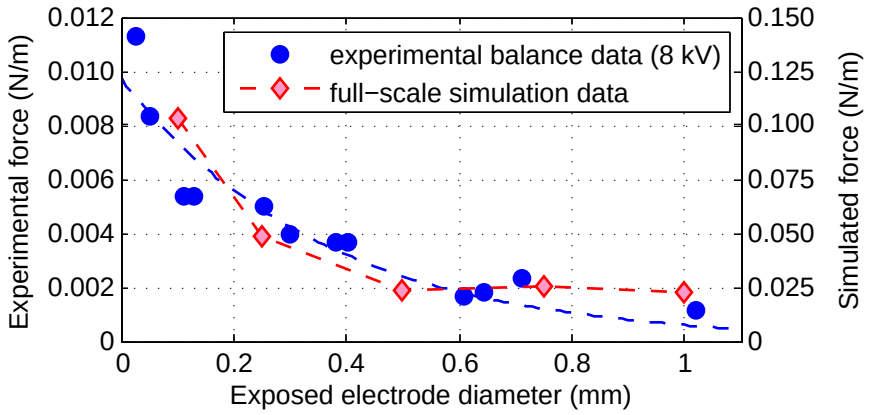

Figure 7.22: Comparison of simulated and experimentally-measured forces for single-barrier actuators. The simulated force data are the cycle-averaged forces of figure 7.13. The experimental values were measured using the electronic balance for a 13 kV amplitude voltage, and are the same data as in figure 4.4.

simulations than for the experiments. As discussed in section 2.4.2, the induced forces generally increase as both voltage amplitude and frequency are raised in this range. Second, the two-dimensional nature of the computational model tends to overestimate the induced forces. The model assumes that all properties, including the induced force, are uniform in the third dimension. As we saw in chapter 5, however, the plasma is generally confined to narrow channels in this third (z) dimension. While the plasma may diffuse in the z direction as it decays (and the plasma may induce a significant force during this decay period), it seems unlikely that the induced force will be uniform in this direction even in when averaged over time. Since the experimentally-measured forces are averaged in the z dimension, they include both regions of plasma and regions of neutral air, reducing the apparent force.

While the induced forces for simulations and measurements of single-barrier actuators with cylindrical electrodes showed the same qualitative trends with exposed electrode diameter, this agreement breaks down when we consider a rectangular exposed electrode. Averaged over the same effective voltage as the other single-barrier simulations, the rectangular electrode actuator discussed in section 7.3.2 induced approximately the same force as did the system with a 0.10 mm diameter exposed electrode. This result is in stark contrast with our experimental measurements

of sections 4.2.1 and 4.2.2, which showed that actuators with long, thin rectangular exposed electrodes induced significantly lower forces than did those with cylindrical electrodes. The absence of the filament-free plasma in the simulations may be responsible for the lack of separation between the devices with cylindrical and circular electrodes. This regime was present in the experimental actuators in which the greatest difference was observed between actuators with the two electrode geometries.

In section 7.3.1 we noted that the simulated time-averaged forces for positive- and negative-going voltages were of comparable sizes. While the extremely closeness of these values, shown in figure 7.13, were the product of the particular simulation durations we chose, the fact that both half cycles contributed significantly to the cycle-averaged force was not. Comparable values of the induced force for positive- and negative-going voltages have also been predicted by the simulations of Boeuf et al. [93]. These findings match up with the experiments of Enloe et al. [75], who found experimentally that the gross positive forces induced during each half cycle of the applied voltage were similar in both sign and magnitude. We note that our reduced-scale simulations predicted a negative net force with negative-going applied voltages for larger electrode diameters, which would contradict the cited experimental measurements. The hypothesis by Enloe et al. [75] that the smaller *net* force during the positive-going half cycle was caused by drag between the induced gas flow and the dielectric surface would explain the differences between the simulation data and the experimental results of Forte et al. [66]. The latter group found significant induced gas flow only during one half cycle of the applied voltage, but made their measurement far downstream of the actuator, after drag could have reduced the positive half cycle-induced flow down to negligible velocities.

In contrast to the single-barrier actuator data, the simulations and experimental measurements of time-averaged forces for double-barrier actuators showed opposite behaviors with changing narrow electrode diameter. As shown in figure 7.23, the simulation predicted an decreasing induced force as the narrow electrode diameter decreased, while the experiments showed the opposite trend. Although neither trend was particularly strong compared to the changes seen for single-barrier devices, the discrepancy is clear and may indicate that an important physical mechanism is missing

from the model. The model did, however, correctly predict that time-averaged forces induced by double-barrier systems were an order of magnitude smaller than those of single-barrier actuators.

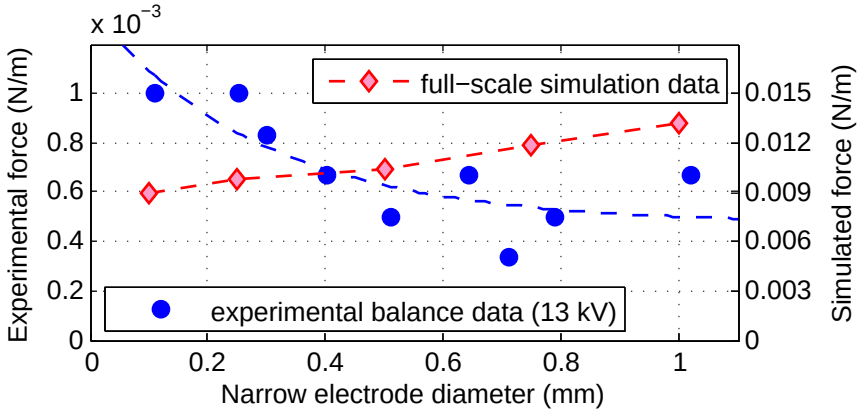

Figure 7.23: Comparison of simulated and experimentally-measured forces for double-barrier actuators. The simulated force data are the cycle-averaged forces of figure 7.17. The experimental values were measured using the electronic balance for an 8 kV amplitude voltage, and are the same data as in figure 4.10.

Chapter 8

Conclusion

We have conducted a variety of physical and computational experiments in order to optimize and better understand surface dielectric barrier discharges for use as aerodynamic actuators. These discharges use oscillating high voltages to excite plasmas in ambient air, and a dielectric layer between two electrodes to suppress the formation of arcs. We have examined both the time-averaged and nanosecond scale behaviors of the actuator systems. In our time-averaged experiments we have made dramatic increases in the induced force, which is expected to translate into improved ability to reduce or eliminate flow separation on airfoils in low-Reynolds number gas flows. Optical imaging of the plasma on short time scales showed plasma structures that varied with both discharge geometry and the slope of the applied voltage. We have qualitatively validated many results of our newly-developed computational model against the experimental data at both time scales, giving us a more detailed picture of the plasma physics.

Our time-averaged force measurements of single-barrier plasma actuators showed that the material of the exposed electrode did not significantly affect either the induced air flow or the dissipated electrical power of the system. In contrast, simultaneously reducing the thickness and length of the exposed electrode, shown in figure 8.1, lead to exponential increases in the induced force, while simultaneously decreasing the required power. In our experiments the ideal design of thin, short electrodes was most easily obtained using thin wire electrodes. The fastest growth in the induced forces was observed as we reduced the electrode diameters below approximately 0.15 mm. We have validated our results by using two measurement techniques: direct force measurements using an electronic balance and flow measurement using a stagnation probe.

Figure 8.1: Single-barrier actuator showing the exposed electrode length and width

We have also conducted the first systematic force measurements of double-barrier discharges, in which both electrodes are insulated, used as plasma actuators. Our design used one narrow cylindrical electrode and one wider electrode with a rectangular cross-section, both placed underneath a dielectric film. The force induced by such actuators was directed from the narrow towards the wide electrode, and increased as the narrow electrode diameter was reduced.

In addition to our time-averaged force measurements, we have examined plasma dynamics on time scales ranging from a few nanoseconds to the applied voltage period of 1 ms using an intensified digital camera. Previous studies have noted that the plasma in single-barrier surface discharges forms in filamentary structures when the voltage applied to the exposed electrode is increasing, and in more diffuse jet-like structures when it is decreasing [71]. We have characterized for the first time, the formation and lifetime for both of these types of microdischarges. Each filamentary microdischarge consists of a small, bright region of plasma that propagates along the dielectric surface. They appear filamentary because the plasma moves along a jagged path, and the camera integrates the emitted light. Such microdischarges required on the order of 100 ns to form for the parameters of our system. In contrast, the jet-like microdischarges appeared to form and decay in time periods shorter than 20 ns.

As we reduced the exposed electrode diameter below the same electrode at which we began to see large increases in the induced force, we also observed a suppression of the filamentary microdischarges and the appearance of a constant weak glow near the exposed electrode. This "filament-free" regime occurred only during the positive-going half cycle of the voltage. Unlike other microdischarges, it did not grow and decay within a hundred nanoseconds, but remained steady and visible until the end of the positive-going half cycle. The correlation between the

suppression of filamentary microdischarges and the strong increase in the induced force suggests that the filaments do not efficiently transfer momentum to the neutral gas.

The microdischarges in double-barrier actuators appeared to include both filamentary and jet-like structures. With a positive-going voltage applied to the narrow electrode, we observed a long filamentary structure and a shorter jet-like structure in the opposite direction. With a negative-going voltage, we saw long jet-like and short filamentary structures arrayed with the directions switched. These results suggest that the form of the microdischarge depends in part on the direction of the local electric field relative to the dielectric surface.

The experimental measurements allow us to make new recommendations for the design of the future single-barrier plasma actuator systems. Being able to the choose the electrode material based on its mechanical and electrical characteristics rather than its secondary electron emission coefficient will ease the task of designers adapting plasma actuators for use in harsh environments such as jet turbines. While designing for maximum efficiency would dictate using the thinnest and shortest achievable exposed electrode, the designer will inevitably need to consider other factors. As the electrode size is reduced, the increasing resistance of the electrode may lead to drops in voltage along the width of the electrode, which in turn would cause non-uniform performance. Of perhaps greater concern will be the erosion of such a small electrode. Plasmas, particularly in systems including high voltages and corrosive gases like oxygen, can quickly sputter or etch surfaces. In our experiments, we observed discoloration and roughening of our polymer dielectric after only tens of minutes of operating time, although we did not study this in detail.

To examine details of the discharge physics not accessible to our experimental techniques, we have developed a two-dimensional fluid model of the system. The model solves Poisson's equation, a set of continuity equations, and a set of drift-diffusion equations to determine the time-dependent plasma behavior, applying many of the same approximations included in other models in the literature. In addition to the abilities of these other models, our code also allows simulation domains with arbitrary electrode shapes and sizes, and dynamically adjusts the time-step size to maintain numerical accuracy while reducing computation times. We have applied the model to examine simulated plasma variations on time scales from several nanoseconds to hundreds of

microseconds, averaging data on the latter scales to approximate time-averaged values. The model successfully reproduced many of the actuator behaviors observed experimentally, and represents a first step towards a detailed understanding of the important physics in the discharge system.

Our simulations of single-barrier systems predicted the occurrence of discrete microdischarge events. With a positive-going voltage applied to the exposed electrode, the plasma formed in a small, dense region which propagated along the dielectric surface. With a negative-going voltage, the plasma formed and decayed more quickly, with the densest region remaining next to the exposed electrode. These simulated structures strongly resembled the microdischarge structures we observed experimentally. The effective time-averaged forces of experimental-scale simulations roughly paralleled the increase in force at reduced exposed electrode diameters seen experimentally, but the code incorrectly predicted that a long rectangular exposed electrode would induce similar levels of force. Simulated microdischarges in double-barrier systems showed somewhat less resemblance to the experimentally observed structures. They did result in discrete microdischarges and a time-averaged force in the same direction as we measured experimentally. In both system geometries, the simulation indicated that the dominant sources of time-averaged force acting on the gas occurred in between microdischarge events, as the plasma decayed.

Our experimental work has shown that the efficiency of a single-barrier plasma actuator can be increased by a factor of 9 over previous studies by using a short and thin exposed electrode. Imaging of the plasma suggests that some of this increase may be due to the appearance of a previously unknown filament-free plasma regime that does not occur when using larger electrodes. Qualitative comparisons between the force and imaging experiments and our simulation results indicate that the fluid model incorporates much of the relevant physics of this type of discharge system. We expect that the significantly larger forces induced by the plasma actuators considered in this work will be able to limit flow separation in a wider range of background flow velocities than previous designs, paving the way to reduce drag and inefficiencies in a variety of aerodynamics applications.

Appendix A: Actuator Construction Procedure

This appendix describes in detail the procedure used to construct the DBD plasma actuators investigated in chapters 4 and 5. All of the accompanying photographs show the construction of a single-barrier device with a cylindrical exposed electrode, and the text includes the adjustments that would be needed to construct a different type of actuator.

1. Cut a section of the dielectric material and tape down the edges on a flat, level surface

   Irregularities in the surface of the working area can lead to bumps in the actuator surface. For the actuators in this work, a metal bar seen in each of the photographs below was used. The surface was leveled to prevent epoxy from flowing to one side. The 0.25 mm thick polyester film used as the dielectric material in this work was shipped on a roll. Because of this, the cut section was curved, as can be seen in the photograph below. In order to ensure a flat dielectric layer we placed film with the edges curved upwards, then taped the edges of the film to the working surface.

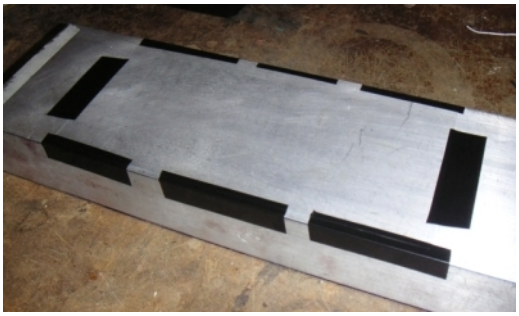

2. Trace an outline of an actuator, cut a buried or wide electrode, and place it on the dielectric

   Using an existing actuator, we traced an outline onto the dielectric film. In this work, all actuators were 4 cm long by 7 cm wide. The outline served as a guide while placing the electrodes and applying epoxy. All actuators in this work used copper foil tape with a non-conductive acrylic adhesive as the buried electrode (for single-barrier discharges) or the wide electrode (for double-barrier discharges). All of these electrodes were 6 cm wide and

1.5 cm long. The cut edge was always placed along the outside boundary, to ensure the smoother factory-cut edge was closer to the other electrode. The tape firmly pressed down to eliminate air bubbles and to prevent the inviscid epoxy from "leaking" between the tape and the dielectric film.

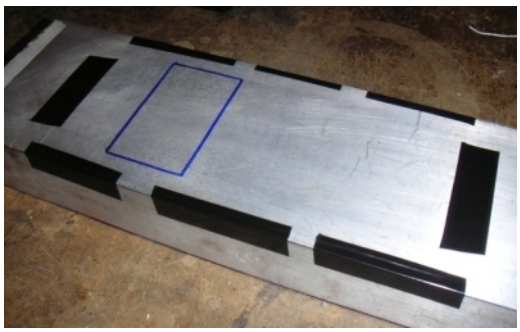
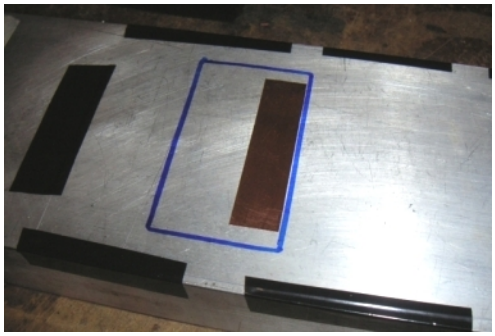

3. Affix a wire to the electrode

   To connect this electrode to the external circuit, a wire is required. A piece of copper tape with a conductive adhesive was applied to connect the wire, both mechanically and electrically, to the electrode. As before, the tape was pressed down firmly to prevent epoxy from seeping in between the wire and the electrode.

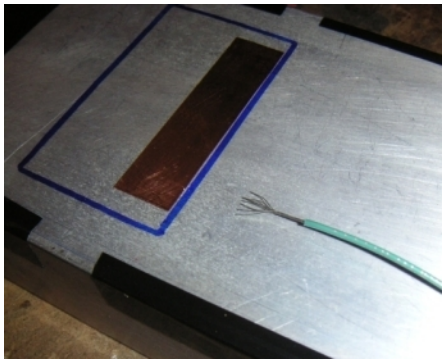
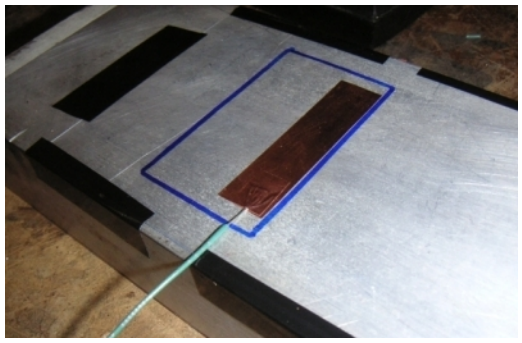

4. Affix a narrow electrode and wire (double-barrier only)

   When constructing a double-barrier actuator, we affixed the narrow electrode to the dielectric film using a procedure similar to that described in steps 8–10 below.

5. Apply layers of insulating epoxy

   We mixed the Stycast 2651-40 epoxy resin and Catalyst 9, both produced by Emerson & Cuming, in a suitable container, and applied a layer to dielectric film inside the outline. After allowing the epoxy to set, the application process was repeated until the epoxy layers were thick enough to completely cover the portions of the wire(s) inside the outlined area. This particular epoxy was chosen for its high dielectric strength, a dielectric constant similar to the film, and for its relatively low viscosity. The low viscosity is required to avoid the formation of air bubbles inside the epoxy. Plasma can form inside these air bubbles (increasing the apparent power use), and the smaller effective thickness of epoxy reduces the total dielectric strength.

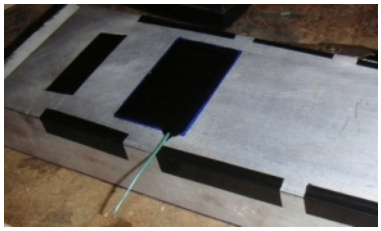

6. Cut, tap, and attach the substrate

   For the substrate, we cut a rectangle of clear, 1 cm thick acrylic the same size as the outline. In one corner (that will be placed away from the electrodes), we drilled and tapped a hole for a $1/4$-20 screw. This hole was used for mechanical mounting the actuator. Onto the existing epoxy, we applied a final thin layer of epoxy and placed the substrate on top. We used weights (two bolts in the photograph here) placed next to the substrate to ensure it did not slide out of place while the epoxy was setting.

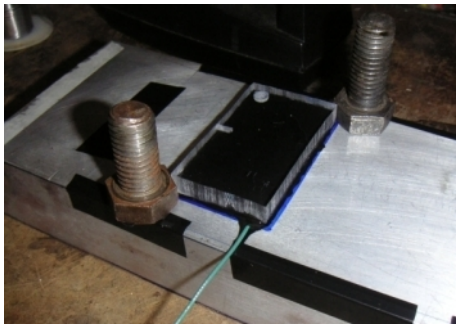

7. Flip over the actuator and remove excess dielectric material

   After removing the tape holding the dielectric to the working surface, we flipped the actuator over and trimmed the excess dielectric film using scissors. Some visible de-bonding between the epoxy and dielectric occurred near the device edges. As long as the space between the electrodes (or what will be the area between the electrodes) did not de-bond, this did not affect actuator operation.

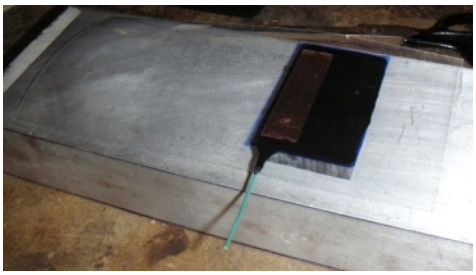

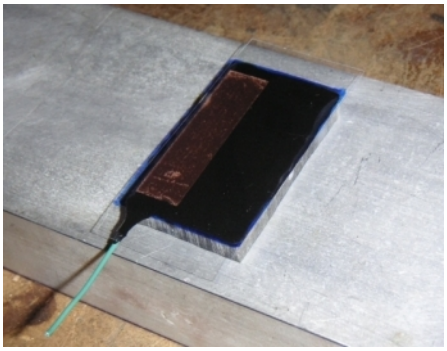

8. Affix a wire to the desired exposed electrode (single-barrier only)

   The electrode in the photos here was a stripped single-stranded copper wire, placed next to the actuator. We chose a connecting wire (white in the photos here) and soldered it to one end of the electrode. When using tungsten or stainless steel exposed electrode, which cannot be soldered to copper, we first spot-welded a small piece of gold-plated nickel wire to the electrode, then soldered the nickel wire to the connecting wire.

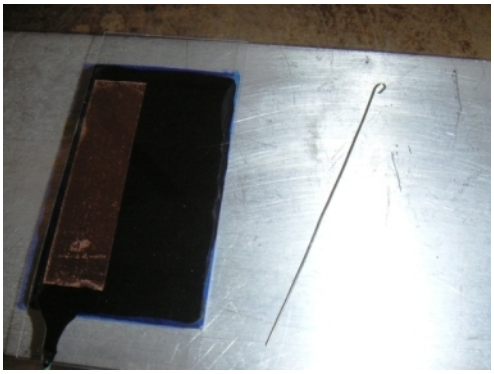

9. Tape the electrode at the desired location, and apply epoxy to the ends (single-barrier only)

   We placed the exposed electrode on the surface at the desired distance (1 mm for all single-barrier actuators described in this work) from the visible edge of the buried electrode. We used strips of transparent tape to hold the exposed electrode in place. With the exposed electrode held at its final position, we applied an insulating epoxy to the ends of the electrode. Since this epoxy was required solely for structural purposes, bubbles were not a concern. Consequently, we used a much more viscous epoxy (usually Hysol 0151, manufactured by Loctite) than used underneath the dielectric layer.

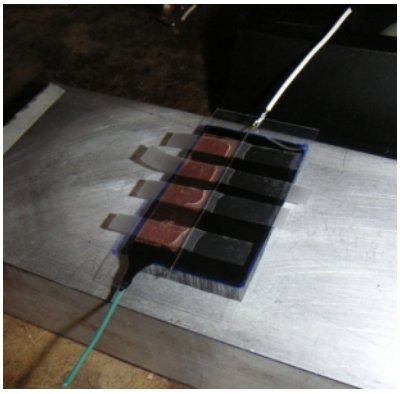

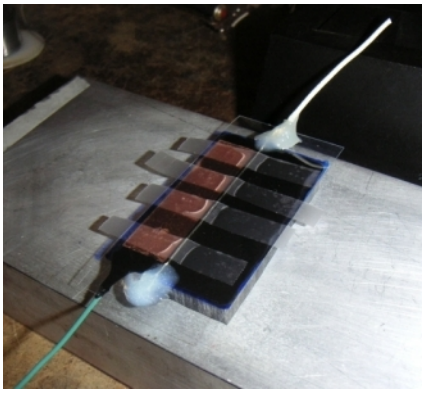

10. Remove tape, trim wires, attach crimp-on connectors

    Prior to operation, we removed the transparent tape, as shown in the photograph below. To avoid wire sagging during balance measurements, we trimmed the connecting wires down to less than 1 cm. Crimp-on connectors were then attached to allow connections to the external circuitry. Examples of finished actuators were also shown in figure 3.4.

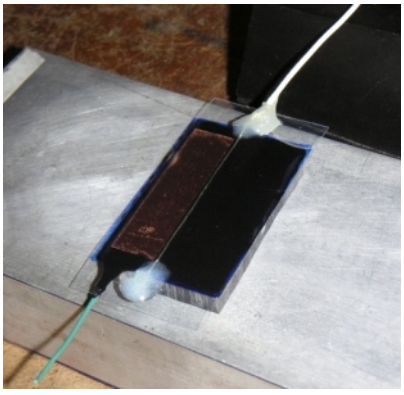

Appendix B: Details of the Computational Model

B.1 The Poisson's Equation Solver

The Poisson equation evaluated at time step $m+1$ using projected densities is given by equation (6.18), repeated here for clarity:

$$\epsilon_0 \nabla^2 \phi^{m+1} = -e \left[n_p^m - n_e^m - n_n^m + \Delta t \left(\frac{\partial n_p}{\partial t} - \frac{\partial n_e}{\partial t} - \frac{\partial n_n}{\partial t} \right) \right].$$

The term in brackets is the projected charge density at time step $m+1$ based on the known densities at time m. At the dielectric surface there will be an additional contribution due to accumulated surface charge.

To work towards a numerical solution to this equation, we first apply the second-order accurate finite difference approximations to the spatial derivatives. Assuming $\Delta x = \Delta y$ for simplicity, we get

$$\begin{aligned} \phi_{i+1,j}^{m+1} + \phi_{i-1,j}^{m+1} + \phi_{i,j+1}^{m+1} + \phi_{i,j-1}^{m+1} - 4\phi_{i,j}^{m+1} = \\ - \frac{e\Delta x^2}{\epsilon_0} \left(n_p^m - n_e^m - n_n^m \right) - \frac{e\Delta t \Delta x^2}{\epsilon_0} \left(\frac{\partial n_p}{\partial t} - \frac{\partial n_e}{\partial t} - \frac{\partial n_n}{\partial t} \right). \end{aligned} \quad \text{(B.1)}$$

The time-derivatives of the densities in equation (B.1) are evaluated using the continuity equations. As described in section 6.2.3, the sources and sink they will cancel out in equation (B.1) and we can write

$$\begin{aligned} \frac{\partial n_p}{\partial t} - \frac{\partial n_e}{\partial t} - \frac{\partial n_e}{\partial t} &= -\nabla \cdot \Gamma_p + \nabla \cdot \Gamma_e + \nabla \cdot \Gamma_n \\ &= -\frac{\partial \Gamma_{px}}{\partial x} - \frac{\partial \Gamma_{py}}{\partial y} + \frac{\partial \Gamma_{ex}}{\partial x} + \frac{\partial \Gamma_{ey}}{\partial y} + \frac{\partial \Gamma_{nx}}{\partial x} + \frac{\partial \Gamma_{ny}}{\partial y}, \end{aligned}$$

where Γ is a particle flux.

The remaining task, then, is to evaluate of the particle flux derivatives in terms of the electrostatic potential. When doing this, we will use the semi-implicit method suggested by Ventzek et al. [105], using densities evaluated at time m and potentials at time $m+1$. The following sections describe how each of these flux terms are evaluated.

B.1.1 Positive Ion Fluxes

We consider the x-directed positive-ion flux first in detail, then describe the other particle fluxes by analogy. Using the drift-diffusion approximation with the semi-implicit scheme described in section 6.2.3,

$$\Gamma_{px} \approx +e{n_p}^m \mu_p {E_x}^{m+1} - e\mu_p T_p \frac{\partial {n_p}^m}{\partial x}.$$

To avoid a grid-based instability we use the Scharfetter-Gummel discretization (see section 6.2.2):

$$\Gamma_{px}\Big|_{i+\frac{1}{2},j} \approx \frac{\mu_p T_p}{\Delta x}\left(\frac{z^{m+1}_{i+\frac{1}{2},j}}{1-e^{z^{m+1}_{i+\frac{1}{2},j}}} n_{p^m_{i+1,j}} + \frac{z^{m+1}_{i+\frac{1}{2},j}}{1-e^{-z^{m+1}_{i+\frac{1}{2},j}}} n_{p^m_{i,j}}\right)$$

where

$$z^{m+1}_{i+\frac{1}{2},j} \equiv \frac{{E_x}^{m+1}_{i+\frac{1}{2},j}\Delta x}{T_p} \approx \frac{-\phi^{m+1}_{i+1,j} + \phi^{m+1}_{i,j}}{T_p} \tag{B.2}$$

for positive ions. Similar expressions can be found for the other directions and species.

In order to linearize the flux, we write $z^{m+1} = z^m + \Delta z$, and assume that Δz, the change in z during a given time step, is small for all particle species. "Small" is quantified below. This allows us to expand the flux expressions in Taylor series and retain only the first two terms:

$$\begin{aligned}
\frac{z+\Delta z}{1-e^{z+\Delta z}} &= \frac{z}{1-e^z} + \Delta z\left[\frac{1}{1-e^z} + \frac{ze^z}{(1-e^z)^2}\right] + \cdots \\
&\approx (z+\Delta z)\left[\frac{1-e^z+ze^z}{(1-e^z)^2}\right] - \frac{z^2e^z}{(1-e^z)^2} \\
&= (z+\Delta z)\,a + b
\end{aligned}$$

where

$$a = \frac{1-e^z+ze^z}{(1-e^z)^2} \tag{B.3}$$

$$b = \frac{-z^2e^z}{(1-e^z)^2}. \tag{B.4}$$

Similarly,

$$\begin{aligned}
\frac{z+\Delta z}{1-e^{-z-\Delta z}} &= \frac{z}{1-e^{-z}} + \Delta z\left[\frac{1}{1-e^{-z}} - \frac{ze^{-z}}{(1-e^{-z})^2}\right] + \cdots \\
&\approx (z+\Delta z)\left[\frac{1-e^z-ze^{-z}}{(1-e^{-z})^2}\right] + \frac{z^2e^{-z}}{(1-e^{-z})^2} \\
&= (z+\Delta z)\,c + d.
\end{aligned}$$

where

$$c = \frac{1 - e^{-z} - ze^{-z}}{(1 - e^{-z})^2} \tag{B.5}$$

$$d = \frac{z^2 e^{-z}}{(1 - e^{-z})^2}. \tag{B.6}$$

Subscripts on a, b, c, and d will indicate which z values to use. A subscript p indicates to use a positive electric field and the positive ion temperature in the definition of z. Subscripts of half-integer indices in i will indicate the use of x-directed electric fields in z.

Accuracy for linear expansions of functions of z normally requires $|\Delta z| \ll 1$, but for this particular case that restriction is significantly loosened. Both $z/(1 - e^z)$ and $z/(1 - e^{-z})$ are approximately linear except near $z = 0$, as seen in figure B.1. If $|z| > 1$, the linearizations are reasonable provided $\Delta z/z > -1$, i.e the electric field does not change sign during a single time step. If $|z| < 1$, the stronger condition $|\Delta z| \ll 1$ is required for strict accuracy. These conditions are used to set the size of the simulation time step, as described in section 6.2.5.

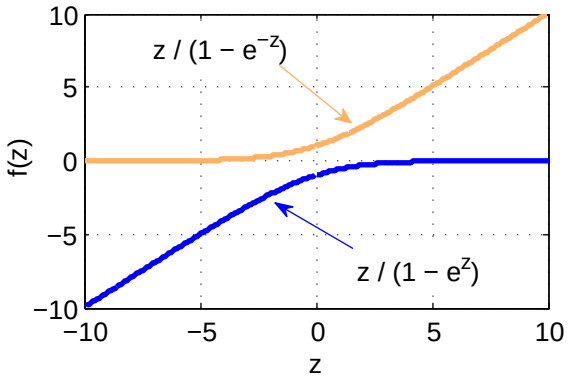

Figure B.1: Two functions of z which are linearized during the derivation of the Poisson's equation solver algorithm

An additional complication exists when implementing equations (B.3)–(B.6) in the actual code: all of these functions have removable singularities at $z = 0$. Consequently, when evaluating these expressions near the singularity we employ Taylor expansions of a, b, c, and d for small z. Deviations from the true limiting values of these functions are smaller than machine round-off errors.

Now we can approximate the linearized spatial derivative of the x-directed positive ion flux as

$$\begin{aligned}\left.\frac{\partial \Gamma_{px}}{\partial x}\right|_{i,j} \approx \frac{1}{\Delta x}\frac{T_p}{\Delta x}\Bigg[&+ \mu_{p_{i+\frac{1}{2},j}}\left(z^{m+1}_{i+\frac{1}{2},j}a_{p_{i+\frac{1}{2},j}} + b_{p_{i+\frac{1}{2},j}}\right) n^{m}_{p_{i+1,j}} \\ &+ \mu_{p_{i+\frac{1}{2},j}}\left(z^{m+1}_{i+\frac{1}{2},j}c_{p_{i+\frac{1}{2},j}} + d_{p_{i+\frac{1}{2},j}}\right) n^{m}_{p_{i,j}} \\ &- \mu_{p_{i-\frac{1}{2},j}}\left(z^{m+1}_{i-\frac{1}{2},j}a_{p_{i-\frac{1}{2},j}} + b_{p_{i-\frac{1}{2},j}}\right) n^{m}_{p_{i,j}} \\ &- \mu_{p_{i-\frac{1}{2},j}}\left(z^{m+1}_{i-\frac{1}{2},j}c_{p_{i-\frac{1}{2},j}} + d_{p_{i-\frac{1}{2},j}}\right) n^{m}_{p_{i-1,j}}\Bigg]\end{aligned} \tag{B.7}$$

with $z^{m+1} = z + \Delta z$. Evaluating the z^{m+1} terms using equation (B.2), our approximation for the flux derivative becomes

$$\begin{aligned}\left.\frac{\partial \Gamma_{px}}{\partial x}\right|_{i,j} \approx \frac{1}{\Delta x^2}\Bigg[&+ \mu_{p_{i+\frac{1}{2},j}}a_{p_{i+\frac{1}{2},j}}\left(-\phi^{m+1}_{i+1,j} + \phi^{m+1}_{i,j}\right) n^{m}_{p_{i+1,j}} \\ &+ \mu_{p_{i+\frac{1}{2},j}}T_p b_{p_{i+\frac{1}{2},j}} n^{m}_{p_{i+1,j}} \\ &+ \mu_{p_{i+\frac{1}{2},j}}c_{p_{i+\frac{1}{2},j}}\left(-\phi^{m+1}_{i+1,j} + \phi^{m+1}_{i,j}\right) n^{m}_{p_{i,j}} \\ &+ \mu_{p_{i+\frac{1}{2},j}}T_p d_{p_{i+\frac{1}{2},j}} n^{m}_{p_{i,j}} \\ &- \mu_{p_{i-\frac{1}{2},j}}a_{p_{i-\frac{1}{2},j}}\left(-\phi^{m+1}_{i,j} + \phi^{m+1}_{i-1,j}\right) n^{m}_{p_{i,j}} \\ &- \mu_{p_{i-\frac{1}{2},j}}T_p b_{p_{i-\frac{1}{2},j}} n^{m}_{p_{i,j}} \\ &- \mu_{p_{i-\frac{1}{2},j}}c_{p_{i-\frac{1}{2},j}}\left(-\phi^{m+1}_{i,j} + \phi^{m+1}_{i-1,j}\right) n^{m}_{p_{i-1,j}} \\ &- \mu_{p_{i-\frac{1}{2},j}}T_p d_{p_{i-\frac{1}{2},j}} n^{m}_{p_{i-1,j}}\Bigg].\end{aligned}$$

Rearranging, we get

$$\begin{aligned}
\left.\frac{\partial \Gamma_{px}}{\partial x}\right|_{i,j} \approx & -\phi_{i+1,j}^{m+1}\frac{\mu_{p_{i+\frac{1}{2},j}}}{\Delta x^2}\left(a_{p_{i+\frac{1}{2},j}} n_{p_{i+1,j}}^{m} + c_{p_{i+\frac{1}{2},j}} n_{p_{i,j}}^{m}\right) \\
& -\phi_{i-1,j}^{m+1}\frac{\mu_{p_{i-\frac{1}{2},j}}}{\Delta x^2}\left(a_{p_{i-\frac{1}{2},j}} n_{p_{i,j}}^{m} + c_{p_{i-\frac{1}{2},j}} n_{p_{i-1,j}}^{m}\right) \\
& +\phi_{i,j}^{m+1}\left[\frac{\mu_{p_{i+\frac{1}{2},j}}}{\Delta x^2}\left(a_{p_{i+\frac{1}{2},j}} n_{p_{i+1,j}}^{m} + c_{p_{i+\frac{1}{2},j}} n_{p_{i,j}}^{m}\right)\right. \\
& \qquad \left. +\frac{\mu_{p_{i-\frac{1}{2},j}}}{\Delta x^2}\left(a_{p_{i-\frac{1}{2},j}} n_{p_{i,j}}^{m} + c_{p_{i-\frac{1}{2},j}} n_{p_{i-1,j}}^{m}\right)\right] \\
& +\frac{\mu_{p_{i+\frac{1}{2},j}} T_p}{\Delta x^2} b_{p_{i+\frac{1}{2},j}} n_{p_{i+\frac{1}{2},j}}^{m} + \frac{\mu_{p_{i+\frac{1}{2},j}} T_p}{\Delta x^2} d_{p_{i+\frac{1}{2},j}} n_{p_{i,j}}^{m} \\
& -\frac{\mu_{p_{i-\frac{1}{2},j}} T_p}{\Delta x^2} b_{p_{i-\frac{1}{2},j}} n_{p_{i,j}}^{m} - \frac{\mu_{p_{i-\frac{1}{2},j}} T_p}{\Delta x^2} d_{p_{i-\frac{1}{2},j}} n_{p_{i-1,j}}^{m}.
\end{aligned}$$

Based on the above approximation, we define some new terms,

$$A_{px}\Big|_{i+\frac{1}{2},j} \equiv \frac{e\Delta t}{\epsilon_0}\mu_{p_{i+\frac{1}{2},j}}\left(a_{p_{i+\frac{1}{2},j}} n_{p_{i+1,j}}^{m} + c_{p_{i+\frac{1}{2},j}} n_{p_{i,j}}^{m}\right) \tag{B.8}$$

$$\begin{aligned}
B_{px}\Big|_{i,j} \equiv & \frac{e\Delta t T_p}{\epsilon_0}\left[\mu_{p_{i+\frac{1}{2},j}} b_{p_{i+\frac{1}{2},j}} n_{p_{i+1,j}}^{m} - \mu_{p_{i-\frac{1}{2},j}} d_{p_{i-\frac{1}{2},j}} n_{p_{i-1,j}}^{m}\right. \\
& \qquad \left. +\left(\mu_{p_{i+\frac{1}{2},j}} d_{p_{i+\frac{1}{2},j}} - \mu_{p_{i-\frac{1}{2},j}} b_{p_{i-\frac{1}{2},j}}\right) n_{p_{i,j}}^{m}\right].
\end{aligned} \tag{B.9}$$

We note that all of the quanities in the A and B terms are evaluated at time step m, and so will not vary during the iterative solution of the Poisson equation for time step $m+1$. Now we can fully describe the spatial derivative of the positive ion flux:

$$\begin{aligned}
-\frac{e\Delta t \Delta x^2}{\epsilon_0}\left(-\left.\frac{\partial \Gamma_{px}}{\partial x}\right|_{i,j}\right) \approx & -\phi_{i+1,j}^{m+1} A_{px}\Big|_{i+\frac{1}{2},j} - \phi_{i-1,j}^{m+1} A_{px}\Big|_{i-\frac{1}{2},j} \\
& + \phi_{i,j}^{m+1}\left(A_{px}\Big|_{i+\frac{1}{2},j} + A_{px}\Big|_{i-\frac{1}{2},j}\right) - B_{px}\Big|_{i,j}.
\end{aligned}$$

Analogously, we define

$$A_{py}\Big|_{i+\frac{1}{2},j} \equiv \frac{e\Delta t\mu_{p_{i,j+\frac{1}{2}}}}{\epsilon_0}\left(a_{p_{i,j+\frac{1}{2}}}n^{m}_{p_{i,j+1}} + c_{p_{i,j+\frac{1}{2}}}n^{m}_{p_{i,j}}\right) \tag{B.10}$$

$$B_{py}\Big|_{i,j} \equiv \frac{e\Delta t T_p}{\epsilon_0}\Bigg(\mu_{p_{i,j+\frac{1}{2}}}b_{p_{i,j+\frac{1}{2}}}n^{m}_{p_{i,j+1}} + \mu_{p_{i,j+\frac{1}{2}}}d_{p_{i,j+\frac{1}{2}}}n^{m}_{p_{i,j}} - \mu_{p_{i,j-\frac{1}{2}}}b_{p_{i,j-\frac{1}{2}}}n^{m}_{p_{i,j}} - \mu_{p_{i,j-\frac{1}{2}}}d_{p_{i,j-\frac{1}{2}}}n^{m}_{p_{i,j-1}}\Bigg) \tag{B.11}$$

for the y-directed flux of positive ions.

B.1.2 Electron Fluxes

The electron flux approximations are similar, except that secondary electron emission may be present near material surfaces:

$$\Gamma_{ex} \approx -e{n_e}^{m}\mu_e{E_x}^{m+1} - e\mu_e T_e\frac{\partial {n_e}^{m}}{\partial x} - \gamma\Gamma_{px},$$

where γ is the secondary electron emission coefficient, which is zero in the gas region. The effects of secondary emission are dealt with separately in the following section; only the change in the bulk electron density is considered for the remainder of this section.

The Scharfetter-Gummel discretization for electron flux is nearly identical to that for ion flux:

$$\Gamma_{ex}\Big|_{i+\frac{1}{2},j} \approx \frac{\mu_e T_e}{\Delta x}\left(\frac{z^{m+1}_{i+\frac{1}{2},j}}{1-e^{z^{m+1}_{i+\frac{1}{2},j}}}n^{m}_{e_{i+1,j}} + \frac{z^{m+1}_{i+\frac{1}{2},j}}{1-e^{-z^{m+1}_{i+\frac{1}{2},j}}}n^{m}_{e_{i,j}}\right)$$

except that now

$$z_{i+\frac{1}{2},j} \equiv \frac{-E_{x_{i+\frac{1}{2},j}}\Delta x}{T_e} = \frac{+\phi_{i+1,j} - \phi_{i,j}}{T_e}$$

for electrons.

Using the same approximations for a small variation in z and the definitions of equations (B.3) to (B.6) (except now using the definition of z for electrons), we can define several terms that will

simplify the resulting expressions:

$$A_{ex}\Big|_{i+\frac{1}{2},j} \equiv \frac{e\Delta t\mu_{e_{i+\frac{1}{2},j}}}{\epsilon_0}\left(a_{e_{i+\frac{1}{2},j}}n^m_{e_{i+1,j}} + c_{e_{i+\frac{1}{2},j}}n^m_{e_{i,j}}\right) \tag{B.12}$$

$$B_{ex}\Big|_{i,j} \equiv \frac{e\Delta tT_e}{\epsilon_0}\Bigg(\mu_{e_{i+\frac{1}{2},j}}b_{e_{i+\frac{1}{2},j}}n^m_{e_{i+1,j}} + \mu_{e_{i+\frac{1}{2},j}}d_{e_{i+\frac{1}{2},j}}n^m_{e_{i,j}} - \mu_{e_{i-\frac{1}{2},j}}b_{e_{i-\frac{1}{2},j}}n^m_{e_{i,j}} - \mu_{e_{i-\frac{1}{2},j}}d_{e_{i-\frac{1}{2},j}}n^m_{e_{i-1,j}}\Bigg), \tag{B.13}$$

so that

$$-\frac{e\Delta t\Delta x^2}{\epsilon_0}\left(+\frac{\partial\Gamma_{ex}}{\partial x}\Big|_{i,j}\right) \approx -\phi^{m+1}_{i+1,j}A_{ex}\Big|_{i+\frac{1}{2},j} - \phi^{m+1}_{i-1,j}A_{ex}\Big|_{i-\frac{1}{2},j} + \phi^{m+1}_{i,j}\left(A_{ex}\Big|_{i+\frac{1}{2},j} + A_{ex}\Big|_{i-\frac{1}{2},j}\right) - B_{ex}\Big|_{i,j}.$$

The analogous definitions are

$$A_{ey}\Big|_{i,j+\frac{1}{2}} \equiv \frac{e\Delta t\mu_{e_{i,j+\frac{1}{2}}}}{\epsilon_0}\left(a_{e_{i,j+\frac{1}{2}}}n^m_{e_{i,j+1}} + c_{e_{i,j+\frac{1}{2}}}n^m_{e_{i,j}}\right) \tag{B.14}$$

and

$$B_{ey}\Big|_{i,j} \equiv \frac{e\Delta tT_e}{\epsilon_0}\Bigg(\mu_{e_{i,j+\frac{1}{2}}}b_{e_{i,j+\frac{1}{2}}}n^m_{e_{i,j+1}} + \mu_{e_{i,j+\frac{1}{2}}}d_{e_{i,j+\frac{1}{2}}}n^m_{e_{i,j}} - \mu_{e_{i,j-\frac{1}{2}}}b_{e_{i,j-\frac{1}{2}}}n^m_{e_{i,j}} - \mu_{e_{i,j-\frac{1}{2}}}d_{e_{i,j-\frac{1}{2}}}n^m_{e_{i,j-1}}\Bigg). \tag{B.15}$$

for the y-directed electron flux.

B.1.3 Secondary Electron Flux

We will consider the x-directed flux of secondary electrons first. Secondary electron flux in this direction must come from vertical surfaces. We assume that only positive ions may cause secondary electron emission. The secondary electron flux is then given by

$$\Gamma^{SE}_{ex}\Big|_{i+\frac{1}{2},j} = -\left(\gamma_{i+1,j} + \gamma_{i,j}\right)\Gamma_{px}\Big|_{i+\frac{1}{2},j}.$$

The two values of γ are added to account for a surface existing at either i or $i+1$. The only time both values will be non-zero will be inside of a material, where Γ_{px} itself must be zero.

To determine the change in electron density, we need the derivative of this flux. Using the constants defined in section B.1.1, this is

$$\begin{aligned}\left.\frac{\partial \Gamma_{ex}^{SE}}{\partial x}\right|_{i,j} \approx \frac{T_p}{(\Delta x)^2}\Bigg\{ &-\left(\gamma_{i+1,j}+\gamma_{i,j}\right)\mu_{p_{i+\frac{1}{2},j}}\Bigg[\left(z_{i+\frac{1}{2},j}^{m+1}a_{p_{i+\frac{1}{2},j}}+b_{p_{i+\frac{1}{2},j}}\right)n_{p_{i+1,j}}^{m} \\ &\qquad +\left(z_{i+\frac{1}{2},j}^{m+1}c_{p_{i+\frac{1}{2},j}}+d_{p_{i+\frac{1}{2},j}}\right)n_{p_{i,j}}^{m}\Bigg] \\ &+\left(\gamma_{i,j}+\gamma_{i-1,j}\right)\mu_{p_{i-\frac{1}{2},j}}\Bigg[\left(z_{i-\frac{1}{2},j}^{m+1}a_{p_{i-\frac{1}{2},j}}+b_{p_{i-\frac{1}{2},j}}\right)n_{p_{i,j}}^{m} \\ &\qquad +\left(z_{i-\frac{1}{2},j}^{m+1}c_{p_{i-\frac{1}{2},j}}+d_{p_{i-\frac{1}{2},j}}\right)n_{p_{i-1,j}}^{m}\Bigg]\Bigg\}\end{aligned}$$

We note that this is identical to equation (B.7), except with each mobility multiplied by a negative secondary electron emission coefficient. Consequently we can construct constants for the extra change in electron density due to secondary electron emission by analogy:

$$A_{ex}^{SE}\Big|_{i+\frac{1}{2},j} \equiv \frac{e\Delta t}{\epsilon_0}\mu_{p_{i+\frac{1}{2},j}}\left(\gamma_{i+1,j}+\gamma_{i,j}\right)\left(a_{p_{i+\frac{1}{2},j}}n_{p_{i+1,j}}^{m}+c_{p_{i+\frac{1}{2},j}}n_{p_{i,j}}^{m}\right) \tag{B.16}$$

and

$$\begin{aligned}B_{ex}^{SE}\Big|_{i,j} \equiv \frac{e\Delta t T_p}{\epsilon_0}\Bigg\{ &+\left(\gamma_{i+1,j}+\gamma_{i,j}\right)\mu_{p_{i+\frac{1}{2},j}}b_{p_{i+\frac{1}{2},j}}n_{p_{i+1,j}}^{m} \\ &-\left(\gamma_{i,j}+\gamma_{i-1,j}\right)\mu_{p_{i-\frac{1}{2},j}}d_{p_{i-\frac{1}{2},j}}n_{p_{i-1,j}}^{m} \\ &+\Bigg[+\left(\gamma_{i+1,j}+\gamma_{i,j}\right)\mu_{p_{i+\frac{1}{2},j}}d_{p_{i+\frac{1}{2},j}} \\ &\qquad -\left(\gamma_{i,j}+\gamma_{i-1,j}\right)\mu_{p_{i-\frac{1}{2},j}}b_{p_{i-\frac{1}{2},j}}\Bigg]n_{p_{i,j}}^{m}\Bigg\}\end{aligned} \tag{B.17}$$

in the x-direction. Then

$$\begin{aligned}-\frac{e\Delta t\Delta x^2}{\epsilon_0}\left(+\left.\frac{\partial \Gamma_{ex}^{SE}}{\partial x}\right|_{i,j}\right) \approx &-\phi_{i+1,j}^{m+1}A^{SE}\Big|_{i+\frac{1}{2},j}-\phi_{i-1,j}^{m+1}A^{SE}\Big|_{i-\frac{1}{2},j} \\ &+\phi_{i,j}^{m+1}\left(A^{SE}\Big|_{i+\frac{1}{2},j}+A^{SE}\Big|_{i-\frac{1}{2},j}\right)-B^{SE}\Big|_{i,j}.\end{aligned} \tag{B.18}$$

Similarly,

$$A_{ey}^{SE}\Big|_{i,j+\frac{1}{2}} \equiv \frac{e\Delta t}{\epsilon_0}\mu_{p_{i,j+\frac{1}{2}}}\left(\gamma_{i,j+1}+\gamma_{i,j}\right)\left(a_{p_{i,j+\frac{1}{2}}}n^{m}_{p_{i,j+1}}+c_{p_{i,j+\frac{1}{2}}}n^{m}_{p_{i,j}}\right) \tag{B.19}$$

and

$$\begin{aligned} B_{ey}^{SE}\Big|_{i,j} \equiv \frac{e\Delta t T_p}{\epsilon_0}\Bigg\{ &+\left(\gamma_{i,j+1}+\gamma_{i,j}\right)\mu_{p_{i,j+\frac{1}{2}}}b_{p_{i,j+\frac{1}{2}}}n^{m}_{p_{i+1,j}} \\ &-\left(\gamma_{i,j}+\gamma_{i,j-1}\right)\mu_{p_{i,j-\frac{1}{2}}}d_{p_{i,j-\frac{1}{2}}}n^{m}_{p_{i,j-1}} \\ &+\Bigg[+\left(\gamma_{i,j+1}+\gamma_{i,j}\right)\mu_{p_{i,j+\frac{1}{2}}}d_{p_{i,j+\frac{1}{2}}} \\ &\quad-\left(\gamma_{i,j}+\gamma_{i,j-1}\right)\mu_{p_{i,j-\frac{1}{2}}}b_{p_{i,j-\frac{1}{2}}}\Bigg]n^{m}_{p_{i,j}}\Bigg\} \end{aligned} \tag{B.20}$$

for the y-direction.

B.1.4 Negative Ion Fluxes

Since the negative ions have a negative charge, their flux can be described in an exact analogy to the electron flux. So

$$\begin{aligned} -\frac{e\Delta t\Delta x^2}{\epsilon_0}\left(+\frac{\partial\Gamma_{nx}}{\partial t}\right)\Bigg|_{i,j} \approx &-\phi^{m+1}_{i+1,j}A_{nx}\Big|_{i+\frac{1}{2},j}-\phi^{m+1}_{i-1,j}A_{nx}\Big|_{i-\frac{1}{2},j} \\ &+\phi^{m+1}_{i,j}\left(A_{nx}\Big|_{i+\frac{1}{2},j}+A_{nx}\Big|_{i-\frac{1}{2},j}\right)-B_{nx}\Big|_{i,j}, \end{aligned}$$

where

$$A_{nx}\Big|_{i+\frac{1}{2},j} \equiv \frac{e\Delta t\mu_{n_{i+\frac{1}{2},j}}}{\epsilon_0}\left(a_{n_{i+\frac{1}{2},j}}n^{m}_{n_{i+1,j}}+c_{n_{i+\frac{1}{2},j}}n^{m}_{n_{i,j}}\right) \tag{B.21}$$

$$\begin{aligned} B_{nx}\Big|_{i,j} \equiv \frac{e\Delta t T_n}{\epsilon_0}\Big(&\mu_{n_{i+\frac{1}{2},j}}b_{n_{i+\frac{1}{2},j}}n^{m}_{n_{i+1,j}}+\mu_{n_{i+\frac{1}{2},j}}d_{n_{i+\frac{1}{2},j}}n^{m}_{n_{i,j}} \\ &-\mu_{n_{i-\frac{1}{2},j}}b_{n_{i-\frac{1}{2},j}}n^{m}_{n_{i,j}}-\mu_{n_{i-\frac{1}{2},j}}d_{n_{i-\frac{1}{2},j}}n^{m}_{n_{i-1,j}}\Big). \end{aligned} \tag{B.22}$$

In the calculations of a_n, b_n, c_n, and d_n, the definition

$$z_{i+\frac{1}{2},j} = -E_x\Delta_x/T_n$$

is used. Similarly,

$$A_{ny}\Big|_{i,j+\frac{1}{2}} \equiv \frac{n\Delta t\mu_{n_{i,j+\frac{1}{2}}}}{\epsilon_0}\left(a_{n_{i,j+\frac{1}{2}}} n_{ni,j+1}^{m} + c_{n_{i,j+\frac{1}{2}}} n_{ni,j}^{m}\right) \tag{B.23}$$

$$B_{ey}\Big|_{i,j} \equiv \frac{e\Delta t T_n}{\epsilon_0}\Bigg(\mu_{n_{i,j+\frac{1}{2}}} b_{n_{i,j+\frac{1}{2}}} n_{ni,j+1}^{m} + \mu_{n_{i,j+\frac{1}{2}}} d_{n_{i,j+\frac{1}{2}}} n_{ni,j}^{m} - \mu_{n_{i,j-\frac{1}{2}}} b_{n_{i,j-\frac{1}{2}}} n_{ni,j}^{m} - \mu_{n_{i,j-\frac{1}{2}}} d_{n_{i,j-\frac{1}{2}}} n_{ni,j-1}^{m}\Bigg). \tag{B.24}$$

for the y-directed negative ion flux.

B.1.5 Modified Poisson Equation

Inserting our approximations for all of the flux derivatives into equation (B.1) yields

$$
\begin{aligned}
\phi_{i+1,j}^{m+1}+\phi_{i-1,j}^{m+1}+\phi_{i,j+1}^{m+1}+\phi_{i,j-1}^{m+1}-4\phi_{i,j}^{m+1} = \\
&-\frac{e\Delta x^2}{\epsilon_0}\left(n_p^m-n_e^m-n_n^m\right) \\
&+B_{px}\Big|_{i,j}+B_{py}\Big|_{i,j}-B_{ex}\Big|_{i,j}-B_{ey}\Big|_{i,j} \\
&-B_{ex}^{SE}\Big|_{i,j}-B_{ey}^{SE}\Big|_{i,j}-B_{nx}\Big|_{i,j}-B_{ny}\Big|_{i,j} \\
&-\phi_{i+1,j}^{m+1}\left(A_{px}\Big|_{i+\frac{1}{2},j}+A_{ex}\Big|_{i+\frac{1}{2},j}+A_{ex}^{SE}\Big|_{i+\frac{1}{2},j}+A_{nx}\Big|_{i+\frac{1}{2},j}\right) \\
&-\phi_{i-1,j}^{m+1}\left(A_{px}\Big|_{i-\frac{1}{2},j}+A_{ex}\Big|_{i-\frac{1}{2},j}+A_{ex}^{SE}\Big|_{i-\frac{1}{2},j}+A_{nx}\Big|_{i-\frac{1}{2},j}\right) \\
&-\phi_{i,j+1}^{m+1}\left(A_{py}\Big|_{i,j+\frac{1}{2}}+A_{ey}\Big|_{i,j+\frac{1}{2}}+A_{ey}^{SE}\Big|_{i,j+\frac{1}{2}}+A_{ny}\Big|_{i,j+\frac{1}{2}}\right) \\
&-\phi_{i,j-1}^{m+1}\left(A_{py}\Big|_{i,j-\frac{1}{2}}+A_{ey}\Big|_{i,j-\frac{1}{2}}+A_{ey}^{SE}\Big|_{i,j-\frac{1}{2}}+A_{ny}\Big|_{i,j-\frac{1}{2}}\right) \\
&+\phi_{i,j}^{m+1}\Bigg(A_{px}\Big|_{i+\frac{1}{2},j}+A_{px}\Big|_{i-\frac{1}{2},j}+A_{py}\Big|_{i,j+\frac{1}{2}}+A_{py}\Big|_{i,j-\frac{1}{2}} \\
&\qquad +A_{ex}\Big|_{i+\frac{1}{2},j}+A_{ex}\Big|_{i-\frac{1}{2},j}+A_{ey}\Big|_{i,j+\frac{1}{2}}+A_{ex}\Big|_{i,j-\frac{1}{2}} \\
&\qquad +A_{ex}^{SE}\Big|_{i+\frac{1}{2},j}+A_{ex}^{SE}\Big|_{i-\frac{1}{2},j}+A_{ey}^{SE}\Big|_{i,j+\frac{1}{2}}+A_{ex}^{SE}\Big|_{i,j-\frac{1}{2}} \\
&\qquad +A_{nx}\Big|_{i+\frac{1}{2},j}+A_{nx}\Big|_{i-\frac{1}{2},j}+A_{ny}\Big|_{i,j+\frac{1}{2}}+A_{nx}\Big|_{i,j-\frac{1}{2}}\Bigg).
\end{aligned}
\tag{B.25}
$$

This leads us to define

$$
\begin{aligned}
A \equiv 4 &+ A_{px}\Big|_{i+\frac{1}{2},j} + A_{px}\Big|_{i-\frac{1}{2},j} + A_{py}\Big|_{i,j+\frac{1}{2}} + A_{py}\Big|_{i,j-\frac{1}{2}} \\
&+ A_{ex}\Big|_{i+\frac{1}{2},j} + A_{ex}\Big|_{i-\frac{1}{2},j} + A_{ey}\Big|_{i,j+\frac{1}{2}} + A_{ey}\Big|_{i,j-\frac{1}{2}} \\
&+ A^{SE}_{ex}\Big|_{i+\frac{1}{2},j} + A^{SE}_{ex}\Big|_{i-\frac{1}{2},j} + A^{SE}_{ey}\Big|_{i,j+\frac{1}{2}} + A^{SE}_{ey}\Big|_{i,j-\frac{1}{2}} \\
&+ A_{nx}\Big|_{i+\frac{1}{2},j} + A_{nx}\Big|_{i-\frac{1}{2},j} + A_{ny}\Big|_{i,j+\frac{1}{2}} + A_{ny}\Big|_{i,j-\frac{1}{2}}
\end{aligned}
$$

and the update terms actually used in the successive over-relaxation algorithm:

$$
C1 \equiv \left(1 + A_{px}\Big|_{i+\frac{1}{2},j} + A_{ex}\Big|_{i+\frac{1}{2},j} + A^{SE}_{ex}\Big|_{i+\frac{1}{2},j} + A_{nx}\Big|_{i+\frac{1}{2},j}\right) \Big/ A \tag{B.26}
$$

$$
C2 \equiv \left(1 + A_{px}\Big|_{i-\frac{1}{2},j} + A_{ex}\Big|_{i-\frac{1}{2},j} + A^{SE}_{ex}\Big|_{i-\frac{1}{2},j} + A_{nx}\Big|_{i-\frac{1}{2},j}\right) \Big/ A \tag{B.27}
$$

$$
C3 \equiv \left(1 + A_{py}\Big|_{i,j+\frac{1}{2}} + A_{ey}\Big|_{i,j+\frac{1}{2}} + A^{SE}_{ey}\Big|_{i,j+\frac{1}{2}} + A_{ny}\Big|_{i,j+\frac{1}{2}}\right) \Big/ A \tag{B.28}
$$

$$
C4 \equiv \left(1 + A_{py}\Big|_{i-\frac{1}{2},j} + A_{ey}\Big|_{i,j-\frac{1}{2}} + A^{SE}_{ey}\Big|_{i,j-\frac{1}{2}} + A_{ny}\Big|_{i,j-\frac{1}{2}}\right) \Big/ A \tag{B.29}
$$

$$
\begin{aligned}
C5 \equiv \Bigg[&+ \frac{e\Delta x^2}{\epsilon_0}\left(n_p^m - n_e^m - n_n^m\right) \\
&- B_{px}\Big|_{i,j} - B_{py}\Big|_{i,j} + B_{ex}\Big|_{i,j} + B_{ey}\Big|_{i,j} \\
&+ B^{SE}_{ex}\Big|_{i,j} + B^{SE}_{ey}\Big|_{i,j} + B_{nx}\Big|_{i,j} + B_{ny}\Big|_{i,j}\Bigg] \Big/ A.
\end{aligned} \tag{B.30}
$$

Using our newly defined terms in equation (B.25) yields the final update expression for the bulk plasma and bulk dielectric regions:

$$
\phi^{m+1}_{i,j} = C1(i,j)\phi^{m+1}_{i+1,j} + C2(i,j)\phi^{m+1}_{i-1,j} + C3(i,j)\phi^{m+1}_{i,j+1} + C4(i,j)\phi^{m+1}_{i,j-1} + C5(i,j). \tag{B.31}
$$

Inside electrodes, the potential must equal the specified voltage, so we set $C1 = C2 = C3 = C4 = 0$ there, and set $C5$ equal to the voltage.

B.1.6 Corrections at the Dielectric Surface

At the dielectric surface, the electrostatic potential is strongly affected both by the presence of surface charge and the change in dielectric constant. In addition, many of the terms described above are zero either at or just below a dielectric surface, so the update terms may be simplified there.

Currently, the simulation code requires that there be only a single, rectangular dielectric region extending from the bottom of the simulation domain to the grid index $j = js$. It fills the entire x-width of the domain. The relative dielectric constant beneath the surface is ϵ_d, and precisely on the surface we take it to be $(1 + \epsilon_d)/2$. All particle densities are set to zero on the surface. The derivation below reflects this geometry.

Consider just the left-hand side of Poisson's equation, evaluated at the dielectric surface. Applying the standard finite difference approximations, the LHS becomes

$$\begin{aligned} -\nabla \cdot \left(\epsilon \vec{E}\right) &= -\epsilon_0 \left[\frac{1+\epsilon_d}{2}\frac{\partial E_x}{\partial x} + \frac{\partial}{\partial y}\left(\epsilon_r E_y\right)\right] \\ &= \epsilon_0 \left(\frac{1+\epsilon_d}{2\Delta x^2}\right)\left(\phi_{i+1,j} + \phi_{i-1,j} - 2\phi_{i,j}\right) \\ &\quad + \left(\frac{\epsilon_0}{\Delta y^2}\right)\left(\phi_{i,j+1} + \epsilon_d \phi_{i,j-1} - 2\frac{1+\epsilon_d}{2}\phi_{i,j}\right). \end{aligned}$$

Assuming $\Delta x = \Delta y$, we can further simplify this to

$$\frac{\epsilon_0}{\Delta x^2}\left[-4\frac{1+\epsilon_d}{2}\phi_{i,j} + \frac{1+\epsilon_d}{2}\phi_{i+1,j} + \frac{1+\epsilon_d}{2}\phi_{i-1,j} + \phi_{i,j+1} + \epsilon_d \phi_{i,j-1}\right].$$

At the dielectric surface the particle densities are all zero, but the right-hand side is not zero. The flux of charge to the surface during all previous time-steps is accounted for in the surface charge. The flux of charge to the surface during the current time-step is accounted for by the non-zero values of some of the flux derivatives. Since there are no particles on the surface, only the y-derivatives of the particle fluxes will be non-zero. Accounting for these features, the RHS of Poisson's equation is

$$\frac{-\sigma}{\Delta x} - e\Delta t\left(-\frac{\partial \Gamma_{py}}{\partial y} + \frac{\partial \Gamma_{ey}}{\partial y} + \frac{\partial \Gamma_{ey}^{SE}}{\partial y} + \frac{\partial \Gamma_{ny}}{\partial y}\right)$$

.

From our earlier description of the bulk plasma,

$$\frac{-e\Delta t\Delta x^2}{\epsilon_0}\left(-\frac{\partial\Gamma_{py}}{\partial y}\right)\Bigg|_{i,js} = -\phi_{i,js+1}A_{py}\Big|_{i,js+\frac{1}{2}} - \phi_{i,js-1}A_{py}\Big|_{i,js-\frac{1}{2}} + \phi_{i,js}\left(A_{py}\Big|_{i,js+\frac{1}{2}} + A_{py}\Big|_{i,js-\frac{1}{2}}\right) - B_{py}\Big|_{i,js},$$

but due to the absence of particles on and under the dielectric surface,

$$A_{py}\Big|_{i,js-\frac{1}{2}} = B_{py}\Big|_{i,js} = 0.$$

The other particle species can be examined in a similar fashion. From the analysis of both right- and left-hand sides of the equation, we now define a new constant on the dielectric surface:

$$A_{i,js} = 4\left(\frac{1+\epsilon_d}{2}\right) + \left(A_{py} + A_{ey} + A_{py}^{SE} + A_{ny}\right)\Big|_{i,js+\frac{1}{2}}. \tag{B.32}$$

Now we may define new update constants similar to those discussed previously:

$$C1(i,js) = \left(\frac{1+\epsilon_d}{2}\right)/A_{i,js} \tag{B.33}$$

$$C2(i,js) = \left(\frac{1+\epsilon_d}{2}\right)/A_{i,js} \tag{B.34}$$

$$C3(i,js) = \left(1 + A_{py}\Big|_{i,js+\frac{1}{2}} + A_{ey}\Big|_{i,js+\frac{1}{2}} + A_{py}^{SE}\Big|_{i,js+\frac{1}{2}} + A_{ny}\Big|_{i,js+\frac{1}{2}}\right)/A_{i,js} \tag{B.35}$$

$$C4(i,js) = \epsilon_d/A_{i,js} \tag{B.36}$$

$$C5(i,js) = \frac{\sigma^m\Delta x}{\epsilon_0}/A_{i,js}. \tag{B.37}$$

B.2 The Continuity Equation Solver

We will consider the case of electrons in detail, then state the algorithms for positive and negative ions by analogy.

B.2.1 Electrons

The continuity equation for electrons is given by

$$\frac{\partial n_e}{\partial t} = -\nabla \cdot \vec{\Gamma}_e + S_{iz} - S_{att} - R_{pe} \tag{B.38}$$

where Γ_e is the electron flux, S_{iz} is the total rate of ionization, S_{att} is the total rate of attachment, and R_{pe} is the total rate of positive ion-electron recombination. In an explicit scheme, the right-hand side of equation (B.38) is evaluated at time step m. In a completely implicit scheme, it is evaluated at $m+1$. Here we use a semi-implicit scheme where the flux divergence is evaluated at $m+1$ and all other terms at m. This allows us to obtain the stability of an implicit scheme while still maintaining much of the simplicity (and fast code execution) of an explicit scheme.

The electron flux consists of the bulk flux plus the flux of secondary electrons emitted from material surfaces. For simplicity, we will group the divergence of the secondary electron flux with the sources and sinks. Our semi-implicit scheme is then written as

$$\frac{\partial n_e}{\partial t} = (-\nabla \cdot \Gamma_e)\Big|^{m+1} + \left[-\nabla \cdot \Gamma_e^{SE} + S_{iz} - S_{att} - R_{pe}\right]\Big|^{m}.$$

Begin by considering the bulk electron flux. As in the Poisson solver, we use the Scharfetter-Gummel discretization (see section 6.2.2) for the flux:

$$\Gamma_{ex}\Big|^{m+1}_{i+\frac{1}{2},j} = \frac{\mu_{e_{i+\frac{1}{2},j}} T_e}{\Delta x}\left(\frac{z^{m+1}_{i+\frac{1}{2},j}}{1-e^{z^{m+1}_{i+\frac{1}{2},j}}} n_{e\,i+1,j}^{m+1} + \frac{z^{m+1}_{i+\frac{1}{2},j}}{1-e^{-z^{m+1}_{i+\frac{1}{2},j}}} n_{e\,i,j}^{m+1}\right).$$

The values of z at $m+1$ are already known, as the Poisson solver executes prior to the continuity solver at each time step. To simplify the flux expressions, we define

$$Z1_{ex}(z) = \frac{\mu_e T_e}{\Delta x}\frac{z}{1-e^z} \quad \text{and} \quad Z2_{ex}(z) = \frac{\mu_e T_e}{\Delta x}\frac{z}{1-e^{-z}},$$

where the subscript ex indicates to use the definition of z appropriate for x-directed electron flux. With these definitions, we can write a simplified expression for the discretized spatial derivative of the flux.

$$\frac{\partial \Gamma_{ex}}{\partial x}\Big|^{m+1}_{i,j} \approx \frac{1}{\Delta x} Z1_{ex}\Big|^{m+1}_{i+\frac{1}{2},j} n_{e\,i+1,j}^{m+1} + \frac{1}{\Delta x}\left(Z2_{ex}\Big|^{m+1}_{i+\frac{1}{2},j} + Z1_{ex}\Big|^{m+1}_{i-\frac{1}{2},j}\right) n_{e\,i,j}^{m+1} - \frac{1}{\Delta x} Z2_{ex}\Big|^{m+1}_{i-\frac{1}{2},j} n_{e\,i-1,j}^{m+1}.$$

To simplify our final update expression for n_e we define

$$A_e \equiv \frac{\Delta t}{\Delta x}\left(Z2_{ex}\Big|_{i+\frac{1}{2},j}^{m+1} - Z1_{ex}\Big|_{i-\frac{1}{2},j}^{m+1}\right) + \frac{\Delta t}{\Delta y}\left(Z2_{ey}\Big|_{i,j+\frac{1}{2}}^{m+1} - Z1_{ey}\Big|_{i,j-\frac{1}{2}}^{m+1}\right).$$

Using this, we then define

$$C1_e(i,j) \equiv \left(-\frac{\Delta t}{\Delta x}Z1_{ex}\Big|_{i+\frac{1}{2},j}^{m+1}\right) \Big/ (1+A_e) \tag{B.39}$$

$$C2_e(i,j) \equiv \left(+\frac{\Delta t}{\Delta x}Z2_{ex}\Big|_{i-\frac{1}{2},j}^{m+1}\right) \Big/ (1+A_e) \tag{B.40}$$

$$C3_e(i,j) \equiv \left(-\frac{\Delta t}{\Delta y}Z1_{ey}\Big|_{i,j+\frac{1}{2}}^{m+1}\right) \Big/ (1+A_e) \tag{B.41}$$

$$C4_e(i,j) \equiv \left(+\frac{\Delta t}{\Delta y}Z2_{ey}\Big|_{i,j-\frac{1}{2}}^{m+1}\right) \Big/ (1+A_e) \tag{B.42}$$

$$C5_e(i,j) \equiv \left[{n_e}_{i,j}^{m} + \Delta t\left(-\nabla\cdot\Gamma_e^{SE} + S_{iz} - S_{att} - R_{pe}\right)_{i,j}^{m}\right] \Big/ (1+A_e) \tag{B.43}$$

so that

$${n_e}_{i,j}^{m+1} = C1_e {n_e}_{i+1,j}^{m+1} + C2_e {n_e}_{i-1,j}^{m+1} + C3_e {n_e}_{i,j+1}^{m+1} + C4_e {n_e}_{i,j-1}^{m+1} + C5_e. \tag{B.44}$$

Equation (B.44) is solved iteratively using the Gauss-Seidel method. For other particle species, all terms except $C5$ can be calculated by direct analogy.

The ionization, attachment, and recombination rates in $C5_e$ are calculated as described in section 6.1.2. The flux of secondary electrons exists only near material boundaries, and is calculated using

$$\Gamma_{ex}^{SE}\Big|_{i+\frac{1}{2},j} = \begin{cases} -\left(\gamma_{i+1,j}+\gamma_{i,j}\right)\Gamma_{px}\Big|_{i+\frac{1}{2},j}, & E_x\cdot\Gamma_{px} > 0 \\ 0, & E_x\cdot\Gamma_{px} < 0 \end{cases}.$$

The separate cases exist because we assume that any ions diffusing into the surface, rather than accelerated by an electric field, will not have enough energy to knock off any electrons. The y-component of the secondary electron flux is computed similarly. The divergence of the flux is determined using the same standard finite difference formulas used elsewhere in this derivation.

B.2.2 Positive Ions

Positive ions are generated via electron-impact ionization, and lost through recombination both with electrons and with negative ions. By analogy to the equations in section B.2.1, we write

$$C1_p(i,j) \equiv \left(-\frac{\Delta t}{\Delta x} Z1_{px} \Big|_{i+\frac{1}{2},j}^{m+1} \right) \Big/ (1 + A_p) \tag{B.45}$$

$$C2_p(i,j) \equiv \left(+\frac{\Delta t}{\Delta x} Z2_{px} \Big|_{i-\frac{1}{2},j}^{m+1} \right) \Big/ (1 + A_p) \tag{B.46}$$

$$C3_p(i,j) \equiv \left(-\frac{\Delta t}{\Delta y} Z1_{py} \Big|_{i,j+\frac{1}{2}}^{m+1} \right) \Big/ (1 + A_p) \tag{B.47}$$

$$C4_p(i,j) \equiv \left(+\frac{\Delta t}{\Delta y} Z2_{py} \Big|_{i,j-\frac{1}{2}}^{m+1} \right) \Big/ (1 + A_p) \tag{B.48}$$

$$C5_p(i,j) \equiv \left[{n_p}_{i,j}^{m} + \Delta t \left(S_{iz} - R_{pe} - R_{pn} \right)_{i,j}^{m} \right] \Big/ (1 + A_p) \,. \tag{B.49}$$

B.2.3 Negative Ions

Negative ions are created via electron attachment to neutral molecules, and lost only through recombination with positive ions. Then for negative ions

$$C1_n(i,j) \equiv \left(-\frac{\Delta t}{\Delta x} Z1_{nx} \Big|_{i+\frac{1}{2},j}^{m+1} \right) \Big/ (1 + A_n) \tag{B.50}$$

$$C2_n(i,j) \equiv \left(+\frac{\Delta t}{\Delta x} Z2_{nx} \Big|_{i-\frac{1}{2},j}^{m+1} \right) \Big/ (1 + A_n) \tag{B.51}$$

$$C3_n(i,j) \equiv \left(-\frac{\Delta t}{\Delta y} Z1_{ny} \Big|_{i,j+\frac{1}{2}}^{m+1} \right) \Big/ (1 + A_n) \tag{B.52}$$

$$C4_n(i,j) \equiv \left(+\frac{\Delta t}{\Delta y} Z2_{ny} \Big|_{i,j-\frac{1}{2}}^{m+1} \right) \Big/ (1 + A_n) \tag{B.53}$$

$$C5_n(i,j) \equiv \left[{n_n}_{i,j}^{m} + \Delta t \left(S_{att} - R_{pn} \right)_{i,j}^{m} \right] \Big/ (1 + A_n) \,. \tag{B.54}$$

Appendix C: List of Symbols

Symbols

A	Constant parameter in the Poisson's or continuity equation solvers
a, b, c, d	Constant parameters in the Poisson's equation solver
B	Constant parameters in the Poisson's equation solver
$\vec{B}$	Magnetic field (T)
a_f	Adjustment factor used in determining Δt
$C1$–$C5$	Constant parameters in the Poisson's or continuity equation solvers
d	Electrode diameter (m)
d_0	Force or linear force density fit parameter (m)
$\vec{E}$	Electric field (V/m)
E/p	Total reduced electric field (V m^{-1} Torr^{-1})
$\mathcal{E}_{iz}$	Ionization energy (eV)
e	Fundamental charge, 1.602×10^{-19} C
$\vec{F}_{\text{body}}$	Body force acting in a control volume (N)
F_{fit}	Force or linear force density fit parameter (N or N/m)
F_{plasma}	Plasma body force (N)
F_{shear}	Shear force (N)
$\vec{F}_{\text{surf}}$	Surface force acting on a control volume (N)
F_0	Force or linear force density fit parameter (m)
F_1	Force or linear force density fit parameter (m)
$\vec{f}_{\text{EHD}}$	Electro-hydrodynamic force density (N/m^3)
i, j	Compuational grid indices in the x and y directions, respectively
js	y grid index of the dielectric surface
L	Unit length (m)
L_0	Gas flow velocity fit parameter (m)
ℓ_c	Chord length of an airfoil (m)
m	Particle mass (kg)

n	Particle number density (m^{-3})
p	Pressure (Pa)
p_{ref}	Reference pressure (Pa)
p_0	Gas stagnation pressure (Pa)
Q	Charge on an electrode (C)
R	Sink rate (m^{-3} s^{-1})
Re_c	Chord Reynolds number
r	Recombination coefficient (m^3 / s)
S	Source rate (m^{-3} s^{-1})
T	Particle temperature (eV)
$\vec{u}$	Gas flow velocity (m/s)
u_{fit}	Skewed Gaussian fit to the measured gas velocity (m/s)
u_0	Gas flow velocity fit parameter (m/s)
V	Applied voltage (V)
V_B	Breakdown voltage (V)
$\vec{v}$	Charged-particle fluid velocity (m/s)
x_{max}	Extent of corona discharge region (m)
y_0	Gas flow velocity fit parameter (m)
$Z1, Z2$	Constant parameters in the continuity equation solver
z	Non-dimensional electric field in the Scharfetter-Gummel discretization
α	Ionization coefficient (m^{-1})
Γ	Particle flux (m^{-2} s^{-1})
γ	Secondary electron emission coefficient
Δx	x-spacing of the computational grid (m)
Δy	y-spacing of the computational grid (m)
Δt	Temporal step size (s)
ϵ	Electrical permittivity of a medium (F/m)
ϵ_0	Permittivity of free space, 8.854×10^{-12} F/m
ϵ_d	Relative permittivity of the dielectric material
η	Electron attachment coefficient (m^{-1})

λ	Mean free path (m)
λ_D	Debye Length (m)
λ_{el}	Mean free path for elastic collisions (m)
λ_{in}	Mean free path for inelastic collisions (m)
λ_ϵ	Energy relaxation length (m)
μ	Particle mobility ($\text{m}^2\ \text{V}^{-1}\ \text{s}^{-1}$)
μ_g	Dynamic viscosity of the neutral gas ($\text{kg m}^{-1}\ \text{s}^{-1}$)
ν	Collision frequency (s^{-1})
ν_m	Effective momentum transfer frequency (s^{-1})
ρ	Mass density (kg m^{-3})
σ	Free surface charge on a dielectric (C / m^2)
σ_p	Plasma conductivity (S / m)
ϕ	Electrostatic potential (V)
ω_c	Cyclotron frequency (s^{-1})

Symbol subscripts

att	due to electron attachment
bulk	away from material surfaces
eff	effective value of a quantity
diel	of a dielectric
e	of electrons
elec	of an electrode
g	of the neutral gas
iz	due to electron-impact ionization
i, j	at the i^{th} and j^{th} grid indices
max, min	maximum and minimum allowed values
N2	of nitrogen gas
n	of negative ions
O2	of oxygen gas
p	of positive ions
x, y, z	in the x, y, or z directions, respectively
α	of a generic charged-particle species
$+$	of all positively-charged particles
$-$	of all negatively-charged particles

Symbol superscripts

m	computational time index
SE	due to secondary electron emission

References

[1] U. Kogelschatz, "Atmospheric-pressure plasma technology," *Plasma Phys. Contr. Fusion*, vol. 46, pp. B63–B75, 2004.

[2] L. S. Hultgren and D. E. Ashpis, "Demonstration of separation delay with glow-discharge plasma actuators," in *41st AIAA Aerospace Sciences Meeting*, Jan. 2003, 2003-1025.

[3] M. L. Post and T. C. Corke, "Separation control on high angle of attack airfoil using plasma actuators," *AIAA J.*, vol. 42, no. 11, pp. 2177–2184, Nov. 2004.

[4] J. R. Roth, "Aerodynamic flow acceleration using paraelectric and peristaltic electrohydrodynamic effects of a One Atmosphere Uniform Glow Discharge Plasma," *Phys. Plasmas*, vol. 10, no. 5, pp. 2117–2126, May 2003.

[5] J. Huang, T. C. Corke, and F. O. Thomas, "Plasma actuators for separation control of low-pressure turbine blades," *AIAA J.*, vol. 44, no. 1, pp. 51–57, Jan. 2006.

[6] O. Sharma, "Impact of Reynolds number on LP turbine performance," in *Minnowbrook II 1997 Workshop on Boundary Layer Transition in Turbomachines*, June 1998, pp. 65–69.

[7] R. J. Volino and L. S. Hultgren, "Measurements in separated and transitional boundary layers under low-pressure turbine airfoil conditions," *J. Turbomachinery*, vol. 123, pp. 189–197, Apr. 2001.

[8] D. Ashpis, "The NASA low-pressure turbine flow physics program," in *Minnowbrook II 1997 Workshop on Boundary Layer Transition in Turbomachines*, June 1998, pp. 45–52.

[9] L. E. Cruz-Barba, S. Manolache, and F. Denes, "Generation of teflon-like layers on cellophane surfaces under atmospheric pressure non-equilibrium SF_6-plasma environments," *Polymer Bull.*, vol. 50, pp. 381–387, 2003.

[10] M. Šimor, J. Ráhel, P. Vojtek, and M. Černák, "Atmospheric-pressure diffuse coplanar surface discharge for surface treatments," *Appl. Phys. Lett.*, vol. 81, no. 15, pp. 2716–2718, Oct. 2002.

[11] D. F. Opaits, G. Neretti, S. H. Zaidi, M. N. Shneider, R. B. Miles, A. V. Likhanskii, and S. O. Macheret, "DBD plasma actuators driven by a combination of low frequency bias voltage and nanosecond pulses," in *46th AIAA Aerospace Sciences Meeting*, Jan. 2008, 2008-1372.

[12] J. W. Baughn, C. O. Porter, B. L. Peterson, T. E. McLaughlin, C. L. Enloe, G. I. Font, and C. Baird, "Momentum transfer for an aerodynamic plasma actuator with an imposed boundary layer," in *44th AIAA Aerospace Sciences Meeting*, Jan. 2006, 2006-168.

[13] J. P. Boeuf and L. C. Pitchford, "Electrohydrodynamic force and aerodynamic flow acceleration in surface dielectric barrier discharge," *J. Appl. Phys.*, vol. 97, no. 103307, May 2005.

[14] J. P. Boeuf, Y. Lagmich, T. Unfer, T. Callegari, and L. C. Pitchford, "Electrohydrodynamic force in dielectric barrier discharge plasma actuators," *J. Phys. D*, vol. 40, pp. 652–662, Jan. 2007.

[15] J. R. Roth, D. M. Sherman, and S. P. Wilkinson, "Electrohydrodynamic flow control with a glow-discharge surface plasma," *AIAA J.*, vol. 38, no. 7, pp. 1166–1172, July 2000.

[16] V. I. Demidov, S. V. Ratynskaia, and K. Rypdal, "Electric probes for plasmas: The link between theory and instrument," *Rev. Sci. Instr.*, vol. 73, no. 10, pp. 3409–3439, 2002.

[17] M. A. Lieberman and A. J. Lichtenberg, *Principles of Plasma Discharges and Materials Processing*. Hoboken, NJ: Wiley, 2005.

[18] E. Basurto, J. de Urquijo, I. Alvarez, and C. Cisneros, "Mobility of He^+, Ne^+, N_2^+, O_2^+, and CO_2^+ in their parent gas," *Phys. Rev. E*, vol. 61, no. 3, pp. 3053–3057, 2000.

[19] CPAT and Kinema Software. The Siglo Data Base. Accessed 14 Mar 2006. [Online]. Available: http://www.siglo-kinema.com

[20] E. H. Warner and J. Kunz, "Corona discharge," *Bulletin of the University of Illinois Engineering Experiment Station*, vol. 16, no. 41, pp. 128–265, June 1919.

[21] J. R. Roth, *Industrial Plasma Engineering: Principles*. Bristol: IoP, 1995.

[22] M. Goldman and A. Goldman, *Corona Discharges*. Academic Press, 1978, vol. 1, pp. 219–290.

[23] L. B. Loeb, *Electrical Coronas: Their Basic Physical Mechanisms*. Berkeley, CA: University of California Press, 1965.

[24] A. Fridman, A. Chirokov, and A. Gutsol, "Non-thermal atmospheric pressure discharges," *J. Phys. D*, vol. 38, pp. R1–R24, 2005.

[25] S. Okazaki, M. Kogoma, M. Uehara, and Y. Kimura, "Appearance of stable glow discharge in air, argon, oxygen, and nitrogen at atmospheric pressure using a 50 Hz source," *J. Phys. D*, vol. 26, pp. 889–892, 1993.

[26] Y. B. Golubovskii, V. A. Maiorov, J. F. Behnke, J. Tepper, and M. Lindmayer, "Study of the homogeneous glow-like discharge in nitrogen at atmospheric pressure," *J. Phys. D*, vol. 37, no. Apr., pp. 1346–1356, 2004.

[27] Z. Fang, Y. Qiu, C. Zhang, and E. Kuffel, "Factors influencing the existence of the homogeneous dielectric barrier discharge in air at atmospheric pressure," *J. Phys. D*, vol. 40, pp. 1401–1407, Feb. 2007.

[28] F. Massines, A. Rabehi, P. Decomps, R. Ben Gadri, P. Ségur, and C. Mayoux, "Experimental and theoretical study of a glow discharge at atmospheric pressure controlled by dielectric barrier," *J. Appl. Phys.*, vol. 83, no. 6, pp. 2950–2957, 1998.

[29] G. Nersisyan, T. Morrow, and W. G. Graham, "Measurements of helium metastable density in an atmospheric pressure glow discharge," *Appl. Phys. Lett.*, vol. 85, no. 9, pp. 1487–1489, Aug. 2004.

[30] J. J. Shi and M. G. Kong, "Radio-frequency dielectric-barrier glow discharges in atmospheric argon," *Appl. Phys. Lett.*, vol. 90, no. 111502, Mar. 2007.

[31] F. Massines and G. Gouda, "A comparison of polypropylene-surface treatment by filamentary, homogeneous and glow discharges in helium at atmospheric pressure," *J. Phys. D*, vol. 31, pp. 3411–3420, 1998.

[32] T. Shirafuji, T. Kitagawa, T. Wakai, and K. Tachibana, "Observation of self-organized filaments in a dielectric barrier discharge of ar gas," *Appl. Phys. Lett.*, vol. 83, no. 12, pp. 2309–2311, Sep. 2003.

[33] L. Stollenwerk, S. Amiranashvili, J. P. Boeuf, and H. G. Purwins, "Measurement and 3D simulation of self-organized filaments in a barrier discharge," *Phys. Rev. Lett.*, vol. 96, no. 255001, June 2006.

[34] D. Trunec, A. Brablec, and J. Buchta, "Atmospheric pressure glow discharge in neon," *J. Phys. D*, vol. 34, pp. 1697–1699, 2001.

[35] U. Kogelschatz, "Filamentary, patterned, and diffuse barrier discharges," *IEEE Trans. Plasma Sci.*, vol. 30, no. 4, pp. 1400–1408, 2002.

[36] R. Brandenburg, V. A. Maiorov, Y. B. Golubovskii, H. E. Wagner, J. Behnke, and J. F. Behnke, "Diffuse barrier discharges in nitrogen with small admixtures of oxygen: discharge mechanism and transition to the filamentary regime," *J. Phys. D*, vol. 38, pp. 2187–2197, Jun. 2005.

[37] D. Korzec, E. G. Finantu-Dinu, M. Teschke, J. Engemann, M. Miclea, K. Kunze, J. Franzke, and K. Niemax, "Characterization of a surface barrier discharge in helium," *Plasma Sources Sci. Technol.*, vol. 15, pp. 345–359, Apr. 2006.

[38] V. I. Gibalov and G. J. Pietsch, "The development of dielectric barrier discharges in gas gaps and on surfaces," *J. Phys. D*, vol. 33, pp. 2618–2636, 2000.

[39] C. L. Enloe, T. E. McLaughlin, R. D. VanDyken, K. D. Kachner, E. J. Jumper, T. C. Corke, M. Post, and O. Haddad, "Mechanisms and responses of a single dielectric barrier plasma actuator: Geometric effects," *AIAA J.*, vol. 42, no. 3, pp. 595–604, Mar. 2004.

[40] V. I. Gibalov and G. J. Pietsch, "Dynamics of dielectric barrier discharges in coplanar arrangements," *J. Phys. D*, vol. 37, pp. 2082–2092, July 2004.

[41] ——, "Properties of dielectric barrier discharges in extended coplanar electrode systems," *J. Phys. D*, vol. 37, pp. 2093–2100, July 2004.

[42] C. Punset, S. Cany, and J. P. Boeuf, "Addressing and sustaining in alternating current coplanar plasma display panels," *J. Appl. Phys.*, vol. 86, no. 1, pp. 124–133, July 1999.

[43] R. Dorai and M. J. Kushner, "Consequences of unburned hydrocarbons on microstreamer dynamics and chemistry during plasma remediation of NO_x using dielectric barrier discharges," *J. Phys. D*, vol. 36, pp. 1075–1083, Apr. 2003.

[44] S. J. Scott, C. C. Figgures, and D. G. Dixon, "Dielectric barrier discharge processing of aerospace materials," *Plasma Sources Sci. Technol.*, vol. 13, pp. 461–465, July 2004.

[45] W. Steer, "Etching of polyimide in an atmospheric pressure dielectric barrier discharge," Master's thesis, University of Wisconsin-Madison, 2000.

[46] E. Moreau, "Airflow control by non-thermal plasma actuators," *J. Phys. D*, vol. 40, pp. 605–636, Oct. 2007.

[47] R. W. Fox and A. T. McDonald, *Introduction to Fluid Mechanics*. New York: Wiley, 1998.

[48] T. C. Corke and M. L. Post, "Overview of plasma flow control: Concepts, optimization, and applications," in *43rd AIAA Aerospace Sciences Meeting*, Jan. 2005, 2005-0563.

[49] D. P. Rizzetta and M. R. Visbal, "Numerical study of active flow control for a transitional highly loaded low-pressure turbine," *J. Fluids Engr.*, vol. 128, pp. 956–967, Sep. 2006.

[50] A. Gross and H. F. Fasel, "Numerical investigation of low-pressure turbine blade separation control," *AIAA J.*, vol. 43, no. 12, pp. 2514–2525, Dec. 2005.

[51] D. P. Rizzetta and M. R. Visbal, "Plasma-based flow-control strategies for transitional highly loaded low-pressure turbines," *J. Fluids Engr.*, vol. 130, no. 041104, Apr. 2008.

[52] F. O. Thomas, A. Kozlov, and T. C. Corke, "Plasma actuators for landing gear noise reduction," in *11th AIAA/CEAS Aeroacoustics Conference*, May 2005, 2005-3010.

[53] G. Raman and A. B. Cain, "Innovative actuators for active flow and noise control," *J. Aerospace Engr.*, vol. 126, pp. 303–324, 2002.

[54] S. Grundmann, M. Frey, and C. Tropea, "Unmanned aerial vehicle (UAV) with plasma actuators for separation control," in *47th AIAA Aerospace Sciences Meeting*, Jan. 2009, 2009-0698.

[55] B. R. McAuliffe and S. A. Sjolander, "Active flow control using steady blowing for a low-pressure turbine cascade," *J. Turbomachinery*, vol. 126, pp. 560–569, Oct. 2004.

[56] M. W. Bettridge, B. L. Smith, and R. E. Spall, "Aerodynamic jet steering using steady blowing and suction," *Exp. Fluids*, vol. 40, pp. 776–785, Feb. 2006.

[57] M. Amitay and F. Cannelle, "Evolution of finite span synthetic jets," *Phys. Fluids*, vol. 18, no. 054101, May 2006.

[58] J. L. Gilarranz, L. W. Traub, and O. K. Rediniotis, "A new class of synthetic jet actuators—Part II: Application to flow separation control," *J. Fluids Engr.*, vol. 127, pp. 377–387, Mar. 2005.

[59] D. You and P. Moin, "Active control of flow separation over an airfoil using synthetic jets," *J. Fluids Structures*, vol. 24, pp. 1349–1357, Oct. 2008.

[60] A. Santhanakrishnan, J. D. Jacob, and Y. B. Suzen, "Flow control using plasma actuators and linear/annular plasma synthetic jet actuators," in *3rd AIAA Flow Control Conference*, June 2006, 2006-3033.

[61] A. Santhanakrishnan and J. D. Jacob, "Flow control with plasma synthetic jet actuators," *J. Phys. D*, vol. 40, pp. 637–651, Jan. 2007.

[62] D. V. Roupassov, I. N. Zavyalov, and A. Y. Starikovskii, "Boundary layer separation plasma control using low-temperature non-equilibrium plasma of gas discharge," in *44th AIAA Aerospace Sciences Meeting*, Jan. 2006, 2006-373.

[63] J. Pons, E. Moreau, and G. Touchard, "Asymmetric surface dielectric barrier discharge in air at atmospheric pressure: Electrical properties and induced airflow characteristics," *J. Phys. D*, vol. 38, pp. 3635–3642, Sep. 2005.

[64] T. N. Jukes, K. S. Choi, G. A. Johnson, and S. J. Scott, "Characterization of surface plasma-induced wall flows through velocity and temperature measurements," *AIAA J.*, vol. 44, no. 4, pp. 764–771, Apr. 2006.

[65] J. R. Roth and X. Dai, "Optimization of the aerodynamic plasma actuator as an electrohydrodynamic (EHD) electrical device," in *44th AIAA Aerospace Sciences Meeting*, Jan. 2006, 2006-1203.

[66] M. Forte, J. Jolibois, J. Pons, E. Moreau, G. Touchard, and M. Cazalens, "Optimization of a dielectric barrier discharge actuator by stationary and non-stationary measurements of the induced flow velocity: application to airflow control," *Exp. Fluids*, vol. 43, no. 6, pp. 917–928, Dec. 2007.

[67] T. Abe, Y. Takizawa, S. Sato, and N. Kimura, "Experimental study for momentum transfer in a dielectric barrier discharge plasma actuator," *AIAA J.*, vol. 46, no. 9, pp. 2248–2256, Sep. 2008.

[68] C. L. Enloe, T. E. McLaughlin, and G. I. Font, "Parameterization of temporal structure in the single-dielectric-barrier aerodynamic plasma actuator," *AIAA J.*, vol. 44, no. 6, pp. 1127–1136, June 2006.

[69] W. Kim, H. Do, M. G. Mungal, and M. A. Cappelli, "On the role of oxygen in dielectric barrier discharge actuation of aerodynamic flows," *Appl. Phys. Lett.*, vol. 91, no. 181501, Oct. 2007.

[70] C. L. Enloe, T. E. McLaughlin, R. D. VanDyken, K. D. Kachner, E. J. Jumper, and T. C. Corke, "Mechanisms and responses of a single dielectric barrier plasma actuator: Plasma morphology," *AIAA J.*, vol. 42, no. 3, pp. 589–594, 2004.

[71] C. L. Enloe, M. G. McHarg, and T. E. McLaughlin, "Time-correlated force production measurements of the dielectric barrier discharge plasma aerodynamic actuator," *J. Appl. Phys.*, vol. 103, no. 073302, April 2008.

[72] D. M. Orlov, G. I. Font, and D. Edelstein, "Characterization of discharge modes of plasma actuators," in *46th AIAA Aerospace Sciences Meeting*, Jan. 2008, 2008-1409.

[73] A. Sasoh, K. Kikuchi, and T. Sakai, "Spatio-temporal filament behaviour in a dielectric barrier discharge plasma actuator," *J. Phys. D*, vol. 40, pp. 4181–4184, June 2007.

[74] M. Forte, L. Leger, J. Pons, E. Moreau, and G. Touchard, "Plasma actuators for airflow control: measurement of the non-stationary induced flow velocity," *J. Electrostatics*, vol. 63, pp. 929–936, 2005.

[75] C. L. Enloe, M. G. McHarg, G. I. Font, and T. E. McLaughlin, "Plasma-induced force and self-induced drag in the dielectric barrier discharge aerodynamic plasma actuator," in *47th AIAA Aerospace Sciences Meeting*, Jan. 2009, 2009-1622.

[76] B. A. Gibson, M. Arjomandi, and R. M. Kelso, "Investigation of the effect of electrode arrangement on plasma actuator performance," in *47th AIAA Aerospace Sciences Meeting*, Jan. 2009, 2009-1003.

[77] K. D. Hall, E. J. Jumper, T. C. Corke, and T. E. McLaughlin, "Potential flow model of a plasma actuator as a lift enhancement device," in *43rd AIAA Aerospace Sciences Meeting*, Jan. 2005, 2005-783.

[78] W. Shyy, B. Jayaraman, and A. Andersson, "Modeling of glow discharge-induced fluid dynamics," *J. Appl. Phys.*, vol. 92, no. 11, pp. 6434–6443, Dec. 2002.

[79] D. M. Orlov and T. C. Corke, "Numerical simulation of aerodynamic plasma actuator effects," in *43rd AIAA Aerospace Sciences Meeting*, Jan. 2005, 2005-1083.

[80] B. E. Mertz and T. C. Corke, "Time-dependent dielectric barrier dishcharge plasma actuator modeling," in *47th AIAA Aerospace Sciences Meeting*, Jan. 2009, 2009-1083.

[81] G. I. Font, "Boundary-layer control with atmospheric plasma discharges," *AIAA J.*, vol. 44, no. 7, pp. 1572–1578, July 2006.

[82] M. A. Huerta and L. D. Ludeking, "Some results of dielectric barrier discharge simulations using the PIC code MAGIC," in *47th AIAA Aerospace Sciences Meeting*, Jan. 2009, 2009-0652.

[83] K. P. Singh and S. Roy, "Simulation of an asymmetric single dielectric barrier plasma actuator," *J. Appl. Phys.*, vol. 98, no. 083303, Oct. 2005.

[84] S. Roy, "Flow actuation using radio frequency in partially ionized collisional plasmas," *Appl. Phys. Lett.*, vol. 86, no. 101502, 2005.

[85] S. Roy, K. P. Singh, and D. V. Gaitonde, "Dielectric barrier plasma dynamics for active control of separated flows," *Appl. Phys. Lett.*, vol. 88, no. 121501, Mar. 2006.

[86] K. P. Singh and S. Roy, "Physics of plasma actuator operating in atmospheric air," *Appl. Phys. Lett.*, vol. 92, no. 111502, Mar. 2008.

[87] A. V. Likhanskii, M. N. Shneider, S. O. Macheret, and R. B. Miles, "Modeling of dielectric barrier discharge plasma actuator in air," *J. Appl. Phys.*, vol. 103, no. 053305, Mar. 2008.

[88] A. V. Likhanskii, V. V. Semak, M. N. Shneider, D. F. Opaits, R. B. Miles, and S. O. Macheret, "The role of the photoionization in the numerical modeling of the DBD plasma actuator," in *47th AIAA Aerospace Sciences Meeting*, Jan. 2009, 2009-0841.

[89] Y. Lagmich, T. Callegari, T. Unfer, L. C. Pitchford, and J. P. Boeuf, "Electrohydrodynamic force and scaling laws in surface dielectric barrier discharges," *Appl. Phys. Lett.*, vol. 90, no. 051502, Feb. 2007.

[90] Y. Lagmich, T. Callegar, L. C. Pitchford, and J. P. Boeuf, "Model description of surface dielectric barrier discharges for flow control," *J. Phys. D*, vol. 41, no. 095205, Apr. 2008.

[91] A. V. Likhanskii, M. N. Shneider, S. O. Macheret, and R. B. Miles, "Modeling of dielectric barrier discharge plasma actuators driven by repetitive nanosecond pulses," *Phys. Plasmas*, vol. 14, no. 073501, July 2007.

[92] T. Unfer, J. P. Boeuf, F. Rogier, and F. Thivet, "Modeling of dielectric barrier discharge and coupling with computational fluid dynamics," in *46th AIAA Aerospace Sciences Meeting*, Jan. 2008, 2008-1375.

[93] J. P. Boeuf, Y. Lagmich, T. Callegari, L. C. Pitchford, and T. Unfer, "New insights in the physics of DBD plasma actuators for flow control," in *46th AIAA Aerospace Sciences Meeting*, Jan. 2008, 2008-1376.

[94] A. R. Hoskinson, N. Hershkowitz, and D. E. Ashpis, "Force measurements of single and double barrier dbd plasma actuators in quiescent air," *J. Phys. D*, vol. 41, no. 24, p. 245209, Dec. 2008.

[95] C. O. Porter, J. W. Baughn, T. E. McLaughlin, and C. L. Enloe, "Plasma actuator force measurements," *AIAA J.*, vol. 45, no. 7, pp. 1562–1570, July 2007.

[96] J. Shin and L. L. Raja, "Run-to-run variations, asymmetric pulses, and long time-scale transient phenomena in dielectric-barrier atmospheric pressure glow discharges," *J. Phys. D*, vol. 40, pp. 3145–3154, May 2007.

[97] Y. B. Suzen, P. G. Huang, J. D. Jacob, and D. E. Ashpis, "Numerical simulations of plasma based flow control applications," in *35th Fluid Dynamics Conference*, June 2005, 2005-4633.

[98] A. R. Hoskinson, L. Oksuz, and N. Hershkowitz, "Microdischarge propagation and expansion in a surface dielectric barrier discharge," *Appl. Phys. Lett.*, vol. 93, no. 22, p. 221501, Dec. 2008.

[99] M. Tuszewski and R. R. White, "Equilibrium properties of Ar / SF_6 inductive plasma discharges," *Plasma Sources Sci. Technol.*, vol. 11, pp. 338–350, Aug. 2002.

[100] D. Q. Posin, "The Townsend coefficients and spark discharge," *Phys. Rev.*, vol. 50, pp. 650–658, Oct. 1936.

[101] J. P. Boeuf, "Numerical model of rf glow discharges," *Phys. Rev. A*, vol. 36, no. 6, pp. 2782–2792, Sep. 1987.

[102] P. J. Drallos, V. P. Nagorny, and W. Williamson Jr., "A kinetic stufy of the local field approximation in simulations of AC plasma display panels," *Plasma Sources Sci. Technol.*, vol. 4, pp. 576–590, 1995.

[103] D. L. Scharfetter and H. K. Gummel, "Large-signal analysis of a silicon read diode oscillator," *IEEE Trans. Electron Dev.*, vol. ED-16, no. 1, pp. 64–77, Jan. 1969.

[104] M. S. Barnes, T. J. Colter, and M. E. Elta, "Large-signal time-domain model of low-pressure rf glow discharges," *J. Appl. Phys.*, vol. 61, no. 1, pp. 81–89, Jan. 1987.

[105] P. L. G. Ventzek, R. J. Hoekstra, and M. J. Kushner, "Two-dimensional modeling of high plasma density inductively coupled sources for materials processing," *J. Vac. Sci. Tech. B*, vol. 12, no. 1, pp. 461–471, Jan/Feb 1994.

[106] Y. Jaluria, *Computer Methods for Engineering*. Philadelphia: Taylor & Francis, 1996.

[107] Condor Team. Condor high throughput computing. Accessed 10 Dec 2008. [Online]. Available: http://www.cs.wisc.edu/condor/

REPORT DOCUMENTATION PAGE	Form Approved OMB No. 0704-0188

1. REPORT DATE *(DD-MM-YYYY)*	2. REPORT TYPE	3. DATES COVERED *(From - To)*
01-09-2012	Final Contractor Report	

4. TITLE AND SUBTITLE
Measurements and Simulations of Surface Dielectric Barrier Discharges Used as Plasma Actuators
Final Report

5a. CONTRACT NUMBER
NNX07AB84A

5b. GRANT NUMBER
FA9550-07-1-0025

5c. PROGRAM ELEMENT NUMBER

6. AUTHOR(S)
Hoskinson, Alan, R.

5d. PROJECT NUMBER

5e. TASK NUMBER

5f. WORK UNIT NUMBER
WBS 561581.02.08.03.47.02.03

7. PERFORMING ORGANIZATION NAME(S) AND ADDRESS(ES)
University of Wisconsin-Madison
1025 West Johnson Street
Madison, Wisconsin 53706

8. PERFORMING ORGANIZATION REPORT NUMBER
E-18218

9. SPONSORING/MONITORING AGENCY NAME(S) AND ADDRESS(ES)
National Aeronautics and Space Administration
Washington, DC 20546-0001

10. SPONSORING/MONITOR'S ACRONYM(S)
NASA

11. SPONSORING/MONITORING REPORT NUMBER
NASA/CR-2012-217628

12. DISTRIBUTION/AVAILABILITY STATEMENT
Unclassified-Unlimited
Subject Categories: 02, 05, 07, 13, and 75
Available electronically at http://www.sti.nasa.gov
This publication is available from the NASA Center for AeroSpace Information, 443-757-5802

13. SUPPLEMENTARY NOTES
This report was submitted as a dissertation in partial fulfillment of the requirements for the degree Doctor of Philosophy for Nuclear Engineering and Engineering Physics to the University of Wisconsin-Madison, Madison, Wisconsin, June 2009. Grant technical monitor, David E. Ashpis, Aeropropulsion Division, Glenn Research Center, organization code RTTO, ashpis@nasa.gov

14. ABSTRACT
This report is a Ph.D. dissertation performed under NRA cooperative agreement and submitted as part of the final report. Asymmetric surface dielectric barrier discharges (DBDs) have shown promise for use as aerodynamic actuators for active flow control. In this project we studied DBD actuators experimentally and numerically. Our DBDs used a symmetric triangular high voltage waveform to generate plasma in atmospheric pressure air. Time-averaged measurements indicated that the induced force of a single barrier actuator design (one electrode insulated from the plasma) can be increased exponentially above the results of previous studies by decreasing both the length and thickness of the electrode exposed to the plasma. This increased force may allow these devices to control flow separation in a wider range of flow environments. Experiments using an intensified digital camera to examine the plasma on time scales of a few nanoseconds showed that, in addition to the previously-observed filamentary and jet-like plasma structures, discharges with very thin exposed electrodes exhibited a weak but constant plasma immediately adjacent to those electrodes. In double-barrier actuators (both electrodes insulated), decreasing the diameter of the narrower electrode lead to increasing forces, and recorded images showed the simultaneous existence of both filamentary and jet-like plasma structures. The development and application of a time-dependent, two-dimensional computational fluid plasma model has aided in understanding the detailed physics of surface DBDs at all-time scales. For simulated single-barrier discharges, the model qualitatively reproduced the filamentary and jet-like microdischarge structures. The model was somewhat successful in reproducing the observed characteristics of double-barrier actuators. For both actuator geometries, the model indicated that the majority of the forces induced on the neutral gas occur in between microdischarges as the plasmas decay.

15. SUBJECT TERMS
Plasma; Dielectric barrier discharge; DBD; Flow control; High voltage

16. SECURITY CLASSIFICATION OF:			17. LIMITATION OF ABSTRACT	18. NUMBER OF PAGES	19a. NAME OF RESPONSIBLE PERSON
a. REPORT	b. ABSTRACT	c. THIS PAGE			STI Help Desk (email:help@sti.nasa.gov)
U	U	U	UU	208	19b. TELEPHONE NUMBER *(include area code)* 443-757-5802